Dissertation zur Erlangung des Doktorgrades
der Fakultät für Chemie und Pharmazie
der Ludwig-Maximilians-Universität München

Synthesis, thermal behavior and thermoelectric properties of disordered tellurides with structures derived from the rocksalt type

Thorsten Schröder

aus

Haltern, Deutschland

2014

Erklärung

Diese Dissertation wurde im Sinne von § 7 der Promotionsordnung vom 28. November 2011 von Herrn Prof. Dr. O. Oeckler betreut.

Eidesstattliche Versicherung

Diese Dissertation wurde eigenständig und ohne unerlaubte Hilfe erarbeitet.

München, 25.07.2014

.....

(Thorsten Schröder)

Dissertation eingereicht am	12.05.2014
1. Gutachter:	Prof. Dr. O. Oeckler
2. Gutachter:	Prof. Dr. W. Schnick
Mündliche Prüfung am	17.06.2014

Für meine Familie

Acknowledgement

First of all, I want to thank Prof. Dr. Oliver Oeckler for supervising my PhD thesis. He mentored me since the time of my bachelor thesis and constantly awoke my interest for solid-state chemistry. Furthermore, I would like to thank him for constructively assisting my scholarship applications. He supported me throughout the thesis with brilliant suggestions and interesting discussions concerning my results and life in general. I am grateful that I was able to work on such an interesting and fertile topic and that he made it possible to present my results not only through my publications, but also on many national and international conferences. His input and ideas perfected my manuscripts.

I want to thank Prof. Dr. Wolfgang Schnick for his generous support of my thesis. I also would like to thank him for supporting my scholarship applications and especially for granting me access to his high-pressure equipment from which many of my results originated. I am more than happy that he is willing to be the second referee of my thesis.

I would like to thank Prof. Dr. Wolfgang Schmahl, Prof. Dr. Hans-Christian Böttcher, Prof. Dr. Konstantin Karaghiosoff and Prof. Dr. Dirk Johrendt for taking time to evaluate my thesis and completing my examination committee.

I am grateful to the Studienstiftung des deutschen Volkes for granting me a PhD scholarship and making this thesis possible.

Furthermore, I like to thank Wolfgang Wünschheim for his support with all IT related topics, Thomas Miller for the single-crystal and temperature-dependent powder X-ray diffraction measurements as well as Christian Minke for all SEM-EDX measurements. Special thanks go to Sylvia Proksch and Olga Lorenz for help with all organizational duties.

I thank my colleagues and friends from lab D2.100 for constant help and support, endless discussion on and off topic and years of an enjoyable working atmosphere. First of all, I would like to thank Tobias Rosenthal for spending endless hours with me at the TEM, investigating the atomic scale. This teamwork was not only very productive, but also a lot of fun. Thank you for your constant support under all circumstances. Next, I would like to thank Matthias Schneider for introducing me to the world of tellurides, for fruitful discussions and

supporting me on my early days of the PhD project. Furthermore, I want to thank Markus Seibald for his constant support as well as exciting football evenings. I am grateful to Felix Fahrnbauer and Lukas Neudert for interesting discussions and enjoyable joint projects. Furthermore, I thank Frauke Thienel, Christine Pösl, Saskia Lupart and Robin Niklaus for completing the perfect cast in this laboratory.

I am thankful to Nadja Giesbrecht, Markus Nentwig, Stefan Schwarzmüller, Daniel Souchay, Stefan Maier, Sabastian Grott and Christian Petermayer for assisting me during their bachelor theses and research internships. Without you I would not have been able to investigate so many materials in such a short time.

Furthermore, I am indebted to thank all cooperation partners, Prof. Dr. Wolfgang Scherer, Dr. Ernst-Wilhelm Scheidt and Dr. Christian Gold from the University of Augsburg, Dr. Christian Stiewe and Dr. Johannes de Boor from the German Aerospace Center as well as Prof. Dr. G. Jeffrey Snyder and Heng Wang from the California Institute of Technology for state-of-the-art thermoelectric measurements. I would also like to thank Rico Berthold from the Max Planck Institute for Chemical Physics of Solids for help with the melt-spinning experiments and Dr. Markus Hölzel for support with the SPODI neutron diffractometer at the FRMII.

I want to thank Peter Schultz, Frank Heinke, Robert Schlegel and PD Dr. Gerald Wagner from the IMKM Leipzig for constant support of my work and constructive discussion. Additionally, I want to thank Simon Welzmiller and Philipp Urban for supplying me a sleeping berth every time I was in Leipzig and for great beam times at the ESRF. I would like to thank all members of Prof. Dr. Schnick's, Prof. Dr. Johrendt's, Prof. Dr. Lotsch's, Prof. Dr. Schmedt auf der Günne's and Dr. Hoch's groups at the LMU Munich, for creating a constructive and enjoyable working atmosphere.

I would also like to thank all of my friends and band members for supporting me and providing plenty of procrastination possibilities.

Last but definitely not least, I would like to thank my family for their strong support especially during the very sad moments in the last couple of years.

Das schönste Glück des denkenden Menschen ist,
das Erforschliche erforscht zu haben
und das Unerforschliche ruhig zu verehren.
(Johann Wolfgang von Goethe)

Table of contents

1 Introduction

1.1 Telluride-based thermoelectric and phase-change materials

Although it is a rare element, many commonly used functional materials are based on tellurium, because tellurides exhibit combinations of desirable properties that can hardly be found in other materials. Both for thermoelectric and for phase-change materials (PCMs), the use of tellurium is almost essential. Thermoelectric materials can either be used for power generation from waste heat or for the construction of cooling or heating devices that establish a temperature gradient when a voltage is applied. Concerning thermoelectric materials, the combination of high electrical conductivities (σ) and high Seebeck coefficients (S) in addition with low thermal conductivities (κ) leads to high thermoelectric figures of merit $ZT = \sigma S^2 T/\kappa$ for many tellurides. Usually, high electrical conductivity leads to high thermal conductivity, because the electronic contribution to the thermal conductivity (κ_e) is proportional to σ according to the Wiedermann-Franz law: $\kappa_e/\sigma = LT$ (with Lorenz numbers L from $1.11 \cdot 10^{-8}$ $W\Omega K^{-2}$ according to the Drude model up to $2.44 \cdot 10^{-8}$ $W\Omega K^{-2}$ according to the free-electron Drude-Sommerfeld model, depending on the nature of the used material). However, it is important to note that the total κ is the sum of κ_e and the phononic contribution to the thermal conductivity (κ_{ph}). This fact and, as a consequence, the possibility to alter κ_{ph} more or less independently of S and σ in order to optimize the thermoelectric properties make tellurides one of the most promising class of thermoelectric materials: In addition to the large atomic weight of tellurium, which itself hinders phonon propagation, many multinary tellurides are highly disordered even though their average structures correspond to simple structure types (cf. Chapter 1.2). Disorder and associated real-structure phenomena such as short-range order, formation of nanostructures or intergrowth of different domains (cf. Chapter 1.3) more strongly increase phonon scattering than they increase electron scattering. This situation can lead to a larger reduction of κ_{ph} (and thus κ) as compared to σ, which subsequently can result in higher ZT values. Thus, the reduction of κ_{ph} is a main focus of research on thermoelectrics.[1]

In addition to the possibilities of optimizing the thermal conductivity of tellurides, their electrical properties are also suitable for application as thermoelectric materials, because many tellurides are small-bandgap semiconductors with high Seebeck coefficients. Again, these properties depend on each other as the Seebeck coefficient depends on the charge-carrier concentration (n) and σ depends on n as well as the charge-carrier mobility (μ).

The structural diversity of tellurides further allows the optimization of these properties by suitable substitutions. These may also change the majority charge-carrier type (electrons or holes) of the materials. This is useful as thermoelectric generators (TEGs) consist of an arrangement of p-type (holes) and n-type (electrons) legs of thermoelectric materials in order to make the electrical current flow possible.[2] In order to determine the efficiency of a thermoelectric generator, the averaged ZT value of both leg materials has to be used.[3]

The long-term goal for thermoelectric generators is their large-scale application as devices for the recovery of energy which is otherwise wasted, but their still rather low efficiencies in combination with high costs narrow the fields of application. However, thermoelectric materials have possible applications due to their non-stationary use that is not feasible for other recovery techniques like heat exchangers. Therefore, thermoelectric materials are used in TEGs at the exhaust pipe of cars and radioisotope TEGs in satellites and spacecrafts or as Peltier coolers in computers and other reversible heating/cooling devices, e. g. in car seats.

In search for better telluride-based thermoelectric materials or ways of increasing the efficiency of already known compounds, e. g. by nanostructuring, another class of materials comes into the focus of research, the PCMs mentioned at the beginning. In all relevant PCMs, the use of tellurides is essential, not necessarily due to the properties mentioned above, but mainly due to their potential to easily form inert glasses when quenched.[4-7] The interplay and reversible switching between metastable crystalline and amorphous regions is used for data storage. This is achieved by laser irradiation in optical media, e. g. in rewritable CDs, DVDs and Blu-ray Discs as well as electrically by applying a voltage (resistance heating) in PCRAM devices. Although the glass formation is the most important feature of PCMs, their use in optical media suggests that their κ should be low in order to have a high data-storage density, i. e. small recording marks. The application in PCRAM indicates that the compounds' σ should be in the range of small-bandgap semiconductors in order to allow resistance heating as well as read-out processes without significantly heating the material. The low κ and intermediate σ in combination with similar compositions compared to the materials already applied as TEGs render PCMs ideal starting points for the discovery of new and the optimization of known thermoelectric materials.[8]

1.2 Structural features of tellurides derived from an fcc tellurium-atom substructure

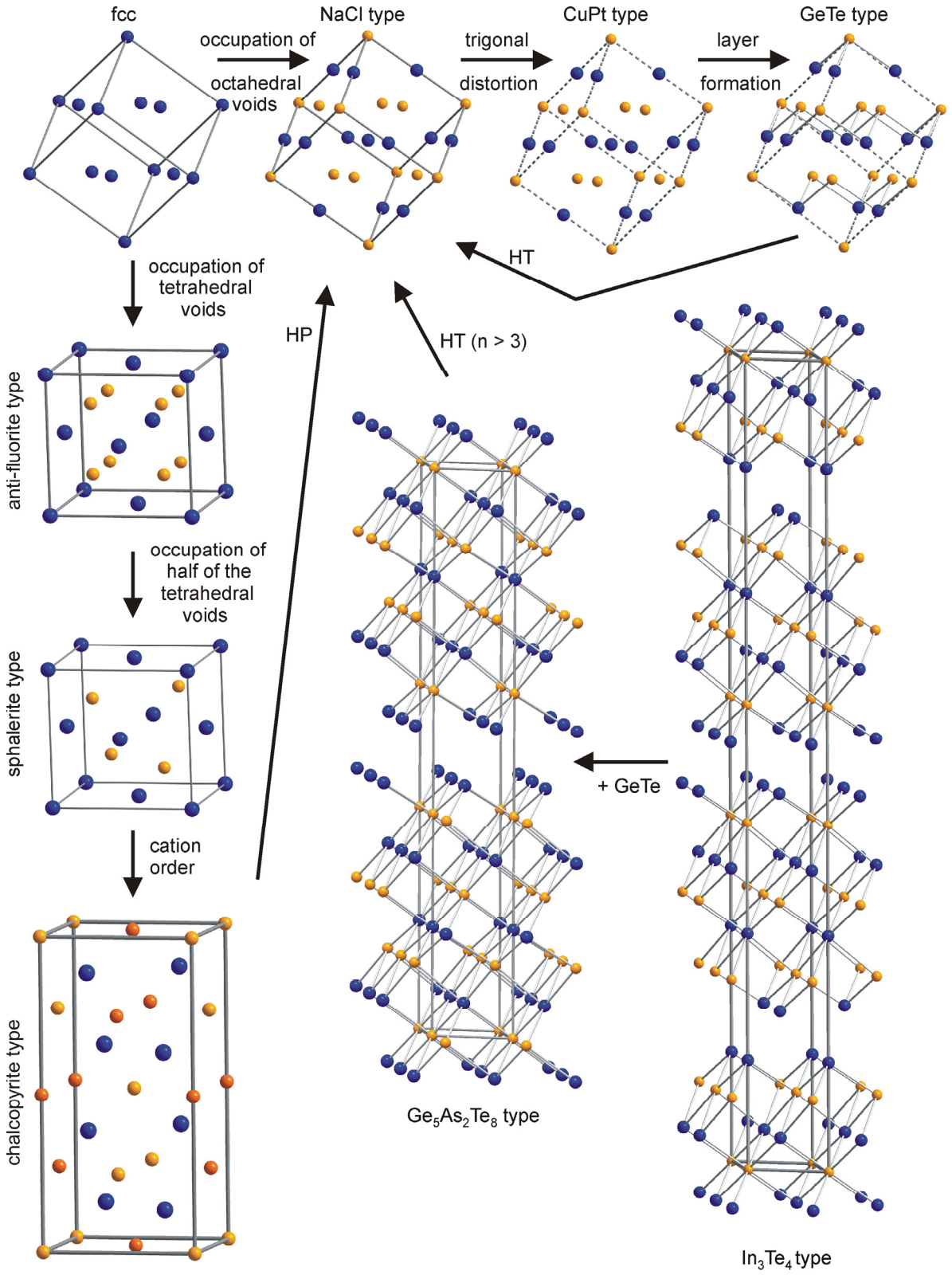

Fig. 1. Schematic overview of possible crystal structures based on more or less distorted face-centered cubic Te-atom substructures.

Many crystal structures of tellurides, often featuring disordered cations, can be derived from a sometimes distorted fcc substructure of Te atoms (cf. Fig. 1). The occupation of the fcc packing's octahedral voids with cations leads to the rocksalt-type structure,[9] which is observed, for example, for $AgSbTe_2$ whose cations are disordered.[10] If this structure is formally stretched along <111>, the trigonal CuPt type is formed; this corresponds to a symmetry reduction from $Fm\bar{3}m$ to $R\bar{3}m$.[11] In the CuPt-type structure, anions occupy the 0 0 0 position and cations the 0 0 0.5 position of a trigonal unit cell in which the original cubic space diagonal corresponds to the trigonal [001] direction. If, in addition, the *z* parameter of the cations significantly deviates from 0.5 within this trigonal unit cell, layers of interconnected corrugated six-membered rings are formed and the crystal structure corresponds to the α-GeTe type. For this structure type, the symmetry is further reduced to the polar space group $R3m$.[12,13] Like GeTe itself, many compounds that crystallize in this structure type form rocksalt-type high-temperature (HT) phases. If it is impossible to differentiate between the cations and anions of the GeTe-type layers, e. g. due to disorder, the crystal structure corresponds to the centrosymmetric gray As-type ($R\bar{3}m$) with only one atom position in the trigonal unit cell.[14]

If instead of the octahedral voids, the tetrahedral voids of the fcc substructure are completely occupied by cations, the crystal structure corresponds to an anti-fluorite type ($Fm\bar{3}m$), e. g. observed for Li_2Te.[15] If every other, i. e. 50%, of the tetrahedral voids are occupied, the symmetry is reduced to $F\bar{4}3m$ in the sphalerite-type structure.[16] When two cations are involved and they alternate, e. g. as in $AgInTe_2$, the tetragonal chalcopyrite type with an approximately doubled *c* lattice parameter is present ($I\bar{4}2d$).[17] In order to form polymorphs with rocksalt-type structures, it is often enough to expose compounds that crystallize in the α-GeTe type to high temperatures, whereas for chalcopyrite-type phases, in accordance with the pressure-coordination rule, high-pressure conditions are necessary.[18]

Many tellurides in which the number of anions exceeds the number of cations form long-periodically ordered trigonal phases. In these structures, a sequence of layers which can be understood as slabs cut out of the rocksalt-type structure (i. e. coordination number 6) are separated by van der Waals gaps perpendicular [001]. The slabs are terminated by Te atom layers and the thickness of these slabs depends on the chemical composition of the compounds. For the homologous series $(GeTe)_nSb_2Te_3$ (so-called GST materials), for example, each slab gains 2 more layers for each added formula unit of GeTe.[19] Depending on the stacking sequence and n, the space groups correspond either to $R\bar{3}m$ or to $P\bar{3}m1$. For $n \geq 3$, these compounds form rocksalt-type high-temperature (HT) phases.[20] Cation vacancies are

randomly disordered over the cation position in these phases. Quenching the cubic HT phases yields metastable nanostructured phases. These can be understood as intermediate states during the formation of the layered trigonal phases. In such metastable phases, vacancy layers with limited lateral extension perpendicular to the cubic <111> directions intersect. In contrast to the equidistant van der Waals gaps of the trigonal structures, the vacancy layers in the metastable phases are not spaced equidistantly. Although the vacancy order in the metastable and in the high-temperature phase is completely different, the average structures of both quenched and HT compounds correspond to the rocksalt-type structure. In thin films, e. g. for PCM applications, a metastable rocksalt-type phase of GST materials can also be observed.[21] Due to the random disorder of cation vacancies, its structure rather corresponds to the HT phase and not to the metastable quenched bulk material; however, recently defect layer formation could also be observed for thin film samples of $(GeTe)_2Sb_2Te_3$.[22] Furthermore, there is an ongoing discussion whether besides to the octahedral coordination of Ge by Te also tetrahedral coordination might play an important role for these thin-film compounds and their amorphous phases. However, there is no consensus decision yet.[23-26]

1.3 Structural chemistry and thermoelectric properties of tellurides

The average structures of most telluride-based thermoelectric materials, even of those that are highly disordered, can be understood on the basis of the structure types mentioned above. Layered trigonal phases such as Bi_2Te_3 and Sb_2Te_3 are applied as thermoelectric materials and crystallize in the long-periodically ordered Bi_2Te_3-type structure, which can be viewed as slabs that consist of 5 atom layers, being terminated by Te atom layers and separated by van der Waals gaps perpendicular [001].[27] Bi_2Te_3 exhibits ZT values of ~ 1 and can easily be turned into a p-type material by alloying with Sb and into an n-type material by substituting Te with Se.[28,29] Furthermore, heterogeneous multilayer superlattices of Sb_2Te_3 and Bi_2Te_3, which can be fabricated by chemical vapor deposition, exhibit ZT values of up to 2.4.[30,31] This superlattice formation is subject of many real-structure investigations.[32,33]

The average structure of $AgSbTe_2$, as mentioned above, corresponds to a rocksalt-type structure with disordered cations.[10] However, there is an ongoing discussion if and how much order of Ag and Sb atoms is present; thus, the structure might be far more complex than expected.[34,35] Furthermore, its actual composition does not correspond to the ideal one but to $Ag_{22}Sb_{28}Te_{50}$, because small amounts of Ag_2Te are formed if the stoichiometric composition is used for synthesis.[36] This is also indicated by the phase diagram[37] and might hint that many published data could have been collected using inhomogeneous samples. Yet, $AgSbTe_2$ is still one of the benchmark systems for p-type thermoelectrics and end member of many thermoelectric solid solutions. $AgSbTe_2$ exhibits ZT values of up to 1.3 at 450 °C.[38] Especially, the very low thermal conductivity of $AgSbTe_2$ is subject of many investigations.[39,40]

When $AgSbTe_2$ is alloyed with GeTe, the intensely investigated solid solution $(GeTe)_x(AgSbTe_2)_{100-x}$ (so-called TAGS-x materials) is formed.[41-44] The most prominent compositions are TAGS-80 and TAGS-85. Both crystallize in the α-GeTe-type structure and form rocksalt-type HT phases at ~ 250 °C. The phase transition temperature is lower than for GeTe itself. The compounds exhibit ZT values of up to 1.7 for TAGS-80 and 1.4 for TAGS-85 at 500 °C.[45] Adjusting the Ag/Sb ratio of the compounds allows further optimization of their charge-carrier concentration and thermal conductivity leading to higher ZT values especially for TAGS-85.[46-48] However, it has not yet been discussed whether the cation vacancies that are a consequence of this adjustment might influence the properties depending on their distribution and degree of ordering possibilities.

PbTe is one of the most versatile and applied thermoelectric materials. Its average structure can be described as a rocksalt-type structure; however, above 100 K the local symmetry is lowered and the centrosymmetry is lost. The simultaneous appearance of local dipoles without a change of the average structure is not fully understood and still under investigation.[49,50] The thermal conductivity of PbTe decreases with increasing temperature, which leads to ZT values of up to 1.0 at 380 °C.[51] There is a plethora of p- or n-type conducting doped variants of PbTe, among them many with high ZT values > 1 in the midrange temperature (350 – 550 °C). PbTe:I or PbTe:Na, for example, exhibit ZT values of up to 1.4 at 530 °C due to their very low κ at elevated temperatures and an optimal charge-carrier concentration.[52,53]

In analogy to heterogeneous Bi_2Te_3/Sb_2Te_3 multi-layer structures, the thermoelectric properties of PbTe can be optimized by forming heterostructures. Cubic PbTe exhibits endotactic precipitates ("nanodots") when it is alloyed with $AgSbTe_2$ in $AgPb_mSbTe_{2+m}$ (LAST-m) or rocksalt-type $NaSbTe_2$ in $NaPb_mSbTe_{2+m}$ (SALT-m). [54-56] For both compounds similar nanostructures are observed and they exhibit very high ZT values such as 1.7 for LAST-18 and 1.6 for SALT-20 at 430 °C. In both compounds, the high ZT values result from the very low κ_{ph} as a consequence of enhanced phonon scattering at the interfaces between the matrix material and the precipitates.

In all of the thermoelectric materials mentioned in this chapter, real-structure phenomena and/or nanoscopic side phases play a crucial role for understanding the origin of their high ZT values. Thus, a combination of different characterization methods needs to be used to gain insight into the structure-property relationships when novel solid solutions with pronounced disorder are investigated. This is especially necessary, when side phases play a role or when "partial" phase transitions are used in order to obtain nanostructured materials with optimized properties.

References

[1] J. R. Sootsman, D. Y. Chung, M. G. Kanatzidis, *Angew. Chem. Int. Ed.* **2009**, *48*, 8616.

[2] R. Saidur, M. Rezaei, W. K. Muzammil, M. H. Hassan, S. Paria, M. Hasanuzzaman, *Renew. Sust. Energ. Rev.* **2012**, *16*, 5649.

[3] M. Martin-Gonzalez, O. Caballero-Calero, P. Diaz-Chao, *Renew. Sust. Energ. Rev.* **2013**, *24*, 288.

[4] M. Wuttig, S. Raoux, *Z. Anorg. Allg. Chem.* **2012**, *638*, 2455.

[5] S. Raoux, *Annu. Rev. Mater. Res.* **2009**, *39*, 9.

[6] T. Matsunaga, H. Morita, R. Kojima, N. Yamada, K. Kifune, Y. Kubota, Y. Tabata, J.-J. Kim, M. Kobata, E. Ikenaga, K. Kobayashi, *J. Appl. Phys.* **2008**, *103*, 093511.

[7] T. Siegrist, P. Merkelbach, M. Wuttig, *Annu. Rev. Condens. Matter Phys*. **2012**, *3*, 215.

[8] M. N. Schneider, T. Rosenthal, C. Stiewe, O. Oeckler, *Z. Kristallogr.* **2010**, *225*, 463.

[9] W. Bragg, *Proc. R. Soc. London* **1914**, *89*, 468.

[10] S. Geller, J. H. Wernick, *Acta Crystallogr.* **1959**, *12*, 46.

[11] C. H. Johannson, J. O. Linde, *Ann. Phys. (Leipzig)* **1927**, *82*, 449.

[12] W. Klemm, G. Frischmuth, *Z. Anorg. Allg. Chem.* **1934**, *218*, 249.

[13] J. Goldak, C. S. Barrett, D. Innes, W. Youdelis, *J. Chem. Phys.* **1966**, *44*, 3323.

[14] A. J. Bradley, *Phil. Mag.* **1924**, *47*, 657.

[15] E. Zintl, A. Harder, B. Dauth, *Z. Elektrochem. Angew. Phys. Chem.* **1934**, *40*, 588.

[16] R. Juza, A. Rabenau, G. Pascher, *Z. Anorg. Allg. Chem.* **1956**, *285*, 61.

[17] H. Hahn, G. Frank, W. Klingler, A.-D. Meyer, G. Störger, *Z. Anorg. Allg. Chem.* **1953**, *271*, 153.

[18] K. J. Range, G. Engert, A. Weiss, *Solid State Commun.* **1969**, *7*, 1749.

[19] L. E. Shelimova, O. G. Karpinskii, V. S. Zemskov, P. P. Konstantinov, *Inorg. Mater.* **2000**, *36*, 235.

[20] T. Rosenthal, M. N. Schneider, C. Stiewe, M. Döblinger, O. Oeckler, *Chem. Mater.* **2011**, *23*, 4349.

[21] T. Matsunaga, N. Yamada, Y. Kubota, *Acta Crystallogr. Sect. B* **2004**, *60*, 685.

[22] U. Ross, A. Lotnyk, E. Thelander, B. Rauschenbach, *Appl. Phys. Lett.* **2014**, *104*, 121904.

[23] A. V. Kolobov, P. Fons, A. I. Frenkel, A. L. Ankudinov, J. Tominaga, T. Uruga, *Nature Mater.* **2004**, *3*, 703.

[24] M. Xu, Y. Q. Cheng, H. W. Sheng, E. Ma, *Phys. Rev. Lett.* **2009**, *103*, 195502.

[25] X. Q. Liu, X. B. Zhang, L. Li, Y. Q. Cheng, Z. G. Yan, M. Xu, X. D. Han, S. B. Zhang, Z. Zhang, E. Ma. *Phys. Rev. Lett.* **2011**, *106*, 025501.

[26] S. Sen, T. G. Edwards, J.-Y. Cho, Y.-C. Joo, *Phys. Rev. Lett.* **2012**, *108*, 195506.

[27] S. A. Semiletov, *Tr. Inst. Kristallogr.* **1954**, *10*, 76.

[28] J. H. Son, M. W. Oh, B. S. Kim, S. D. Park, B. K. Min, M. H. Kim, H. W. Lee, *J. Alloys Compd.* **2013**, *566*, 168.

[29] X. Z. Cai, X. Fan, Z. Z. Rong, F. Yang, Z. H. Gan, G. Q. Li, *J. Phys. D: Appl. Phys.* **2014**, *47*, 115101.

[30] R. Venkatasubramanian, E. Siivola, T. Colpitts, B. O'Quinn, *Nature* **2001**, *413*, 597.

[31] M. Winkler, X. Liu, U. Schürmann, J. D. König, L. Kienle, W. Bensch, H. Böttner, *Z. Anorg. Allg. Chem.* **2012**, *638*, 2441.

[32] U. Schürmann, M. Winkler, J. D. König, X. Liu, V. Duppel, W. Bensch, H. Böttner, L. Kienle, *Adv. Eng. Mater.* **2012**, *14*, 139.

[33] J. D. König, M. Winkler, S. Buller, W. Bensch, U. Schürmann, L. Kienle, H. Böttner, *J. Electron. Mater.* **2011**, *40*, 1266.

[34] T. Ishihara, *J. Phys. Soc. Jpn.* **1962**, *17*, 719.

[35] S. S. Ragimov, S. A. Aliev, *Inorg. Mater.* **2007**, *43*, 1184.

[36] J. D. Sugar, D. L. Medlin, *J. Alloys Compd.* **2009**, *478*, 75.

[37] R. Marin-Ayral, B. Legendre, G. Brun, B. Liautard, J. Tedenac, *Thermochim. Acta* **1988**, *131*, 37.

[38] C. Wood, *Rep. Prog. Phys.* **1988**, *51*, 459.

[39] D. T. Morelli, V. Jovovic, J. P. Heremans, *Phys. Rev. Lett.* **2008**, *101*, 035901.

[40] M. D. Nielsen, V. Ozolins, J. P. Heremans, *Energy Environ. Sci.* **2013**, *6*, 570.

[41] B. A. Cook, M. J. Kramer, X. Wei, J. L. Harringa, E. M. Levin, *J. Appl. Phys.* **2007**, *101*, 053715.

[42] S. K. Plachkova, *Phys. Status Solidi A* **1984**, *83*, 349.

[43] S. H. Yang, T. J. Zhu, T. Sun, S. N. Zhang, X. B. Zhao, J. He, *Nanotechnol.* **2008**, *19*, 245707.

[44] F. D. Rosi, J. P. Dismukes, E. F. Hockings, *Electron. Eng.* **1960**, *79*, 450.

[45] J. Davidow, Y. Gelbstein, *J. Electron. Mater.* **2013**, *42*, 1542.

[46] G. C. Christakudis, S. K. Plachkova, L. E. Shelimova, E. S. Avilov, *Phys. Status Solidi A* **1991**, *128*, 465.

[47] T. Zhu, H. Gao, Y. Chen, X. B. Zhao, *J. Mater. Chem. A* **2014**, *2*, 3251.

[48] Y. Chen, C. M. Jaworski, Y. B. Gao, H. Wang, T. J. Zhu, G. J. Snyder, J. P. Heremans, X. B. Zhao, *New J. Phys.* **2014**, *16*, 013057.

[49] K. M. O. Jensen, E. S. Bozin, C. D. Malliakas, M. B. Stone, M. D. Lumsden, M. G. Kantzidis, S. M. Shapiro, S. J. L Billinge, *Phys. Rev. B* **2012**, *86*, 085313.

[50] T. Weber, *Chimia* **2014**, *68*, 60.

[51] Z. H. Dughaish, *Phys. B.* **2002**, *322*, 205.

[52] Y. Takagiwa, Y. Pei, G. Pomrehn, G. J. Snyder, *Appl. Phys. Lett.* **2012**, *101*, 098102.

[53] Y. Pei, A. LaLonde, S. Iwanaga, G. J. Snyder, *Energy Environ. Sci.* **2011**, *4*, 2085.

[54] K. F. Hsu, S. Loo, F. Guo, W. Chen, J. S. Dyck, C. Uher, T. Hogan, E. K. Polychroniadis, M. G. Kanatzidis, *Science* **2004**, *303*, 818.

[55] B. A. Cook, M. J. Kramer, J. L. Harringa, M.-K. Han, D.-Y. Chung, M. G. Kanatzidis, *Adv. Funct. Mater.* **2009**, *19*, 1254.

[56] P. F. P. Poudeu, J. D'Angelo, A. D. Downey, J. L. Short, T. P. Hogan, M. G. Kanatzidis, *Angew. Chem. Int. Ed.* **2006**, *45*, 3835.

2 Metastable compounds obtained under extreme conditions

2.1 Overview

$(GeTe)_nSb_2Te_3$ (GST materials), which represent the most important class of phase-change materials (PCMs), exhibit high thermoelectric figures of merits both for rocksalt-type thin film compounds with random occupation of the cation position with cations and vacancies as well as for quenched bulk materials that are characterized by a nanostructure of unequally spaced intersecting vacancy layers with limited lateral extension.[1,2] Cubic thin film $(GeTe)_8Sb_2Te_3$ exhibits a ZT value of up to 0.7 at 120 °C, whereas a ZT values of up to 1.3 at 450 °C can be observed for nanostructured bulk material of $(GeTe)_{12}Sb_2Te_3$. However, the thermoelectric properties of trigonal layered modifications of GST materials are inferior to those of their pseudo-cubic nanostructured modifications.[2] Beyond GST materials, only few compounds easily form inert glasses which can be reversibly switched to metastable crystalline phases upon laser irradiation and thus could be applied as PCMs in rewritable data-storage devices. Among these compounds are $GeBi_2Te_4$ (GBT, cf. Chapter 2.2), $Ag_{3.4}In_{3.7}Sb_{76.4}Te_{16.5}$ (AIST, cf. Chapter 2.3) and In_3SbTe_2 (IST, cf. Chapter 3.2).[3,4] GBT materials constitute a homologous series $(GeTe)_nBi_2Te_3$, which consists of long-periodically ordered trigonal phases that are comparable to the trigonal modifications of GST (cf. Chapter 1.2).[5] The GeTe content n thus defines the number of layers within the rocksalt-type slabs, which are separated by van der Waals gaps perpendicular [001], and, as a consequence, the stacking sequence (*P*- or *R*-type, cf. Chapter 1.2). $GeBi_2Te_4$ crystallizes in the spacegroup $R\bar{3}m$ with a 21*R*-type stacking sequence, i. e. slabs that consist of seven layers.[6] While Bi_2Te_3 exhibits ZT values of up to 1 which can easily be further increased by suitable substitutions,[7,8] $GeBi_2Te_4$ is an inefficient thermoelectric material due to the very low Seebeck coefficient of ~ 20 µV/K at 200 °C.[9] In accordance with GST, it would be interesting to investigate the properties and real structure of a cubic modification of $GeBi_2Te_4$. In situ high-pressure (HP) investigations of $Ge_2Sb_2Te_5$ show that the metastable cubic thin-film compounds do not transform to the trigonal modification upon increasing the pressure up to 10 GPa before they become amorphous.[10] HP experiments were performed on $GeBi_2Te_4$ (cf. Chapter 2.2), because the density of a hypothetical cubic modification of $GeBi_2Te_4$ is expected to be larger than that of the layered modification containing van der Waals gaps. Syntheses under HP conditions yield novel metastable modifications which crystallize in a CuPt-type average structure, but differ in their real structure depending on the thermal

treatment of the compounds under HP. In contrast, fast quenching experiments at ambient pressure like melt-spinning yields 21*R*-type $GeBi_2Te_4$ with nanoscopic domains. Further experiments revealed the influence of the particle sizes and thus grain-boundary concentrations on the thermoelectric properties.

$Ag_{3.4}In_{3.7}Sb_{76.4}Te_{16.5}$ is known as a thin film compound and is the only PCM except for GST that is actually used in rewritable CDs.[11] X-ray investigations on thin films show that AIST crystallizes in a gray As-type (*A*7) structure and decomposes upon heating. AIST does not have a stable modification; its stable state corresponds to a mixture of an In-doped antimony telluride $Sb_{7.9}Te$:In with an *A*7 average structure and different commensurately and incommensurately modulated modifications and chalcopyrite-type $AgInTe_2$.[12] A cubic HP phase has been reported for AIST samples as well as for $AgInTe_2$, which adopts the NaCl-type structure at pressures higher than 1.5 GPa and 350 °C.[13,14] Both fast quenching and syntheses under HP conditions yield metastable gray As-type AIST (cf. Chapter 2.3). All atoms share a single Wyckoff position. Thus, the crystal structure of AIST seems well suited for thermoelectric applications, because disorder is often associated with a low thermal conductivity and thus beneficial for the thermoelectric properties. As expected, slightly inhomogeneous annealed melt-spun AIST exhibits low thermal conductivities of 1.2 W/Km at room temperature (RT); however, the low Seebeck coefficient of ~ 30 µV/K limits the ZT values to < 0.01.

Like the well-known thermoelectric material $AgSbTe_2$, $AgInTe_2$ features both monovalent and trivalent cations whose charges are compensated by Te. However, their crystal structures and thermoelectric properties differ significantly. While $AgSbTe_2$ crystallizes in a rocksalt-type structure featuring disordered cations,[15] for $AgInTe_2$ no disorder of the cations has been reported and it crystallizes in the chalcopyrite-type structure,[16] which is a superstructure of the sphalerite type, i. e. it exhibits tetrahedral coordination of both cations and anions. The ZT values of $AgSbTe_2$, 0.3 at RT and 1.3 at 450 °C, are remarkable,[17] whereas the ZT values of chalcopyrite-type $AgInTe_2$ are < 0.1 in that temperature range.[18] It would be interesting to investigate rocksalt-type $AgInTe_2$, but unfortunately its HP phase quickly retransforms to the chalcopyrite type after decompression. However, it is possible to synthesize rocksalt-type solid solutions $AgIn_xSb_{1-x}Te_2$ under high pressure (cf. Chapter 2.4). The thermal conductivity of these inert phases is the lowest one among all rocksalt-type tellurides, but the Seebeck coefficient is lower than that of $AgSbTe_2$. Analogous to $AgSbTe_2$ at ambient pressure, where alloying with GeTe leads to solid solutions $(GeTe)_x(AgSbTe_2)_{100-x}$ (TAGS materials) which exhibit even higher ZT values.[19-23], $AgIn_xSb_{1-x}Te_2$ and $AgInTe_2$ form solid solutions with

GeTe under HP conditions (cf. Chapter 2.5). However, in contrast to $AgIn_xSb_{1-x}Te_2$, $(GeTe)_xAgIn_ySb_{1-y}Te_2$ compounds with In contents ≤ 3.6 atom% can be obtained without applying high pressure. Below 125 °C, the ZT value of $(GeTe)_{5.5}AgInTe_2$ is even higher than that of TAGS-85, $(GeTe)_{5.5}AgSbTe_2$.

References

[1]. E.-R. Sittner, K. S. Siegert, P. Jost, C. Schlockermann, F. R. L. Lange, M. Wuttig, *Phys. Status Solidi A* **2013**, *210*, 147.

[2] T. Rosenthal, M. N. Schneider, C. Stiewe, M. Döblinger, O. Oeckler, *Chem. Mater.* **2011**, *23*, 4349.

[3] T. Matsunaga, N. Yamada, *Jpn. J. Appl. Phys.* **2004**, *43*, 4704.

[4] E. T. Kim, J. Y. Lee, Y. T. Kim, *Phys. Status Solidi (RRL)* **2009**, *3*, 103.

[5] L. E. Shelimova, O. G. Karpinskii, V. S. Zemskov, P. P. Konstantinov, *Inorg. Mater.* **2000**, *36*, 235.

[6] L. E. Shelimova, O. G. Karpinskii, P. P. Konstantinov, E. S. Avilov, M. A. Kretova, V. S. Zemskov, *Inorg. Mater.* **2004**, *40*, 451.

[7] J. H. Son, M. W. Oh, B. S. Kim, S. D. Park, B. K. Min, M. H. Kim, H. W. Lee, *J. Alloys Compd.* **2013**, *566*, 168.

[8] X. Z. Cai, X. Fan, Z. Z. Rong, F. Yang, Z. H. Gan, G. Q. Li, *J. Phys. D: Appl. Phys.* **2014**, *47*, 115101.

[9] L. E. Shelimova, P. P. Konstantinov, O. G. Karpinskii, E. S. Avilov, M. A. Kretova, V. S. Zemskov, *J. Alloys Comp.* **2001**, *329*, 50.

[10] A. V. Kolobov, J. Haines, A. Pradel, M. Ribes, P. Fons, J. Tominaga, Y. Katayama, T. Hammouda, T. Uruga, *Phys. Rev. Lett.* **2006**, *97*, 035701.

[11] T. Matsunaga, Y. Umetani, N. Yamada, *Phys. Rev. B* **2001**, *64*, 184116.

[12] T. Matsunaga, R. Kojima, N. Yamada, Y. Kubota, K. Kifune, *Acta Crystallogr. Sect. B.* **2012**, *68*, 559.

[13] M. Krbal, A. V. Kolobov, P. Fons, J. Haines, A. Pradel, M. Ribes, A. A. Piarristeguy, C. Levelut, R. Le Parc, A. Agafonov, M. Hanfland, J. Tominaga, *Phys. Rev. B* **2011**, *83*, 024105.

[14] K. J. Range, G. Engert, A. Weiss, *Solid State Commun.* **1969**, *7*, 1749.

[15] S. Geller, J. H. Wernick, *Acta Crystallogr.* **1959**, *12*, 46.

[16] H. Hahn, G. Frank, W. Klingler, A.-D. Meyer, G. Störger, *Z. Anorg. Allg. Chem.* **1953**, *271*, 153.

[17] C. Wood, *Rep. Prog. Phys.* **1988**, *51*, 459.

[18] Y. Aikebaier, K. Kurosaki, T. Sugahara, Y. Ohishi, H. Muta, S. Yamanaka, *Mater. Sci. Eng. B* **2012**, *177*, 999.

[19] B. A. Cook, M. J. Kramer, X. Wei, J. L. Harringa, E. M. Levin, *J. Appl. Phys.* **2007**, *101*, 053715.

[20] S. K. Plachkova, *Phys. Status Solidi A* **1984**, *83*, 349.

[21] J. Davidow, Y. Gelbstein, *J. Electron. Mater.* **2013**, *42*, 1542.

[22] S. H.Yang, T. J. Zhu, T. Sun, S. N. Zhang, X. B. Zhao, J. He, *Nanotechnol.* **2008**, *19*, 245707.

[23] F. D. Rosi, J. P. Dismukes, E. F. Hockings, *Electr. Eng.* **1960**, *79*, 450.

2.2 Nanostructures in metastable $GeBi_2Te_4$ obtained by high-pressure synthesis and rapid quenching and their influence on physical properties

Thorsten Schröder, Matthias N. Schneider, Tobias Rosenthal, Andreas Eisele, Christian Gold, Ernst-Wilhelm Scheidt, Wolfgang Scherer, Rico Berthold, Oliver Oeckler
Phys. Rev. B **2011**, *84,* 184104.

Abstract

We report on a new metastable modification of $GeBi_2Te_4$ obtained by high-pressure high-temperature synthesis. It crystallizes in the CuPt type, different nanostructures are induced by various temperature programs under a constant pressure of 12 GPa. The particle size changes from < 10 nm in quenched samples to > 100 nm for melts slowly crystallized under high pressure. The smaller the domains the more random is their orientation distribution. The nanostructure has a high impact on the temperature characteristics of the electrical resistivity. The domain size determines whether the compounds are metallic or semiconducting. In the latter case, the semiconducting behavior is due to the scattering of electrons at domain and/or grain boundaries. Intermediate behavior that starts off metal-like and changes to semiconducting at higher temperature has been observed for samples thermally quenched from the solid state at high-pressure. Resistivity measurements of the high-pressure samples involving multiple heating and cooling sequences lead to a significant reduction of internal stress and finally approach a state which is characterized by a $\rho(T)$ hysteresis. Our results show the large influence of the domain size and the grain boundary concentration on the properties of the materials and reveal how properties like the thermoelectric figure of merit (ZT) depend on the preparation technique. By the microstructuring of stable $GeBi_2Te_4$, the ZT value drops by one order of magnitude.

2.2.1 Introduction

Tellurides play important roles in various fields of application such as phase-change materials (PCMs) for data storage as well as a broad range of high-performance thermoelectrics. Interestingly, most of the relevant tellurides are not thermodynamically stable. Metastability

is, for example, a crucial property of PCMs used in optical as well as electrical rewritable storage devices (DVD-RW, BD-RE, PC-RAM, etc.).[1,2] The recording and erasing process involves the fast and reversible switching between amorphous and metastable disordered crystalline phases with simple average structures which exhibit the A7 (gray arsenic) or the rocksalt structure type. Metastability and disorder are essential to reach extremely short switching times for writing or erasing large amounts of data as no long-distance diffusion is required and as both structural states are inert enough to guarantee reliable long-time data storage. The required material properties of PCMs, are, at least in part, similar to those that are crucial in the field of thermoelectrics.[3] However, it remains unclear if the thermoelectric effect itself is important in electrically switchable PCMs.

The long-time goal of most research activities on thermoelectrics, which interconvert thermal and electrical energy, is the generation of electrical energy from waste heat. The efficiency of thermoelectrics depends on the dimensionless figure of merit $ZT = S^2T / \rho\kappa$ (with the Seebeck coefficient S, the electrical resistivity ρ, and the thermal conductivity κ). As all these quantities depend on the charge carrier concentration, they cannot be optimized independently. The electrical resistivity and the electronic part of the thermal conductivity are inversely proportional to each other according to the Wiedemann-Franz law. Therefore, the only way to decrease the overall thermal conductivity without significantly increasing the electrical resistivity is to influence the phononic part of the thermal conductivity. This can be achieved, for instance, by introducing nanostructures. Phase transitions associated with the formation of long-periodically ordered structures, twinning, or (partial) decomposition may yield nanostructures that scatter phonons rather effectively and therefore enhance the thermoelectric properties. Nanostructures are, of course, metastable states, especially if they are obtained by partial stabilization of highly disordered metastable phases. This can be accomplished by various quenching techniques. However, care must be taken not to completely reach the fully ordered equilibrium state.[4-11]

In addition to the common characteristic feature that the compounds are metastable, many efficient thermoelectrics (e.g. $AgPb_mSbTe_{2+m}$ (LAST),[12] $NaPb_mSbTe_{2+m}$ (SALT),[13] $(AgSbTe_2)_{1-m}(GeTe)_m$ (TAGS),[14] or Bi_2Te_3) contain more or less the same chemical elements in similar ratios as well-known PCMs (e.g. $(GeTe)_n(Sb_2Te_3)$ (GST),[15-17] $Ag_{3.4}In_{3.7}Sb_{76.4}Te_{16.5}$ (AIST)).[18] Inspired by GST-based PCMs in PC-RAM and BD-RE devices, the investigation of the thermoelectric properties of $(GeTe)_{12}(Sb_2Te_3)$ yielded ZT values of ~1.3 at 450 °C.[3] These compounds exhibit cubic high-temperature phases with Ge, Sb and vacancies disordered on the cation sites of the rocksalt-type structure, which can be

quenched as pseudocubic bulk material. The high *ZT* value can be related to short-range vacancy ordering effects. Similar metastable rocksalt-type phases of GBT (Ge/Bi/Te) materials have been reported for thin-film samples obtained by sputtering and exhibit rapid phase-change behavior that can be induced by laser irradiation.[19] However, in this case the rocksalt-type phase does not exist as a stable high-temperature phase (it is in fact unstable at any temperature). Therefore, quenching experiments using bulk samples do not yield cubic or pseudocubic phases, but the stable rhombohedral layered modifications which are similar to stable GST phases. Therefore, it is essential to apply methods beyond conventional solid-state synthesis to obtain metastable GBT compounds as bulk materials. Fast quenching methods such as melt-spinning as well as high-pressure experiments seem promising in order to obtain different nanostructures that can be correlated with the corresponding thermoelectric properties.

In this report, we focus on $GeBi_2Te_4$, which is one of the peritectic compounds that can be found on the pseudo-binary line GeTe-Bi_2Te_3 in the Ge/Bi/Te phase diagram. The stable modification of $GeBi_2Te_4$ crystallizes in a rhombohedral long-range ordered 21*R*-type structure (space group $R\bar{3}m$, no. 166) with 21 hexagonal atom layers in each unit cell (Fig. 1).[20] These 21 layers form three blocks of 7 layers each, which can be described as a distorted cutout of the rocksalt structure type due to the octahedral coordination of the cations. Adjacent blocks are linked via van der Waals gaps by tellurium···tellurium interactions. In contrast to this stable phase, the metastable cubic modification found for thin-film samples experiments corresponds to a rocksalt-type structure $(Ge_{0.25}Bi_{0.5}\square_{0.25})Te$ displaying cation defects.[19,21] A phase transition towards the stable state therefore involves a vacancy rearrangement. Layer-like defect ordering and subsequent relaxation leads to the formation of the van der Waals gaps. Intermediate structures between the cubic and the 21*R*-type phases could be observed for $Ge_2Bi_2Te_5$ in annealing experiments on thin films.[22] They involve a shear deformation which may also be important for the phase-change mechanism.

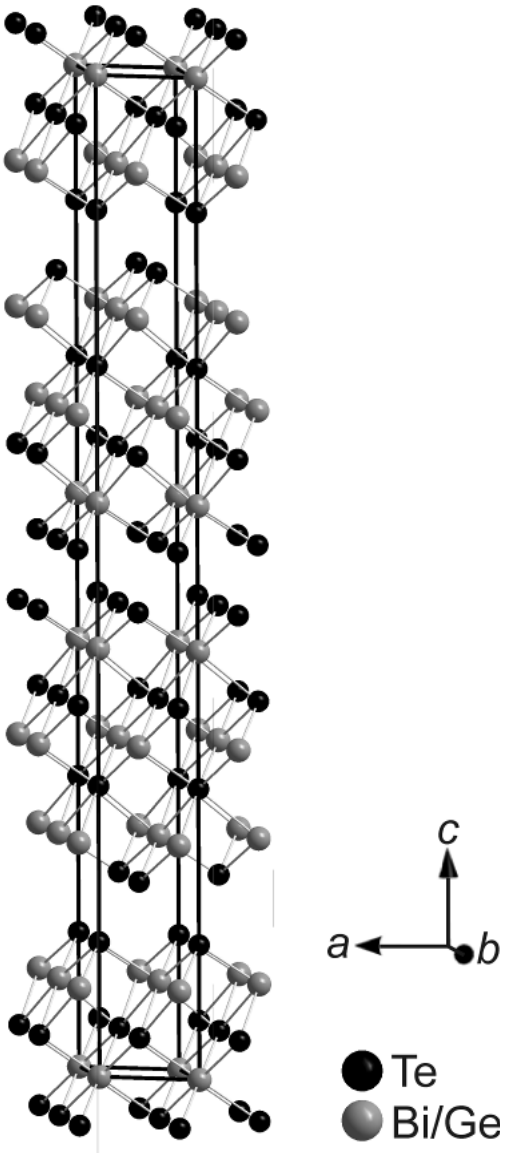

Fig. 1. Crystal structure of stable 21*R*-type $GeBi_2Te_4$ (the small percentage of anti-site disorder is neglected).

2.2.2 Experimental details

Synthesis

Bulk samples with the nominal composition $GeBi_2Te_4$ were prepared by heating a stoichiometric mixture (e.g., 0.3 g) of the pure elements (germanium 99.999 %, Sigma Aldrich; bismuth 99.999 %, Smart Elements; tellurium 99.999 %, Alfa Aesar) in sealed silica glass ampoules to 950 °C under argon atmosphere. The resulting melts were quenched to room temperature in water and used as starting material for the following syntheses. After quenching, some ingots were annealed at 500 °C to obtain the stable 21*R*-type modification.

High-pressure experiments were performed using the multi-anvil technique with a hydraulic press (Voggenreiter, Mainleus, Germany).[23-26] Quenched $GeBi_2Te_4$ was powdered, loaded into a cylindrical capsule of hexagonal boron nitride (Henze, Kempten, Germany) and sealed with a BN cap. The capsule was centered within two nested graphite tubes, which acted as an electrical resistance furnace. The remaining volume at both ends of the sample capsule was filled with two cylindrical pieces of magnesium oxide. The arrangement was placed into a zirconia tube and then transferred into a pierced Cr_2O_3-doped MgO octahedron (edge length 14 mm, Ceramic Substrates & Components, Isle of Wight, Great Britain). Eight truncated tungsten carbide cubes (truncation edge length 8 mm) separated by pyrophyllite gaskets served as anvils for the compression of the octahedron. Two plates of molybdenum provided electrical contact for the graphite tubes. The assembly was compressed up to a constant pressure of 12 GPa in 350 minutes. At this pressure, three temperature programs were applied (see Table 1). Samples were prepared by heating to 850 °C and subsequently (1) quenching the melt by turning off the furnace (melt-quenched samples), or (2) cooling the sample to 200 °C within 5 hours and then turning off the furnace (solid-quenched samples). A third type (3) of high-pressure samples was prepared by cooling the samples to room temperature within 4 hours (slowly cooled samples). After the temperature program the pressure was reduced to ambient pressure within 1050 minutes.

Table 1. High-pressure sample overview

denotation	pressure	temperature program
melt-quenched	12 GPa	quenched from melt (850 °C)
solid-quenched	12 GPa	quenched from 200 °C
slowly cooled	12 GPa	slowly cooled from 850 °C to RT

A melt-spinning apparatus (model SC, Bühler, Germany) was used in order to obtain high quenching rates (up to approximately 10^9 K/s) at ambient pressure. Powdered $GeBi_2Te_4$ was loaded into a tantalum blast pipe, which was placed over a rotating copper wheel (60 Hz). Both the tantalum blast pipe and the copper wheel were placed in a recipient, which was evacuated and/or filled with argon. The powder was melted using a water-cooled high-frequency coil (high frequency generator Himmel HIT 12, Himmelwerk Hoch- & Mittelfrequenzanlagen GmbH, Germany) and then sprayed onto the rotating copper wheel under an argon pressure of 500 mbar by applying an excess argon pressure connected to the tantalum blast pipe. The melt hits the copper wheel and solidifies immediately. Flat particles

with the size of about 5 × 2 × 0.2 mm^3 were hurled away from the wheel onto a collecting tray.

EDX analysis

EDX (energy dispersive X-Ray) spectra were recorded using a JSM-6500F (Jeol, USA) scanning electron microscope with EDX detector (model 7418, Oxford Instruments, Great Britain). For each particle or fragment of the ingot, respectively, the results of five point analyses were averaged and the error limits were estimated from their variance.

X-ray diffraction

X-ray powder patterns were recorded with a Huber G670 Guinier camera equipped with a fixed imaging plate and integrated read-out system using Cu-$K_{\alpha 1}$ radiation (Ge monochromator, λ = 1.54059 Å). Specimens were prepared by crushing representative parts of the samples and fixing the powder on Mylar foils using silicone grease. Low-temperature measurements between 10 K and 300 K were obtained using a cryo cooling system (Cooling head, CTI-Cyrogenics, model 22 CP). The phase homogeneity was assessed and lattice parameters were determined by pattern fitting (Rietveld method) using the program TOPAS.[27] Temperature-dependent powder diffraction experiments at temperatures above 300 K were performed with a STOE Stadi P powder diffractometer equipped with an imaging plate detector system using Mo-$K_{\alpha 1}$ radiation (Ge monochromator, λ = 0.71093 Å) in Debye–Scherrer geometry. Powdered specimens were filled into silica glass capillaries with 0.3 mm diameter and sealed with silicone grease under argon atmosphere. During the measurement, the samples were heated up to 600 °C in a graphite furnace and then cooled to room temperature with a heating/cooling rate of 5 K/min.

Transmission electron microscopy

For transmission electron microscopy studies, finely ground samples were dispersed in ethanol and distributed on copper grids coated with a holey carbon film (S166-2, Plano GmbH, Germany). The grids were fixed on a double tilt holder. Selected area electron diffraction (SAED) and high resolution transmission electron microscopy (HRTEM) were done on a JEM2011 (Jeol Ltd., Japan) with a tungsten thermal emitter and an acceleration

voltage of 200 kV equipped with a TVIPS CCD (model 114, resolution: 1k x 1k). Further HRTEM, SAED and EDX measurements were done on a Titan 80-300 (FEI, USA) with a field emission gun operated at 300 kV equipped with a TEM TOPS 30 EDX spectrometer (EDAX, Germany). Images were recorded using an UltraScan 1000 camera (Gatan, USA, resolution: 2k × 2k). HRTEM and SAED data was evaluated using the Digital Micrograph and EMS software,[28,29] for STEM and EDX data the program ES Vision was used.[30]

Electrical and thermal transport measurements

The temperature dependent resistivity $\rho(T)$ of various stable and metastable $GeBi_2Te_4$ modifications were measured by a standard four-probe dc method employing a constant current of 5 mA and using a physical property measurement system (PPMS, Quantum Design). The data were collected in the temperature range of 2 – 300 K by cooling and heating sequences in which the temperature changed at a rate of 0.5 K/min. The uncertainty of the absolute electrical resistivity values (approx. 20 – 30 %) has been estimated by taking into account the errors in specifying the sample dimensions.
The thermoelectric power $S(T)$ and the thermal conductivity $\kappa(T)$ of samples crystallizing in the stable $GeBi_2Te_4$ modification were measured simultaneously using the commercial thermal transport option of the PPMS. This is based on a relaxation method employing one heater and two thermometers to determine the induced thermal voltage and the temperature gradient along the sample in a temperature range between 4 K and 300 K. These measurements were carried out using bar-shaped samples with typical dimensions of about $1 \times 2 \times 5$ mm^3 during a heating process at a rate of 0.5 K/min. The total accuracy of $S(T)$ and $\kappa(T)$ is about 5%.

2.2.3 Results and discussion

2.2.3.1 Structure of quenched HP-$GeBi_2Te_4$

The powder diffraction pattern of a sample obtained by quenching the melt of $GeBi_2Te_4$ under a constant pressure of 12 GPa (i.e. switching off the furnace) could be indexed assuming a rhombohedral unit cell with a = 4.3508(3) Å and c = 11.234(2) Å. Starting from an α-GeTe-type structure model (space group $R3m$), which allows many degrees of freedom, Ge, Bi and vacancies were placed on the cation position (occupancy factors 0.25 for Ge and 0.5 for Bi)

and Te (fully occupied) on the anion position. The occupancy factors were derived from the nominal composition, which is confirmed by the EDX results (for all $GeBi_2Te_4$ samples between $Ge_{0.9(1)}Bi_{2.2(1)}Te_4$ and $Ge_{1.1(1)}Bi_{2.0(1)}Te_4$). The Rietveld refinement (shown in Fig. 2) turned out that there is no evidence for non-centrosymmetry of the average structure, as in contrast to α-GeTe, all cation-anion distances are equal within two standard deviations. Therefore, the average structure seems not to be layered, and the space group can be identified as $R\bar{3}m$ (no. 166). Details of the Rietveld analysis and the refined atomic parameters are given in Tables 2 and 3, respectively.

Table 2. Crystal data and Rietveld refinement of melt-quenched $GeBi_2Te_4$

sum formula	$GeBi_2Te_4$
molar mass (in g/mol)	1000.97
lattice parameters (in Å)	a = 4.3508(3) Å; c = 11.234(2)
cell volume (in Å³)	184.16(5)
radiation	Cu-$K_{\alpha1}$ (λ = 1.540596 Å)
density (in g/cm³)	6.769(2)
space group	$R\bar{3}m$ (no. 166)
2 theta range	22° < 2θ < 95°
number of reflections	32
refined parameters	12 structural / 36 background
constraints	2
profile function	fundamental parameter approach
step width (2θ)	0.005°
R_{wp}; R_p	0.0135; 0.0104

Table 3. Atom positions and displacement parameters of HP-$GeBi_2Te_4$

atom	Wyck.	x y z	s.o.f.	U_{eq}	$U_{11} = U_{22} = 2U_{12}$	U_{33}	U_{13}=U_{23}
Te	3*a*	0 0 0	1	0.15(2)	0.017(11)	0.48(7)	0
Bi/Ge	3*b*	0 0 1/2	Bi 0.5 Ge 0.25	0.18(2)	0.008(11)	0.43(6)	0

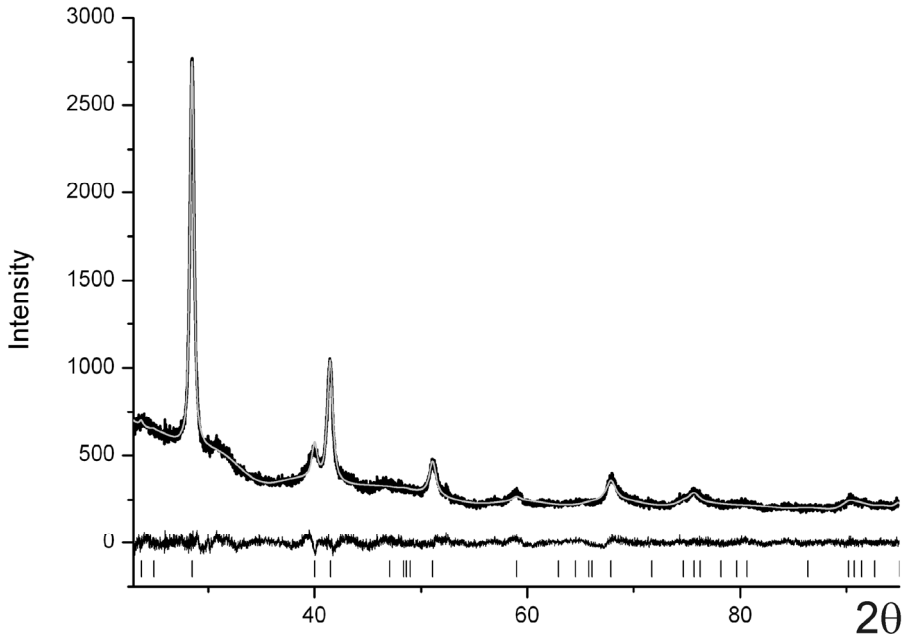

Fig. 2. Rietveld refinement of melt-quenched HP-$GeBi_2Te_4$: experimental powder pattern (black), calculated pattern (gray), and difference plot (black) and tick marks (black, straight lines).

The average structure model derived from Bragg reflections corresponds to the CuPt-type structure, a rhombohedrally distorted variant of the rocksalt type, derived from the latter by stretching the unit cell along <111>. In fact, the powder pattern contains no significant evidence for different scattering densities on anion and cation positions, as disordered germanium, bismuth and vacancies lead to an average electron count of 49.5 at the cation position and tellurium involves 52 electrons on the anion position. Thus, the structure might formally be described assuming the α-Hg type with just one Wyckoff position for all atoms, however, electron diffraction patterns clearly show the CuPt type's reflections *hkl* with *h*, *k*, *l* = 2n+1 whose intensity (similar to the rocksalt case) can only be observed in case of different scattering densities for cation and anion sites (see next section). Of course, a certain degree of anti-site disorder cannot be excluded; however, such phenomena have been thoroughly investigated for Ge/Sb/Te phases, where the amount of anti-site disorder is either very small or not significant.[17,31] Although the refinement fits the experimental data, the structure model does not correspond to an ordered compound; and the disorder goes far beyond the cation disorder itself. The "average" structure from Bragg data can only be described with very prolate atomic displacement ellipsoids as can be seen in Fig. 3; so in fact there is no average structure with, at least in part, "normal" atom positions. These results suggest that a cubic rocksalt-type phase is formed under high pressure, but partially relaxes to a layered trigonal

structure as soon as the pressure is released. The short-range order in this phase may locally correspond to the structure of the stable room temperature phase. Obviously, the high vacancy concentration of 25 % on the cation sites does not allow a completely random vacancy distribution at ambient conditions.

The powder diffraction patterns of the slowly cooled and solid-quenched samples, respectively, do not differ significantly from those of samples that were quenched from the melt, although the micro-/nanostructures are significantly different (see below). However, Table 4 shows that the lattice parameters of the average structures vary slightly. All trigonal *c*/*a* ratios are almost equally far from that of the trigonal setting of a unit cell with cubic metrics (2.45).

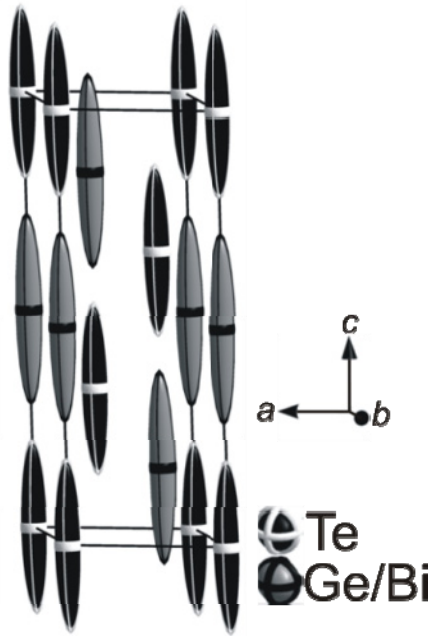

Fig. 3. "Average" structure model of metastable HP-$GeBi_2Te_4$ as determined from Bragg data (displacement ellipsoids for 99% probability).

Table 4. Comparison of the lattice parameters of various high-pressure samples (cf. text)

denotation	*a* (Å)	*c* (Å)	*c*/*a*	Volume (Å^3)
melt-quenched	4.3502(4)	11.234(2)	2.582	184.05(5)
solid-quenched	4.347(2)	11.184(5)	2.573	183.1(2)
slowly cooled	4.3495(5)	11.043(3)	2.539	180.93(7)

Fig. 4 shows that temperature-dependent powder diffraction experiments and ex-situ annealing of high-pressure samples (for 36 hours at 300 °C) prove that the high pressure phase is metastable at ambient pressure. The reflections of the layered 21*R*-type structure reappear when the metastable compound is heated over 200 °C.

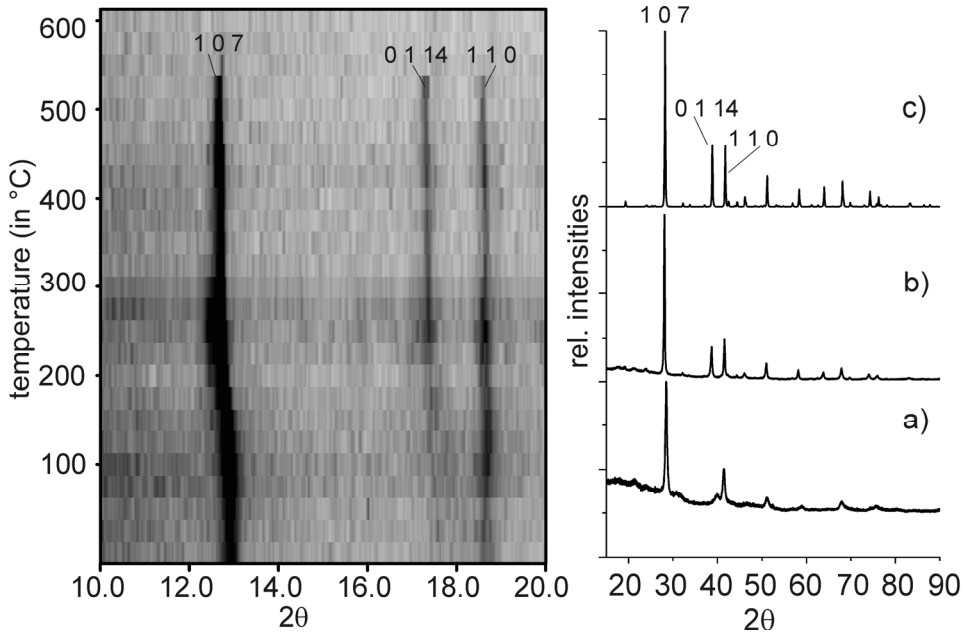

Fig. 4. Temperature-dependent PXRD (left, room temperature to 600 °C, Mo-$K_{\alpha 1}$ radiation - intensity from 0 (white) to maximum (black)) of the melt-quenched HP phase; PXRD (Cu-$K_{\alpha 1}$ radiation) of the melt-quenched sample (right): a) as removed from the press, b) after annealing for 36 h at 300 °C, c) calculated powder pattern of 21*R*-type $GeBi_2Te_4$.

2.2.3.2 Nucleation mechanism and nanostructuring

The nanostructure of the melt-quenched sample which is shown in Fig. 5a) is characterized by a broad range of different domain orientations with domain sizes < 10 nm. The domains are intergrown, but there are no coherent domain walls. Therefore, the SAED pattern corresponds to the combination of multiple patterns and not to a single crystallite. A few grains with larger domains can be found, but they are rare exceptions. Thus, quenching the melt under a high constant pressure leads to nucleation dominated growth.

The solid-quenched sample exhibits larger and more anisotropic domains with average dimensions ≥ 10 nm. Therefore, it is possible to obtain single crystalline SAED patterns as shown in Fig. 5b) if larger domains are selected. These patterns contain reflections *hkl* with *h*, *k*, *l* = 2n+1, which implies that there are different scattering densities for anion and cation sites, respectively. There are no pronounced diffuse streaks in the SAED patterns. Thus, there is no pronounced intermediate-range order corresponding to extended vacancy layers or van der Waals gaps within the domains as they are known from the stable trigonal phases.

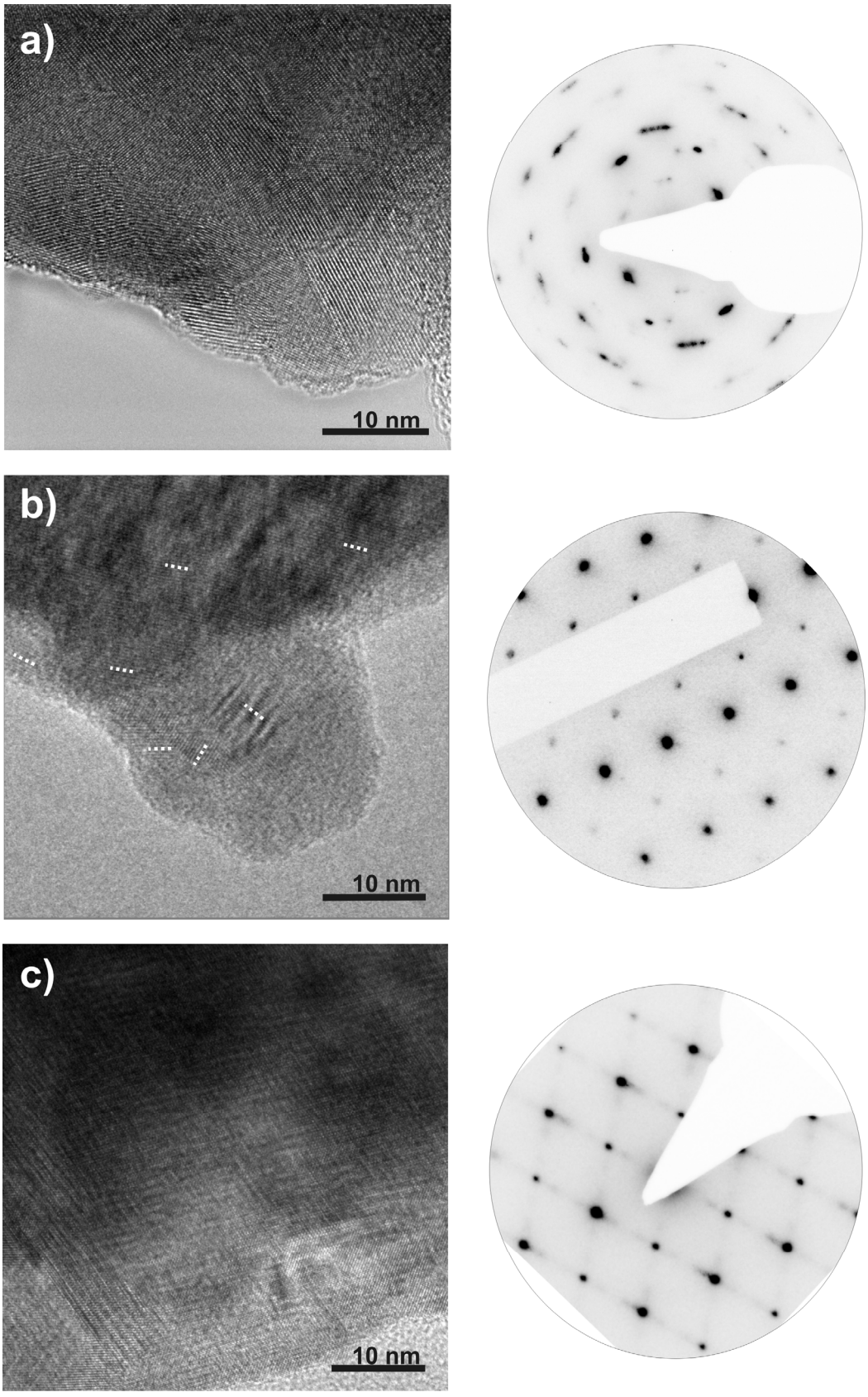

Fig. 5. HRTEM images (left) and the corresponding SAED (right) a) of the melt-quenched sample (Titan 80-300); b) of the solid-quenched sample, some domain orientations are highlighted with white dashed lines (JEM 2011); c) of the slow cooled sample; here different domain orientations overlap (Titan 80-300).

Probably the lack of vacancy ordering limits the maximal domain size as vacancies might aggregate at domain boundaries. The crystallites are larger than the ones in the melt-quenched HP sample; yet, the domains are still randomly oriented. The domain shape is more anisotropic than in the melt-quenched sample.

Fig. 5c) shows that the slowly cooled sample has large crystallites ≥ 100 nm. Twinned areas next to single-domain areas can be observed. All slowly cooled samples exhibit extended vacancy layers which lead to van der Waals gaps if the adjacent Te atom layers relax. Therefore, diffuse streaks can be observed in the corresponding SAED patterns. These large domains indicate fast growth crystallization rather than nucleation dominated growth. The relative orientation of the twin domains corresponds to the <111> directions of a pseudo-cubic structure. This corroborates the assumption that there is a cubic high-pressure phase of $GeBi_2Te_4$ which, upon a phase transition towards a trigonal phase, involves fourfold twinning according to the *translationengleiche* cubic → rhombohedral group-subgroup relationship.

The powder X-ray diffraction pattern (PXRD) pattern of melt-spun $GeBi_2Te_4$ corresponds to that of the ordered 21*R*-type structure and not to the PXRD patterns of the high pressure samples. Yet, melt-spun $GeBi_2Te_4$ exhibits small intergrown domains, the smallest ones with a diameter of ~10 nm as shown in Fig. 6 larger domains are also present. The domain orientation changes within one grain, however, not as randomly as in the quenched high-pressure samples.

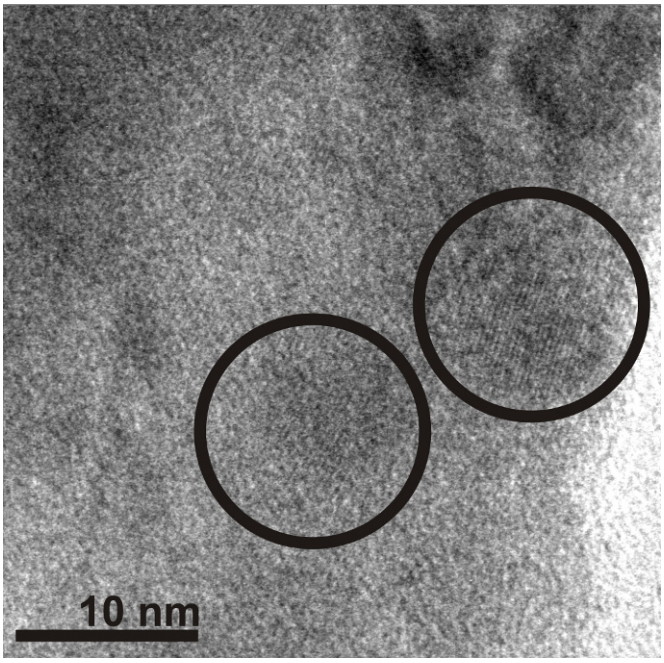

Fig. 6. HRTEM image of a melt-spun sample of $GeBi_2Te_4$; two well-ordered domains of the stable layered phase are highlighted by black circles.

2.2.3.3 Influence of the nanostructure on the electrical resistivity

The following section conduces to the understanding of the influence of the nanostructure of the metastable modifications of HP-$GeBi_2Te_4$ on the temperature dependent resistivity ρ(T). Therefore the resistivity of three different metastable quenched samples – slowly cooled, solid-quenched and melt-quenched – were synthesized and compared with an annealed ingot as well as a melt-spun particle, both crystallizing in the stable modification.

Stable and melt-spun modification of $GeBi_2Te_4$

The resistivity of an annealed ingot of the stable ambient-pressure modification of $GeBi_2Te_4$ is plotted vs. temperature in the range between 2 K and 300 K in Fig. 7a). The decrease of $\rho(T)$ with decreasing temperature suggests metal-like behavior. However, the high residual resistivity ρ_0 of about 0.3 mΩ cm together with the small residual resistivity ratio of RRR = ρ(300 K)/ρ(2 K) = 2.52 suggest the presence of severe disorder. The metallic conductivity behavior depends on two different scattering processes. The temperature independent residual resistivity ρ_0 originates from the scattering of conduction electrons by defects (impurity atoms, grain boundaries etc.). In the present case this is probably due to the Ge/Bi disorder at the cation sites. The second – temperature dependent – process is due to the scattering of conduction electrons by phonon excitations. These two processes yield the description of simple metals via the Bloch-Grüneisen (BG) relation.

$$\rho_{BG}(T) = \rho_0 + \frac{4B}{\Theta_D}\left(\frac{T}{\Theta_D}\right)^5 \int_0^{\Theta_D/T} \frac{z^5 \, dz}{(e^z - 1)(1 - e^{-z})}$$

where B is the temperature-independent electron-phonon interaction strength, Θ_D the Debye-temperature and $z = \hbar\omega/k_BT$.

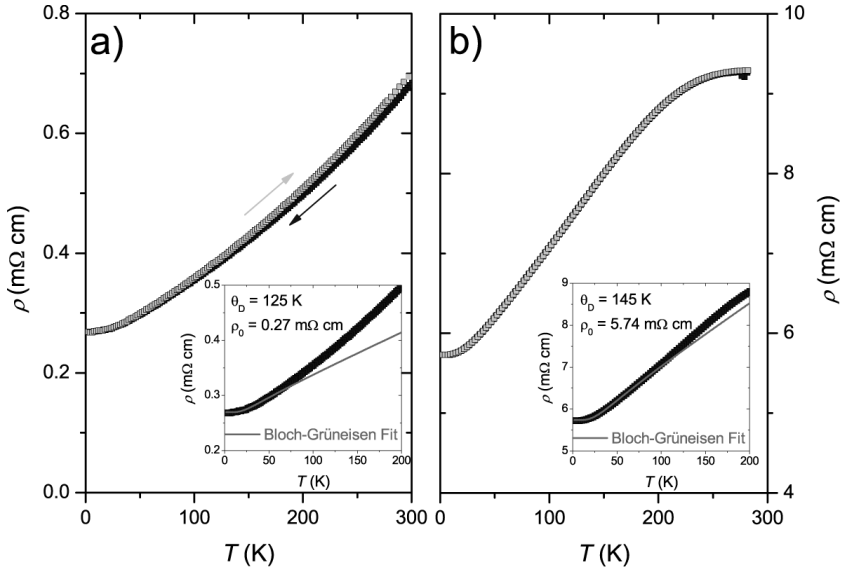

Fig. 7. Comparison of the temperature-dependent resistivity of a) an annealed ingot of 21*R*-type $GeBi_2Te_4$ and of b) a melt-spun particle of $GeBi_2Te_4$. The inserts show the low-temperature behavior together with a fit according to the Bloch-Grüneisen relationship (solid line). The arrows denote cooling and heating sequences, respectively.

The insert of Fig. 7a) depicts the resistivity behavior $\rho(T)$ of the stable $GeBi_2Te_4$ modification in comparison with a corresponding data fit employing the Bloch-Grüneisen (BG) relationship. The BG relation fits the experimental sufficiently well only at temperatures below ~ 40 K. For higher temperatures, $\rho(T)$ displays larger values than those expected by the BG relation for metallic behavior. This suggests an onset of semiconducting behavior at elevated temperatures in accordance with the high residual resistivity and the small RRR value. Furthermore, $\rho(T)$ of the annealed ingot reflects fully reversible behavior between cooling and heating sequences only below 40 K in the region where experimental data can be fitted by the BG relation. This reversibility can also be retrieved in the metastable modifications of $GeBi_2Te_4$ (see subsequent discussion).

The deviation from metallic behavior above a certain temperature, becomes more evident in the resistivity of the melt-spun particle (see Fig. 7.b)), although in this case the BG relation fits the experimental data well up to ~ 60 K. However, the residual resistivity ρ_0 increases by a factor of 20 in comparison to the annealed ingot. Furthermore, $\rho(T)$ of the melt-spun particle starts to saturate already at ~ 9.3 mΩ cm in the high temperature regime. The higher resistivity can be attributed to the reduction of the grain size (up to 10 nm) and can therefore be related to the increasing number of domain and grain boundaries acting as scattering centers. The saturation below room temperature is in line with a transition from metal-like to a degenerate semiconducting behavior as supported by the description via the BG formalism (see insert Fig. 7b)) at low temperatures, which also takes the temperature dependency of the

charge carrier density into account.[32] Such a two-regime behavior was recently reported for Ge-based clathrate I compounds as well as Sb-based skutterudites.[33-35]

These results point out that the nanostructure, e.g. the domain size and the relative orientation, influence the temperature characteristics of the resistivity behavior even if the crystal structure is maintained (21*R* type).

Metastable quenched HP-$GeBi_2Te_4$

All three high-pressure samples are characterized by pronounced irreversible temperature dependencies of $\rho(T)$ for repeated cooling and heating cycles in the temperature range between 44 and 260 K. This is shown for the slowly cooled sample of HP-$GeBi_2Te_4$ in Fig. 8 There is a drastic change of the hysteretic behavior when the $\rho(T)$ sequences of cycle one and two are compared. However, already after the third cooling/heating sequence the hysteresis curves remain rather invariant. There is, however, a subtle decrease of the resistivity (and of the $\rho(T)$ minima at ca. 35 K - 38 K) with increasing number of cooling/heating cycles.

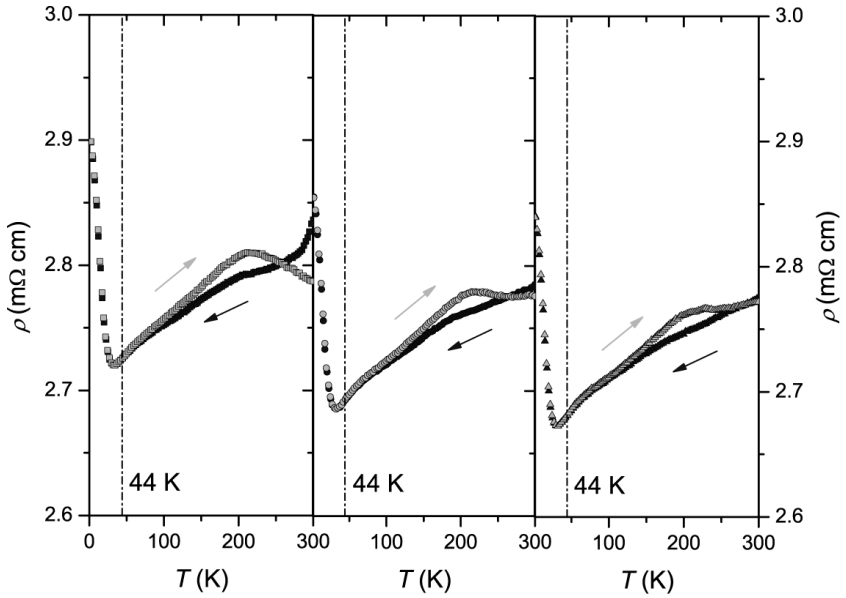

Fig. 8. Temperature-dependent resistivity of a slowly cooled HP-$GeBi_2Te_4$ sample; from left to right three successive cooling (black) and heating (gray) sequences, approaching a final state.

In the final state after more than three successive cooling and heating sequences, the resistivity $\rho(T)$ shows a metal-like behavior above 35 K and an insulating one for lower temperatures, similar to the behavior observed, e.g., for didymium skutterudites $(Pr,Nd)(Fe,Co)_4Sb_{12}$ and $(Pr,Nd)(Fe,Ni)_4Sb_{12}$.[36] Below 44 K heating and cooling curves

show reversibility, while above 44 K a hysteresis with a maximal splitting of 0.014 mΩ cm at ~ 208 K occurs. One may speculate that the $\rho(T)$ behavior in the reversible regions is mainly controlled by the intrinsic resistivity of the grains, whereas above 44 K the resistivity of the grain boundaries starts to dominate, as observed in case of in the stable $GeBi_2Te_4$ modification (see previous discussion, Fig. 7a)).

In Fig. 9 the temperature-dependent resistivity behavior of three metastable high-pressure samples of $GeBi_2Te_4$ obtained by different cooling/quenching procedures is compared. All three samples are characterized by a hysteretic $\rho(T)$ behavior which also depends on the number cooling/heating sequences applied (vide supra; Fig. 8). However, in order to study exclusively the competition between the intrinsic resistivity of the domains with that of the grain boundaries only those $\rho(T)$ cooling/heating curves were depicted in Fig. 9 which remained invariant after several measuring cycles. All of the three samples possess reversible temperature dependence below ~ 40 K. Above that temperature, the temperature characteristics of the resistivity changes from metallic-like (slowly cooled) to semiconducting (melt-quenched sample). Hence, the temperature-dependent resistivity behavior critically depends on the sample history, especially on the cooling/quenching approach applied. In contrast, the hysteretic behavior above 40 K remains a characteristic feature of all the three different samples.

The occurrence of such hysteresis effects could be due to either a first-order phase transition or the presence of internal stress. A first-order phase transition can be excluded based on temperature dependent X-ray experiments, which do not reveal any significant change in the powder diffraction pattern down to 15 K (except for a trivial change of lattice parameters), as well as by specific heat studies (not shown here) which do not indicate any phase transformation. Therefore, the hysteretic $\rho(T)$ behavior is probably due to the internal stress of the grains. The extent of the hysteresis changes drastically with an increasing domain size and the number of their relative orientation in the different samples. Accordingly, the slowly cooled sample is characterized by the smallest hysteresis splitting of all three samples (see Fig. 9a). This is consistent with the expected small change of internal stress as a consequence of the large domain size ($\geq$ 100 nm) and the presence of only few domain orientations as evidenced by the HRTEM studies. A similar, but more pronounced splitting is therefore found in case of the melt-quenched sample (see Fig. 9c)) which is characterized by very small particles (< 10 nm) showing many different orientations. However, the solid-quenched sample reveals the strongest splitting of all metastable $GeBi_2Te_4$ compounds (see Fig. 9b)). This is probably a result of the strongly anisotropic size of the grains.

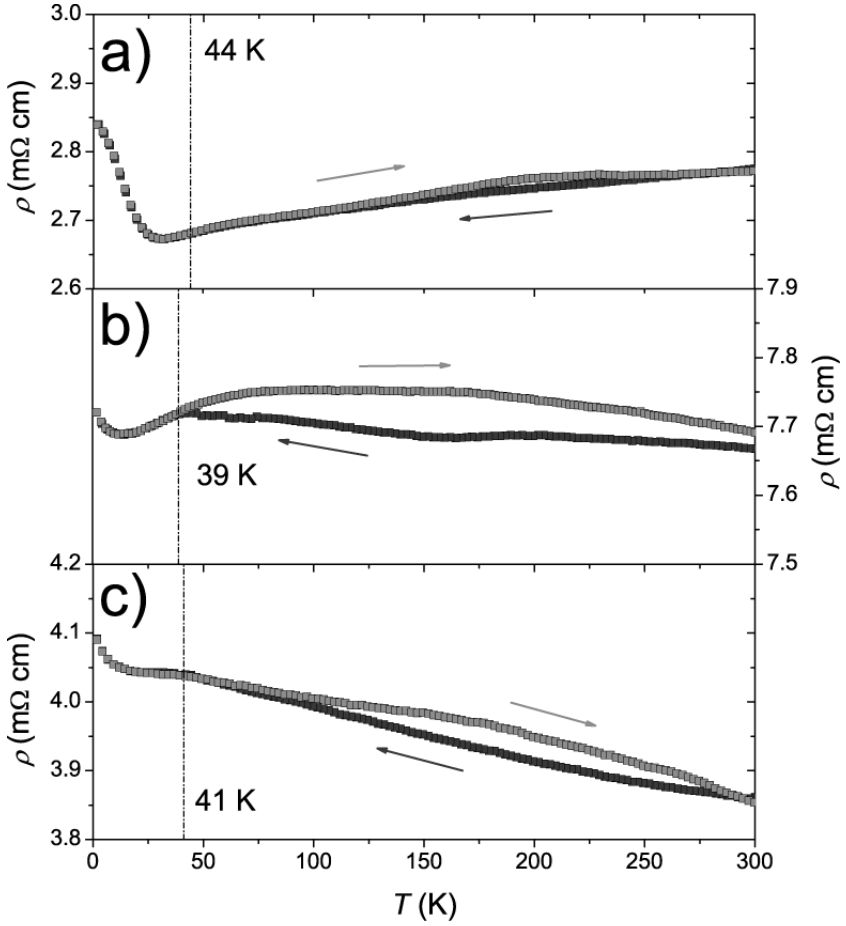

Fig. 9. Final state of the cooling (black) and heating (gray) sequences of the temperature dependent resistivity of a) slowly cooled b) solid-quenched and c) melt-quenched high-pressure samples of $GeBi_2Te_4$

Due to this type of nanostructuring, the total resistivity of these samples is not only affected by the intrinsic structure and disorder of the domains but also by a contribution of the microscopic nature of the domain and/or grain boundaries. The change of the residual resistivity in Fig. 9 suggests that also the dominant scattering mechanisms might differ in the three samples. The slowly cooled high-pressure sample exhibits the lowest residual resistivity and the most pronounced similarity to the stable modification (e.g. metallic conductivity at ambient temperature; see Fig. 7a). This is basically due to the fact that this sample exhibits the largest domains of the three high-pressure systems and displays a disordered pseudocubic layered structure. The melt-quenched sample, however, shows semiconducting behavior between 41 K and room temperature in spite of the isotropy and rather random orientation of its domains. The temperature dependence of the resistivity is therefore dominated by the grain boundaries' contributions. The solid-quenched sample indicates the highest residual resistivity of all the high-pressure species under investigation. This remarkably high value in

combination with the pronounced grain anisotropy implies a coexistence of both scattering mechanisms discussed (see above). The $\rho(T)$ behavior of the solid-quenched modification, however, marks an intermediate behavior and thus adopts to the high-temperature behavior of the slowly cooled and mimics the low-temperature behavior of the melt-quenched one.

Influence of grain boundaries on ZT

In order to investigate the influence of the sample preparation techniques on the thermoelectric figure of merit *ZT*, the thermal and electrical transport properties of three characteristic samples were measured between 4 K and room temperature. In this respect, the annealed ingot of stable 21*R*-type $GeBi_2Te_4$ represents a benchmark sample which is compared with two pellet samples (samples two and three). Sample two is a pellet pressed of 21*R*-$GeBi_2Te_4$ powder while the third sample is a pellet composed of cold-pressed powder of the melt-spun 21*R*-$GeBi_2Te_4$. It was not possible to perform such measurements with the high-pressure samples due to their small sample volumes.

A comparison of the $\rho(T)$ behavior of these three samples is plotted in Fig. 10a)-c). The $\rho(T)$ behavior of the annealed ingot and that of the melt spun sample were already characterized as metal-like in Fig. 7. In contrast, $\rho(T)$ of the two pellets do not shows metal-like conductivity behavior. In addition, ρ_0 increases by a factor of about 30 and 60 in case of both pellet samples, irrespective of the sample's origin (stable modification or melt-spun 21*R*-$GeBi_2Te_4$ sample, respectively). Two closely related control parameters might be responsible for observation of semiconducting behavior, namely the nano- or microstructure formation by different synthesis routes and the process of pellet pressing itself. Both lead to an increasing number of grain boundaries and therefore trigger the increase of ρ_0 and the change of the $\rho(T)$ behavior.

These observations are consistent with the thermal conductivity $\kappa(T)$ behavior shown in Fig. 11a) and b). The total thermal conductivity κ_{total} of solids can be expressed as the sum of an electrical κ_{el} as well as a phononic κ_{ph} contribution. The electrical contribution was estimated from the electrical resistivity (cf. Fig. 10) via the Wiedemann-Franz law. Subtracting this part from the experimentally determined total thermal conductivity yields the phononic contribution.

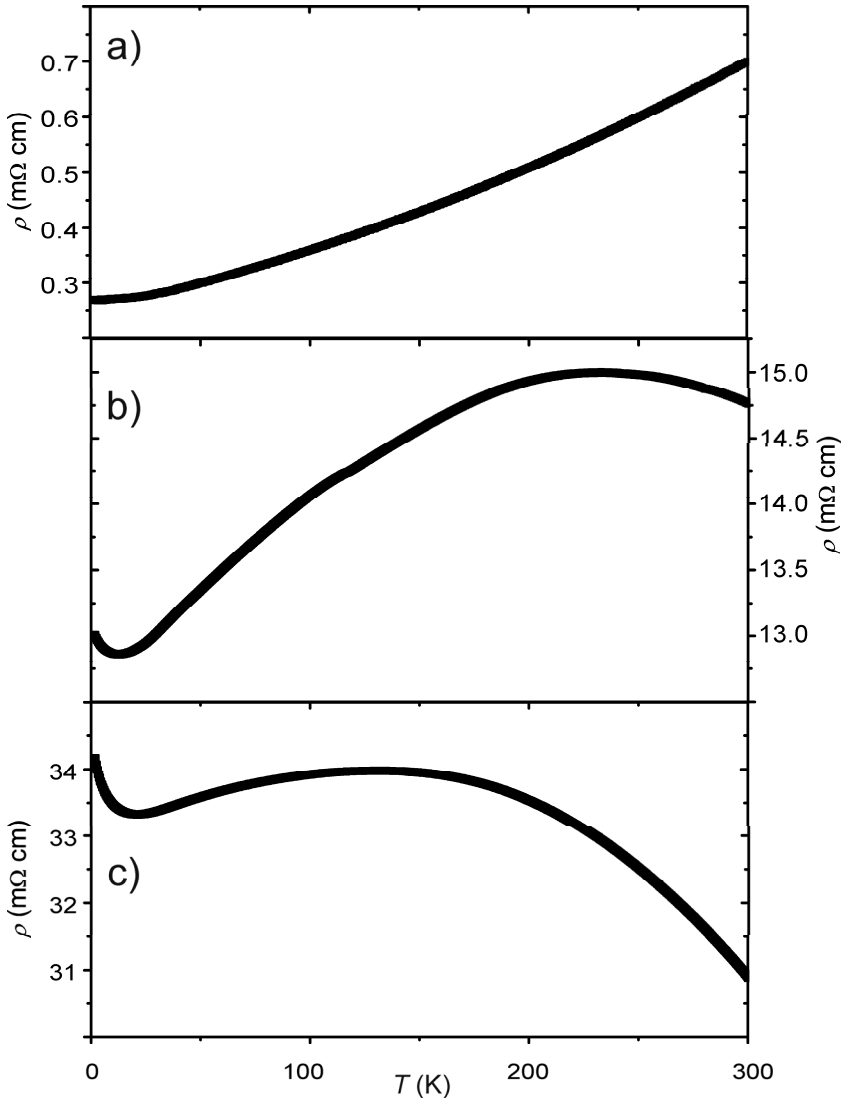

Fig. 10. Comparison of the temperature dependent resistivity ρ(T) (heating from 2 to 300 K) of a) an annealed ingot of $GeBi_2Te_4$, b) a pressed powder pellet of 21*R*-$GeBi_2Te_4$ and c) a pressed powder pellet of melt-spun $GeBi_2Te_4$.

In Fig. 11a), κ_{total} of the annealed ingot of the stable modification is composed of significant contributions from κ_{ph} and κ_{el}. While at room temperature both parts coexist and contribute approximately by the amount to κ_{total}, a phonon dominated state is observed below 50 K. The maximum of κ_{ph} at about 13 K displays the onset of phonon umklapp scattering which effectuates a decrease of κ_{ph} above a certain temperature. Such kind of maximum depends only weakly on the Debye temperature and occurs well below $\Theta_D/10$. The low-temperature slope of κ_{ph} thus indicates defect scattering and becomes large when the number of defects is small.

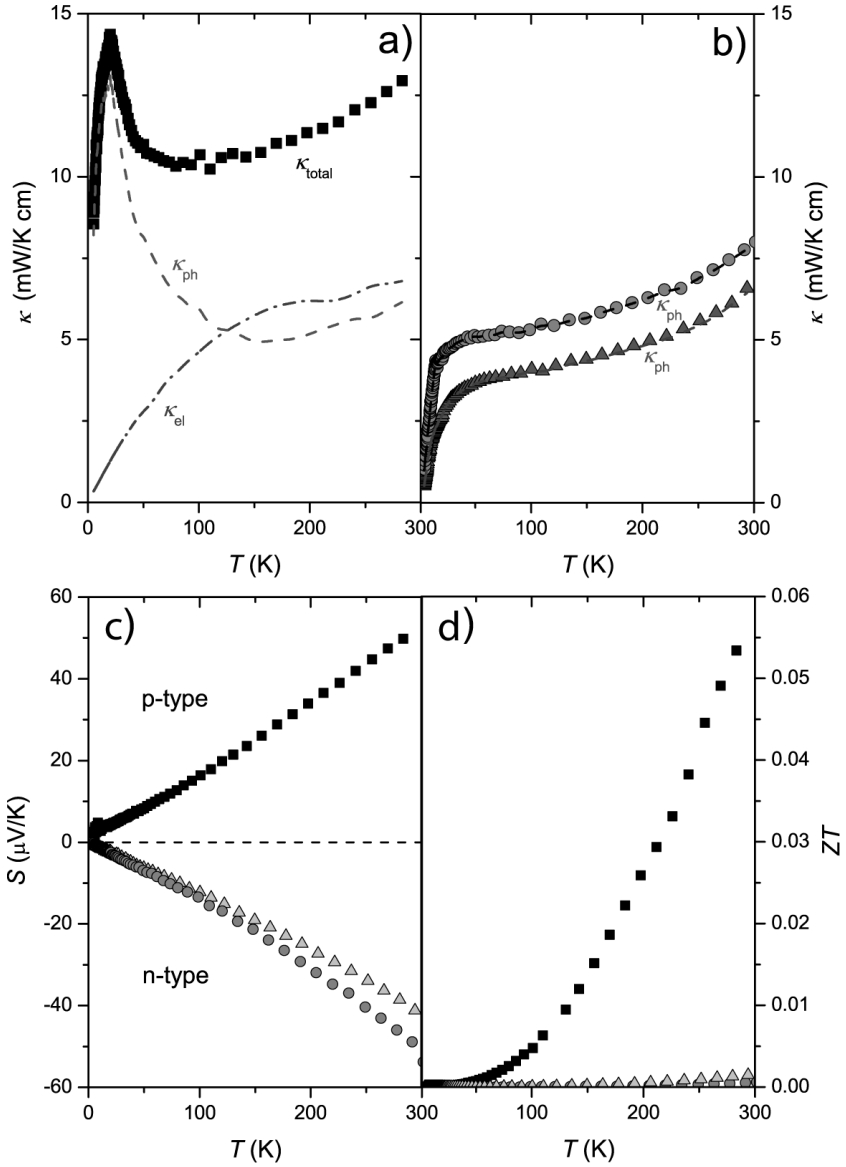

Fig. 11. Temperature characteristics a) of the total thermal conductivity, κ_{total}, (black squares), the phonon contribution, κ_{ph}, (dashed line) and electronic contribution, κ_{el}, (dashed and dotted line) for the annealed ingot of $GeBi_2Te_4$; b) of κ_{total} for the pressed powder pellet of 21*R*-type $GeBi_2Te_4$ (gray circles) and the powder pressed pellet of melt-spun $GeBi_2Te_4$ (gray triangles) and the phonon contributions (dashed lines, dark gray); c) of the Seebeck coefficient and d) of the *ZT* value for the annealed ingot (black squares), the pressed powder pellet of 21*R*-type $GeBi_2Te_4$ (gray circles) and the pressed powder pellet of melt-spun $GeBi_2Te_4$ (light gray triangles).

A comparison with the $\kappa(T)$ results of the two pellets indicate an overall and significant reduction of $\kappa_{total}(T)$ (Fig. 11b)). Generally, κ_{ph} of the thermal conductivity of both samples follows the pattern of κ_{total} while the κ_{el} contribution vanishes as expected in the light of the high resistivity values observed. Furthermore, the change of the low-temperature slope of κ_{ph} hints to an increase of phonon scattering at boundaries and/or point defects. Hence, the

reduced thermal conductivity of the pellet-pressed samples originates mainly from the enhancement of these scattering processes.

The thermopower $S(T)$ of the three samples is depicted in Fig. 11c). For the annealed ingot of the stable modification, an increase of the thermopower up to about + 50 μV/K at room temperature can be observed. The positive sign of $S(T)$ between 4 K and 300 K reveals the characteristic behavior of a p-type material. The featureless, almost linear temperature dependence of $S(T)$ indicates the absence of any significant correlations within the charge carriers and is expected for the diffusion thermopower above the Debye temperature (125 K). In this temperature region electron-phonon scattering is the dominant scattering mechanism and given by

$$S_{\mathrm{d}}(T > \Theta_{\mathrm{D}}) = \frac{\pi^2 k_{\mathrm{B}}{}^2 2m_{\mathrm{e}}}{|e|\hbar^2 (3n\pi^2)^{2/3}} \cdot T$$

with $k_{\mathrm{B}} = 1.38065 \cdot 10^{-23}$ J/K, $m_{\mathrm{e}} = 9.10938 \cdot 10^{-31}$ kg, $e = 1.60218 \cdot 10^{-19}$ C, and $h = 6.62607 \cdot 10^{-34}$ Js. According to this equation, the slope below 300 K yields a density of charge carriers of $3.4 \cdot 10^{21}$ cm^{-3}.

In contrast to its influence on $\rho(T)$ and $\kappa(T)$, the method of synthesis has no drastic influence on $S(T)$ except for the remarkable change of sign in the thermopower of the pellets from positive (p-type) to negative (n-type). The absolute values of $S(T)$ as well as the carrier concentration (~ 10^{21} cm^{-3}) of the pellet samples remain more or less the same.

The ZT values, for the three samples, calculated from the present results are shown in Fig. 11d). For the annealed ingot of the stable modification a ZT value of 0.055 was reached at room temperature. The ZT values of both pellet samples where found to be one order of magnitude lower, which disqualifies these sample from thermoelectric applications. Significant scattering of the charge carriers on grain boundaries results in high resistivity values for the micro- or nanostructured samples and, as a consequence, in a small electronic contribution to the thermal conductivity.

2.2.4 Conclusion

Quenching melts of $GeBi_2Te_4$ at high pressure yields metastable samples whose average structure is related to the rocksalt type, similar to samples obtained by laser irradiation of thin films for PCM applications. Partial relaxation towards the stable trigonal layered modification leads to a rhombohedrally distorted crystal structure. The metastable state can be completely

relaxed by annealing. Concerning PCMs, the nucleation mechanisms are important. “Nucleation dominated growth” begins spontaneously at different spots in the amorphous phase and therefore leads to a multitude of grains, which have no crystallographic relation to each other. We have shown that the crystallization of melts during rapid quenching is very similar, an intermediate solid amorphous phase might be discussed for bulk samples as well, but cannot be confirmed by our experiments. The domain size and therefore probably the nucleation mechanism depends on the temperature regime, including quenching rates, which were applied under a constant pressure of 12 GPa. The nanostructures obtained and especially the corresponding domain and grain boundaries have a large influence on the temperature characteristics of the electrical resistivity. In the high pressure compounds, the characteristics of the electrical resistivity changes from metal-like to semiconducting behavior with decreasing domain size and more randomly oriented domains, because the resistivity becomes more dominated by scattering of the electrons at the domain or grain boundaries. The temperature regime during the synthesis therefore determines at which temperature this type of scattering becomes dominant. However, multiple heating and cooling sequences in course of the resistivity measurements show that the system seems to approach a final state. Apparently, internal stress needs to be reduced before the measurements yield invariant $\rho(T)$ sequences, but even after the stabilization a hysteretic behavior remains.

As a consequence, the preparation technique has a large influence on the ZT value as shown by measurements on samples that exhibit the stable layered structure. The thermal conductivity is influenced by the electronic contribution, which decreases significantly in pressed pellets with many grain boundaries; however, it is accompanied by the corresponding increase of the electrical resistivity. Therefore, the ZT value drops by more than an order of magnitude because the phononic contribution becomes dominant. These findings illustrate the importance of the thermal conditioning of thermoelectrics, especially in order to ensure sufficient electrical conductivity. It is often difficult to reproduce thermoelectric materials with distinct properties; because different methods of synthesis (like hot press, high pressure experiments or conventional solid-state preparation techniques), annealing times and temperatures lead to various amounts of grain boundaries and therefore strong deviations in ZT.

Acknowledgements

We thank T. Miller and M. Rotter for the temperature-dependent powder diffraction experiments, C. Minke for SEM operation and EDX analyses, and M. Döblinger for help with TEM operation. We are indebted to Dr. G. Kreiner for providing access to the melt-spinner and gratefully acknowledge Prof. Dr. W. Schnick's generous support of this work. This investigation was funded by the Deutsche Forschungsgemeinschaft (grants OE530/1-2 and SCHE487/12-1) and the Studienstiftung des deutschen Volkes.

References

[1] W. Bensch, M. Wuttig, *Chem. Unserer Zeit* **2010**, *44*, 92.

[2] S. Raoux, *Annu. Rev. Mater. Res.* **2009**, *39*, 9.

[3] M. N. Schneider, T. Rosenthal, C. Stiewe, O. Oeckler, *Z. Kristallogr.* **2010**, *225*, 463.

[4] J. Sommerlatte, K. Nielsch, H. Böttner, *Phys. J.* **2007**, *6*, 35.

[5] A. Bulusu, D. G. Walker, *Superlattice Microstruct.* **2008**, *44*, 36.

[6] A. Majumdar, *Science* **2004**, *303*, 777.

[7] M. S. Dresselhaus, G. Chen, M. Y. Tang, R. Yang, H. Lee, D. Wang, Z. Ren, J.-P. Fleurial, P. Gogna, *Adv. Mater.* **2007**, *19*, 1.

[8] D. L. Medlin, G. J. Snyder, *Curr. Opin. Colloid Interface Sci.* **2009**, *14*, 226.

[9] M. G. Kanatzidis, *Chem. Mater.* **2010**, *22*, 648.

[10] Y. C. Lan, A. J. Minnich, G. Chen, Z. F. Ren, *Adv. Funct. Mater.* **2010**, *20*, 357.

[11] J. R. Sootsman, D. Y. Chung, M. G. Kanatzidis, *Angew. Chem. Int. Ed.* **2009**, *48*, 8616.

[12] B. A. Cook, M. J. Kramer, J. L. Harringa, M.-K. Han, D.-Y. Chung, M. G. Kanatzidis, *Adv. Funct. Mater.* **2009**, *19*, 1254.

[13] P. F. P. Poudeu, J. D'Angelo, A. D. Downey, J. L. Short, T. P. Hogan, M. G. Kanatzidis, *Angew. Chem. Int. Ed.* **2006**, *45*, 3835.

[14] F. D. Rosi, J.P. Dismukes, E. F. Hockings, *Electron Eng.* **1960**, *79*, 450.

[15] T. Matsunaga, N. Yamada, *Phys. Rev. B* **2004**, *69*, 104111.

[16] T. Matsunaga, N. Yamada, Y. Kubota, *Acta Crystallogr. Sect. B* **2004**, *60*, 685.

[17] T. Matsunaga, R. Kojima, N. Yamada, K. Kifune, Y. Kubota, Y. Tabata, M. Takata, *Inorg. Chem.* **2006**, *45*, 2235.

[18] T. Matsunaga, Y. Umetani, N. Yamada, *Phys. Rev. B* **2001**, *64*, 184116.

[19] T. Matsunaga, N. Yamada, *Jpn. J. Appl. Phys.* **2004**, *43*, 4704.

[20] L. E. Shelimova, O. G. Karpinskii, P. P. Konstantinov, E. S. Avilov, M. A. Kretova, V. S. Zemskov, *Inorg. Mater.* **2004**, *5*, 451.

[21] S.-I. Shamoto, N. Yamada, T. Matsunaga, T. Proffen, *Phys. B.* **2006**, *72*, 574.

[22] C. W. Sun, J. Y. Lee, Y. T. Kim, *Phys. Stat. Sol. RRL* **2009**, *3*, 254.

[23] D. Walker, M. A. Carpenter, C. M. Hitch, *Am. Mineral.* **1990**, *75*, 1020.

[24] D. Walker, *Am. Mineral.* **1991**, *76*, 1092.

[25] D. C. Rubie, *Phase Trans.* **1999**, *68*, 431.

[26] H. Huppertz, *Z. Naturforsch. B* **2001**, *56*, 697.

[27] *TOPAS-Academic*, *V. 4.1*, Coelho Software, Brisbane, Australia, **2007**.

[28] *DigitalMicrograph 3.6.1*, Gatan Software, Pleasanton, USA, **1999**.

[29] P. A. Stadelmann, *Ultramicroscopy* **1987**, *21*, 131.

[30] *ESVision*, *4.0.164*, Emispec Systems Inc., Tempe, USA, **1994-2002**.

[31] P. P. Konstantinov, L. E. Shelimova, E. S. Avilov, M. A. Kretova, V. S. Zemskov, *Inorg. Mater.* **2001**, *37*, 662.

[32] N. Melnychenko-Koblyuk, A. Grystsiv, St. Berger, H. Kaldarar, H. Michor, F. Röhrbacher, E. Royanian, E. Bauer, P. Rogl, H. Schmid, G. Giester, *J. Phys. Condens. Matter* **2007**, *19*, 046203.

[33] C. Candolfi, U. Aydemir, M. Baitinger, N. Oeschler, F. Steglich, Y. Grin, *J. Electron. Mater.* **2010**, *39*, 2039.

[34] A. Grytsiv, P. Rogl, St. Berger, Ch. Paul, H. Michor, E. Bauer, G. Hilscher, C. Godart, P. Knoll, M. Musso, W. Lottermoser, A. Saccone, R. Ferro, T. Roisnel, H. Noel, *J. Phys. Condens. Matter* **2002**, *14*, 7071.

[35] G. Rogl, A. Grytsiv, E. Bauer, P. Rogl, M. Zehetbauer, *Intermetallics* **2010**, *18*, 394.

[36] G. Rogl, A. Grytsiv, E. Bauer, P. Rogl, M. Zehetbauer, *Intermetallics* **2010**, *18*, 57.

2.3 Two synthetic approaches to $Ag_{3.4}In_{3.7}Sb_{76.4}Te_{16.5}$ bulk samples and their transport properties

Thorsten Schröder, Tobias Rosenthal, Christian Gold, Ernst-Wilhelm Scheidt, Wolfgang Schnick, Oliver Oeckler

Z. Anorg. Allg. Chem. **2013**, *639*, 2868 – 2874.

Abstract

Bulk samples with the chemical composition of the AIST phase-change material $Ag_{3.4}In_{3.7}Sb_{76.4}Te_{16.5}$ were synthesized by melt spinning as well as under high-pressure conditions (12 GPa), respectively. Rietveld refinements as well as selected-area electron diffraction patterns and high-resolution transmission electron images show that both types of samples crystallize in the gray As structure type. All atoms are disordered on one Wyckoff position. The metrics of the high-pressure sample appear compressed along [001] compared to the ones of the melt-spun sample. This may be attributed to strain, probably caused by twinning, which relaxes at higher temperatures (starting at ca. 130 °C). The compounds decompose at 250 °C and a structural change of the Sb-rich Sb/Te phase was observed at 440 °C. The thermoelectric properties of an annealed sample with $AgInTe_2$ impurities were measured and result in a ZT value of 0.003 at room temperature, which strongly increases with temperature.

2.3.1 Introduction

The chemical compositions as well as the thermal and electrical transport properties of some phase-change materials (PCMs) are remarkably similar to those of thermoelectric materials.[1] While thin films of phase-change materials are used as active layers for optical and electrical rewritable data-storage devices,[2-6] bulk samples of thermoelectric materials may reversibly interconvert heat, i. e. a temperature gradient, and electrical energy.[7-11] Currently, mainly two classes of PCMs are applied, germanium antimony tellurides (GST materials) and compounds in the system Ag/In/Sb/Te (AIST materials), respectively. While the thermoelectric properties of GST materials have been discussed for thin films as well as for

nanostructured quenched bulk materials,[1,12,13] neither structural nor thermoelectric data of bulk samples have been reported for AIST materials.

There are variants of AIST materials with different compositions; however, $Ag_{3.4}In_{3.7}Sb_{76.4}Te_{16.5}$ is the most prominent one. In thin films, it crystallizes in the gray As (*A*7) structure type, i. e. like pure Sb, upon laser irradiation.[14] All four elements are randomly disordered on one Wyckoff position. In addition to the expected thermal expansion of the lattice parameters, high-temperature experiments revealed that the compound decomposes into $AgInTe_2$ and a Sb-rich antimony telluride at 270 °C.[15] While $AgInTe_2$ remains present up to its melting point, the structure of the antimony telluride varies when the temperature is increased. This structural transformation probably leads towards a long-periodically ordered layered phase which is a member of the homologous series of stable compounds $(Sb_2)_k(Sb_2Te_3)_m$.[16,17] Possible stacking variants depend on k and m; their crystal structures are often difficult to differentiate as they correspond to very similar diffraction patterns ("pseudo-homometry").[18]

The optical properties and thermal stability of AIST materials strongly depend on the dopants Ag and In.[19,20] The same holds for high-pressure phase transitions. Whereas Sb_2Te transforms to an orthorhombic modification at 7-9 GPa before forming a body-centered tetragonal structure at 12.3 -15 GPa and a body-centered cubic one at > 28 GPa, $Ag_{11}In_6Sb_{55}Te_{28}$ shows only one phase transition to a body-centered tetragonal structure at 12.4 GPa;[21] however, an additional primitive cubic phase was reported when the sample was exposed to pressures between 3.4 – 12.4 GPa for several days. $AgInTe_2$, which forms upon annealing AIST, exhibits a rock-salt type structure under high pressure, but retransforms to the chalcopyrite-type structure upon decompression.[22] Quaternary solid solutions $AgIn_xSb_{1-x}Te_2$ are accessible by high-pressure synthesis.[23] They also crystallize in rocksalt-type structures, but in contrast to pure $AgInTe_2$ these high-pressure phases are inert at ambient pressure.

Therefore, high-pressure synthesis appears to be a promising route to metastable crystalline bulk material of AIST that is similar to the material present in PCM films. This allows one to characterize the transport properties of e. g. $Ag_{3.4}In_{3.7}Sb_{76.4}Te_{16.5}$. Such samples are not accessible by cooling or quenching melts; however, rapid quenching by melt spinning may mimic the conditions that are present during thin-film fabrication.

2.3.2 Results and discussion

2.3.2.1 Sample characterization

Conventional solid-state synthesis like quenching ampoules containing stoichiometric melts in water or long-term annealing of inhomogeneous ingots or pellets always lead to samples completely decomposed in a trigonal antimony telluride and chalcopyrite-type $AgInTe_2$. Samples that appear homogeneous according to their powder X-ray diffraction (PXRD) patterns can, however, be obtained by increasing the quenching rate, which can be achieved by melt-spinning (details cf. Experimental Section). In contrast to annealed or water-quenched ingots, the diffraction patterns of melt-spun samples show almost no reflections of $AgInTe_2$ (a small trace might be indicated by one very broad reflection, cf. Fig. 1). High-pressure high-temperature syntheses, i. e. quenching the sample from 850 °C under a pressure of 12 GPa also yield quaternary yet micro-/nanocrystalline samples, whereas lower pressures (e. g. 2.5 GPa) lead to inhomogeneous samples which consist of multiple phases. Both the melt-spun sample (MS-AIST) and the sample synthesized at 12 GPa (HP-AIST) are long-term stable at ambient conditions and not sensitive against air or water.

The meltspun sample's composition of $Ag_{3.7(2)}In_{4.1(3)}Sb_{79(2)}Te_{13(2)}$ as determined by SEM-EDX agrees quite well with the nominal composition of $Ag_{3.4}In_{3.7}Sb_{76.4}Te_{16.5}$ taking into account the uncertainties of the method. In contrast, for the HP-AIST the individual EDX points differ significantly, which might be caused by both their lumpy shape and very rough surface. The average of three typical analyses yields $Ag_{1.1(3)}In_{2.4(12)}Sb_{83(4)}Te_{14(2)}$, but Ag-richer areas could also be observed. However, high-temperature experiments indicate that both MS-AIST and HP-AIST contain the same overall composition (see below).

2.3.2.2 Crystal structure

The powder diffraction patterns of HP-AIST and MS-AIST (cf. Fig. 1) can both be indexed assuming rhombohedral metrics similar to that known from thin-film AIST samples. For optimal comparability of the two Rietveld refinements, the same set of parameters was refined for each data set. Based on the nominal composition, all atoms were constrained with fixed site occupancies according to the nominal composition on the same 00*z* (6*c*) position, *z* and a common isotropic displacement parameter was refined. Preferred orientation, which is common for layer-like compounds, was fitted with 4^{th} order spherical harmonics. The

anisotropic broadening of the reflection profiles of HP-AIST was treated by the LeBail-Jouanneaux algorithm.[24] Crystal data and atomic parameters are given in Tables 1 and 2, respectively. Further details of the crystal structure investigations may be obtained from Fachinformationszentrum Karlsruhe, 76344 Eggenstein-Leopoldshafen, Germany (Fax: +49 7247 808 666; email: crysdata@fiz-karlsruhe.de, http://www.fiz-karlsruhe.de/request_for_deposited_data.html) on quoting the depository numbers CSD-426574 for HP-AIST and CSD-426575 for MS-AIST.

The average structure of both compounds corresponds to the gray-As type (*A*7) structure; however, there are obvious differences in the powder diffraction patterns. The reflections of HP-AIST are broader than those of MS-AIST and the lattice parameters differ significantly. HP-AIST has a smaller unit-cell volume due to its shorter *c* lattice parameter, yet, its *a* lattice parameter is slightly larger than that of MS-AIST. The metrics of HP-AIST is closer to cubic (c/a = 2.54, regular value for the trigonal setting of a cubic cell: 2.45) than that of MS-AIST (c/a = 2.62) which is "stretched" along [001]. This difference would be expected for the sample under *in situ* high-pressure. Apparently the relaxation of its lattice after decompression is kinetically inhibited. This could be explained by a cubic high-pressure phase that becomes rhombohedral after decompression (see below, cf. Fig. 2 top). This would involve the formation of twin domains whose nano- or microcrystalline texture may lead to pronounced strain and cause the broad reflections. The *z* coordinate of the atom position in MS-AIST is 0.2400(1), the one of HP-AIST is 0.2450(5). The *z* value of the melt-spun sample is closer to the one reported for AIST (z = 0.2357(5))[14] in thin films. The *z* value of the high pressure sample is close to 0.25, which would correspond to the α-Hg structure type, i. e. no formation of *A*7-type layers. The *A*7 average structure of HP-AIST is confirmed by selected area electron diffraction (SAED) patterns (see below, cf. Fig. 2 top) which exhibit the *A*7 type's $01\bar{1}$ reflection that does not exist for the α-Hg type.

Table 1. Results of the Rietveld refinements for $Ag_{3.4}In_{.3.7}Sb_{76.4}Te_{16.5}$ prepared under high-pressure conditions (HP) and by melt spinning (MS).

$Ag_{3.4}In_{.3.7}Sb_{76.4}Te_{16.5}$	HP	MS
molar mass / g mol^{-1}	12199.44	12199.44
F(000)	305.7	
crystal system / space group	trigonal / $R\bar{3}m$ (no. 166)	
lattice parameters / Å	a = 4.3380(3) c = 11.004(1)	a = 4.3032(1) c = 11.2623(3)
cell volume / Å^3	179.33(3)	180.610(11)
density (X-ray) / g cm^{-3}	6.778(1)	6.730(1)
absorption coefficient / mm^{-1}	175.3	174.1
radiation	Cu-$K_{\alpha1}$ (λ = 1.540596 Å)	
2θ range / °	22 ≤ 2θ ≤ 100	
no. of data points	14601	
profile function	fundamental parameter approach	
constraints	6	
number of reflections	29	
refined parameters / thereof background	42 / 24	
R_p / R_{wp}	0.0139 / 0.0175	0.0300 / 0.0447
R_{Bragg}	0.0012	0.0171

Table 2. Atom positions, site occupancy factors (*s.o.f.*) and displacement parameters (B_{iso} / Å^2) for $Ag_{3.4}In_{.3.7}Sb_{76.4}Te_{16.5}$ prepared under high-pressure conditions (HP) and by melt spinning (MS).

sample	atom	*x y z*	*s.o.f.*	B_{iso}
HP	Ag/In/Sb/Te	0 0 0.2450(5)	0.034/0.037/0.764/0.165	0.75(5)
MS	Ag/In/Sb/Te	0 0 0.2400(1)	0.034/0.037/0.764/0.165	2.17(2)

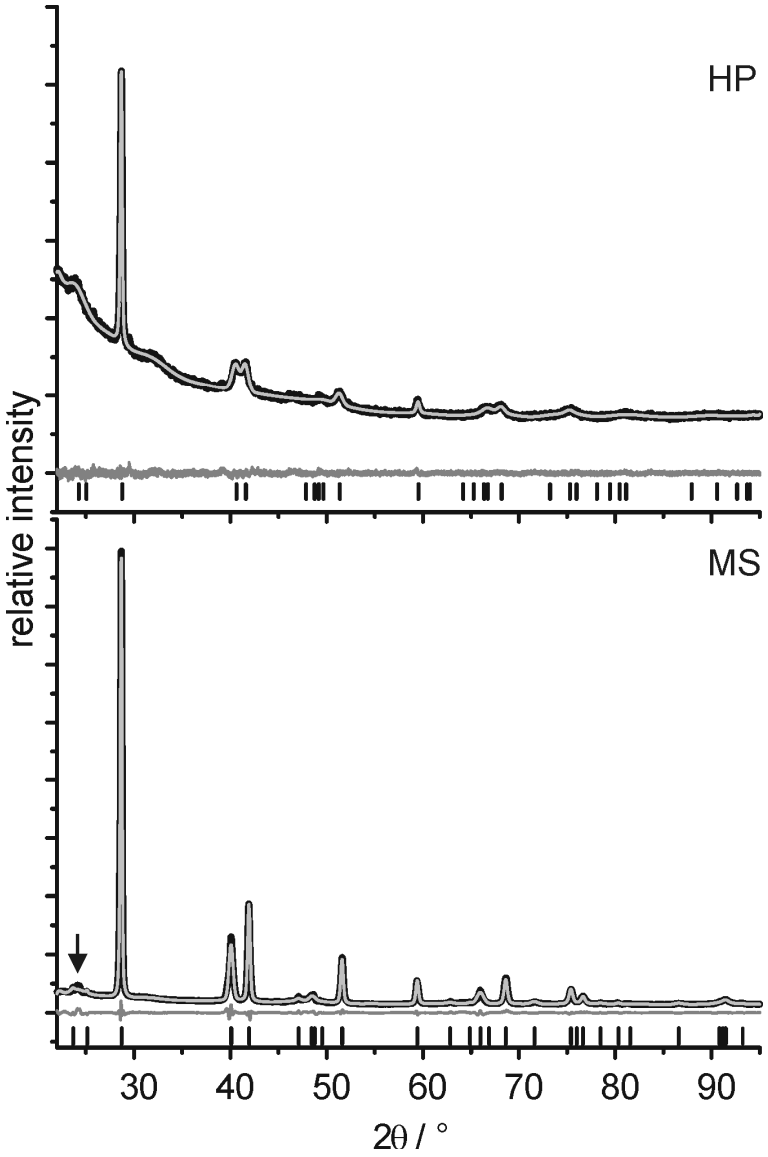

Fig. 1. Rietveld fits for $Ag_{3.4}In_{.3.7}Sb_{76.4}Te_{16.5}$ prepared under high-pressure conditions (top, "HP") and by melt spinning (bottom, "MS"). Experimental (black) and calculated data (gray); difference plot (gray, below), peak positions (black, vertical lines); the arrow marks a maximum that might be attributed to a trace of $AgInTe_2$.

2.3.2.3 Electron microscopy and diffraction

The SAED patterns in Figure 2 show that both samples crystallize in the *A*7 structure type. Patterns along the [211] zone axes contain the characteristic $01\bar{1}$ reflection with the same d-values as found in the corresponding powder patterns. These d-values can only be observed if $z \neq 0.25$, i. e. when *A*7-type layers are present – this formally involves the formation of a superstructure of the α-Hg type. The [100] zone axis SAED pattern of MS-AIST further shows the characteristic 003 reflection. The SAED pattern of the high-pressure sample exhibits very broad reflections which split at higher diffraction angles. This is due to a domain

structure, probably twin domains which might be the result of a phase transformation from a cubic high-pressure phase to the present rhombohedral one. Such a domain structure with canted domains could also explain the strain present in HP-AIST as mentioned above.

HRTEM images of MS-AIST (cf. Figure 3), whose composition was confirmed by EDX with spatial resolution, corroborate that there are no pronounced stacking faults or other short-range real-structure phenomena, which is consistent with the absence of characteristic diffuse scattering in SAED patterns. An image simulation based on the results of the Rietveld refinement of MS-AIST exhibits the same contrasts as the experimental image and thus further confirms the assignment of the *A*7 structure type.

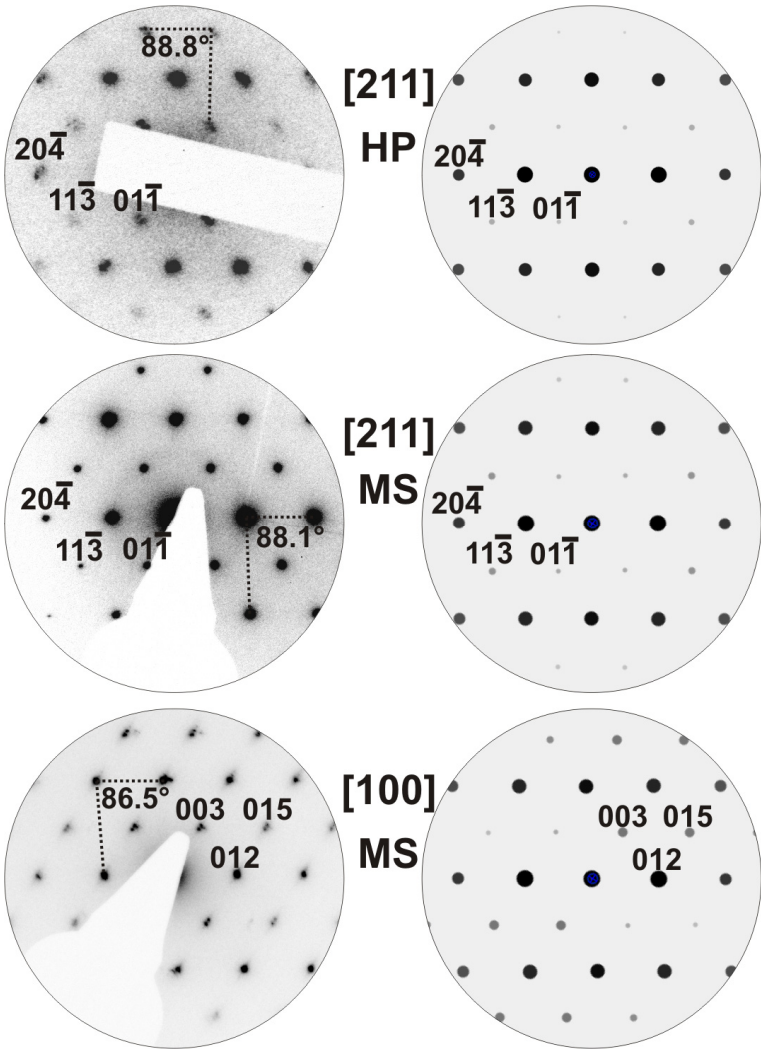

Fig. 2. SAED patterns of $Ag_{3.4}In_{3.7}Sb_{76.4}Te_{16.5}$: zone axis [211] of HP-AIST (top, left) and MS-AIST (middle, left) as well as zone axis [100] for MS-AIST (bottom, left); and corresponding simulations of the SAED patterns (kinematical approach) based on the results of the Rietveld refinements (right).

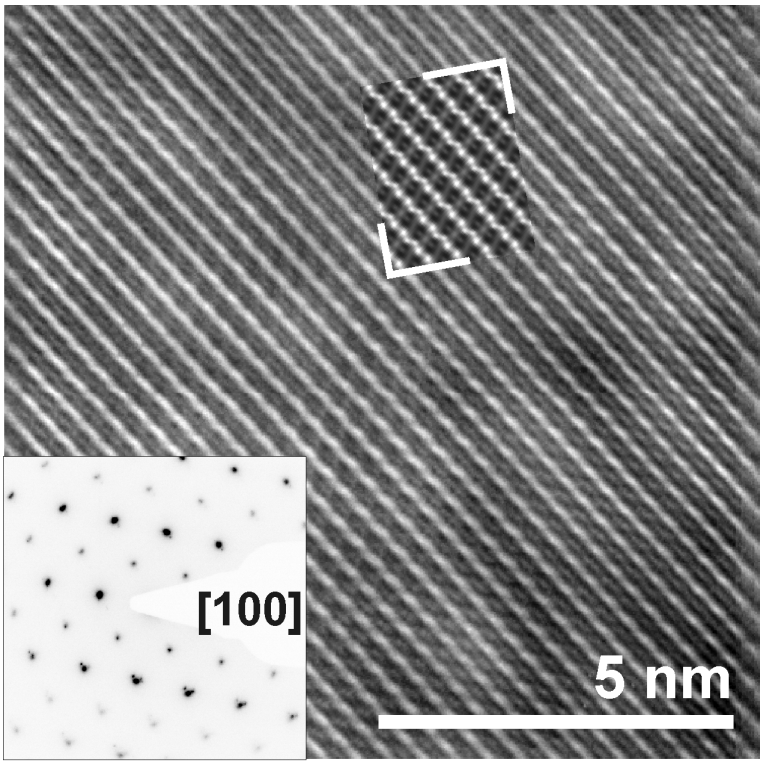

Fig. 3. Fourier filtered HRTEM image (zone axis [100]) of MS-AIST (top) with multislice image simulation (inset, defocus -64 nm, thickness 4.3 nm) and corresponding SAED pattern (bottom left).

2.3.2.4 Thermal behavior

The PXRD patterns of HP-AIST and MS-AIST differ up to 250 °C (cf. Fig. 4) but become very similar at higher temperatures. From 130 to 240 °C the metrics of HP-AIST relaxes upon heating and approaches that of MS-AIST. This corroborates that the different *c*/*a* ratios of both samples are indeed due to strain in HP-AIST which is reduced during heating.

At ~250 °C chalcopyrite-type $AgInTe_2$ is formed; its strongest reflection at ~ 11° 2θ becomes clearly visible. A rhombohedral Sb-rich antimony telluride represents the main phase (see also Fig. 5), probably doped with a small amount of In. It resembles Sb_8Te,[15] which has an *A*7 average structure, but forms various commensurately and incommensurately modulated modifications depending on the temperature and the annealing time:

$$Ag_{3.4}In_{3.7}Sb_{76.4}Te_{16.5} \rightarrow 3.4\ AgInTe_2 + In_{0.3}Sb_{76.4}Te_{9.7} \approx Sb_{7.9}Te{:}In$$

At ~ 440 °C the thermal expansion of the Sb-rich phase changes; some reflection positions, e. g. at 18° and 29° 2θ, shift to higher values upon heating. At this temperature, the structure

forms a long-periodically ordered layered compound of the type $(Sb_2)_k(Sb_2Te_3)_m$[16,17] as discussed in detail in Ref. [15]. However, the diffraction patterns are too noisy to analyze whether there is a fully ordered compound or an intermediate phase with a disordered stacking sequence.

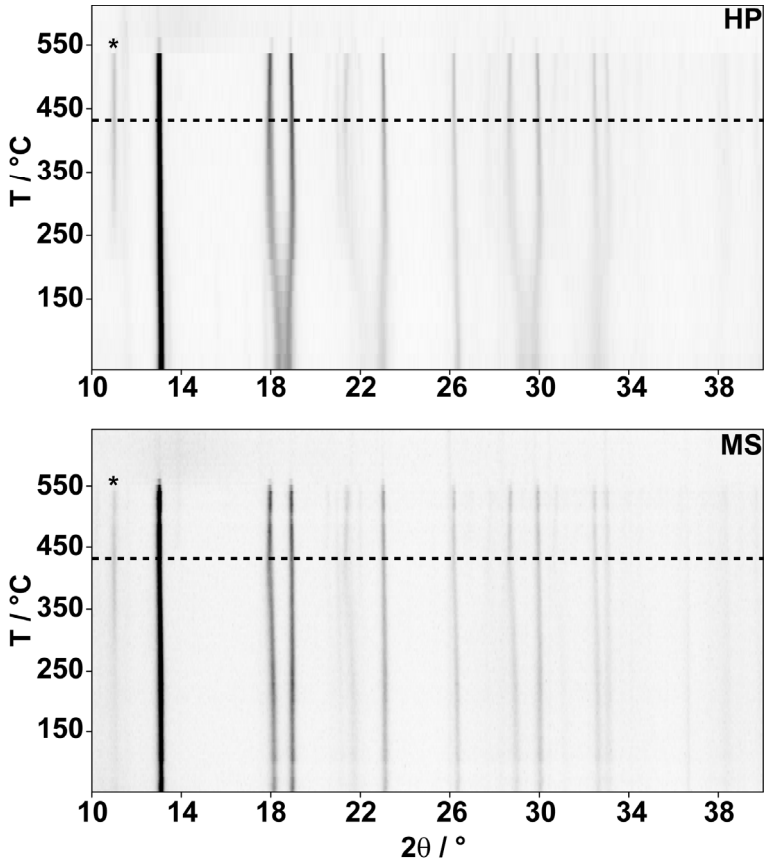

Fig. 4. Temperature-dependent X-ray diffraction patterns of $Ag_{3.4}In_{3.7}Sb_{76.4}Te_{16.5}$ prepared under high-pressure conditions (top, HP) and by melt spinning (bottom, MS). The strongest reflection of $AgInTe_2$ is marked by *. The dashed line marks the formation of a long-periodic Sb-rich phase.[15]

2.3.2.5 Transport properties

In order to characterize the thermoelectric properties of AIST material, a cylindrical pellet of MS-AIST was prepared by annealing compressed powder at 310 °C for 36 h. As the high-pressure sample is too small to establish a temperature gradient for Seebeck measurements and the individual melt-spun particles are too brittle for fixing contacts, this is the only reasonable way to obtain physical measurements (cf. Fig. 6). Without annealing, a cold-pressed pellet of melt-spun particles would exhibit very high resistivity values caused by grain boundaries as observed for melt-spun $GeBi_2Te_4$.[25] Thermal treatment at 310 °C leads to

the decomposition mentioned above (cf. Fig. 5); however, the temperature is below the phase transition temperature to the long-periodic layered Sb-rich Sb telluride. Although the refined phase ratio of 12.4 wt-% $AgInTe_2$ to 87.6 wt-% $Sb_{7.9}Te$:In (crystallizing in the *A*7 structure type) indicates almost complete decomposition, it is still interesting to investigate the thermoelectric properties of this material. Both phases probably contain all elements involved. Furthermore, heterogeneous materials like $(PbTe)_mAgSbTe_2$ (LAST) with precipitates of PbTe in an $AgSbTe_2$ matrix have recently received much attention due to their high thermoelectric figures of merit.[26]

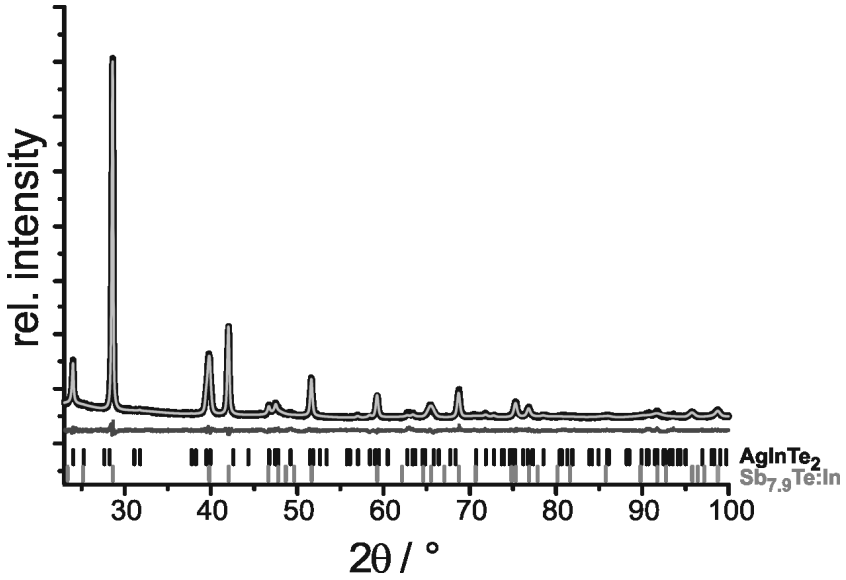

Fig. 5. Rietveld fit for MS-AIST ($Ag_{3.4}In_{3.7}Sb_{76.4}Te_{16.5}$) annealed for 36 h at 310 °C (R_p = 0.0170, R_{wp} = 0.0227, R_{Bragg} = 0.0084). Experimental (black) and calculated data (gray); difference plot (gray, below), peak positions of chalcopyrite-type $AgInTe_2$ (black, vertical lines) and gray-As type $Sb_{7.9}Te$:In (gray, vertical lines).

The temperature characteristics of the electrical resistivity (ρ) of decomposed AIST is metallic with 5.42 mΩcm (~185 S/cm) at room temperature (RT). This is rather high for a metal and might be caused by electron scattering at the grain boundaries. Such an effect may also cause the low thermal conductivity (κ) of 1.25 W/Km at RT, which is much lower than reported values for crystalline AIST thin films (4 W/Km at RT).[27] The Seebeck coefficient (S) of ~ 30 μV/K at RT is rather low compared to typical thermoelectric materials. These values lead to $ZT = S^2T / \kappa\rho$ of 0.003 at RT, which is low, but strongly increases with temperature.

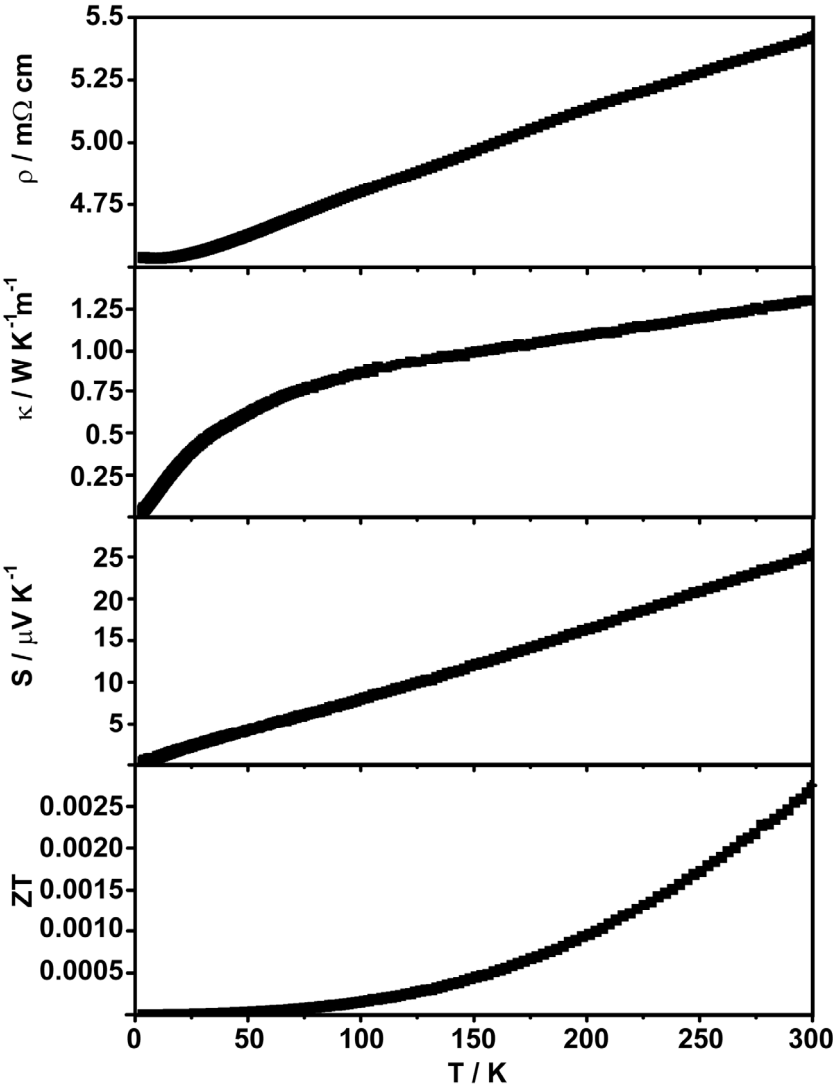

Fig. 6. Electrical resistivity, thermal conductivity, Seebeck coefficient and ZT value (from top to bottom) of a decomposed AIST pellet prepared by melt-spinning and subsequent annealing.

2.3.3 Conclusions

Both fast quenching (MS-AIST) and high-pressure synthesis (HP-AIST) lead to bulk material of the composition $Ag_{3.4}In_{3.7}Sb_{76.4}Te_{16.5}$ that corresponds to the well-known AIST PCM. Both Rietveld refinements as well as SAED patterns and HRTEM images show that the materials crystallize in the gray As (*A*7) structure type in which all atoms share the same Wyckoff position. The metrics and atom-layer distances of MS-AIST and HP-AIST differ significantly. The high-pressure sample appears to be closer to cubic and the layer formation is less pronounced than in MS-AIST. This leads to the conclusion that there is a cubic high-pressure phase and multiple twins of rhombohedral *A*7-type domains form upon decompression. The stress involved leads to pronounced strain and the high-pressure phase seems to be partially

retained. Quaternary AIST is not thermodynamically stable. In contrast to GST PCMs, there is no corresponding homogeneous stable crystalline phase, but the compound decomposes when annealed and $AgInTe_2$ is formed. Thus, single-phase bulk material is not accessible by conventional solid-state synthesis. However, during melt spinning the solidification is so fast that the nucleation of $AgInTe_2$ crystals is suppressed. Concerning HP-AIST, the existence of a simple cubic high-pressure phase of AIST, which was observed in *in situ* high-pressure experiments at > 3.4 GPa (for slightly different composition),[21] and the fact that $AgInTe_2$ forms a rocksalt-type high-pressure phase > 2 GPa[22] is crucial. Indium is only soluble in Sb-rich phases if it is coordinated in a (possibly distorted) octahedral fashion. As In is usually coordinated tetrahedrally, high pressure is required to promote octahedral coordination according to the pressure-coordination rule. The fact that cubic AIST phases only form at 3.4 - 12.4 GPa after several days of compression explains why experiments at lower pressures yield completely inhomogeneous samples.[21]

The lattice strain in HP-AIST relaxes at 130 °C so that samples become comparable to MS-AIST at higher temperatures. Thus, both samples decompose at ca. 250 °C when $AgInTe_2$ is formed.

The decomposition at high temperatures is a drawback for hypothetical thermoelectric applications. However, as expected from the comparable materials' requirements of PCMs and thermoelectric materials,[1] the thermal conductivity and electrical resistivity of decomposed AIST are in the range of good thermoelectrics. However, the low Seebeck coefficient, which has no important effect on the performance of PCMs, is the reason for the low thermoelectric figure of merit.

2.3.4 Experimental section

Synthesis

For the synthesis of starting materials for the high-pressure and melt-spinning experiments, stoichiometric mixtures (ca. 2 g) of the elements (silver 99.9999%, Alfa Aesar; indium 99.999%, Smart Elements; antimony 99.9999%, Smart Elements; tellurium 99.999%, Alfa Aesar) were melted at 950 °C in sealed silica glass ampoules under argon atmosphere and quenched in water to room temperature. The starting material contained mixtures of chalcopyrite-type $AgInTe_2$ and a trigonal (possibly doped) antimony telluride.

In order to provide high quenching rates (up to 10^7 K/s), the starting material was powdered and filled into a tantalum blast pipe of a melt-spinning apparatus (model SC, Bühler,

Germany). The material was melted using a water cooled high-frequency coil (high frequency generator Himmel HIT 12, Himmelwerk Hoch- & Mittelfrequenzanlagen GmbH, Germany) and afterwards sprayed on a rotating copper wheel (60 Hz) under an argon atmosphere of 500 mbar by using an excess argon pressure connected to the blast pipe. Due to the large heat sink, the material solidifies immediately. The resulting tinsel-like particles (about $5 \cdot 2 \cdot 0.2$ mm^3) were hurled away from the wheel onto a collecting tray. The whole setup was placed in a recipient that could be evacuated and/or filled with argon. For the thermoelectric characterization a cylindrical pellet of this sample (6 mm diameter) was compacted using a hydraulic press (22.5 kN) and subsequently annealed for 36 hours at 310 °C.

For syntheses under high-pressure conditions, a multi-anvil hydraulic press (Voggenreiter, Mainleus, Germany) was used.[28 -31] The quenched starting material was finely ground and densely loaded into a cylindical crucible, which was sealed with a cap, both made of hexagonal BN (Henze, Kempten, Germany). Heating the sample under high-pressure conditions was realized using an electrical resistance furnace, which consisted of two nested graphite tubes in which the crucible was centered. Two MgO discs were used to fill the remaining volume at the ends of the larger graphite tube. This arrangement was centered into a zirconia tube and then placed in a pierced Cr_2O_3-doped MgO octahedron (edge length 14 mm, Ceramic Substrates & Components, Isle of Wight, Great Britain). Two Mo plates at the ends of the zirconia tube ensured the electrical contact between the graphite tubes and two of the eight truncated WC cubes (edge length 8 mm) serving as anvils for the compression, between which the octahedron was placed. The cubes were separated by pyrophyllite gaskets. Within 350 min, the assembly was compressed to a pressure of 12 GPa. At this pressure, the temperature was increased to about 850 °C within 30 min and kept at this temperature for 30 min. Subsequently, the sample was quenched by the switching off the furnace. Afterwards, the pressure was reduced to ambient pressure within 1050 min.

X-ray diffraction

X-ray powder diffraction was performed with a Huber G670 Guinier camera with a fixed imaging plate and an integrated read-out system (Cu-$K_{\alpha 1}$ radiation, Ge(111) monochromator, λ = 1.54051 Å). Representative parts of the samples were crushed and fixed between Mylar foils using vacuum grease. The phase homogeneity was evaluated and Rietveld refinements were carried out using the program TOPAS.[32] For the collection of temperature-dependent powder diffraction patterns, a STOE Stadi P diffractometer with a imaging plate detector

system in a modified Debye-Scherrer geometry using Mo-$K_{\alpha 1}$ radiation (Ge(111) monochromator, λ = 0.71093 Å) was used. Powders were filled into silica glass capillaries (0.3 mm diameter), which were sealed with vacuum grease under argon atmosphere. During the measurements, the samples were heated up to 600 °C with a heating rate of 10 K/min.

Electron microscopy and X-ray spectroscopy

For transmission electron microscopy, the samples were finely ground, dispersed in ethanol and distributed on copper grids coated with a holey carbon film (S166-2, Plano GmbH, Germany) which were then fixed on a double-tilt holder. SAED patterns of HP-AIST were collected using a JEM2011 (Jeol Ltd., Japan) with a tungsten thermal emitter and an acceleration voltage of 200 kV equipped with a TVIPS CCD (model 114, resolution: 1k x 1k). HRTEM images, SAED patterns and EDX spectra of MS-AIST was measured using a Titan 80-300 (FEI, USA) with a field-emission gun operated at 300 kV equipped with a TEM TOPS 30 EDX spectrometer (EDAX, Germany). Images were recorded using an UltraScan 1000 camera (Gatan, USA, resolution 2k x 2k). HRTEM and SAED data were evaluated using the Digital Micrograph and EMS software packages;[33,34] ES Vision was used for EDX data evaluation.[35] For the HRTEM simulations, the multislice algorithm was used with the following parameters: spherical aberration C_s = 0.6 mm, semi convergence angle α = 2.1 mrad, energy spread ΔE = 0.9 eV and spread of focus of 3.6 nm.
Using a JSM-6500F (Jeol, USA) scanning electron microscope (SEM) equipped with a energy dispersive X-ray (EDX) detector (model 7418, Oxford Instruments, Great Britain), X-ray spectra of the ingot resulting from the high-pressure synthesis as well as melt-spun particles were recorded.

Electrical and thermal transport properties

The pellet of annealed MS-AIST was used for thermoelectric characterization. The temperature-dependent electrical conductivity was measured using a standard four-probe dc method with a physical property measurement system (PPMS, Quantum Design) employing a constant current of 5 mA. The data were collected in the temperature range of 2 – 300 K with a heating/cooling rate of 2 K/min. The uncertainty of the absolute electrical resistivity has been estimated to be ~20%. In addition, the thermal conductivity and the thermoelectric power were measured simultaneously using the thermal transport option of the PPMS. This is

based on a relaxation method employing one heater and two thermometers to determine the induced thermal voltage and the temperature gradient along the sample from 4 K to 300 K with a heating rate of 0.5 K/min. The relative error of these values is about 5%.

Acknowledgement

We thank T. Miller for the temperature-dependent powder diffraction experiments and C. Minke for SEM operation and EDX analyses. We are deeply grateful to Prof. Dr. W. Scherer for his generous support of this study. Furthermore, we thank PD Dr. G. Kreiner and R. Berthold for help with the melt-spinning experiments. This investigation was funded by the Deutsche Forschungsgemeinschaft (grant OE530/1-2) and the Studienstiftung des deutschen Volkes (scholarship for T.S.).

References

[1] M. N. Schneider, T. Rosenthal, C. Stiewe, O. Oeckler, *Z. Kristallogr.* **2010**, *225*, 463.

[2] M. Wuttig, S. Raoux, *Z. Anorg. Allg. Chem.* **2012**, *638*, 2455.

[3] T. Siegrist, P. Merkelbach, M. Wuttig, *Annu. Rev. Condens. Matter Phys.* **2012**, *3*, 215.

[4] S. Raoux, *Annu. Rev. Mater. Res.* **2009**, *39*, 9.

[5] M. Wuttig, N. Yamada, *Nature* **2007**, *6*, 824.

[6] D. Lencer, M. Salinga, B. Grabowski, T. Hickel, J. Neugebauer, M. Wuttig, *Nature Mater.* **2008**, *7*, 972.

[7] D. L. Medlin, G. J. Snyder, *Curr. Opin. Colloid In.* **2009**, *14*, 226.

[8] M. G. Kanatzidis, *Chem. Mater.* **2010**, *22*, 648.

[9] J. R. Sootsman, D. Y. Chung, M. G. Kanatzidis, *Angew. Chem. Int. Ed.* **2009**, *48*, 8616.

[10] Y. C. Lan, A. J. Minnich, G. Chen, Z.F. Ren, *Adv. Funct. Mater.* **2010**, *20*, 357.

[11] G. J. Snyder, E. S. Toberer, *Nature Mater.* **2008**, *7*, 105.

[12] E.-R. Sittner, K. S. Siegert, P. Jost, C. Schlockermann, F. R. L. Lange, M. Wuttig, *Phys. Status Solidi A* **2013**, *210*, 147.

[13] T. Rosenthal, M. N. Schneider, C. Stiewe, M. Döblinger, O. Oeckler, *Chem. Mater.* **2011**, *23*, 4349.

[14] T. Matsunaga, Y. Umetani, N. Yamada, *Phys. Rev. B* **2001**, *64*, 184116.

[15] T. Matsunaga, R. Kojima, N. Yamada, Y. Kubota, K. Kifune, *Acta Crystallogr. Sect. B* **2012**, *68*, 559.

[16] P. F. P. Poudeu, M. G. Kanatzidis, *Chem. Commun.* **2005**, *21*, 2672.

[17] K. Kifune, Y. Kubota, T. Matsunaga, N. Yamada, *Acta Crystallogr. Sect. B* **2005**, *61*, 492.

[18] M. N. Schneider, M. Seibald, P. Lagally, O. Oeckler, *J. Appl. Crystallogr.* **2010**, *43*, 1012.

[19] H. Tashiro, M. Harigaya, Y. Kageyama, K. Ito, M. Shinotsuka, K. Tani, A. Watada, N. Yiwata, Y. Nakata, S. Emura, *Jpn. J. Appl. Phys.* **2002**, *41*, 3758.

[20] M. L. Lee, L. P. Shi, Y. T. Tian, C. L. Gan, X. S. Miao, *Phys. Status Solidi A* **2008**, *205*, 340.

[21] M. Krbal. A. V. Kolobov, P. Fons, J. Haines, A. Pradel, M. Ribes, A. A. Piarristeguy, C. Levelut, R. Le

Parc, A. Agafonov, M. Hanfland, J. Tominaga, *Phys. Rev. B* **2011**, *83*, 024105.

[22] K. J. Range, G. Engert, A. Weiss, *Solid State Commun.* **1969**, *7*, 1749.

[23] T. Schröder, T. Rosenthal, D. Souchay, C. Petermayer, S. Grott, E.-W. Scheidt, C. Gold, W. Scherer, O. Oeckler, *J. Solid State Chem.* **2013**, *206*, 20.

[24] A. LeBail, A. Jouanneaux, *J. Appl. Crystallogr.* **1997**, *30*, 265

[25] T. Schröder, M. N. Schneider, T. Rosenthal, A. Eisele, C. Gold, E.-W. Scheidt, W. Scherer, R. Berthold, O. Oeckler, *Phys. Rev. B* **2011**, *84*, 184104.

[26] K. F. Hsu, S. Loo, F. Guo, W. Chen, J. S. Dyck, C. Uher, T. Hogan, E. K. Polychroniadis, M. G. Kanatzidis, *Science* **2004**, *303*, 818.

[27] X. Jiao, J. Wei, F. Gan, M. Xiao, *Appl. Phys. A* **2009**, *94*, 627.

[28] D. Walker, M. A.Carpenter, C. M. Hitch, *Am. Mineral.* **1990**, *75*, 1020.

[29] D. Walker, *Am. Mineral.* **1991**, *76*, 1092.

[30] D. C. Rubie, *Phase Trans.* **1999**, *68*, 431.

[31] H. Huppertz, *Z. Naturforsch. B* **2001**, *56*, 697.

[32] *TOPAS-Academic*, *V. 4.1*, Coelho Software, Brisbane, Australia, **2007**.

[33] *DigitalMicrograph 3.6.1*, Gatan Software, Pleasanton, USA, **1999**.

[34] P. A. Stadelmann, *Ultramicroscopy* **1987**, *21*, 131.

[35] *ESVision, 4.0.164*, Emispec Systems Inc., Tempe, USA, **1994-2002**.

2.4 A high-pressure route to thermoelectrics with low thermal conductivity: the solid solution series $AgIn_xSb_{1-x}Te_2$

Thorsten Schröder, Tobias Rosenthal, Daniel Souchay, Christian Petermayer, Sebastian Grott, Ernst-Wilhelm Scheidt, Christian Gold, Wolfgang Scherer, Oliver Oeckler
J. Solid State Chem. **2013**, *206*, 20 – 26.

Abstract

Metastable rocksalt-type phases of the solid solution series $AgIn_xSb_{1-x}Te_2$ (x = 0.1, 0.2, 0.4, 0.5 and 0.6) were prepared by high-pressure synthesis at 2.5 GPa and 400 °C. In these structures, the coordination number of In^{3+} is six, in contrast to chalcopyrite ambient-pressure $AgInTe_2$ with fourfold In^{3+} coordination. Transmission electron microscopy shows that real-structure phenomena and a certain degree of short-range order are present, yet not very pronounced. All three cations are statistically disordered. The high degree of disorder is probably the reason why $AgIn_xSb_{1-x}Te_2$ samples with $0.4 < x < 0.6$ exhibit very low thermal conductivities with a total $\kappa < 0.5$ W/Km and a lattice contribution of $\kappa_{ph} \sim 0.3$ W/Km at room temperature. These are lower than those of other rocksalt-type tellurides at room temperature; e. g., the well-known thermoelectric $AgSbTe_2$ ($\kappa \sim 0.6$ W/Km). The highest ZT value (0.15 at 300 K) is observed for $AgIn_{0.5}Sb_{0.5}Te_2$, mainly due to its high Seebeck coefficient of 160 μV/K. Temperature-dependent X-ray powder patterns indicate that the solid solutions are metastable at ambient pressure. At 150 °C, the quaternary compounds decompose into chalcopyrite-type $AgInTe_2$ and rocksalt-type $AgSbTe_2$.

2.4.1 Introduction

The interconversion of thermal and electrical energy by means of thermoelectrics is intensely researched, the long-term goal being the efficient generation of electrical energy from waste heat and the development of novel materials for Peltier coolers or small heating devices. The dimensionless figure of merit $ZT = S^2\sigma T / \kappa$ (Seebeck coefficient S, electrical conductivity σ, thermal conductivity κ)[1] is a measure of the efficiency of the conversion process. All quantities involved depend on the charge carriers' concentration and mobility and therefore cannot be optimized independently. According to the Wiedemann-Franz law, σ and the

electronic part of the thermal conductivity (κ_{el}) are proportional to each other. Increasing the mobility of the charge carriers and thus σ, in addition, usually lowers the absolute value of S. Therefore, a common approach to improving thermoelectrics aims at decreasing the phononic part of the thermal conductivity (κ_{ph}) without significantly interfering with the electronic properties. This paradigm suggests that effective phonon scattering is important, which can be achieved by creating nano-domain structures, e. g. twin domains in TAGS, i. e. $(AgSbTe_2)_{1-n}(GeTe)_n$,[2-4] or short-range ordered defect layers in GST materials, i. e. $(GeTe)_nSb_2Te_3$.[5,6] Domain structures often result from phase transitions or, in case of heterogeneous systems, from partial phase separation.[7-14] Exsolution may lead to endotactic nanodots, e. g. in LAST ($AgPb_nSbTe_{2+n}$).[15] As nanostructures and other real-structure effects as well as phase transitions play an important role, transmission electron microscopy and temperature-dependent X-ray diffraction are very valuable tools for structure elucidation.

Synthetic approaches to lowering κ_{ph} may include the application of high pressure or fast quenching (e. g. melt spinning) during crystallization. Stress as well as short crystallization times usually yield smaller grain sizes (i. e. more grain boundaries) and more pronounced real-structure effects. Both features may scatter phonons more effectively than electrons.[16,17]

A large number of ternary I-V-VI_2 phases exhibit very low intrinsic thermal conductivities (< 1 W/Km),[18,19] the most prominent compound being $AgSbTe_2$ with $\kappa \approx 0.6$ W/Km at room temperature (RT). It is characterized by ZT values of ~0.3 at RT and up to 1.3 at 400 °C, respectively;[20] and represents both the end member of TAGS solid solutions and the matrix of LAST materials.[2-4,15] All of these materials, including nanostructured ones, exhibit cation disorder in sometimes distorted rocksalt-type crystal structures.

In contrast to $AgSbTe_2$, $AgInTe_2$ crystallizes in the chalcopyrite structure type, a superstructure of the sphalerite type where all cations are tetrahedrally coordinated by Te. In accordance with the pressure-coordination rule, $AgInTe_2$ transforms to a rocksalt-type structure under high pressure; however, phases with tetrahedrally coordinated In^{3+} are formed again after decompression within a few days.[21] For $AgInSe_2$, rocksalt-type high-pressure phases are metastable at ambient pressure when In is partially substituted by Sb.[22] Thus, one can expect that cation-disordered rocksalt-type members of a solid solution series $AgInTe_2$-$AgSbTe_2$ are accessible by high-pressure high-temperature syntheses and may be metastable at ambient conditions. For these phases, no thermoelectric data are available. However, chalcopyrite-type $AgInTe_2$ exhibits a thermal conductivity of ~ 2 W/Km at 300 K,[14,23] more than three times higher than that of $AgSbTe_2$. The thermal conductivities of quaternary solid

solutions may be expected to be even lower than those of ternary I-V-VI_2 compounds due to the fact that the number of disordered cation types is higher.

The element combination Ag/In/Sb/Te ("AIST") is an intriguing one as it plays an important role in the field of phase-change materials for rewritable optical data storage (e. g. $Ag_{3.4}In_{3.7}Sb_{76.4}Te_{16.5}$ on CD-RWs).[24] As the required material properties for phase-change materials are comparable to those for thermoelectrics,[5] the present study aims at characterizing the thermoelectric properties and structural features as well as stability ranges of AIST materials prepared by high-pressure high-temperature synthesis.

2.4.2 Experimental

Synthesis

Bulk samples with the nominal compositions $AgIn_xSb_{1-x}Te_2$ (x = 0.1, 0.2, 0.4, 0.5 and 0.6) were prepared by heating stoichiometric mixtures (e. g., 1.5 g) of the pure elements (silver 99.9999%, Alfa Aesar; indium 99.999%, Smart Elements; antimony 99.9999%, Smart Elements; tellurium 99.999 %, Alfa Aesar) in sealed silica glass ampoules to 950 °C under argon atmosphere. The resulting melts were quenched to RT in water. They contain mixtures of chalcopyrite-type $AgInTe_2$ and rocksalt-type $AgSbTe_2$ and were used as starting materials for high-pressure syntheses.

High-pressure experiments were performed using a multi-anvil hydraulic press (Voggenreiter, Mainleus, Germany).[25-28] Quenched $AgIn_xSb_{1-x}Te_2$ was powdered, loaded into a cylindrical crucible made of hexagonal BN (Henze, Kempten, Germany) and sealed with a BN cap. In order to obtain an electrical resistance furnace; the capsule was centered within two nested graphite tubes. The remaining volume at both ends of the outer graphite tube was filled with two MgO discs. The arrangement, surrounded by a zirconia tube, was then placed into a pierced truncated Cr_2O_3-doped MgO octahedron (edge length 25 mm, Ceramic Substrates & Components, Isle of Wight, Great Britain). Eight truncated tungsten carbide cubes (truncation edge length 17 mm) served as anvils for the compression of the truncated octahedron, they were separated by pyrophyllite gaskets. The graphite tubes were electrically contacted by two Mo plates. The assembly was compressed up to a pressure of 2.5 GPa in 2 h. At this constant pressure, samples were prepared by annealing at 400 °C for 5 h and subsequently quenching the sample by turning off the furnace. After quenching the sample, the pressure was maintained for 1 h to ensure that RT was reached. Subsequently, the pressure was reduced to ambient pressure within 6 h.

EDX analysis

EDX (energy dispersive X-Ray) spectra of representative pieces of crushed bulk samples were recorded using a JSM-6500F (Jeol, USA) scanning electron microscope with EDX detector (model 7418, Oxford Instruments, Great Britain). For each sample, the results of five point analyses were averaged and the errors were estimated from their variance (see Table 1).

Table 1. EDX results for $AgIn_xSb_{1-x}Te_2$ (averaged from 5 point analyses each)

sum formula	atom-% (calc.)	atom-% (EDX)
$AgIn_{0.6}Sb_{0.4}Te_2$	Ag: 25; In: 15; Sb: 10; Te: 50	Ag: 23.1(7); In: 14.8(4); Sb: 11.6(3); Te: 50.5(9)
$AgIn_{0.5}Sb_{0.5}Te_2$	Ag: 25; In: 12.5; Sb: 12.5; Te: 50	Ag: 24.2(3); In: 12.1(6); Sb: 13.5(5); Te: 50.2(5)
$AgIn_{0.4}Sb_{0.6}Te_2$	Ag: 25; In: 10; Sb: 15; Te: 50	Ag: 24.9(5); In: 8.9(3); Sb: 16.0(5); Te: 50.2(6)
$AgIn_{0.2}Sb_{0.8}Te_2$	Ag: 25; In: 5; Sb: 20; Te: 50	Ag: 24.5(4); In: 4.5(3); Sb: 20.9(3); Te: 50.1(4)
$AgIn_{0.1}Sb_{0.9}Te_2$	Ag: 25; In: 2.5; Sb: 22.5; Te: 50	Ag: 24.5(5); In: 2.2(5); Sb: 23.5(5); Te: 49.7(6)

X-ray diffraction

X-ray powder patterns were recorded with a Huber G670 Guinier camera equipped with a fixed imaging plate and integrated read-out system using Cu-$K_{\alpha1}$ radiation (Ge monochromator, λ = 1.54051 Å). Specimens were prepared by crushing representative parts of the samples and fixing the powder on Mylar foils using vacuum grease. The phase homogeneity was evaluated and lattice parameters were determined by pattern fitting (Rietveld method) using the program TOPAS.[29] Temperature-dependent powder diffraction experiments were performed with a STOE Stadi P powder diffractometer equipped with an imaging plate detector system using Mo-$K_{\alpha1}$ radiation (Ge monochromator, λ = 0.71093 Å) in a modified Debye–Scherrer geometry. Powdered specimens were filled into silica glass capillaries with 0.3 mm diameter and sealed with vacuum grease under argon atmosphere. During the measurement, the samples were heated up to 600 °C in a graphite furnace with a heating rate of 5 K/min.

Transmission electron microscopy

For transmission electron microscopy, finely ground samples were dispersed in ethanol and distributed on copper grids coated with a holey carbon film (S166-2, Plano GmbH, Germany). The grids were fixed on a double-tilt holder. Selected area electron diffraction (SAED), high resolution transmission electron microscopy (HRTEM) and EDX measurements were done on a Titan 80-300 (FEI, USA) with a field emission gun operated at 300 kV equipped with a TEM TOPS 30 EDX spectrometer (EDAX, Germany). Images were recorded using an UltraScan 1000 camera (Gatan, USA, resolution: 2k x 2k). HRTEM and SAED data were evaluated using the programs Digital Micrograph[30] and EMS,[31] EDX data were processed with ES Vision.[32]

Electrical and thermal transport measurements

The temperature-dependent conductivities $\sigma(T)$ of the samples were measured by a standard four-probe dc method employing a constant current of 5 mA with a physical property measurement system (PPMS, Quantum Design). The data were collected in the temperature range of 2 – 300 K by cooling and heating sequences in which the temperature changed at a rate of 0.5 K min^{-1}. The uncertainty of the absolute electrical resistivity has been estimated by taking into account the errors in specifying the sample dimensions; it amounts to ~ 20 %. The thermoelectric power $S(T)$ and the thermal conductivity $\kappa(T)$ of samples were measured simultaneously using the thermal transport option of the PPMS. This is based on a relaxation method employing one heater and two thermometers to determine the induced thermal voltage and the temperature gradient along the sample in a temperature range between 4 K and 300 K. These measurements were carried out using bar-shaped samples with typical dimensions between 4 and 7 mm^3 during a heating process at a rate of 0.5 $Kmin^{-1}$. The total accuracy of the $S(T)$ and $\kappa(T)$ values is about 5%.

2.4.3 Results and discussion

2.4.3.1 Crystal structure

The powder diffraction patterns of the compounds of the solid solution series $AgIn_xSb_{1-x}Te_2$ with x = 0.1, 0.3, 0.4, 0.5 and 0.6, which were obtained by thermal quenching under a

constant pressure of 2.5 GPa, could be indexed assuming cubic metrics. For $x > 0.6$, the samples were inhomogeneous. The average structure (for $x \leq 0.6$) derived from Bragg reflections corresponds to the rocksalt type (space group $Fm\bar{3}m$, no. 225), which has been reported for $AgSbTe_2$ ($x = 0$) at ambient pressure and for the high-pressure phase of $AgInTe_2$ ($x = 1$).[33,20] The powder patterns contain little evidence for different scattering densities on anion and cation positions due to the similar electron counts; however, very weak intensities can be observed for the NaCl type's reflections hkl with h, k, l = 2n+1 (more pronounced in electron diffraction patterns, see below). Thus, Ag, In and Sb were placed on the cation position (occupancy factors 0.5 for Ag, $^{x}/_{2}$ for In and $0.5 - {}^{x}/_{2}$ for Sb), whereas full occupancy by Te was assumed on the anion site. The occupancy factors were set according to the nominal composition of the starting materials, which was confirmed by EDX measurements (see Table 1). A common isotropic displacement parameter was used for the cations; the one for Te was refined separately. Slight preferred orientation was taken into account using the March-Dollase algorithm. Representative profile fits resulting from Rietveld refinements for $AgIn_{0.5}Sb_{0.5}Te_2$ and $AgIn_{0.6}Sb_{0.4}Te_2$ are shown in Fig. 1 (the Rietveld fit for $x = 0.1$, 0.2 and 0.4 can be found in the Supplementary Information). Crystal data and the refined atomic parameters are given in Tables 2 and 3, respectively. Further details of the crystal structure investigations may be obtained from Fachinformationszentrum Karlsruhe, 76344 Eggenstein-Leopoldshafen, Germany (fax: (+49)7247-808-666; e-mail: crysdata@fiz-karlsruhe.de, http://www.fiz-karlsruhe.de /request_for_deposited_data.html) on quoting the depository numbers CSD-426090, CSD-426089, CSD-426086, CSD-426088 and CSD-426087 for $x = 0.1$, 0.2, 0.4, 0.5 and 0.6, respectively.

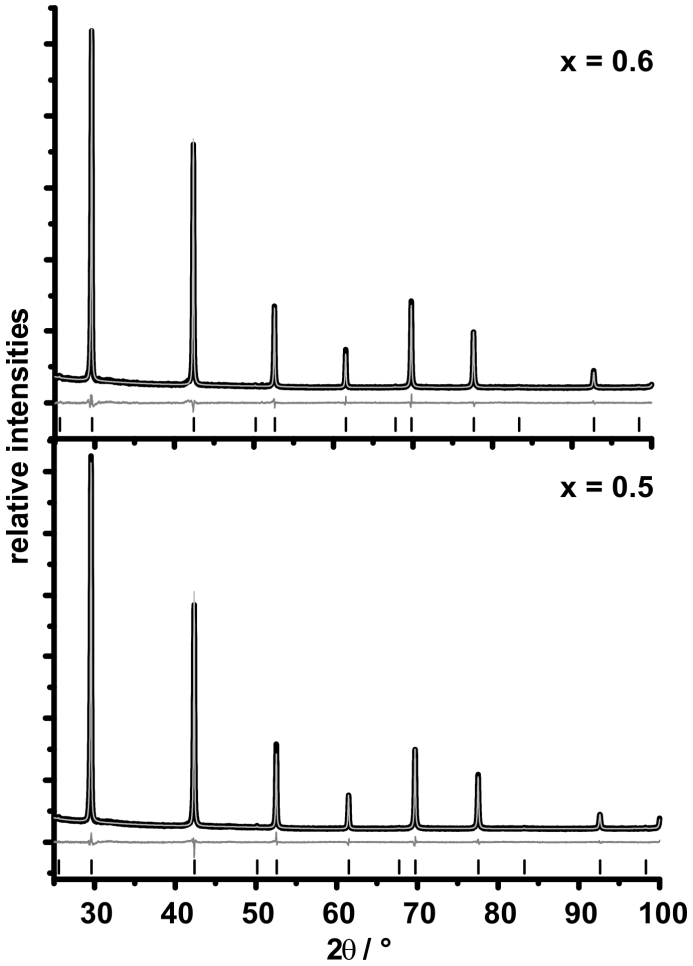

Fig. 1. Rietveld fits for $AgIn_{0.5}Sb_{0.5}Te_2$ (bottom) and $AgIn_{0.6}Sb_{0.4}Te_2$ (top); experimental (black) and calculated data (gray); difference plot (gray, below), peak positions (black, vertical lines).

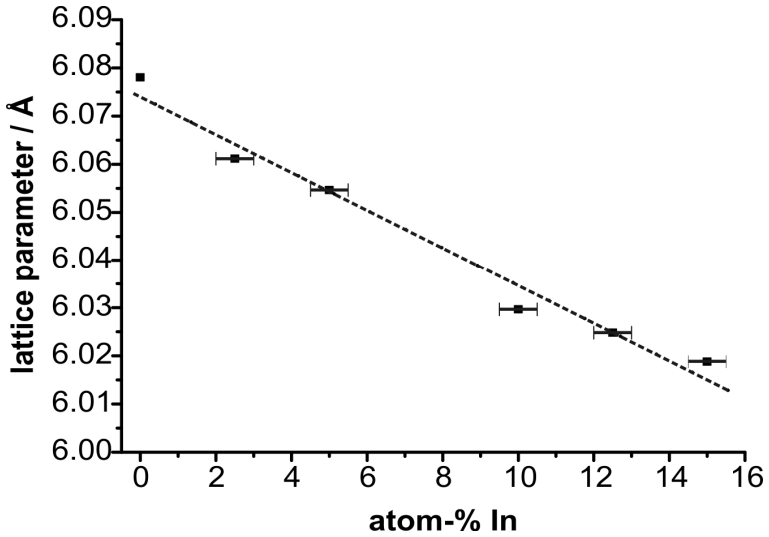

Fig. 2. Vegard's plot for $AgIn_xSb_{1-x}Te_2$ (dotted line: least-squares fit) with estimated error bars of 0.5 atom-% (see text); the atom-% refer to the sum formula (i. e., $AgInTe_2$ would correspond to 25 atom-% In); value for $AgSbTe_2$ from ref. [32].

Table 2. Results of the Rietveld refinements for $AgIn_{0.1}Sb_{0.9}Te_2$, $AgIn_{0.2}Sb_{0.8}Te_2$, $AgIn_{0.4}Sb_{0.6}Te_2$, $AgIn_{0.5}Sb_{0.5}Te_2$, and $AgIn_{0.6}Sb_{0.4}Te_2$.

Sum formula	$AgIn_{0.1}Sb_{0.9}Te_2$	$AgIn_{0.2}Sb_{0.8}Te_2$	$AgIn_{0.4}Sb_{0.6}Te_2$	$AgIn_{0.5}Sb_{0.5}Te_2$	$AgIn_{0.6}Sb_{0.4}Te_2$
Molar mass / g mol^{-1}	484.13	483.44	482.05	481.36	480.66
$F(000)$	403.6	403.2	402.4	402	401.6
Crystal system / space group (no.)	cubic / $Fm\bar{3}m$ (no.225)				
Lattice parameter / Å	6.06114(2)	6.05464(2)	6.02965(2)	6.02483(2)	6.01881(2)
Cell volume / Å^3	222.671(2)	221.955(2)	219.218(2)	218.693(2)	218.038(2)
Density (X-ray) / g cm^{-3}	7.221	7.234	7.303	7.310	7.321
Radiation	Cu-$K_{\alpha1}$ (λ = 1.540596 Å)				
2θ range / °	$20 \leq 2\theta \leq 100$				
Profile function	fundamental parameter approach				
Constraints	2				
Number of reflections	15				
Refined parameters / thereof background	23 / 12	23 / 12	23 / 12	23 / 12	23 / 12
R_p / R_{wp}	0.0168 / 0.0239	0.0186 / 0.0259	0.0149 / 0.0209	0.0173 / 0.0238	0.0170 / 0.0244
Gof	0.841	0.937	0.743	0.888	0.890

Table 3. Atom positions, occupancy and displacement parameters (B_{eq}) for $AgIn_{0.1}Sb_{0.9}Te_2$, $AgIn_{0.2}Sb_{0.8}Te_2$, $AgIn_{0.4}Sb_{0.6}Te_2$, $AgIn_{0.5}Sb_{0.5}Te_2$, and $AgIn_{0.6}Sb_{0.4}Te_2$.

Sum formula	Atom	Wyckoff position	x y z	s.o.f.	B_{eq}
$AgIn_{0.1}Sb_{0.9}Te_2$	Ag/In/Sb	4*a*	0 0 0	0.5/0.05/0.45	2.36(2)
	Te	4*b*	$^1/_2$ $^1/_2$ $^1/_2$	1	1.57(2)
$AgIn_{0.2}Sb_{0.8}Te_2$	Ag/In/Sb	4*a*	0 0 0	0.5/0.1/0.4	2.34(3)
	Te	4*b*	$^1/_2$ $^1/_2$ $^1/_2$	1	1.58(2)
$AgIn_{0.4}Sb_{0.6}Te_2$	Ag/In/Sb	4*a*	0 0 0	0.5/0.2/0.3	1.53(2)
	Te	4*b*	$^1/_2$ $^1/_2$ $^1/_2$	1	1.18(2)
$AgIn_{0.5}Sb_{0.5}Te_2$	Ag/In/Sb	4*a*	0 0 0	0.5/0.25/0.25	1.35(2)
	Te	4*b*	$^1/_2$ $^1/_2$ $^1/_2$	1	0.90(2)
$AgIn_{0.6}Sb_{0.4}Te_2$	Ag/In/Sb	4*a*	0 0 0	0.5/0.3/0.2	1.29(2)
	Te	4*b*	$^1/_2$ $^1/_2$ $^1/_2$	1	0.83(2)

The lattice parameters approximately fulfil Vegard's law (see Fig. 2) up to x = 0.6; indicating a solid solution series. The standard deviations of the lattice parameters are negligible compared to the uncertainties of the composition of high-pressure samples. The latter were estimated from the variance of EDX analyses and their deviation from the starting compositions. The lattice parameter of $AgSbTe_2$ deviates slightly more from the least-squares fit than the other values. This might be due to the fact that $AgSbTe_2$ cannot be synthesized without minor amounts of Ag_2Te so that its actual composition has been given as $Ag_{19}Sb_{29}Te_{52}$.[34]

2.4.3.2 Thermal behavior

Temperature-dependent powder X-ray diffraction patterns (Fig. 3 middle and bottom, additional ones in the Supplementary Information) show that, for instance, $AgIn_{0.5}Sb_{0.5}Te_2$ and $AgIn_{0.1}Sb_{0.9}Te_2$ decompose upon heating. The higher the In concentration, the lower the temperature that is required for the transition to the stable state, which corresponds to a mixture of rocksalt-type $AgSbTe_2$ and chalcopyrite-type $AgInTe_2$. The decomposition of $AgIn_xSb_{1-x}Te_2$ starts at 120 °C for x = 0.6, at 140 °C for x = 0.5 and 0.4, at 160 °C for x = 0.2 and at 200 °C for x = 0.1. This is consistent with the fact that samples with x > 0.6 are not long-term stable even at RT.

Chalcopyrite-type $AgInTe_2$ begins to form while the diffraction pattern is still dominated by the reflections of the rocksalt-type phase. The intensity of the latter's Bragg peaks is rather invariant, however, the reflection positions shift upon heating. This is due to the formation of $AgSbTe_2$ which has the same structure type but displays a slightly different lattice parameter (a = 6.078 Å).[32] It might still contain small amounts of In. As indicated by the dashed rectangles in Fig. 3, an additional reflection is observed at intermediate temperature which disappears when the rocksalt-type reflections of (possibly In-doped) $AgSbTe_2$ become stronger at higher temperature. This single reflection is not sufficient to decide if the rocksalt-type phase is distorted (reflection splitting) or if an additional intermediate phase (e. g. a silver telluride) is present. The diagram for x = 0.1 shows that at least at high temperatures, small amounts of In are soluble in $AgSbTe_2$ as the chalcopyrite-type reflections disappear without another phase being formed.

2.4.3.3 Electron microscopy of $AgIn_{0.5}Sb_{0.5}Te_2$

Electron microscopy studies of $AgIn_{0.5}Sb_{0.5}Te_2$ confirm the results of the Rietveld refinements. The *d*-values observed in selected area electron diffraction (SAED) patterns (Fig. 4) are consistent with those found in the Rietveld fit of the corresponding X-ray powder data (cf. Fig. 1, bottom). The rocksalt type's reflections with h, k, l = 2n+1 are clearly visible. Samples are chemically homogeneous according to TEM-EDX. There are just very weak diffuse intensities; this means that there are no pronounced short-range cation ordering phenomena, atomic size effect[35] or other real-structure features. However, the scattering contrast between the elements involved is small, so that a possible small degree short-range

order without relaxation is hard to detect. There are no discrete maxima between the Bragg reflections in SAEDs which would indicate a tendency to form a superstructure.

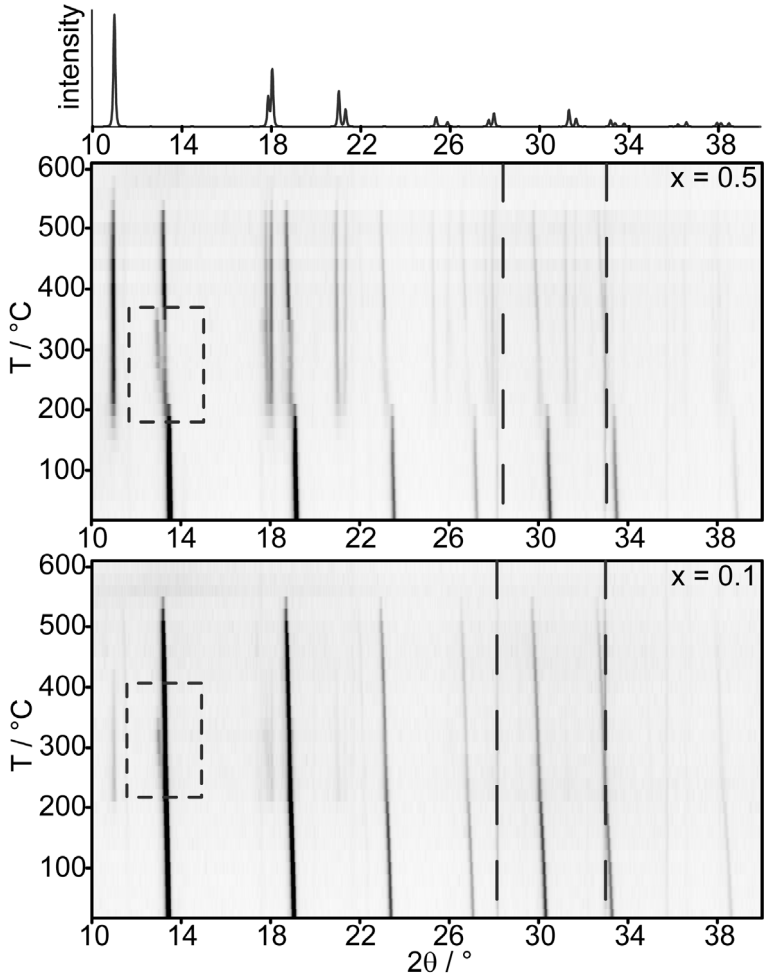

Fig. 3. Simulated powder X-ray diffraction pattern of chalcopyrite-type $AgInTe_2$ at ambient conditions (top), temperature dependent powder X-ray diffraction patterns of $AgIn_{0.5}Sb_{0.5}Te_2$ (middle) and $AgIn_{0.1}Sb_{0.9}Te_2$ (bottom); reflections caused by the furnace material are indicated by dashed lines; the decomposition of the rocksalt-type phase is marked by dashed rectangles.

In the HRTEM images in Figures 4 and 5, few planar defects can be observed in the fringe areas of the crystallites. In contrast to the Fourier transforms of these areas, the SAED patterns of whole small crystallites or of thicker areas exhibit less pronounced diffuse intensities. Therefore, such defects are rather rare effects in thin areas. It remains unclear whether they are due to the high-pressure high-temperature synthesis or induced by the TEM sample preparation.

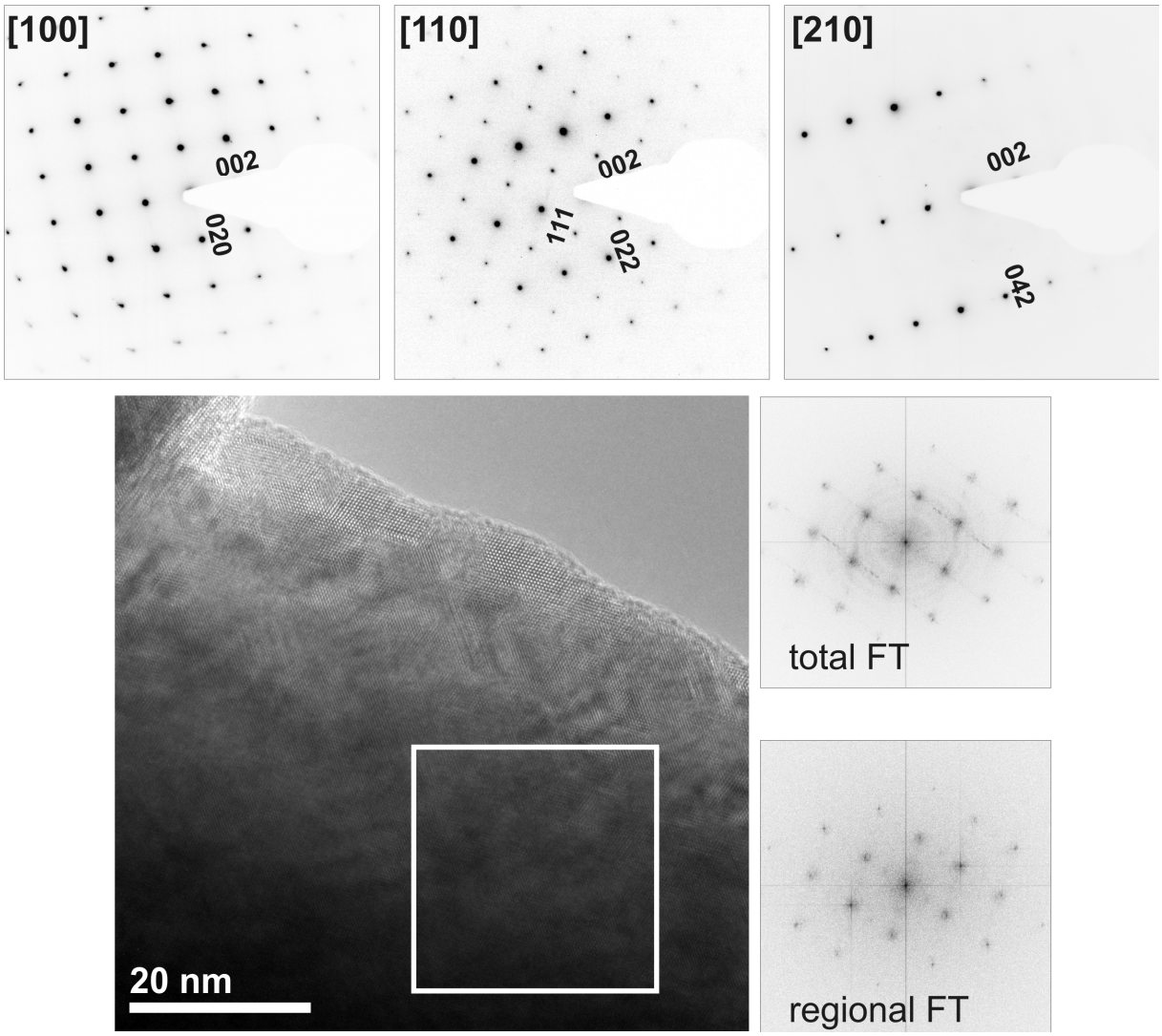

Fig. 4. SAED patterns of the zone axes [100], [110] and [210] (top) of rocksalt-type $AgIn_{0.5}Sb_{0.5}Te_2$; HRTEM image of $AgIn_{0.5}Sb_{0.5}Te_2$ (bottom, left) with the corresponding Fourier transforms of the whole image (middle right) and of the region marked with the white square (bottom right).

2.4.3.4 Thermoelectric properties

All investigated compounds of the series $AgIn_xSb_{1-x}Te_2$ are p-type semiconductors. The electrical conductivity (Figure 6, top) increases with x, although at low temperatures the values for x = 0.4 and 0.5 are similar. For x = 0.6, σ is higher by one order of magnitude compared to the other samples. Below RT, κ of all samples is very low (Figure 6; third from top), less than 0.5 W/Km. In line with the electrical contribution to κ, the absolute values of the thermal conductivities exhibit a comparable trend with respect to x as the electrical conductivities. For all samples, κ_{ph} at 300 K is in the same range of 0.35 – 0.29 W/Km. Due to the low σ of x = 0.4 and 0.5, the electrical contribution κ_{el} to the total κ is rather small (cf.

Figure 6). The thermal conductivity of all samples is lower than that of both $AgSbTe_2$ (~ 0.6 W/Km at 300K) and $AgInTe_2$ (~ 2 W/Km at 300K).[18] This strong decrease in κ, especially κ_{ph}, upon doping might be caused by the increased disorder at the cation position.

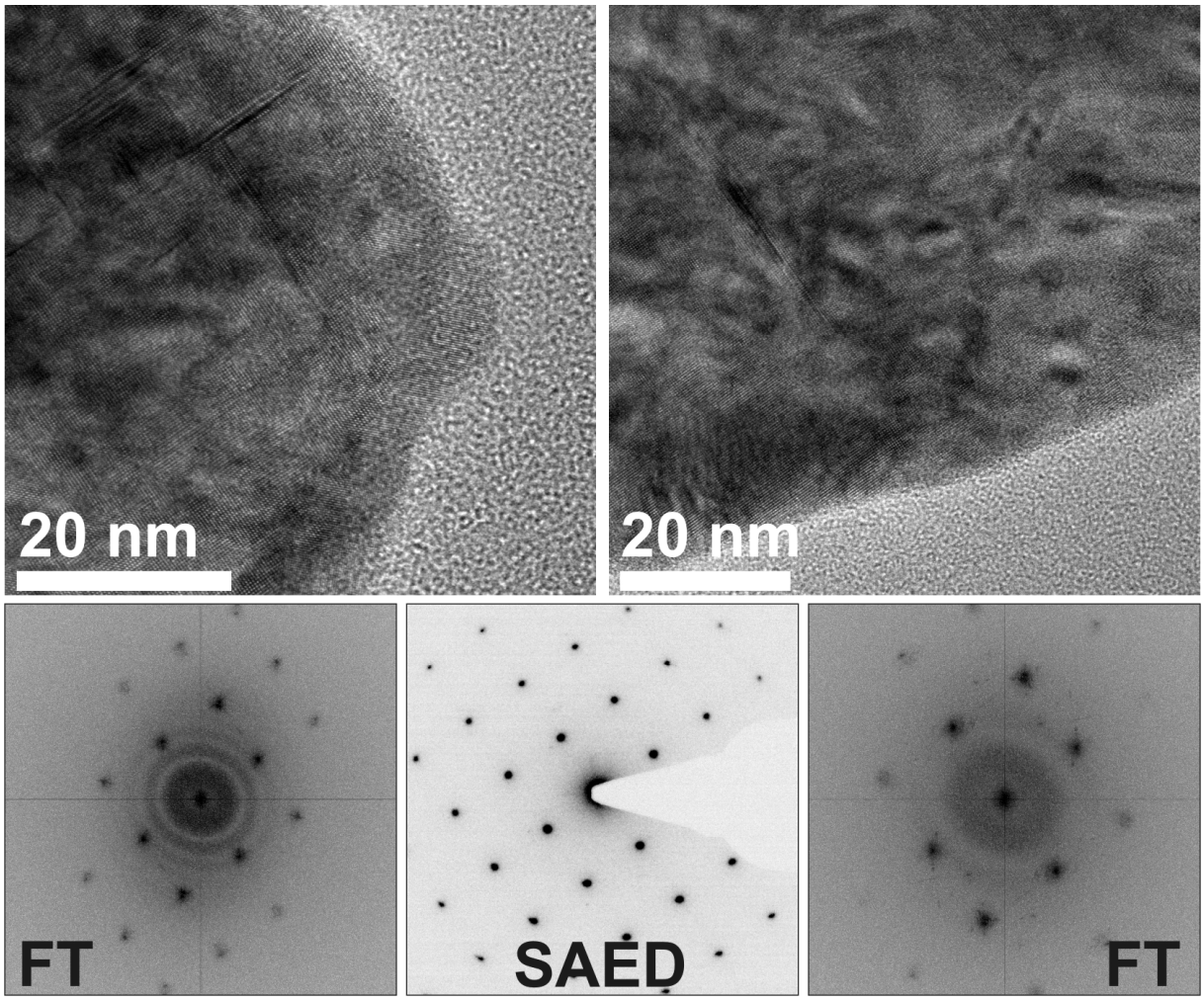

Fig. 5. Electron microscopy $AgIn_{0.5}Sb_{0.5}Te_2$ (zone axis [100]): HRTEM images of two different areas of the same crystallite (top) with the corresponding Fourier transforms (FT, bottom) and the SAED pattern (bottom, middle) of the crystallite. The rather strong contrasts originate from thickness variations (the sample was crushed from an ingot obtained under high-pressure conditions).

$AgIn_{0.5}Sb_{0.5}Te_2$ exhibits the highest Seebeck coefficient (Figure 6; second from top) of the quaternary samples; at RT it amounts to 160 μV/K. This probably indicates a rather high charge carrier concentration. The differences in the ZT values of the samples investigated are mainly due to the different Seebeck coefficients; thus, $AgIn_{0.5}Sb_{0.5}Te_2$ exhibits the highest ZT value (0.15 at 300K) (Figure 6; bottom). This is lower than that of $AgSbTe_2$ (ZT = ~0.3 at 300 K) because of the latter's higher Seebeck coefficient (~240 μV/K at 300 K). However, the observed ZT value of $AgIn_{0.5}Sb_{0.5}Te_2$ falls in the same range as corresponding values of other tellurium-based high-performance p-type thermoelectrics at 300 K.[14] In comparison, the

thermoelectric properties of chalcopyrite-type $AgInTe_2$, which exhibits a maximum ZT value of 0.06 at 600 K and <0.01 at 300 K,[23] are less suitable for potential applications.

2.4.4 Conclusion

High-pressure high-temperature syntheses have been shown to lead to solid solutions $AgIn_xSb_{1-x}Te_2$ that are metastable at ambient conditions and are yet not accessible by other synthetic approaches. The novel phases exhibit thermoelectric figures of merit *ZT* up to 0.15 which are comparable to many high-performance thermoelectrics and outperform those of chalcopyrite-type $AgInTe_2$, but are still lower than in the benchmark system $AgSbTe_2$ at room temperature ($ZT \sim 0.3$).[20] Most likely, the cation disorder is the true physical origin of the significantly reduced thermal conductivity in the solid solutions, especially as the phononic contribution is dominant. Thus, further optimization of the power factor $S^2\sigma$, possibly by additional doping, might lead to materials with better performance than $AgSbTe_2$ at low temperatures. To the best of our knowledge, the quenched high-pressure phases exhibit the lowest thermal conductivities among all rocksalt-type tellurides (e.g. $NaSbTe_2$, $AgSbTe_2$ or $NaBiTe_2$) at room temperature.

In general, high-pressure phase transitions may be an intriguing way towards novel thermoelectrics. As high pressure favors higher coordination numbers, solid solutions may be accessible in many systems that are characterized by immiscibility gaps. Although the decomposition of the quenched high-pressure phase $AgIn_{0.5}Sb_{0.5}Te_2$ into $AgInTe_2$ and $AgSbTe_2$ is a drawback for high-temperature applications, careful annealing may be used to produce materials that are heterogeneous on the nanoscale and possibly exhibit endotactic nano-precipitates. As the exsolution of chalcopyrite type $AgInTe_2$ starts before the cubic compound decomposes, such nanostructuring of the material by nanodots comparable to LAST materials may be achieved in a controllable fashion. In addition, phase transitions may further produce favorable domain structures. The synthesis of nanostructured solid solutions displaying low thermal conductivities is thus a promising approach which warrants further exploration.

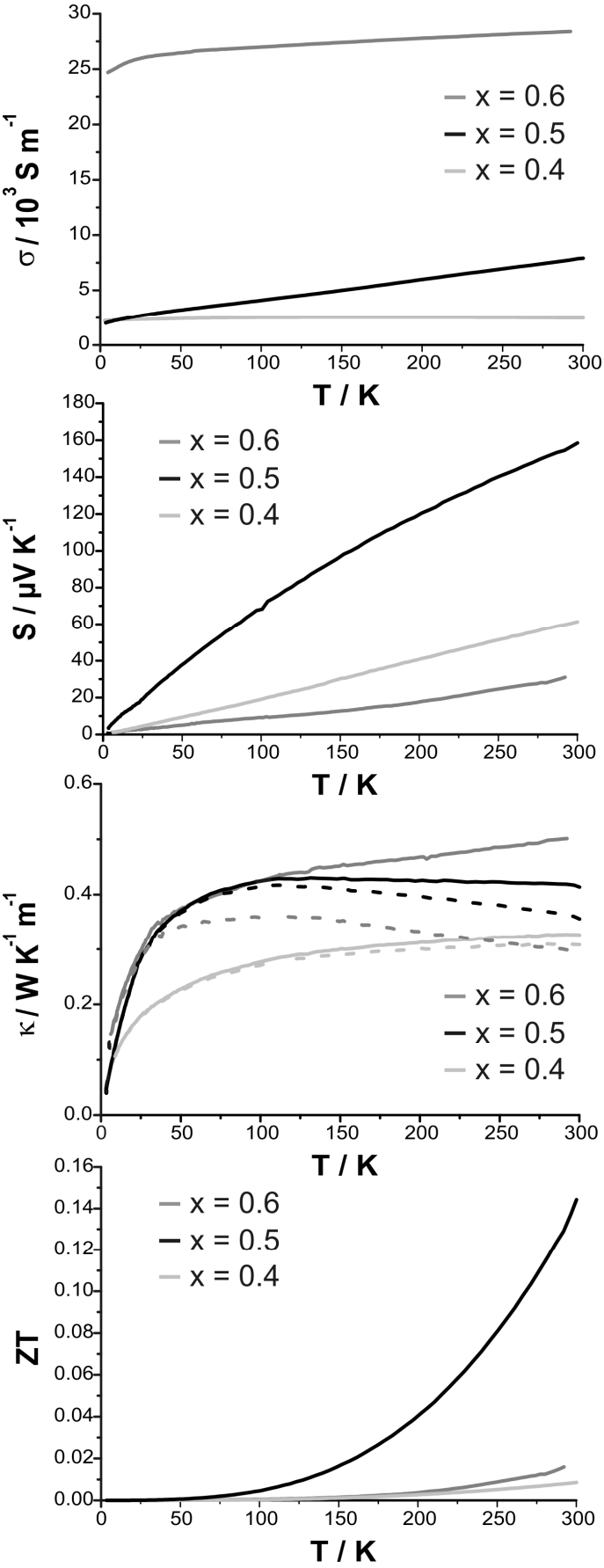

Fig. 6. Electrical conductivity (top), Seebeck coefficients (second from top), total (solid lines) and phononic (broken lines) thermal conductivities (third from top), and ZT values (bottom) of $AgIn_{0.4}Sb_{0.6}Te_2$ (light gray), $AgIn_{0.5}Sb_{0.5}Te_2$ (black) and $AgIn_{0.6}Sb_{0.4}Te_2$ (dark gray).

Acknowledgments

We thank T. Miller for the temperature-dependent powder diffraction experiments, C. Minke for SEM operation and EDX analyses. We are deeply grateful to Prof. Dr. W. Schnick for his generous support of this study, especially for providing the high-pressure equipment. This investigation was funded by the Deutsche Forschungsgemeinschaft (grant OE530/1-2) and the Studienstiftung des deutschen Volkes.

Supplementary information

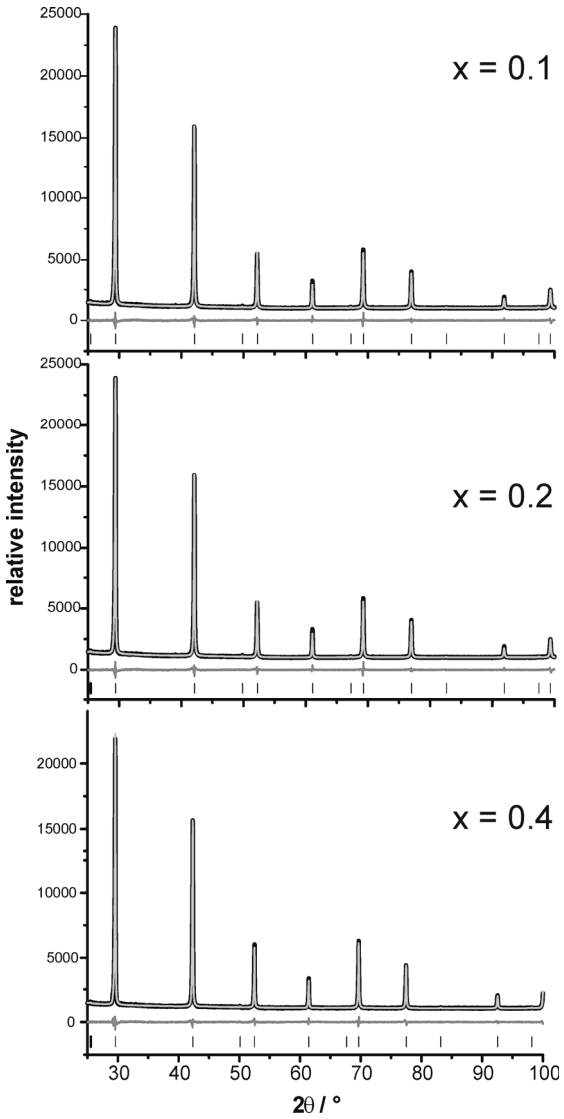

Fig. S1. Rietveld fits for $AgIn_{0.1}Sb_{0.9}Te_2$ (top), $AgIn_{0.2}Sb_{0.8}Te_2$ (middle) and $AgIn_{0.4}Sb_{0.6}Te_2$ (bottom); experimental data (black); calculated data (light gray); difference plot (gray, below), peak positions (black, vertical lines).

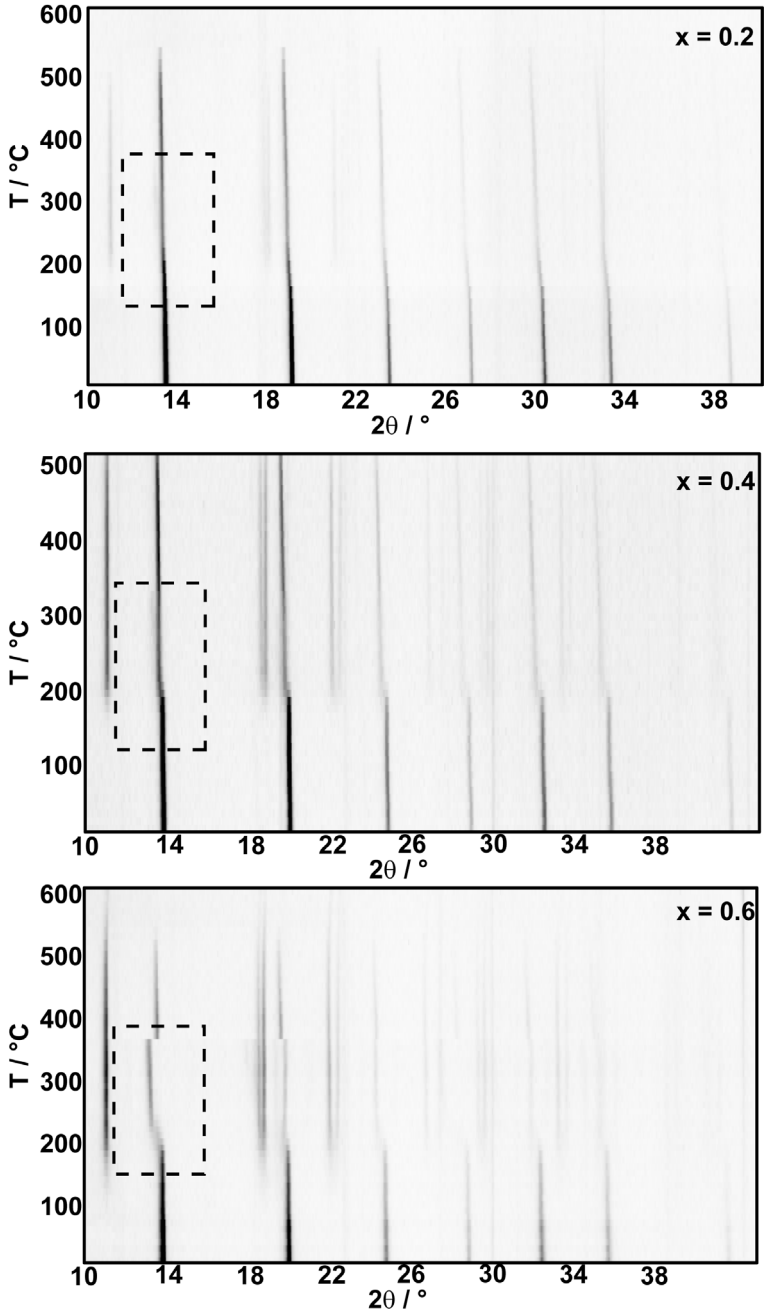

Fig. S2. Temperature dependent powder X-ray diffraction patterns of $AgIn_{0.2}Sb_{0.8}Te_2$ (top), $AgIn_{0.4}Sb_{0.6}Te_2$ (middle) and $AgIn_{0.6}Sb_{0.4}Te_2$ (bottom); the decomposition of the rocksalt-type phase is marked by dashed rectangles.

References

[1] H. J. Goldsmid, *Thermoelectric Refrigeration*, Plenum Press, New York, **1964**.

[2] S.H. Yang, T.J. Zhu, T. Sun, J. He, S.N. Zhang, X.B. Zhao, *Nanotechnology* **2008**, *19*, 245707.

[3] F.D. Rosi, J.P. Dismukes, E. F. Hockings, *Electron. Eng.* **1960**, *79*, 450.

[4] S.K. Plachkova, *Phys. Status Solidi A* **1984**, *83*, 349.

[5] M.N. Schneider, T. Rosenthal, C. Stiewe, O. Oeckler, *Z. Kristallogr.* **2010**, *225*, 463.

[6] T. Rosenthal, M.N. Schneider, C. Stiewe, M. Döblinger, O. Oeckler, *Chem. Mater.* **2011**, *23*, 4349.

[7] J. Sommerlatte, K. Nielsch, H. Böttner, *Phys. J.* **2007**, *6*, 35.

[8] A. Bulusu, D.G. Walker, *Superlattice Microst.* **2008**, *44*, 1.

[9] A. Majumdar, *Science* **2004**, *303*, 777.

[10] M.S. Dresselhaus, G. Chen, M.Y. Tang, R. Yang, H. Lee, D. Wang, Z. Ren, J.-P. Fleurial, P. Gogna, *Adv. Mater.* **2007**, *19*, 1.

[11] D.L. Medlin, G.J. Snyder, *Curr. Opin. Colloid Interface Sci.* **2009**, *14*, 226.

[12] M.G. Kanatzidis, *Chem. Mater.* **2010**, *22*, 648.

[13] Y.C. Lan, A.J. Minnich, G. Chen, Z.F. Ren, *Adv. Funct. Mater.* **2010**, *20*, 357.

[14] J.R. Sootsman, D.Y. Chung, M.G. Kanatzidis, *Angew. Chem. Int. Ed.* **2009**, *48*, 8616.

[15] B.A. Cook, M.J. Kramer, J.L. Harringa, M.-K. Han, D.-Y. Chung, M.G. Kanatzidis, *Adv. Funct. Mater.* **2009**, *19*, 1254.

[16] G. Rogl, D. Setman, E. Schafler, J. Horky, M. Kerber, M. Zehetbauer, M. Falmbigl, P. Rogl, E. Royanian, E. Bauer, *Acta Mater.* **2012**, *60*, 2146.

[17] T. Schröder, M.N. Schneider, T. Rosenthal, A. Eisele, C. Gold, E.-W. Scheidt, W. Scherer, R. Berthold, O. Oeckler, *Phys. Rev. B* **2011**, *84*, 184104.

[18] D.T. Morelli, V. Jovovic, J.P. Heremans, *Phys. Rev. Lett.* **2008**, *101*, 035901.

[19] M.D. Nielsen, V. Ozolins, J.P. Heremans, *Energy Environ. Sci.* **2013**, *6*, 570.

[20] C. Wood, *Rep. Prog. Phys.* **1988**, *51*, 459.

[21] K.J. Range, G. Engert, A. Weiss, *Sol. State Comm.* **1969**, *7*, 1749.

[22] W. Schanow, K.J. Range, *Mater. Res. Bull.* **1983**, *18*, 39.

[23] Y. Aikebaier, K. Kurosaki, T. Sugahara, Y. Ohishi, H. Muta, S. Yamanaka, *Mater. Sci. Eng. B* **2012**, *177*, 999.

[24] T. Matsunaga, J. Akola, S. Kohara, T. Honma, K. Kobayashi, E. Ikenaga, R.O. Jones, N. Yamada, M. Takata, R. Kojima, *Nature Mater.* **2011**, *10*, 129.

[25] D. Walker, M.A.Carpenter, C.M. Hitch, *Am. Mineral.* **1990**, *75*, 1020.

[26] D. Walker, *Am. Mineral.* **1991**, *76*, 1092.

[27] D.C. Rubie, *Phase Trans.* **1999**, *68*, 431.

[28] H. Huppertz, *Z. Naturforsch. B* **2001**, *56*, 697.

[29] *TOPAS-Academic*, *V. 4.1*, Coelho Software, Brisbane, Australia, **2007**.

[30] *DigitalMicrograph 3.6.1*, Gatan Software, Pleasanton, USA, **1999**.

[31] P.A. Stadelmann, *Ultramicroscopy* **1987**, *21*, 131.

[32] *ESVision*, *4.0.164*, Emispec Systems Inc., Tempe, USA, **1994-2002**.

[33] S. Geller, J.H. Wernick, *Acta Crystallogr.* **1959**, *12*, 46.

[34] R. Marin-Ayral, B. Legendre, G. Brun, B. Liautard, J. Tedenac, *Thermochim. Acta* **1988**, *131*, 37.

[35] M. Pasciak, R. Welberry, *Z. Kristallogr.* **2011**, *226*, 113.

2.5 TAGS-related indium compounds and their thermoelectric properties – the solid solution series $(GeTe)_xAgIn_ySb_{1-y}Te_2$ (x = 1 – 12; y = 0.5 and 1)

Thorsten Schröder, Tobias Rosenthal, Nadja Giesbrecht, Stefan Maier, Ernst-Wilhelm Scheidt, Wolfgang Scherer, G. Jeffrey Snyder, Wolfgang Schnick, Oliver Oeckler
J. Mater. Chem. A **2014**, *2*, 6384 – 6395.

Abstract

Various members of the solid solution series $(GeTe)_xAgIn_ySb_{1-y}Te_2$ can be obtained by quenching high-temperature phases (x = 12 for y = 1 and x > 5 for y = 0.5). In contrast, high-temperature high-pressure conditions (2.5 GPa, 350 °C) are required for the synthesis of members with In contents > 3.6 atom-% (such as x < 12 for y = 1 and x < 5 for y = 0.5) in order to avoid the formation of $AgInTe_2$. The latter exhibits tetrahedrally coordinated indium atoms at ambient conditions and therefore does not form mixed crystals with tellurides of germanium and antimony that are characterized by sixfold coordinated atom sites. Solid solutions with $x \leq 5$ crystallize in rocksalt-type structures with octahedrally coordinated indium, whereas the ones with x > 5 adopt the α-GeTe structure type (3+3 coordination). Thus, in all samples investigated, 3 or 4 cations are disordered at one Wyckoff position. The quenched high-temperature or high-pressure phases, respectively, are almost homogeneous. Their powder X-ray diffraction patterns suggest pure phases; yet, high-resolution electron microscopy occasionally reveals a very small extent of nanoscopic precipitates as well as dislocations and twinning. $(GeTe)_{5.5}AgIn_{0.5}Sb_{0.5}Te_2$ shows a maximal ZT value of 0.75 even when (partial) decomposition into the TAGS material $(GeTe)_{11}AgSbTe_2$ and chalcopyrite-type $AgInTe_2$ has occurred at 300 °C. $(GeTe)_{5.5}AgInTe_2$ prepared under high-pressure conditions exhibits a ZT value of 0.6 at 125 °C, i. e. far below the decomposition temperature and thus is an interesting new low-temperature thermoelectric material.

2.5.1 Introduction

Under ambient conditions, In is tetrahedrally coordinated by Te in chalcopyrite-type $AgInTe_2$.[1] A rocksalt-type high-pressure polymorph with octahedral coordination of In has

been described; however, upon decompression, this phase cannot be obtained as a metastable material as it transforms back to the chalcopyrite structure type.[2] This shows the strong tendency of In to be tetrahedrally coordinated. It is possible to obtain comparable metastable, i. e. kinetically inert, compounds with octahedrally coordinated In by partially substituting In in $AgInTe_2$ by Sb; however, high-pressure conditions are always required to synthesize these compounds.[3] This substitution leads to the rocksalt-type solid solution series $AgIn_ySb_{1-y}Te_2$. Its member $AgIn_{0.5}Sb_{0.5}Te_2$ exhibits a dimensionless thermoelectric figure of merit $ZT = S^2\sigma T/\kappa$ (with the Seebeck coefficient S, the electrical conductivity σ, the temperature T and the thermal conductivity κ)[4] of 0.15 at room temperature (RT). Due to the solid-solution alloying, the low thermal conductivities of both end members $AgInTe_2$ and $AgSbTe_2$ (κ ~ 2 W/Km and 0.6 W/Km,[5] respectively) are further reduced to 0.4 W/Km at RT. These compounds decompose to chalcopyrite-type $AgInTe_2$ and rocksalt-type $AgSbTe_2$ at temperatures > 150 °C. In general, tellurides crystallizing in these structure types exhibit very good thermoelectric properties: rocksalt-type compounds mainly due to their low lattice thermal conductivities,[6] and materials with structures derived from sphalerite (e. g. $Cu_2Zn_{1-x}Fe_xGeSe_4$, $CuGaTe_2$, $CuInTe_2$) predominantly due to their high Seebeck coefficients.[7-10]

Despite the lower κ of$AgIn_{0.5}Sb_{0.5}Te_2$, the ZT value of $AgSbTe_2$ at RT (~ 0.3) is higher due to its a higher Seebeck coefficient.[11] It is well known that the thermoelectric properties of $AgSbTe_2$ can further be improved in solid solutions with GeTe,[12,13] resulting in so-called TAGS materials $(GeTe)_x(AgSbTe_2)$.[14-17] These compounds have been the subject of many investigations because of their high ZT values (up to 1.7) at elevated temperatures.[18,19] Further optimization of TAGS materials was achieved by substituting Ge by Sn as well as by doping with rare-earth elements.[20-22] However, to the best of our knowledge, the substitution of Sb with In has not been investigated, probably because many of these compounds cannot be obtained by classical solid-state synthesis as they would contain octahedrally coordinated In.

Consequently, solid solutions between GeTe, $AgInTe_2$ and additional $AgSbTe_2$ are intriguing as they would probably combine the effects known from TAGS with the low thermal conductivity of $AgIn_{0.5}Sb_{0.5}Te_2$ and thus might exhibit high ZT values. Here we report on solid solutions $(GeTe)_x(AgInTe_2)$ which we call TIGS in analogy to TAGS and on compounds $(GeTe)_xAgIn_{0.5}Sb_{0.5}Te_2$, i. e. TAGS materials in which half of the Sb is substituted by In.

2.5.2 Experimental

Synthesis

Samples of $(GeTe)_xAgIn_ySb_{1-y}Te_2$ (x = 1 – 12; y = 0.5, 1) were prepared by reacting stoichiometric mixtures of the elements (germanium 99.999%, Sigma-Aldrich; silver 99.9999%, Alfa Aesar; antimony 99.9999%, Smart Elements; indium 99.996%, Smart Elements; tellurium 99.999%, Alfa Aesar) at 950 °C for 12 h in sealed silica ampoules under argon atmosphere. The ampoules containing the resulting melts were quenched in water and subsequently annealed for 3 days at 550 °C. After that, the ampoules containing the annealed ingots were quenched in water. This synthesis route yielded $(GeTe)_xAgIn_ySb_{1-y}Te_2$ samples with x = 12 and y = 1 as well as those with x = 5, 5.5, 7 or 12 and y = 0.5 which were homogeneous according to powder X-ray diffraction patterns (cf. section *Crystal structure*). Samples with higher overall In contents, i. e. x = 1, 5, 5.5, 7 and y =1 or x = 1 and y = 0.5 were not single-phase (see below); they were used as starting materials for further high-pressure (HP) synthesis.

A multi-anvil hydraulic press (Voggenreiter, Mainleus, Germany) was used for the HP experiments.[23-26] The finely ground starting materials were densely loaded in crucibles sealed with caps (material: hexagonal boron nitride, Henze, Kempten, Germany). These were centered in two nested graphite tubes, which acted as a resistance furnace. In order to keep the inner graphite tube in place, the remaining volume at both ends of the outer tube was filled with MgO discs. This arrangement was surrounded by a zirconia tube and placed in pierced Cr_2O_3-doped MgO octahedron (edge length 25 mm, Ceramic Substrates & Components, Isle of Wight, Great Britain). In order to electrically contact the graphite tubes, Mo plates were used that were connected to two of the eight truncated tungsten carbide cubes (truncation edge length 17 mm), which served as anvils for the compression. These cubes were separated by pyrophyllite gaskets. Within two hours, this assembly was compressed to 2.5 GPa. At this pressure, the temperature was raised to 350 °C within 30 min and the samples were subsequently kept at this temperature for 8 h. Afterwards, the samples were quenched to room temperature by switching off the furnace. The arrangement was kept under pressure for another hour to ensure that the sample was cooled down completely before reducing the pressure to ambient conditions within 6 h.

X-ray diffraction

Powder X-ray diffraction (PXRD) patterns of the finely ground samples fixed between Mylar foils on a flat sample holder with vacuum grease were collected using a Huber G670 Guinier camera (Cu-$K_{\alpha1}$ radiation, Ge(111) monochromator, λ = 1.54051 Å) with a fixed imaging plate and an integrated read-out system.

Temperature-dependent PXRD patterns were measured using a STOE Stadi P diffractometer (Mo-$K_{\alpha1}$ radiation, Ge(111) monochromator, λ = 0.71093 Å) with an imaging plate detector system in a modified Debye-Scherrer geometry. The powdered samples were filled into silica glass capillaries (0.3 mm diameter) under argon atmosphere and sealed with vacuum grease. Data were measured up to 600 °C with a heating rate of 10 °C/min in 20 °C steps. For $(GeTe)_{5.5}AgIn_{0.5}Sb_{0.5}Te_2$, further diffraction patterns were recorded from 600 °C to RT with a cooling rate of 5 °C/min.

Phase homogeneity was evaluated using WINXPOW[27] and Rietveld refinements were carried out using the program TOPAS.[28]

Electron microscopy, diffraction and X-ray spectroscopy

A JSM-6500F (Jeol, USA) scanning electron microscope (SEM) equipped with an energy dispersive X-ray (EDX) detector (model 7418, Oxford Instruments, Great Britain) was used for the collection of X-ray spectra of representative parts of the samples. The results of 5 - 15 point analyses were averaged. The compositions determined can be found in Table S1 and S2 in the Supplementary Information.

For high-resolution transmission electron microscopy (HRTEM), the samples were ground, dispersed in ethanol and distributed on copper grids coated with a holey carbon film (S166-2, Plano GmbH, Germany) which were subsequently fixed on a double-tilt holder. HRTEM images and selected area electron diffraction (SAED) patterns were recorded using a Titan 80-300 (FEI, USA) with a field-emission gun operated at 300 kV equipped with a TEM TOPS 30 EDX spectrometer (EDAX, Germany). The images were recorded using an UltraScan 1000 camera (Gatan, USA, resolution 2k x 2k). For HRTEM and SAED data evaluation, the Digital Micrograph and EMS software packages were used;[29,30] EDX data were evaluated with ES Vision.[31]

Thermoelectric characterization

The thermoelectric properties of $(GeTe)_{5.5}AgIn_{0.5}Sb_{0.5}Te_2$ prepared by quenching the sample from 550 °C were determined from 25 °C to 500 °C. The electrical conductivity σ was measured in 50 K steps at a heating rate of 150 K/h using the van der Pauw method[32] and pressure-assisted Nb contacts in an in-house built facility at Caltech.[33] The Seebeck coefficient S was determined using Chromel-Nb thermocouples in steps of 61 K at a heating rate of 150 K/h and a temperature oscillation rate of ± 7.5 K.[34] The thermal diffusivity D_{th} was measured using a LFA457 MicroFlash (Netzsch, Germany) laser flash system. The thermal conductivity was calculated according to $\kappa = D_{th} \cdot C_p \cdot d$ with a calculated heat capacity C_p using the Dulong-Petit approximation and the density d determined by weighing the sample and measuring its dimensions. The combined uncertainty of the measurements is ca. 20% for the ZT value.

The thermoelectric properties of a $(GeTe)_{5.5}AgInTe_2$ sample prepared under high-pressure conditions were characterized between 4 K and 400 K using a physical property measurement system (PPMS, Quantum Design). The temperature dependent electrical resistivity ρ was measured using a standard four-probe dc method by employing a constant current of 5 mA with a cooling/heating rate of 2 K/min, the estimated uncertainty of ρ amounts to ca. 10 %. The thermal transport option of the PPMS with a cooling/heating rate of 0.5 K/min was used to measure the κ and S values simultaneously. The measurements relied on a relaxation method employing one heater and two thermometers to determine the induced thermal voltage and the temperature gradient along the sample. The uncertainty of these values is approximately 5%.

2.5.3 Results and discussion

2.5.3.1 Sample characterization and optimal conditions for syntheses

The present investigation focuses on compounds $(GeTe)_xAgIn_ySb_{1-y}Te_2$ with x = 1, 5, 5.5, 7 and 12 for y = 0.5 and 1, which cover a broad range of In-substituted TAGS materials. The stoichiometry includes In contents from 16.7 atom-% in $(GeTe)AgInTe_2$ down to 1.8 atom-% in $(GeTe)_{12}AgIn_{0.5}Sb_{0.5}Te_2$. Quenched melts with In-rich compositions such as $(GeTe)_xAgInTe_2$ (x = 1 - 7) contain mixtures of chalcopyrite-type $AgInTe_2$ and GeTe. In contrast, related homogeneous TAGS materials, i. e. $(GeTe)_xAgSbTe_2$, are easily obtained.[15]

However, syntheses under high-pressure high-temperature conditions (2.5 GPa and 350 °C for all high-pressure experiments mentioned in this article) yield samples of, for instance, $(GeTe)AgInTe_2$ and $(GeTe)AgIn_{0.5}Sb_{0.5}Te_2$ with rocksalt type structure whose PXRD patterns exhibit no reflections of side phases (cf. section *Crystal structure*).

The compositional range investigated allows one to elucidate the influence of In on the reaction products under various synthesis conditions. It turned out that samples of $(GeTe)_xAgInTe_2$ with $x < 12$ and $(GeTe)_xAgIn_{0.5}Sb_{0.5}Te_2$ with $x < 5$, all of which contain more than 3.6 atom-% In, consist of mixtures of $AgInTe_2$ and GeTe or $(GeTe)_{2x}AgSbTe_2$, respectively, both after quenching the melt and after quenching solid ingots after annealing them at 550 °C. For such In-rich compounds, high-pressure conditions are required to obtain samples that are single-phase according to their PXRD patterns. In contrast, single-phase compounds (according to PXRD) with In contents ≤ 3.6 atom-%, i. e. $(GeTe)_{12}AgInTe_2$ and $(GeTe)_xAgIn_{0.5}Sb_{0.5}Te_2$ $x \geq 5$, respectively, can be obtained by quenching the samples after annealing them at 550 °C (existence range of high-temperature (HT) phases, cf. *Thermal behavior* section).

The chemical compositions of all compounds whose PXRD patterns show no side phases were determined by SEM-EDX measurements. They agree very well with the nominal composition (cf. Tables S1 and S2 in the Supplementary Information).

2.5.3.2 Crystal structure

PXRD patterns of $(GeTe)_xAgIn_ySb_{1-y}Te_2$,samples (cf. Fig. 1 and 2) without reflections from side phases (synthesis with or without HP depending on the In content as described above) could be indexed assuming cubic metrics for $x \leq 5.5$; however, for $x = 5.5$ the structure is rhombohedral (see below). Samples with $x > 5.5$ clearly show reflection splittings in conformity with rhombohedral unit-cell dimensions. All structures were refined using the Rietveld method. Even if the metrics is cubic, rhombohedral structures must be considered as suggested by the reflection splittings for $x > 5.5$. Symmetry reduction is not unusual in comparable compounds that are pseudocubic from the point of view of lattice parameters. Therefore, refinements in space groups with rhombohedral symmetry were tested, especially in *R*3*m*, which corresponds to the α-GeTe type.[12,13] In the trigonal setting, the *z* parameter of the cations is a measure for the formation of layers when the anions of the polar structure are fixed on the origin. If *z* deviates significantly from 0.5, GeTe-type layers are formed which correspond to a binary variant of the A7 structure type of gray arsenic.

The cation positions in all structure models were occupied according to the nominal composition with Ge, Ag, In, and Sb if present, refining a common displacement parameter for all cations on a shared Wyckoff site (i. e. a common *z* parameter in rhombohedral compounds); the anion position was occupied with Te whose displacement parameter was refined individually. Due to the use of a flat sample holder, preferred orientation had to be taken into account, using 4th order spherical harmonics with a single parameter for $x \leq 5$ (cubic) and with 3 parameters for $x \geq 5.5$ (trigonal). Anisotropic broadening of the reflection profiles was refined for $(GeTe)_xAgInTe_2$ (with x = 5.5, 7 and 12) and $(GeTe)_xAgIn_{0.5}Sb_{0.5}Te_2$ (with x = 7 and 12) using the LeBail-Jouanneaux algorithm.[35] In addition to the profile fits of the Rietveld refinements in Fig. 1 and 2, crystal data and details of the structure refinement as well as the atomic parameters are given in Tables 1 and 2, respectively, for the TIGS compounds and in Tables 3 and 4, respectively, for the quinary compounds. Further details of the crystal structure investigations may be obtained from Fachinformationszentrum Karlsruhe, 76344 Eggenstein-Leopoldshafen, Germany (fax: (+49)7247-808-666; e-mail: crysdata@fiz-karlsruhe.de, http://www.fiz-karlsruhe.de/request_for_deposited_data.html) on quoting the depository numbers CSD 426809, 426800, 426805, 426808 and 426803 for $(GeTe)_xAgInTe_2$ with x = 1, 5, 5.5, 7 and 12, respectively, or CSD 426807, 426801, 426804, 426802 and 426806 for $(GeTe)_xAgIn_{0.5}Sb_{0.5}Te_2$ with x = 1, 5, 5.5, 7 and 12, respectively.

It turned out that the average structure of the samples with $x \leq 5$ corresponds to the rocksalt structure type. The atom positions refined in trigonal space groups (for testing purposes) do not deviate from those of the rocksalt type, which in combination with the cubic unit cell confirms the assumption of a cubic average structure. In these compounds, the lattice parameter *a* and thus the average cation-anion distance, which corresponds to *a*/2, decreases with increasing Ge content both for TIGS compounds as well as for the quinary $(GeTe)_xAgIn_{0.5}Sb_{0.5}Te_2$ phases. The lattice parameters of the latter phases are slightly larger than those of the corresponding Sb-free TIGS samples.

The compounds with $x > 5$ display, however, rhombohedral symmetry. Although for x = 5.5, the refined *c*/*a* ratios (2.451 for $(GeTe)_{5.5}AgInTe_2$ and 2.459 for $(GeTe)_{5.5}AgIn_{0.5}Sb_{0.5}Te_2$) deviate only slightly from that of the rhombohedral setting of a cubic unit cell (*c*/*a* = 2.449), the *z* parameter of the cations clearly indicates the formation of α-GeTe-type layers which precludes cubic symmetry. This becomes more pronounced for increasing GeTe contents ($x > 5.5$) where, in addition, the reflection splittings in the PXRD patterns strongly support rhombohedral structures. With increasing GeTe content, i. e. from x = 5.5 to x = 12, the *a* lattice parameters become smaller and the *c* lattice parameters become larger. These opposite

trends lead to a non-linear change of the unit-cell volumes. For the rhombohedral TIGS compounds, the unit-cell volumes are smaller than those of the quinary $(GeTe)_xAgIn_{0.5}Sb_{0.5}Te_2$ compounds. Yet, the shortest cation-tellurium bond lengths are slightly larger in the TIGS samples e. g. 2.8609(9) Å for $(GeTe)_{12}AgInTe_2$ and 2.8546(8) Å for $(GeTe)_{12}AgIn_{0.5}Sb_{0.5}Te_2$, which can be explained by a less pronounced tendency towards layered structures in TIGS.

Table 1. Crystal data and results of the Rietveld refinements of $(GeTe)AgInTe_2$, $(GeTe)_5AgInTe_2$, $(GeTe)_{5.5}AgInTe_2$, $(GeTe)_7AgInTe_2$ and $(GeTe)_{12}AgInTe_2$.

compound	$(GeTe)AgInTe_2$	$(GeTe)_5AgInTe_2$	$(GeTe)_{5.5}AgInTe_2$	$(GeTe)_7AgInTe_2$	$(GeTe)_{12}AgInTe_2$
asymmetric unit	$Ge_{1/3}Ag_{1/3}In_{1/3}Te$	$Ge_{5/7}Ag_{1/7}In_{1/7}Te$	$Ge_{11/15}Ag_{2/15}In_{2/15}Te$	$Ge_{7/9}Ag_{1/9}In_{1/9}Te$	$Ge_{12/14}Ag_{1/14}In_{1/14}Te$
molar mass (of asymmetric unit) / g mol^{-1}	225.94	211.29	210.44	208.81	205.64
$F(000)$	378.5	354.3	264.7	262.7	258.7
crystal system / space group (no.)	cubic / $Fm\bar{3}m$ (225)			trigonal / $R3m$ (160)	
Z	4			3	
lattice parameters / Å	5.96391(2)	5.95766(3)	a = 4.21824(2) c =10.3378(1)	a = 4.20056(2) c = 10.4188(1)	a = 4.18692(3) c = 10.5211(1)
cell volume / Å^3	212.126(2)	211.460(3)	159.302(2)	159.207(2)	159.728(3)
density (X-ray) / g cm^{-3}	7.075	6.637	6.581	6.534	6.413
absorption coefficient / mm^{-1}	163.93	140.433	138.55	135.87	130.40
radiation	Cu-$K_{\alpha1}$ (λ = 1.540596 Å)				
2θ range / °	20 – 100				
no. of data points	16001				
no. of reflections	13			30	
constraints	2			4	
refined parameters / thereof background	23 / 12			39 / 12	
R_p / R_{wp}	0.0151 / 0.0216	0.0195 / 0.0277	0.0170 / 0.0255	0.0148 / 0.0204	0.0206 / 0.0306
R_{Bragg}	0.0156	0.0108	0.0117	0.0120	0.0062
Goof	0.746	0.974	0.941	0.684	1.101

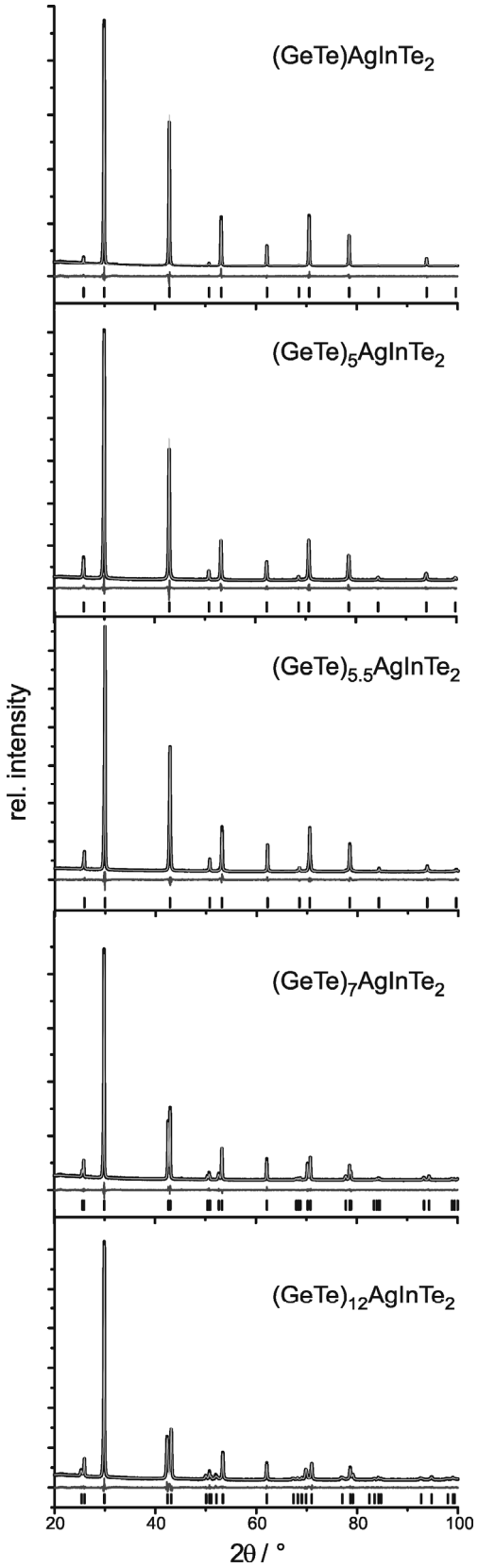

Fig. 1. Rietveld fits for $(GeTe)_xAgInTe_2$ (x = 1, 5, 5.5, 7 and 12; from top to bottom – HP synthesis except for x = 12): experimental (black) and calculated data (gray); difference plot (gray, below); peak positions (black, vertical lines).

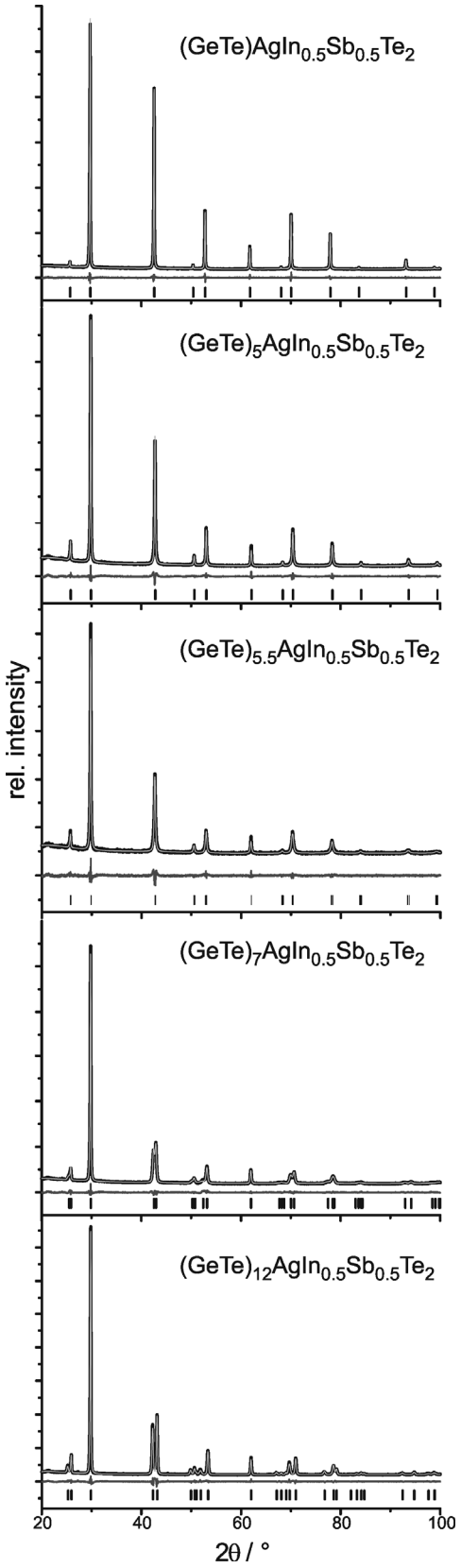

Fig. 2. Rietveld fits for $(GeTe)_xAgIn_{0.5}Sb_{0.5}Te_2$ (x = 1, 5, 5.5, 7 and 12; from top to bottom – HP synthesis for x = 1): experimental (black) and calculated data (gray); difference plot (gray, below); peak positions (black, vertical lines).

Table 2. Atom positions, occupancy factors and isotropic displacement parameters (B_{iso} in $Å^2$) for $(GeTe)AgInTe_2$, $(GeTe)_5AgInTe_2$, $(GeTe)_{5.5}AgInTe_2$, $(GeTe)_7AgInTe_2$ and $(GeTe)_{12}AgInTe_2$.

sample	atom positions	x y z	s.o.f.	B_{iso}
$(GeTe)AgInTe_2$	Ge/Ag/In	0 0 0	1/3 1/3 1/3	1.508(15)
	Te	0.5 0.5 0.5	1	0.797(12)
$(GeTe)_5AgInTe_2$	Ge/Ag/In	0 0 0	5/7 1/7 1/7	1.980(14)
	Te	0.5 0.5 0.5	1	0.810(11)
$(GeTe)_{5.5}AgInTe_2$	Ge/Ag/In	0 0 0.4834(4)	11/15 2/15 2/15	1.28(6)
	Te	0 0 0	1	1.11(2)
$(GeTe)_7AgInTe_2$	Ge/Ag/In	0 0 0.48596(18)	7/9 1/9 1/9	2.05(3)
	Te	0 0 0	1	1.057(14)
$(GeTe)_{12}AgInTe_2$	Ge/Ag/In	0 0 0.47877(16)	12/14 1/14 1/14	1.81(3)
	Te	0 0 0	1	0.847(18)

Table 3. Crystal data and results of the Rietveld refinements of $(GeTe)AgIn_{0.5}Sb_{0.5}Te_2$, $(GeTe)_5AgIn_{0.5}Sb_{0.5}Te_2$, $(GeTe)_{5.5}AgIn_{0.5}Sb_{0.5}Te_2$, $(GeTe)_7AgIn_{0.5}Sb_{0.5}Te_2$ and $(GeTe)_{12}AgIn_{0.5}Sb_{0.5}Te_2$.

compound	$(GeTe)AgIn_{0.5}Sb_{0.5}Te_2$	$(GeTe)_5AgIn_{0.5}Sb_{0.5}Te_2$	$(GeTe)_{5.5}AgIn_{0.5}Sb_{0.5}Te_2$	$(GeTe)_7AgIn_{0.5}Sb_{0.5}Te_2$	$(GeTe)_{12}AgIn_{0.5}Sb_{0.5}Te_2$
asymmetric unit	$Ge_{1/3}Ag_{1/3}In_{1/6}Sb_{1/6}Te$	$Ge_{5/7}Ag_{1/7}In_{1/14}Sb_{1/14}Te$	$Ge_{11/15}Ag_{2/15}In_{1/15}Sb_{1/15}Te$	$Ge_{7/9}Ag_{1/9}In_{1/18}Sb_{1/18}Te$	$Ge_{12/14}Ag_{1/14}In_{1/28}Sb_{1/28}Te$
molar mass (of asymmetric unit)/ g mol^{-1}	227.21	211.67	211.02	209.31	206.00
$F(000)$	380	354.7	265.2	263.1	259.1
crystal system / space group (no.)	cubic / $Fm\bar{3}m$ (225)		trigonal / $R3m$ (160)	trigonal / $R3m$ (160)	
Z	4			3	
lattice parameters / Å	5.99892(1)	5.97300(4)	a = 4.2218(1) c = 10.3821(4)	a = 4.20712(5) c = 10.4602(2)	a = 4.18601(3) c = 10.5582(1)
cell volume / $Å^3$	215.883(1)	213.097(4)	160.255(11)	160.340(6)	160.222(3)
density (X-ray) / g cm^{-3}	6.991	6.598	6.560	6.503	6.405
absorption coefficient / mm^{-1}	163.48	140.28	138.75	135.78	130.58
radiation			Cu-$K_{\alpha1}$ (λ = 1.540596 Å)		
2θ range / °			20 - 100		
no. of data points			16001		
no. of reflections	13		30	30	
constraints	3		6	6	
refined parameters / thereof background	23 / 12		27 / 12	39 / 12	
R_p / R_{wp}	0.0150 / 0.0210	0.0217 / 0.0313	0.0165 / 0.0241	0.0183 / 0.0252	0.0233 / 0.0355
R_{Bragg}	0.0032	0.0043	0.0064	0.0082	0.0064
Goof	0.7220	1.120	0.781	0.889	1.310

Table 4. Atom positions, occupancy factors and isotropic displacement parameters (B_{iso} in $Å^2$) for $(GeTe)AgIn_{0.5}Sb_{0.5}Te_2$, $(GeTe)_5AgIn_{0.5}Sb_{0.5}Te_2$, $(GeTe)_{5.5}AgIn_{0.5}Sb_{0.5}Te_2$, $(GeTe)_7AgIn_{0.5}Sb_{0.5}Te_2$ and $(GeTe)_{12}AgIn_{0.5}Sb_{0.5}Te_2$.

sample	atom positions	x y z	s.o.f.	B_{iso}
$(GeTe)AgIn_{0.5}Sb_{0.5}Te_2$	Ge/Ag/In/Sb Te	0 0 0 0.5 0.5 0.5	1/3 1/3 1/6 1/6 1	2.176(12) 1.462(10)
$(GeTe)_5AgIn_{0.5}Sb_{0.5}Te_2$	Ge/Ag/In/Sb Te	0 0 0 0.5 0.5 0.5	5/7 1/7 1/14 1/14 1	2.37(2) 0.810(18)
$(GeTe)_{5.5}AgIn_{0.5}Sb_{0.5}Te_2$	Ge/Ag/In/Sb Te	0 0 0.4857(8) 0 0 0	11/15 2/15 1/15 1/15 1	2.00(11) 1.14(5)
$(GeTe)_7AgIn_{0.5}Sb_{0.5}Te_2$	Ge/Ag/In/Sb Te	0 0 0.4813(2) 0 0 0	7/9 1/9 1/18 1/18 1	1.65(4) 1.32(2)
$(GeTe)_{12}AgIn_{0.5}Sb_{0.5}Te_2$	Ge/Ag/In/Sb Te	0 0 0.47722(14) 0 0 0	12/14 1/14 1/28 1/28 1	1.71(3) 0.991(19)

Also note that the cations' *z* parameter value of $(GeTe)_7AgInTe_2$ does not lie between those of $(GeTe)_{5.5}AgInTe_2$ and $(GeTe)_{12}AgInTe_2$, which is probably related to the fact that $(GeTe)_{5.5}AgInTe_2$ and $(GeTe)_7AgInTe_2$ had to be synthesized under HP conditions, whereas $(GeTe)_{12}AgInTe_2$ was synthesized by quenching the sample after annealing it at 550 °C.

2.5.3.3 Electron microscopy and diffraction

HRTEM and SAED were performed on $(GeTe)_{5.5}AgIn_{0.5}Sb_{0.5}Te_2$ and $(GeTe)_7AgIn_{0.5}Sb_{0.5}Te_2$ which were both synthesized by annealing the samples at 550 °C and subsequent quenching through a two phase region (cf. *Thermal behavior* section). The former's metrics are very close to cubic, the latter's are clearly rhombohedral. Although the angle between the directions [012]* and $[01\bar{4}]$* (which correspond to cubic [110]* and [001]*, respectively) of $(GeTe)_{5.5}AgIn_{0.5}Sb_{0.5}Te_2$ is calculated as 89.7° from the structure model obtained by Rietveld refinement, the SAED patterns in Fig. 3 show more pronounced deviations from 90°. This may be due to local variations of the composition – possibly as a consequence of the fast quenching – or metric relaxation in the small crystallites investigated. In quenched bulk samples the domains may be strained and thus the metrics remains closer to the one of the HT phase.

Although the samples appear homogeneous in PXRD patterns, the HRTEM images in Fig. 4 and 5 show two different kinds of precipitates. Both $(GeTe)_{5.5}AgIn_{0.5}Sb_{0.5}Te_2$ and $(GeTe)_7AgIn_{0.5}Sb_{0.5}Te_2$ contain Ag-rich precipitates (Fig. 4). These may consist of Ag_2Te, which was observed as a side phase in $AgSbTe_2$,[36] or Ag_7Te_4,[37] which might be an intermediate phase during the formation of Ag_2Te. Both compounds exhibit d values (e. g. 6.8 Å, 3.4 Å) close to those observed in SAED patterns and Fourier transforms of HRTEM images.

Fig. 5 shows In-rich precipitates in $(GeTe)_7AgIn_{0.5}Sb_{0.5}Te_2$ which most likely correspond to $AgInTe_2$ which is also expected from the temperature-dependent phase equlibria (see below). However, only very few precipitates can be observed and they are too small to contribute significantly to the PXRD patterns. The formation of precipitates also causes slight deviations in the compositions of the matrix crystallites which might contribute to the deviating metrics observed in the SAED patterns in Fig. 3 as the most pronounced metric deviations occur next to the precipitates. In addition, characteristic dislocations and twinning have also been observed in these materials (cf. Fig. S1 in the Supplementary Information and also weak additional maxima in Fig. 3a).

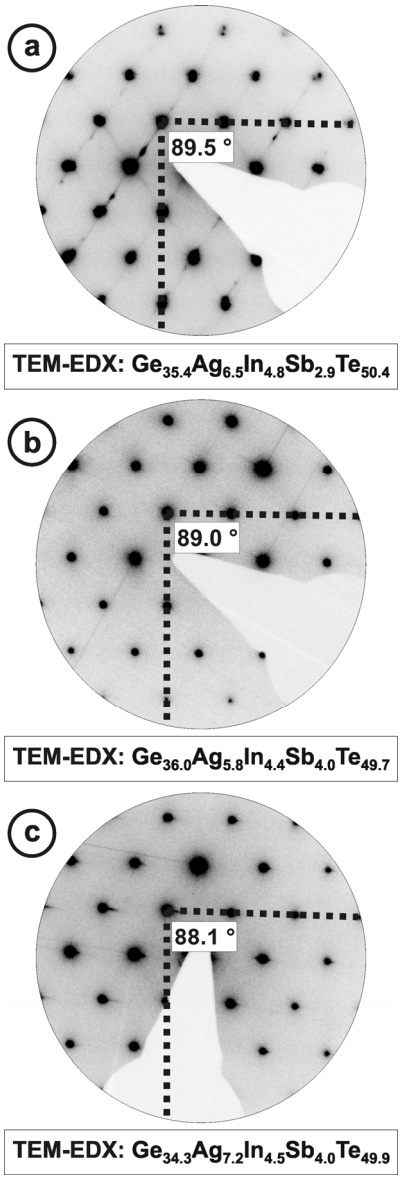

Fig. 3. SAED patterns of the <100> zone axis of different crystallites in a sample of $(GeTe)_{5.5}AgIn_{0.5}Sb_{0.5}Te_2$ (a and b: different areas of the same crystallite, c: other crystallite). The [012]* (horizontal) and [01 $\bar{4}$]* (vertical) directions are marked with dotted lines and the angle between them is given; TEM-EDX analyses of the corresponding areas are given below each SAED (calculated composition: $Ge_{36.7}Ag_{6.7}In_{3.3}Sb_{3.3}Te_{50}$).

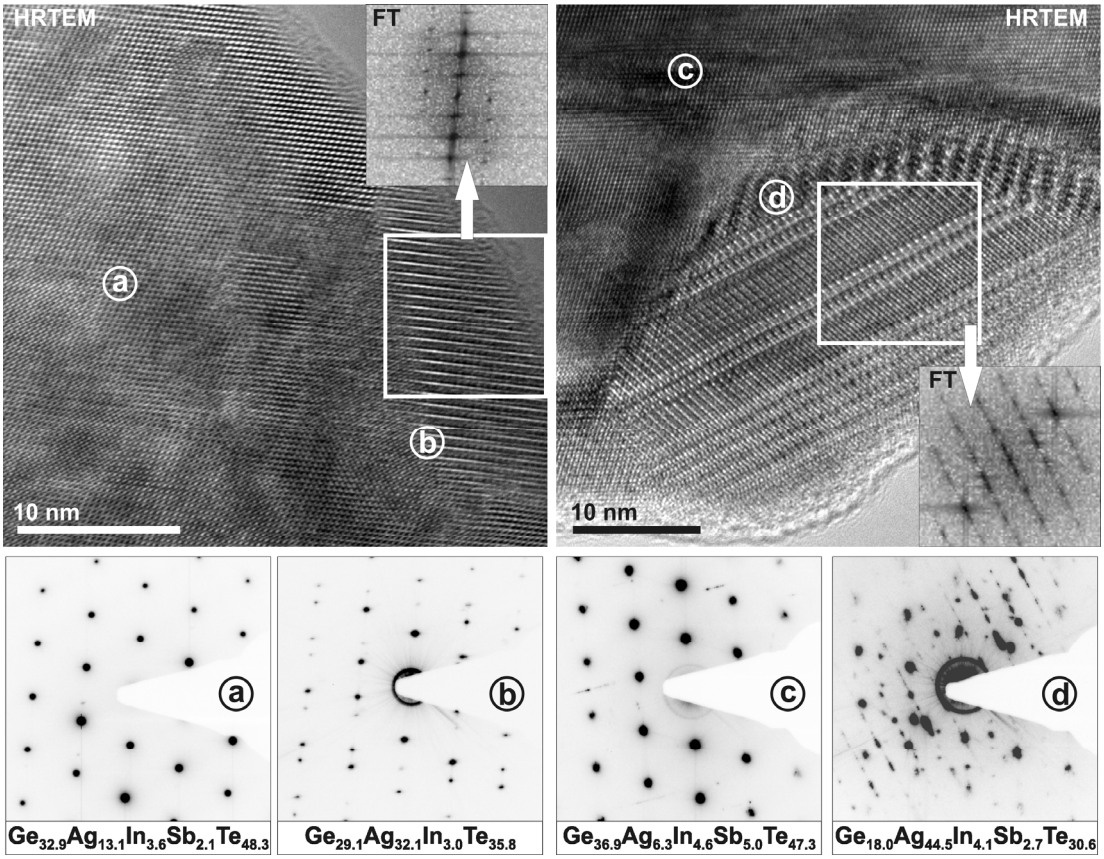

Fig. 4. HRTEM images (zone axis <100> with respect to the rhombohedral matrices, top) of silver-rich precipitates in $(GeTe)_{5.5}AgIn_{0.5}Sb_{0.5}Te_2$ (left) and in $(GeTe)_7AgIn_{0.5}Sb_{0.5}Te_2$ (right) with corresponding Fourier transforms of the precipitates (insets) and SAED patterns (irradiated area ca. 50 - 100 nm, bottom) with composition (in atom-%, from TEM-EDX, irradiated area ca. 10 - 20 nm) of the matrix areas (a, c) and areas that contain the matrix and the precipitates (b, d; b also shows twinning of the matrix, see also Fig. S1 in the Supplementary Information).

2.5.3.4 Thermal behavior

The fact that In-poor $(GeTe)_xAgIn_ySb_{1-y}Te_2$ compounds with x = 12 for y =1 and x ≥ 5 for y = 0.5 can be synthesized without applying HP by annealing at 550 °C and subsequent quenching may be explained by the existence of thermodynamically stable, homogeneous HT phases. The PXRD patterns in Fig. 6 show the temperature-dependent phase transitions of four rocksalt-type samples during the heating process: $(GeTe)AgInTe_2$, $(GeTe)AgIn_{0.5}Sb_{0.5}Te_2$ and $(GeTe)_5AgInTe_2$, which were prepared under HP conditions, and $(GeTe)_5AgIn_{0.5}Sb_{0.5}Te_2$, which was prepared by quenching from 550 °C. Upon heating, the cubic phases decompose by forming chalcopyrite-type $AgInTe_2$. Assuming complete decomposition as a reasonable approximation, the main phase is GeTe or $(GeTe)_{2x}AgSbTe_2$, respectively. However, these might be doped with small amounts of In. $(GeTe)AgInTe_2$

decomposes into $AgInTe_2$ and GeTe at ~150 °C. No HT phase is formed, both compounds melt at individual temperatures. For $(GeTe)AgIn_{0.5}Sb_{0.5}Te_2$, the decomposition reaction into $AgInTe_2$ and $(GeTe)_2AgSbTe_2$ starts at ~200 °C. The intensity of the strongest reflection of $AgInTe_2$ at ~11° 2θ becomes weaker at around 520 °C, which might be attributed to melting or a reaction with $(GeTe)_2AgSbTe_2$, which however does not result in a homogeneous quinary HT phase. $(GeTe)_5AgInTe_2$ shows a similar decomposition reaction as $(GeTe)AgInTe_2$ starting at ~220 °C; however, a quaternary HT phase is formed at ~480 °C and the reflections of $AgInTe_2$ vanish completely. This re-reaction is also confirmed by the non-linear increase in the lattice parameter *a* of the rocksalt-type phase (best visible for the reflections at 31° and 34° 2θ). Although a HT phase exists at 550 °C, quenching it does not yield a homogeneous compound; $AgInTe_2$ was always found as a side phase so that HP synthesis was necessary as described above (Section *Sample characterization and optimal conditions for synthesis*). Probably, the cooling rate is not sufficient to avoid the partial decomposition. As expected, $(GeTe)_5AgIn_{0.5}Sb_{0.5}Te_2$ decomposes into $AgInTe_2$ and $(GeTe)_{10}AgSbTe_2$ at ~240 °C. A quinary HT phase is formed which can be quenched to obtain a metastable sample which is homogeneous according to its PXRD pattern.

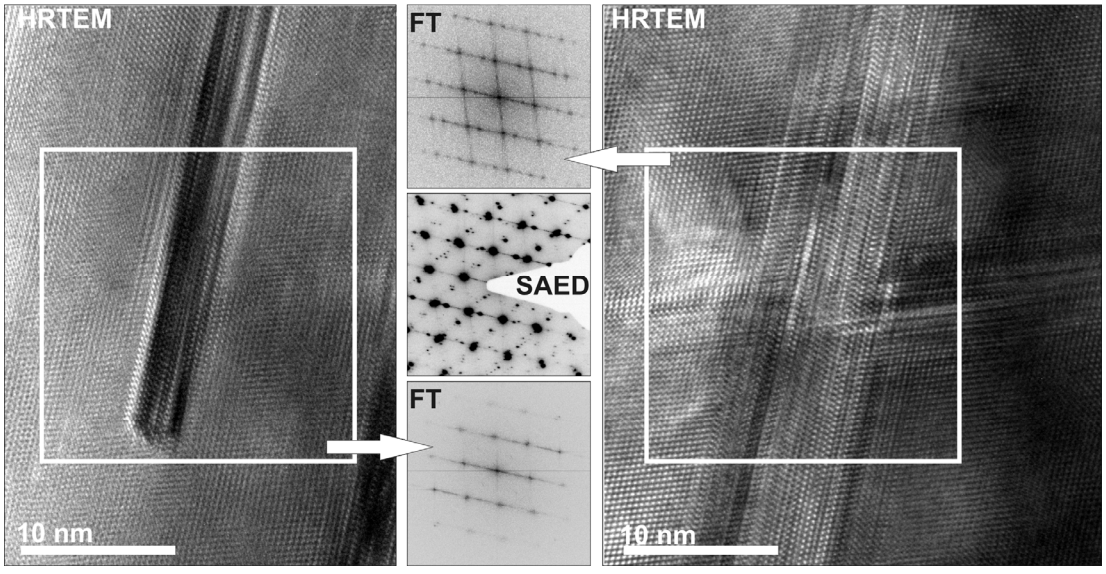

Fig. 5. HRTEM images viewed along the <100> zone axis of two different crystal areas of rhombohedral $(GeTe)_7AgIn_{0.5}Sb_{0.5}Te_2$ with $AgInTe_2$ precipitates, the corresponding Fourier transforms (FT) and an SAED pattern from the crystallite corresponding to the HRTEM on the right side; TEM-EDX of areas containing the precipitates yield $Ge_7Ag_5In_{26}Sb_6Te_{56}$ (left) and $Ag_{26}In_{23}Te_{51}$ (right), these analyses only show a trend as the beam cannot be focused exclusively on the precipitates.

Temperature dependent PXRD of $(GeTe)_{5.5}AgIn_{0.5}Sb_{0.5}Te_2$ (see Fig. 7, also concerning the numbering of the transitions) reveal that in addition to the decomposition, structural phase transitions of the trigonal compounds occur during heating and cooling. At ~100 °C (1) the phase transition from trigonal (α-GeTe type) to cubic (rocksalt type) takes place in the quinary quenched compound. At ~240 °C (2) the compound decomposes into $AgInTe_2$ and – assuming complete decomposition – $(GeTe)_{11}AgSbTe_2$. The homogeneous HT phase begins to form at 400 °C (3), whereas upon slow cooling, the decomposition into $AgInTe_2$ and $(GeTe)_{11}AgSbTe_2$ starts at ~340 °C (4). The different temperatures for the formation and decomposition of the HT phase, respectively, probably reflect time and particle-size dependence. During heating (3), relatively large grains of $AgInTe_2$ react with $(GeTe)_{11}AgSbTe_2$ while during cooling (4) $AgInTe_2$ grains need to nucleate and to grow, and the very broad reflections of nanoscale precipitates may not be visible in PXRD patterns. As discussed above, there may be very small amounts of other nanoscale precipitates that do not contribute to the PXRD patterns, especially when quenching leads through a two-phase region. While $AgInTe_2$ remains present, the cubic to trigonal phase transition (5) of the main phase $(GeTe)_{11}AgSbTe_2$ takes place at ~140 °C. The difference between the trigonal to cubic (1) and cubic to trigonal (5) phase transition temperatures is due to the change of the main phase's composition from $(GeTe)_{5.5}AgIn_{0.5}Sb_{0.5}Te_2$ to $(GeTe)_{11}AgSbTe_2$. Therefore, the phase transition temperatures increases and gets closer to the one of pure GeTe.[38]

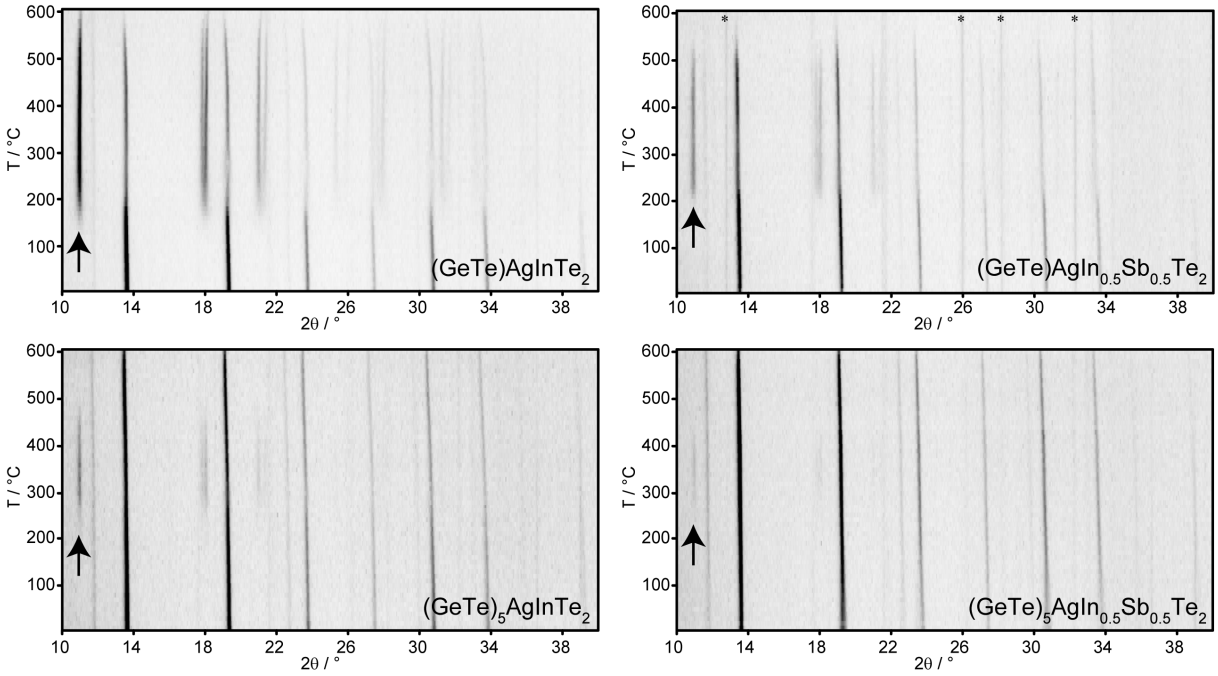

Fig. 6. Temperature-dependent X-ray powder diffraction patterns of $(GeTe)_xAgIn_ySb_{1-y}Te_2$ for x = 1 (top) and 5 (bottom); y = 1 (left) and 0.5 (right); asterisks (*) mark reflections caused by the furnace; the arrows mark the strongest reflection of $AgInTe_2$.

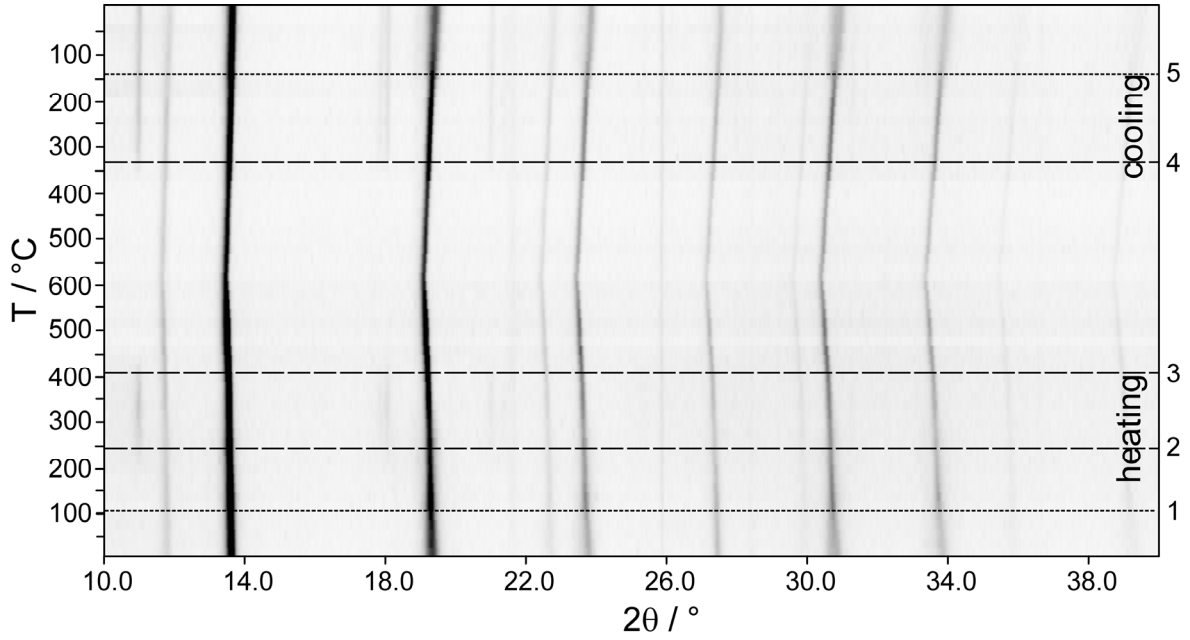

Fig. 7. Temperature-dependent X-ray powder diffraction pattern of $(GeTe)_{5.5}AgIn_{0.5}Sb_{0.5}Te_2$: (1) the reflections become sharper as the rhombohedral splitting of the α-GeTe type's pattern vanishes during the phase transition to the rocksalt-type structure; (2) decomposition to $AgInTe_2$ and $(GeTe)_{11}AgSbTe_2$; (3) formation of a cubic quinary HT phase; (4) decomposition to $AgInTe_2$ and $(GeTe)_{11}AgSbTe_2$; (5) cubic to trigonal phase transition of $(GeTe)_{11}AgSbTe_2$.

2.5.3.5 High-temperature thermoelectric properties of $(GeTe)_{5.5}AgIn_{0.5}Sb_{0.5}Te_2$

The thermoelectric properties of $(GeTe)_{5.5}AgIn_{0.5}Sb_{0.5}Te_2$ (cf. Fig. 8), which was prepared by annealing at 550 °C (stability region of the quinary HT phase) and subsequent quenching can be understood by the temperature dependent PXRD pattern in Fig. 7. During heating, σ exhibits metallic characteristics and decreases from 1100 to 750 S/cm; this is only slightly affected by the decomposition into chalcopyrite-type $AgInTe_2$ and $(GeTe)_{11}AgSbTe_2$. However, for the quinary cubic HT phase σ increases again, probably because the interfaces caused by nanoscopic $AgInTe_2$ precipitates (cf. Section *Electron microscopy and diffraction*) vanish and thus do not scatter electrons anymore. Upon cooling, the characteristics of σ is parallel to the heating curve. The heating and cooling curves of κ are very similar. In the two-phase region the slope of κ is not as steep as for lower and higher temperatures. However, this part of the κ curve should not be over-interpreted as the assumption of constant heat capacity (according to Dulong-Petit) may not be a good approximation during the decomposition reaction. S increases up to a maximum at ~300 °C, i. e. in the two-phase area. For the quinary cubic HT phase, S decreases slightly with increasing temperature. Upon cooling, S is slightly

larger than at the same temperatures during heating. This is a consequence of the above mentioned reactions and phase transitions. In general, the characteristics of the thermoelectric properties nicely reflect the phase transitions observed in the temperature dependent PXRD pattern. The discussion of the maximal ZT should be restricted to the cooling curve below 350 °C. During heating and in the two-phase regions, the absolute values of the properties are not reliable (no well-defined heat capacity, see above) and there may be a pronounced time dependence due to reactions and nucleation processes. The highest ZT value of 0.75 at 300 °C can be observed close to the decomposition into $AgInTe_2$ and $(GeTe)_{11}AgSbTe_2$. Low-temperature experiments are not promising, because the ZT value has already dropped to 0.35 at room temperature.

2.5.3.6 Low-temperature thermoelectric properties of $(GeTe)_{5.5}AgInTe_2$

The thermoelectric properties of the TIGS sample $(GeTe)_{5.5}AgInTe_2$ (Fig. 9) were measured from RT down to 4 K and then up to 400 K, i. e. far below the decomposition temperature. The heating and cooling curves for all properties are almost similar within the experimental errors and do not indicate pronounced irreversible processes (the slight deviation between the κ values during cooling and heating sequences between 50 and 150 K is probably due to contact problems). The subtle hysteretic behavior between 40 and 300 K may be comparable to that observed in metastable modifications of $GeBi_2Te_4$ where the extent of the hysteresis could be correlated with the average domain size of the crystalline samples.[39] The high residual resistivity of 1.015 mΩcm together with the remarkably small residual resistivity ratio of RRR = ρ(300 K) / ρ(2 K) = 1.08 clearly confirms the presence of significant disorder in $(GeTe)_{5.5}AgInTe_2$. Furthermore, the sequential change of the sign of the slope, dρ/dT supports the presence of a crossover-scenario between a degenerated semiconducting and metallic-like behavior of $(GeTe)_{5.5}AgInTe_2$. This observation may be due to different scattering processes caused (*i*) by the temperature independent residual resistivity originating from electron-impurity scattering (impurity atoms, grain boundaries, etc.) and (*ii*) the temperature dependent contribution due to electron-phonon scattering. From 150 K to 400 K, σ(T) exhibits metallic-like characteristics and the absolute values between RT and 400 K are approximately in the same range as the corresponding ones of $(GeTe)_{5.5}AgIn_{0.5}Sb_{0.5}Te_2$. The absolute κ values of the TIGS sample are slightly larger compared with the ones in $(GeTe)_{5.5}AgIn_{0.5}Sb_{0.5}Te_2$ at room temperature. This hints for a less pronounced disorder in $(GeTe)_{5.5}AgInTe_2$ *vs*. $(GeTe)_{5.5}AgIn_{0.5}Sb_{0.5}Te_2$. The increase of S is steeper for TIGS than for

$(GeTe)_{5.5}AgIn_{0.5}Sb_{0.5}Te_2$ which compensates the higher κ and leads to a higher ZT value of 0.6 at 400 K.

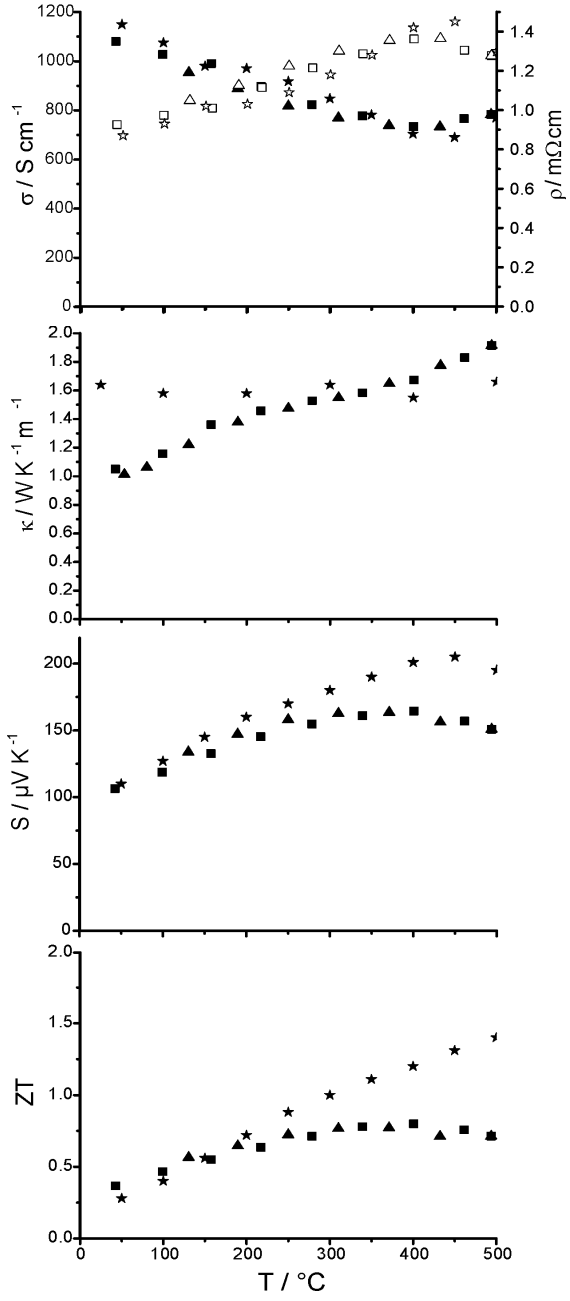

Fig. 8. Thermoelectric properties of $(GeTe)_{5.5}AgIn_{0.5}Sb_{0.5}Te_2$ (heating curves: ■; cooling curves: ▲), from top to bottom: electrical conductivity and resistivity (solid and empty symbols, respectively), thermal conductivity, Seebeck coefficient and ZT value in comparison to values for TAGS-85 (asterisks) taken from reference [19].

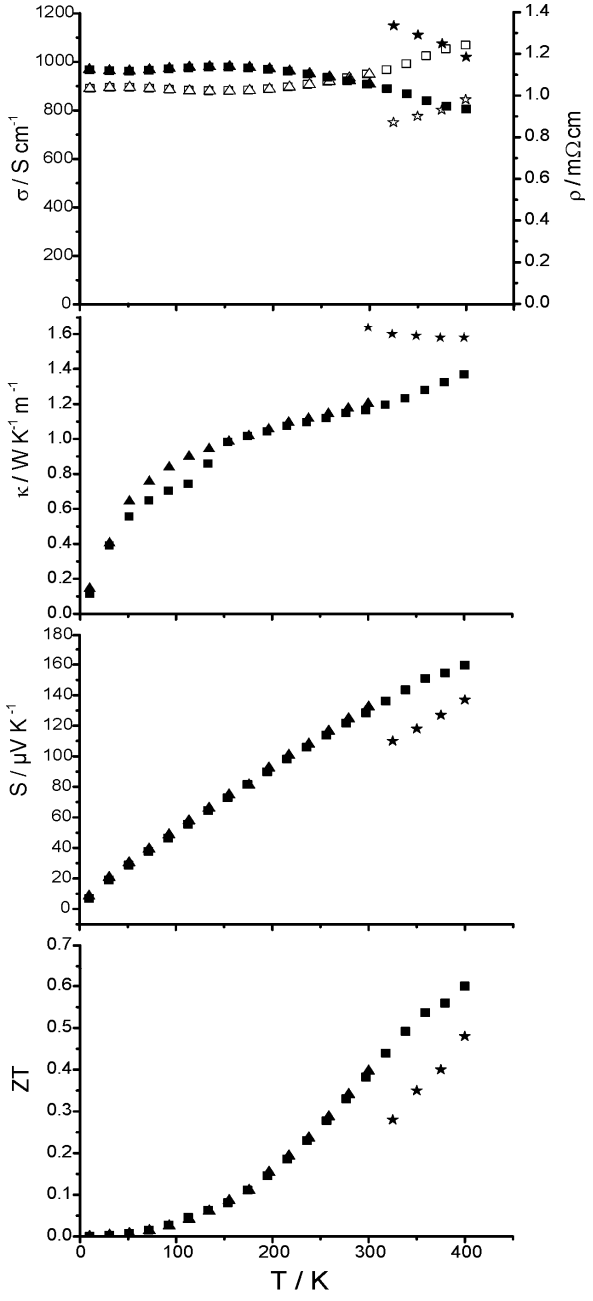

Fig. 9. Thermoelectric properties of $(GeTe)_{5.5}AgInTe_2$ (heating curve: ■; cooling curve: ▲), from top to bottom: electrical conductivity and resistivity (solid and empty symbols, respectively), thermal conductivity, Seebeck coefficient and ZT value in comparison to values for TAGS-85 (asterisks) taken from reference [19].

2.5.4 Conclusion

Members of the solid solution series between GeTe and $AgInTe_2$ or $AgIn_{0.5}Sb_{0.5}Te_2$, respectively, crystallize in disordered rocksalt-type structures for GeTe contents $1 < x \leq 5$ and in disordered α-GeTe-type structures for $5 < x < 12$. In such $(GeTe)_xAgIn_ySb_{1-y}Te_2$ phases, In is octahedrally coordinated by Te or exhibits a 3+3 coordination in a trigonal antiprismatic fashion, respectively, whereas in general, In prefers to be tetrahedrally coordinated by Te. Thus, the synthesis of homogeneous In-rich samples with more than 3.6 atom-% In (i. e. $x < 12$ for $y = 1$ and $x < 5$ for $y = 0.5$) requires high-pressure conditions, because the octahedral coordination of In is energetically favored under HP conditions (pressure-coordination rule). Samples with an In content ≤ 3.6 atom-% (i. e. $x = 12$ for $y = 1$ and $x \geq 5$ for $y = 0.5$) do not require HP synthesis and can be obtained by quenching after annealing the samples at 550 °C. All $(GeTe)_xAgIn_ySb_{1-y}Te_2$ phases investigated decompose into chalcopyrite-type $AgInTe_2$ and GeTe or $(GeTe)_{2x}AgSbTe_2$ for $y = 1$ or 0.5, respectively, upon heating at ambient pressure. The decomposition temperature depends on the In content and is higher for samples with lower In contents. However, the cubic HT phases of GeTe or $(GeTe)_{2x}AgSbTe_2$ react with small amounts of $AgInTe_2$. At high temperature, solid solutions are favored by entropy as indicated by the observation of rocksalt-type HT phases for In contents up to 7-8 atom-% at temperatures above ~450 °C (the exact temperature depends on the In content). Although no side phase can be observed in the PXRD patterns, quenching leads to nanoscopic precipitates of $AgInTe_2$ and Ag-rich domains. Thus, the applied quenching rates cannot completely suppress the nucleation of $AgInTe_2$ during the decomposition reaction. $(GeTe)_{5.5}AgIn_{0.5}Sb_{0.5}Te_2$ quenched from the rocksalt-type HT phase exhibits a maximum ZT value of 0.75 at 300 °C close to the decomposition into $AgInTe_2$ and $(GeTe)_{11}AgSbTe_2$ but only 0.5 at 125 °C where $(GeTe)_{5.5}AgInTe_2$ prepared under HP conditions exhibits ZT = 0.6. As expected the latter's κ is slightly higher than that of the quinary compound, but this is outbalanced by the higher Seebeck coefficient. TIGS's ZT value is higher than that of the corresponding TAGS-85[19] in the investigated temperature range.

Both the $(GeTe)_xAgIn_{0.5}Sb_{0.5}Te_2$ as well as the TIGS samples show promising new ways towards high-performance thermoelectric materials. While TIGS compounds prepared under high-pressure conditions exhibit remarkable ZT values close to RT and up to 125 °C, both the more pronounced disorder and the decomposition of $(GeTe)_{5.5}AgIn_{0.5}Sb_{0.5}Te_2$ might provide possible control parameters to decrease the thermal conductivity without significantly affecting the electrical conductivity.

Acknowledgement

We thank Christian Minke and Dr. Markus Seibald for SEM operation and EDX analyses and Thomas Miller (LMU Munich) for the temperature-dependent powder diffraction experiments. Furthermore, we thank Fivos Drymiotis (California Institute of Technology) for help with the thermoelectric measurements and PD Dr. Gerald Wagner (Leipzig University) for his help with the HRTEM interpretation. This investigation was funded by the Deutsche Forschungsgemeinschaft (grant OE530/1-2) and the Studienstiftung des deutschen Volkes (scholarship for T.S.).

Supplementary information

Table S1. Results of the SEM-EDX analyses (averaged from 5 - 15 point analyses per sample) of $(GeTe)AgInTe_2$, $(GeTe)_5AgInTe_2$, $(GeTe)_{5.5}AgInTe_2$, $(GeTe)_7AgInTe_2$ and $(GeTe)_{12}AgInTe_2$.

sample	atom-% calc.	atom-% found
$(GeTe)AgInTe_2$	Ge: 16.7; Ag: 16.7; In: 16.7; Te: 50.0	Ge: 17.9(4); Ag: 16.0(4); In: 16.5(4); Te: 49.6(6)
$(GeTe)_5AgInTe_2$	Ge: 35.7; Ag: 7.1; In: 7.1; Te: 50.0	Ge: 36.0(14); Ag: 7.2(4); In: 7.3(4); Te: 50(1)
$(GeTe)_{5.5}AgInTe_2$	Ge: 36.7; Ag: 6.7; In: 6.7; Te: 50.0	Ge: 37.1(15); Ag: 6.5(4); In: 6.9(4); Te: 49.5(8)
$(GeTe)_7AgInTe_2$	Ge: 38.9; Ag: 5.6; In: 5.6; Te: 50.0	Ge: 39.7(16); Ag: 5.5(5); In: 5.4(6); Te: 49.4(8)
$(GeTe)_{12}AgInTe_2$	Ge: 42.9; Ag: 3.6; In: 3.6; Te: 50.0	Ge: 44(1); Ag: 3.2(7); In: 3.6(4); Te: 49.3(7)

Table S2. Results of the SEM-EDX analyses (averaged from 5 - 15 point analyses per sample) of $(GeTe)AgIn_{0.5}Sb_{0.5}Te_2$, $(GeTe)_5AgIn_{0.5}Sb_{0.5}Te_2$, $(GeTe)_{5.5}AgIn_{0.5}Sb_{0.5}Te_2$, $(GeTe)_7AgIn_{0.5}Sb_{0.5}Te_2$.and $(GeTe)_{12}AgIn_{0.5}Sb_{0.5}Te_2$

sample	atom-% calc.	atom-% found
$(GeTe)AgIn_{0.5}Sb_{0.5}Te_2$	Ge: 16.7; Ag: 16.7; Sb: 8.3; In: 8.3; Te: 50.0	Ge: 17.3(7); Ag: 16.2(5); Sb: 9.0(6); In: 8.0(5); Te: 49.6(4)
$(GeTe)_5AgIn_{0.5}Sb_{0.5}Te_2$	Ge: 35.7; Ag: 7.1; Sb: 3.6; In: 3.6; Te: 50.0	Ge: 37.7(9); Ag: 6.6(1); Sb: 3.9(4); In: 3.3(3); Te: 48.5(7)
$(GeTe)_{5.5}AgIn_{0.5}Sb_{0.5}Te_2$	Ge: 36.7; Ag: 6.7; Sb: 3.3; In: 3.3; Te: 50.0	Ge: 37.1(1); Ag: 6.5(5); Sb: 3.5(1); In: 3.3(1); Te: 49.6(5)
$(GeTe)_7AgIn_{0.5}Sb_{0.5}Te_2$	Ge: 38.9; Ag: 5.6; Sb: 2.8; In: 2.8; Te: 50.0	Ge: 40(1); Ag: 5.2(4); Sb: 2.9(4); In: 2.7(3); Te: 48.9(9)
$(GeTe)_{12}AgIn_{0.5}Sb_{0.5}Te_2$	Ge: 42.9; Ag: 3.6; In: 1.8; Sb: 1.8 Te: 50.0	Ge: 41.8(9); Ag: 3.8(3); In: 1.9(3); Sb: 2.2(5) Te: 50.3(7)

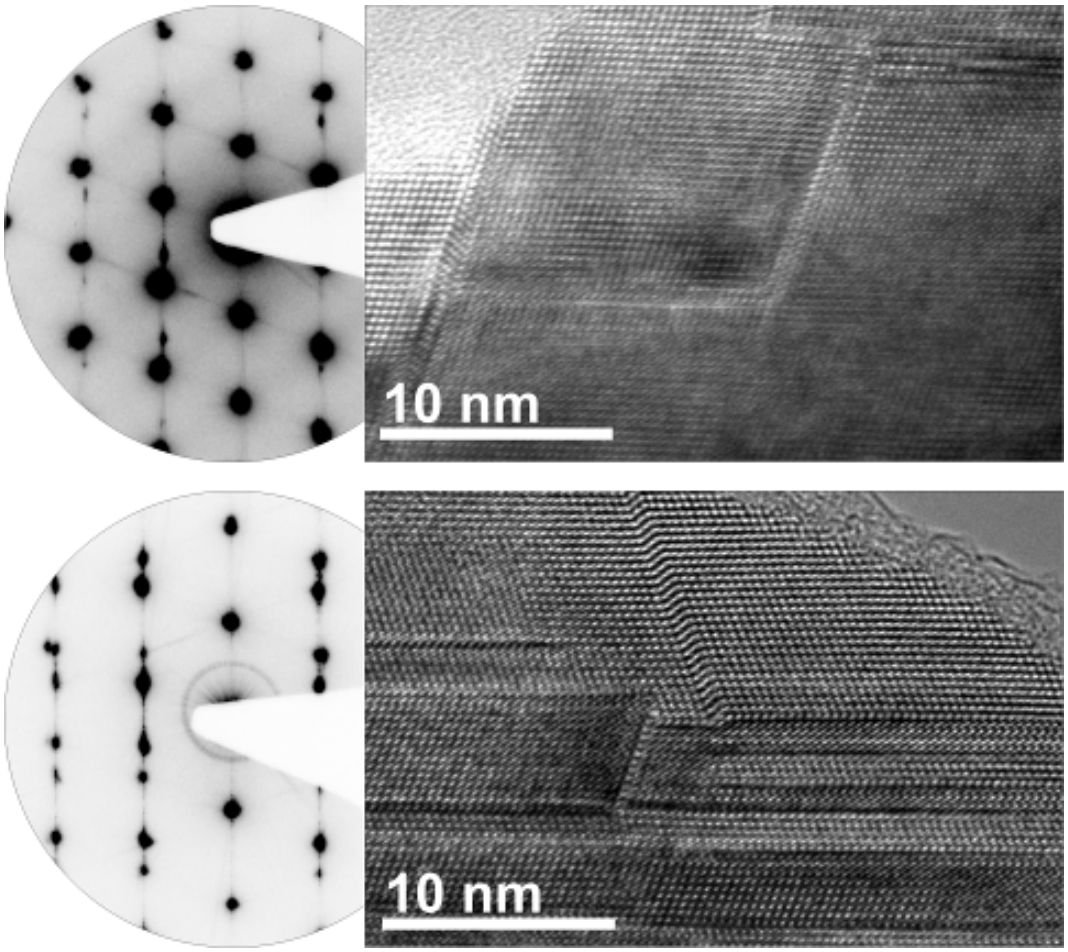

Fig. S1. HRTEM images (right) and the corresponding SAED patterns (left) of crystal areas with dislocations and twin domains: $(GeTe)_{5.5}AgIn_{0.5}Sb_{0.5}Te_2$ (top) and $(GeTe)_7AgIn_{0.5}Sb_{0.5}Te_2$ (bottom).

References

[1] H. Hahn, G. Frank, W. Klingler, A. D. Meyer, G. Störger, *Z. Anorg. Allg. Chem.* **1953**, *271*, 153.

[2] K. J. Range, G. Engert, A. Weiss, *Solid State Commun.* **1969**, *7*, 1749.

[3] T. Schröder, T. Rosenthal, D. Souchay, C. Petermayer, S. Grott, E.-W. Scheidt, C. Gold, W. Scherer, O. Oeckler, *J. Solid State Chem.* **2013**, *206*, 20.

[4] H. J. Goldsmid, *Thermoelectric Refrigeration*, Plenum Press, New York, **1964**.

[5] D. T. Morelli, V. Jovovic, J. P. Heremans, *Phys. Rev. Lett.* **2008**, *101*, 035901.

[6] M. D. Nielsen, V. Ozolins, J. P. Heremans, *Energy Environ. Sci.* **2013**, *6*, 570.

[7] W. G. Zeier, Y. Z. Pei, G. Pomrehn, T. Day, N. Heinz, C. P. Heinrich, G. J. Snyder, W. Tremel, *J. Am. Chem. Soc.* **2013**, *135*, 726.

[8] A. Yusufu, K. Kurosaki, Y. Ohishi, H. Muta, S. Yamanaka, *Jpn. J. Appl. Phys.* **2013**, *52*, 081801.

[9] T. Plirdpring, K. Kurosaki, A. Kosuaga, T. Day, S. Firdosy, V. Ravi, G. J. Snyder, A. Harnwunggmoung, T. Sugahara, Y. Ohishi, H. Muta, S. Yamanaka, *Adv. Mater.* **2012**, *24*, 3622.

[10] R. Liu, L. Xi, H. Liu, X. Shi, W. Zhang, L. Chen, *Chem. Commun.* **2012**, *48*, 3818.

[11] C. Wood, *Rep. Prog. Phys.* **1988**, *51*, 459.

[12] W. Klemm, G.Frischmuth, *Z. Anorg. Allg. Chem.* **1934**, *218*, 249.

[13] J. Goldak, C. S. Barrett, D. Innes, W. Youdelis, *J. Chem. Phys.* **1966**, *44*, 3323.

[14] B. A. Cook, M. J. Kramer, X. Wei, J. L. Harringa, E. M. Levin, *J. Appl. Phys.* **2007**, *101*, 053715.

[15] S. K. Plachkova, *Phys. Status Solidi A* **1984**, *83*, 349.

[16] S. H. Yang, T. J. Zhu, T. Sun, S. N. Zhang, X. B. Zhao, J. He, *Nanotechnol.* **2008**, *19*, 245707.

[17] F. D. Rosi, J. P. Dismukes, E. F. Hockings, *Electron. Eng.* **1960**, *79*, 450.

[18] G. C. Christakudis, S. K. Plachkova, L. E. Shelimova, E. S. Avilov, *Phys. Status Solidi A* **1991**, *128*, 465.

[19] J. Davidow, Y. Gelbstein, *J. Electron. Mater.* **2013**, *42*, 1542.

[20] X. Shi, J. R. Salvador, J. Yang, H. Wang, *Sci. Adv. Mater.* **2011**, *3*, 667.

[21] E. M. Levin, B. A. Cook, J. L. Harringa, S. L. Bud'ko, R. Venkatasubramanian, K. Schmidt-Rohr, *Adv. Funct. Mater.* **2011**, *21*, 441.

[22] E. M. Levin, S. L. Bud'ko, K. Schmidt-Rohr, *Adv. Funct. Mater.* **2012**, *22*, 2766.

[23] D. Walker, M. A.Carpenter, C. M. Hitch, *Am. Mineral.* **1990**, *75*, 1020.

[24] D. Walker, *Am. Mineral.* **1991**, *76*, 1092.

[25] D. C. Rubie, *Phase Trans.* **1999**, *68*, 431.

[26] H. Huppertz, *Z. Naturforsch. B* **2001**, *56*, 697.

[27] WINXPOW, v2.12 ed., Stoe & Cie GmbH, Darmstadt, Germany, **2005**.

[28] *TOPAS-Academic*, *V. 4.1*, Coelho Software, Brisbane, Australia, **2007**.

[29] *DigitalMicrograph 3.6.1*, Gatan Software, Pleasanton, USA, **1999**.

[30] P. A. Stadelmann, *Ultramicroscopy* **1987**, *21*, 131.

[31] *ESVision*, *4.0.164*, Emispec Systems Inc., Tempe, USA, **1994-2002**.

[32] L. J. van der Pauw, *Philips Res. Rep.* **1958**, *13*, 1.

[33] K. A. Borup, E. S. Toberer, L. D. Zoltan, G. Nakatsukasa, M. Errico, J. P. Fleurial, B. B. Iversen, G. J. Snyder, *Rev. Sci. Instrum.* **2012**, *83*, 123902.

[34] S. Iwanaga, E. S. Toberer, A. LaLonde, G. J. Snyder, *Rev. Sci. Instrum.* **2011**, *82*, 063905.

[35] A. LeBail, A. Jouanneaux, *J. Appl. Crystallogr.* **1997**, *30*, 265.

[36] R. Marin-Ayral, B. Lendre, G. Brun, B.Liautard, J. Tedenac, *Thermochim. Acta* **1988**, *131*, 37.

[37] R. M. Imamov, Z. G. Pinsker, *Sov. Phys. Crystallogr.* **1966**, *11*, 182.

[38] T. Chattopadhyay, J. Boucherle, H. von Schnering, *J. Phys. C* **1987**, *20*, 1431.

[39] T. Schröder, M. N. Schneider, T. Rosenthal, A. Eisele, C. Gold, E.-W. Scheidt, W. Scherer, R. Berthold, O. Oeckler, *Phys. Rev. B* **2011**, *84*, 184104.

3 Compounds with disordered cubic high-temperature phases

3.1 Overview

All metastable phases discussed in Chapter 2 are characterized by either disorder of the cations or in the case of $Ag_{3.4}In_{3.7}Sb_{76.4}Te_{16.5}$ disorder of all involved elements on one single Wyckoff position.[1] In contrast, In_3SbTe_2, which was proposed as a phase-change material (PCM) for PCRAM applications, exhibits a rocksalt-type high-temperature (HT) phase that can be quenched as a metastable modification displaying disordered anions.[2] However, different ordering variants were proposed.[3] Comparable to $Ag_{3.4}In_{3.7}Sb_{76.4}Te_{16.5}$ (cf. Chapter 2.3), the stable state of samples with the composition In_3SbTe_2 at room temperature (RT) corresponds to a mixture of two phases, in this case sphalerite-type InSb and TlSe-type InTe. In both compounds In is coordinated tetrahedrally by Sb or Te, respectively. In_3SbTe_2 is supposed to have four bit states that can be differentiated by the absolute values of their electrical resistivity.[4] Although magnetic measurements have shown that no In^{2+} is present,[5] i. e. delocalized electrons and metal-like electrical conductivity (σ) can be expected, the reported σ of a slightly inhomogeneous sample of In_3SbTe_2 is in a reasonable range for thermoelectric materials. In order to investigate possible superstructure formation or other real-structure phenomena, a combination of X-ray, neutron and electron diffraction methods was employed. The average structure of quenched In_3SbTe_2 was confirmed and corresponds to a rocksalt-type structure with Sb and Te randomly sharing the anion position. No superstructure was observed, but diffuse intensities indicate a local displacement of the atoms from the average positions along <100> (cf. Chapter 3.2). The determined transport properties show that homogeneous In_3SbTe_2 is a metal.

The results for In_3SbTe_2 and $(GeTe)_xAgIn_ySb_{1-y}Te_2$ (with $x \geq 5$, $y = 0.5$ and 1; cf. Chapter 3.5), show that many tellurides form rocksalt-type HT phases. Other examples are $(GeTe)_{\geq 3}Sb_2Te_3$ (GST) materials which exhibit such rocksalt-type HT phases.[6] Quenching their HT phases yields metastable nanostructured phases with intersecting defect layers. For $(GeTe)_{12}Sb_2Te_3$, this nanostructure is associated with ZT values of up to 1.3 at 450 °C, because phonons are more effectively scattered at the defect layers than electrons. Recently, the ZT value of $(GeTe)_x(AgSbTe_2)_{100-x}$ (TAGS) materials could be increased by adjusting the Ag/Sb which results in compounds $(GeTe)_{85}(Ag_ySbTe_{y/2+1.5})_{15}$. The origin of the ZT value increase is explained with an optimal charge-carrier concentration and a lower thermal conductivity than in conventional TAGS materials with an Ag/Sb ratio of 1. However, the consequence of this adjustment for all values of $y < 1$ is the existence of cation vacancies

within the structures, because the number of anions exceeds the number of cations. Cation vacancies and their possible ordering, which might be expected to correspond to the short-range vacancy ordering in metastable GST materials was not considered so far.[7-9] In this thesis, the influence of the vacancy concentration on real-structure phenomena and the thermoelectric properties was investigated. $Ge_{0.53}Ag_{0.13}Sb_{0.27}\square_{0.07}Te_1$ and $Ge_{0.61}Ag_{0.11}Sb_{0.22}\square_{0.06}Te_1$ exhibit several phase transitions upon heating and cooling that involve differently arranged cation vacancies comparable to those of GST materials, respectively. The phononic contribution to the thermal conductivity in TAGS compounds with cation vacancies and quenched GST materials is very small. The hindered phonon propagation might be attributed to the large mass difference of involved elements and the vacancy layers, i. e. suppressed harmonic oscillation. Quenched $Ge_{0.53}Ag_{0.13}Sb_{0.27}\square_{0.07}Te_1$ and $Ge_{0.61}Ag_{0.11}Sb_{0.22}\square_{0.06}Te_1$ contain similar short-range ordering motifs as reported for GST materials (cf. Chapter 3.3). The nanostructured phase of $Ge_{0.53}Ag_{0.13}Sb_{0.27}\square_{0.07}Te_1$ has remarkable thermoelectric properties and exhibits a ZT value of 1.3 at 160 °C.

All described phase transitions are reconstructive and strongly affect the thermoelectric properties. In order to obtain compounds that exhibit displacive phase transitions with less influence on the thermoelectric properties, but maintain a large mass difference of the involved elements, Ag in TAGS was substituted by Li, the lightest metal. As observed for the solid solutions between GeTe and $AgInTe_2$, $AgIn_{0.5}Sb_{0.5}Te_2$ or Sb_2Te_3, respectively, the structural chemistry of the solid solution $(GeTe)_x(LiSbTe_2)_2$ mainly depends on the GeTe content. Interestingly, in rocksalt-type phases of $(GeTe)_x(LiSbTe_2)_2$ with x = 2 and 3, small amounts of Ge occupy the tetrahedral voids instead of octahedral voids, in accordance with a controversial discussion about partial tetrahedral coordination of Ge by Te in metastable and amorphous phases of GST materials for PCM application.[10-13] The phononic contribution to the thermal conductivity of $(GeTe)_x(LiSbTe_2)_2$, which only displays a reversible displacive phase transition upon heating, is as low as for corresponding GST samples with cation vacancies (cf. Chapter 3.4). Thus, Li can be viewed as a “pseudo-vacancy”.

Furthermore, compounds with both cation vacancies and monovalent cations lighter than Ag, i. e. Li or Na, could be obtained. Comparable to TAGS compounds with vacancies, quenched $Ge_{0.61}Li_{0.11}Sb_{0.22}\square_{0.06}Te_1$ and $Ge_{0.61}Na_{0.11}Sb_{0.22}\square_{0.06}Te_1$ crystallize in a rocksalt-type structure (cf. powder pattern, Fig. 1 left). Both compounds exhibit two phase transitions upon heating; however, in both cases side phases can be observed, which are still under investigation. The thermoelectric properties, especially those of $Ge_{0.61}Na_{0.11}Sb_{0.22}\square_{0.06}Te_1$ (cf. Fig. 1 right) are very promising and exhibit ZT values of ~ 1.7 below 200 °C, which is even higher than those

published for nanostructured $Ge_{0.53}Ag_{0.13}Sb_{0.27}\square_{0.07}Te_1$. The cubic HT phase of $Ge_{0.61}Na_{0.11}Sb_{0.22}\square_{0.06}Te_1$ seems to exhibit ZT values of up to ~ 2.4 at 500 °C in some measurements. However, the influence of the sequence of the measurements of κ, σ and S has not yet been investigated.

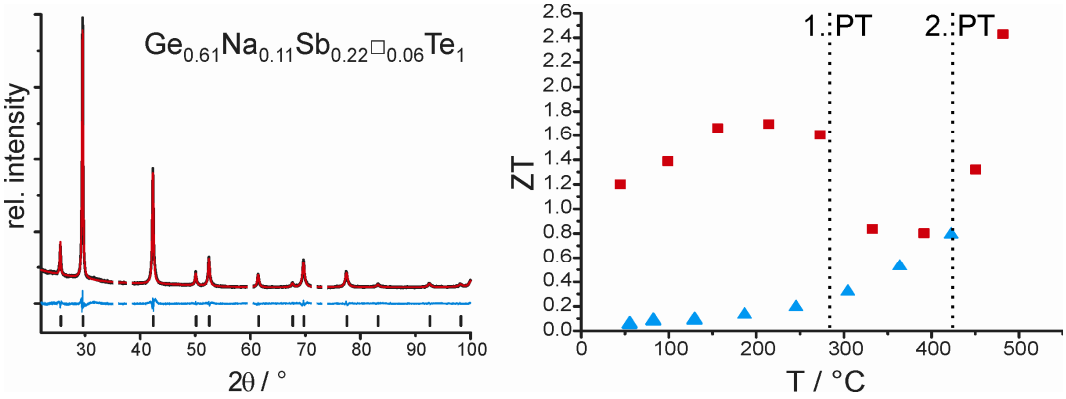

Fig. 1. Left: Rietveld fit for rocksalt-type $Ge_{0.61}Na_{0.11}Sb_{0.22}\square_{0.06}Te_1$ (space group: $Fm\bar{3}m$; a = 6.02705(7) Å; R_p = 0.0191, R_{wp} = 0.0255, R_{Bragg} = 0.0045, *Goof* = 0.984; EDX: $Ge_{0.64(2)}Na_{0.08(2)}Sb_{0.24(1)}Te_1$) prepared by quenching a stoichiometric melt of the elements under argon atmosphere and subsequently annealing the resulting ingot at 550 °C for 5 days before quenching it to room temperature. Reflections caused by the grinding material were cut out. Right: ZT values of $Ge_{0.61}Na_{0.11}Sb_{0.22}\square_{0.06}Te_1$ during heating (red squares) and cooling (blue triangles). The temperatures of the first and second phase transition (1. PT and 2. PT) during heating are marked by dashed lines.

References

[1] T. Matsunaga, Y. Umetani, N. Yamada, *Phys. Rev. B* **2001**, *64*, 184116.

[2] K. Deneke, A. Rabenau, *Z. Anorg. Allg. Chem.* **1964**, *333*, 201.

[3] C. S. Kim, J. Y. Lee, Y. T. Kim, *Appl. Phys. Lett.* **2012**, *100*, 151903.

[4] Y. I. Kim, E. T. Kim, J. Y. Lee, Y. T. Kim, *Appl. Phys. Lett.* **2011**, *98*, 091915.

[5] A. Rabenau, K. Deneke, M. M. van der Meij, *Angew. Chem. Int. Ed.* **1964**, *3*, 588.

[6] T. Rosenthal, M. N. Schneider, C. Stiewe, M. Döblinger, O. Oeckler, *Chem. Mater.* **2011**, *23*, 4349.

[7] G. C. Christakudis, S. K. Plachkova, L. E. Shelimova, E. S. Avilov, *Phys. Status Solidi A* **1991**, *128*, 465.

[8] T. Zhu, H. Gao, Y. Chen, X. B. Zhao, *J. Mater. Chem. A* **2014**, *2*, 3251.

[9] Y. Chen, C. M. Jaworski, Y. B. Gao, H. Wang, T. J. Zhu, G. J. Snyder, J. P. Heremans, X. B. Zhao, *New J. Phys.* **2014**, *16*, 013057.

[10] A. V. Kolobov, P. Fons, A. I. Frenkel, A. L. Ankudinov, J. Tominaga, T. Uruga, *Nature Mater.* **2004**, *3*, 703.

[11] M. Xu, Y. Q. Cheng, H. W. Sheng, E. Ma, *Phys Rev. Lett.* **2009**, *103*, 195502.

[12] X. Q. Liu, X. B. Zhang, L. Li, Y. Q. Cheng, Z. G. Yan, M. Xu, X. D. Han, S. B. Zhang, Z. Zhang, E. Ma. *Phys. Rev. Lett.* **2011**, *106*, 025501.

[13] S. Sen, T. G. Edwards, J.-Y. Cho, Y.-C. Joo, *Phys. Rev. Lett.* **2012**, *108*, 195506.

3.2 Disorder and transport properties of In_3SbTe_2 – an X-ray, neutron and electron diffraction study

Thorsten Schröder, Tobias Rosenthal, Sebastian Grott, Christian Stiewe, Johannes de Boor, Oliver Oeckler

Z. Anorg. Allg. Chem. **2013**, *639*, 2536 – 2541.

Abstract

Quenched metastable In_3SbTe_2 was investigated by X-ray and neutron powder diffraction as well as by single-crystal X-ray diffraction. The average structure corresponds to the rocksalt type, the anion position being occupied by Sb and Te. Neutron data indicate no antisite disorder of In and Sb. The compound is a high-temperature phase that can be quenched to yield a metastable compound at ambient temperature which, upon heating, decomposes at ~ 320 °C into InSb and InTe. Diffuse scattering in reconstructed X-ray and selected area electron diffraction patterns indicates local distortions of the crystal structure due to static atom displacement along <100> from the average positions, caused by the different size of the anions, but no superstructure. The electrical conductivity of In_3SbTe_2 is $3.2 \cdot 10^4$ S/cm at 25 °C, the temperature characteristics corresponds to metallic behavior. Consequently, the thermal conductivity is also rather high. The decomposition into InSb and InTe reduces the electrical conductivity by a factor of 3 in heterogeneous microstructures.

3.2.1 Introduction

Rocksalt-type tellurides with cation disorder play an important role in the field of thermoelectrics. Compounds like $AgSbTe_2$ and $NaSbTe_2$ possess good electrical properties as their thermal conductivities are rather low.[1] In_3SbTe_2 (IST) is a high-temperature phase on the pseudo-binary line InSb – InTe in the ternary system In-Sb-Te.[2] Upon cooling stoichiometric melts, IST is formed by a peritectic reaction at ~ 570 °C. Further cooling leads to eutectoid decomposition at ~ 420 °C, where InTe and InSb are formed. Quenching the IST high-temperature phase yields a metastable compound that crystallizes in a disordered rocksalt-type structure, Sb and Te sharing the anion position. However, recent investigations of thin-film samples by means of transmission electron microscopy (TEM) indicated a

superstructure of the rocksalt-type.[3] The formal oxidation state of In might be assumed as II; however, according to magnetic measurements no In^{2+} is present. The electrical resistivity of the metallic compound has been reported as $7.2 \cdot 10^{-4}$ Ωcm (i. e. electrical conductivity $1.4 \cdot 10^3$ S/cm), yet, the samples contained impurities of InSb. Superconductivity was observed below 0.9 K.[4] IST has been suggested as a phase-change material (PCM) for data storage in phase-change random access memory (PCRAM) devices.[5] It is supposed to have distinct electrical resistance intervals that might allow one to distinguish four different bit states and thus make multibit storage possible. In the respective thin films, state "0" corresponds to an amorphous phase, state "1" is the amorphous phase with beginning InSb crystallization, state "2" the amorphous phase with larger InSb grains and InTe precipitates and state "3" resembles the metastable cubic compound which is also accessible as bulk material.[6] For PCRAMs, a certain degree of electrical resistivity (up to 10^4 Ω cm at room temperature) is essential as switching between the amorphous and crystalline states is achieved by "resistance heating" using electrical pulses of variable current and duration.[7]

Until now there are basically two classes of PCMs in application, the so-called GST materials and AIST materials, respectively. AIST materials, i. e. silver indium antimony tellurides such as $Ag_{3.4}In_{3.7}Sb_{76.4}Te_{16.5}$, are used on rewritable CDs [8] and can be viewed as doped Sb, maintaining its gray-As structure type.[9] The more widely used GST materials, i. e. germanium antimony tellurides $(GeTe)_n(Sb_2Te_3)$, resemble IST with respect to their rocksalt-type high-temperature phase; however, GST exhibits cation disorder in contrast to IST's anion disorder.[10-12] Recently, the influence of In doping on the phase-change properties of GST materials has been investigated.[13] This bridges the gap between GST and IST, especially as quaternary solid solutions of $(Ge_2Sb_2Te_5)_{1-x}(In_3SbTe_2)_x$ have been reported as thin films with optimized phase transition temperatures due to lower cation-anion binding energies in this phase.[14]

Quenched bulk samples of GST materials, in addition, have been shown to achieve high thermoelectric figures of merit *ZT*, e. g. up to 1.3 at 450 °C for metastable $(GeTe)_n(Sb_2Te_3)$ compounds with n = 12 and 19.[15,16] Their average crystal structure corresponds to a slightly distorted rocksalt type and is characterized by pronounced real-structure effect, especially intersecting vacancy layers perpendicular to the cubic <111> directions.

In this report we pursue the idea that IST may exhibit comparable real structure effects and properties. Neutron and X-ray diffraction are combined with TEM studies and the electrical and thermal transport properties of bulk samples are characterized.

3.2.2 Results and discussion

3.2.2.1 Crystal structure of the quenched high-temperature phase

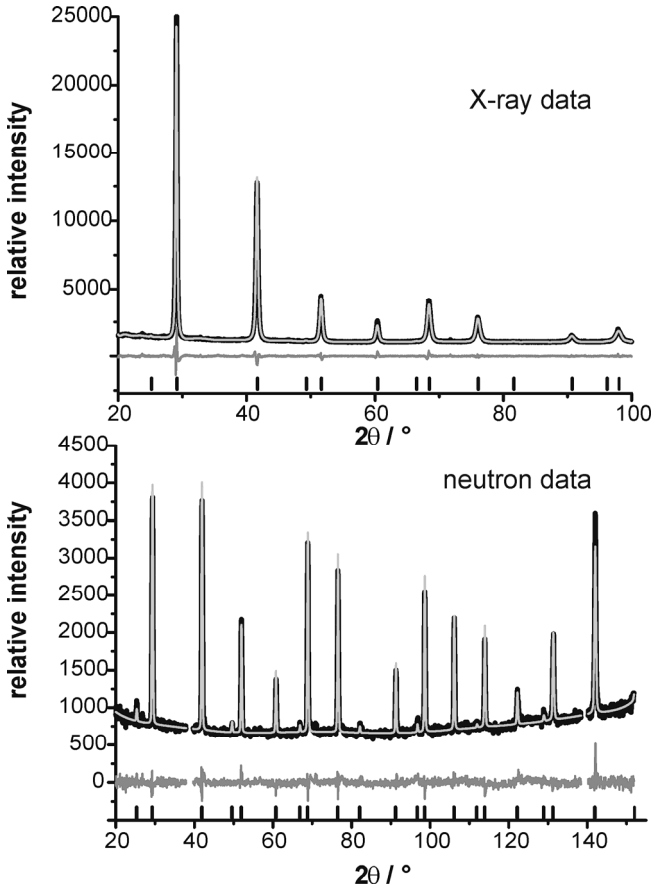

Fig. 1. Results of the joint Rietveld refinement on X-ray data (top, R_p = 0.0217, R_{wp} = 0.0311, R_{Bragg} = 0.0132, *GooF* = 1.166) and neutron data (bottom, R_p = 0.0409, R_{wp} = 0.0533, R_{Bragg} = 0.0533, *GooF* = 1.531) for In_3SbTe_2, experimental powder patterns (black), calculated data (light gray), difference plots (dark gray) and reflection positions (black vertical lines). Two parasitic reflections at 39° and 139° 2θ from the experimental setup in the neutron diffraction pattern were cut out.

Both the X-ray and neutron powder diffraction patterns of IST (cf. Fig. 1) can be indexed on the basis of the cubic face-centered unit cell reported for the high-temperature phase.[2] At first glance, the X-ray diffraction pattern indicates a simple cubic (α-Po type) structure model with random disorder of all elements as the NaCl type's reflections hkl with h, k, l = 2n+1 are very weak due to the similar electron count of the elements involved. They are evident in selected area electron diffraction (SAED) patterns (see below) and in neutron powder diffraction patterns. The latter are useful as the neutron scattering length of In (4.065 fm) is significantly different from those of Sb (5.57 fm) and Te (5.80 fm). The X-ray powder data were included in order to obtain precise lattice parameters. No deviation from the cubic metrics could be

observed and no superstructure reflections were found. A joint refinement on X-ray and neutron data confirms that the average structure corresponds to a rocksalt-type structure (space group $Fm\bar{3}m$, no. 225) with anion disorder. Refinement results for the occupancy factors depend on the treatment of the displacement parameters. However, all variants do not indicate significant antisite disorder of In. If a common displacement parameter for the anion and cation sites is used, the occupancy factor of In is 1.11(1); thus, the cation position can be assumed to be fully occupied by In. When the occupancies are set to the nominal composition, the cation position has a slightly larger displacement parameter than the anion site. For the refinement of the single crystal data; consequently, full occupancy of all sites was assumed, occupying the cation site with In. The occupancy factors for the anion site were set to $^1/_3$ for Sb and $^2/_3$ for Te in accordance with the nominal composition, which was verified by EDX (see Experimental Section). A common displacement parameter was refined for the atoms on the anion site, the larger one was assigned to In as derived from neutron data. Crystal data and refinement details are given in Table 1. The refined atom parameters are given in Table 2. Further details of the crystal structure investigation may be obtained from Fachinformationszentrum Karlsruhe, 76344 Eggenstein-Leopoldshafen, Germany (fax: (+49)7247-808-666; e-mail: crysdata@fiz-karlsruhe.de, http://www.fiz-karlsruhe.de /request_for_deposited_data.html) on quoting the depository number CSD-426338.

A reconstructed *hk*0 reciprocal lattice section shows diffuse intensity that interconnects the Bragg reflections (Figure 2). These broad streaks can also be observed in corresponding SAED patterns. They are obviously due to static displacements as the In-Sb distances differ from the In-Te distances. As the streaks run along <100>*, the displacements are predominantly along <100>. Such diffuse intensities are known from intermetallics like $Ni_{0.9}Al_{0.1}$ as well as from ferroelectrics like $PbZn_{0.33}Nb_{0.67}O_3$, although there they are sometimes accompanied by further short-range order effects or superstructure formation.[17-19] There is no significant intensity variation on the streaks; therefore displacements in IST exhibit no pronounced short-range order.

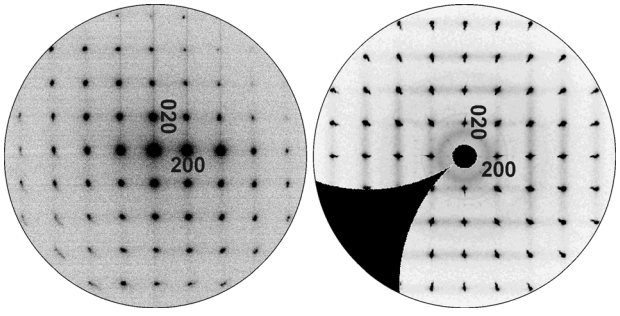

Fig. 2. SAED pattern of zone axis [100] (left) and *hk*0 reciprocal lattice section reconstructed from X-ray data of an In_3SbTe_2 single crystal selected from a crushed ingot (right).

Table 1. Crystal data and refinement details of the refinement of single crystal data of In_3SbTe_2.

Chem. formula	In_3SbTe_2
Asymmetric unit	$InSb_{0.33}Te_{0.67}$
Molar weight / g mol^{-1}	240.47
F(000)	402.7
Temperature / K	293(2)
Z	4
Crystal system	cubic
Lattice parameter / Å	6.1227(1) [c]
Cell volume / Å^3	229.525(11)
Space group	$Fm\bar{3}m$ (no. 225)
Calculated density / g cm^{-1}	6.96
Wavelength / Å	0.56085 (Ag-K□)
Absorption coefficient / mm^{-1}	11.6
2θ range	9.1° – 60.2°
Measured reflections	1245
R_{int} / R_σ	0.0539 / 0.0127
Independent reflections	56 (all with $I > 2\sigma(I)$)
Parameters / constraints	4 / 0
R_1 [a] (all reflections)	0.0259
wR_2 [b] (all reflections)	0.0690
GooF	1.305
Extinction coefficient	0.93(10)
$\Delta\rho_{max}$ / $\Delta\rho_{min}$	0.78 / –2.22

[a] $R1 = \Sigma|F_o - F_c|/\Sigma|F_o|$. [b] $wR2 = \Sigma[w(F_o^2 - F_c^2)^2]/[w(F_o^2)^2]]^{1/2}$; $w = 1/[\sigma^2(F_o^2) + (aP)^2 + bP]$ with $P = [Max(0, F_o^2) + 2F_c^2]/3$. [c] from powder data.

Table 2. Atom positions, occupancy factors and isotropic displacement factors (in Å^2) of In_3SbTe_2.

atom	Wyckoff pos.	*x y z*	*s.o.f.*	U_{iso}
In	4*a*	0 0 0	1	0.0219(3)
Sb/Te	4*b*	½ ½ ½	0.333 / 0.667	0.0166(4)

3.2.2.2 Thermal behavior

Quenched metastable IST is inert up to 320 °C (cf. Figure 3) and then decomposes into InSb and InTe in accordance with the phase diagram.[2] Figure 4 shows a Rietveld refinement for the pattern acquired at 400 °C. At this temperature, the decomposition is still incomplete; 34% InSb and 60% InTe coexist with 6% In_3SbTe_2. The ratio of InSb to InTe is approximately 1:2 as expected from the composition. During the whole heating experiment, the ternary phase never vanished completely, probably as the heating was too fast to reach an equilibrium state. At ~ 420 °C, the ternary cubic high-temperature phase is formed as a stable compound. Above 570 °C, the phase decomposes peritectically into a melt and InTe.

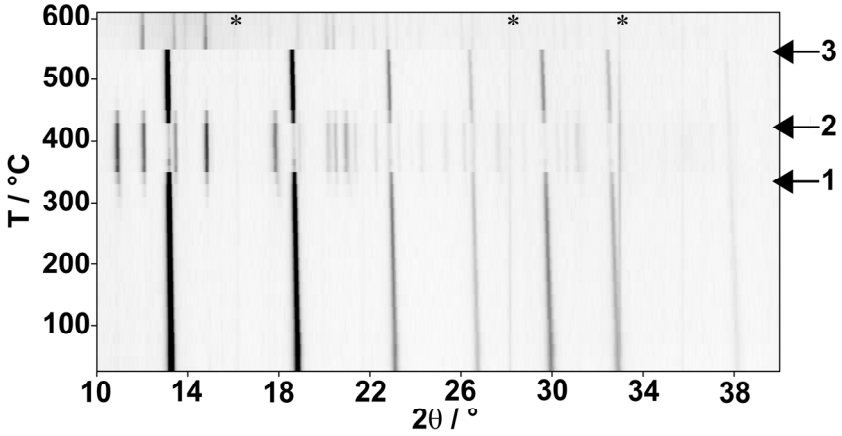

Fig. 3. Temperature-dependent powder X-ray diffraction patterns during the heating of quenched In_3SbTe_2; arrow 1 marks the temperature at which the decomposition into InSb and InTe begins; arrow 2 marks the temperature at which the transformation to the cubic high-temperature phase takes place; arrow 3 marks the temperature at which the peritectic reaction to InTe and melt begins; * marks reflections caused by the furnace.

3.2.2.3 Electron microscopy and diffraction

SAED patterns exhibit *d* values that correspond to those determined by X-ray diffraction, e. g. d_{200} = 3.08 Å ([100] zone axis, Figure 2, X-ray data: 3.06 Å) and d_{111} = 3.54 ([110] zone axis, Figure 5a, X-ray data: 3.54 Å). The SAED patterns of the [100] zone axis (cf. Figure 2, left) resemble the X-ray diffraction pattern (cf. Figure 2, right) with diffuse intensities along <100>*. The corresponding displacements are too small to have a significant impact on HRTEM images. In contrast, most SAED patterns of zone axis [110] show no diffuse intensities; however, additional reflections are occasionally observed along <111>* which seem to indicate a threefold superstructure (Figure 5b). In some SAED patterns (e.g. Figure

5c), there are diffuse streaks between the NaCl-type reflections and the additional ones along <111>*. HRTEM investigations furthermore prove the presence of domains with varying orientations as shown in Figure 6.

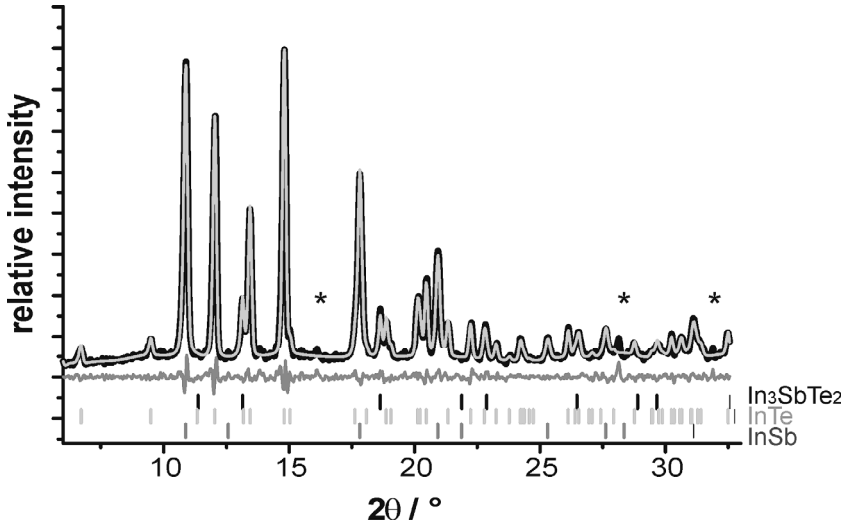

Fig. 4. Rietveld fit of X-ray data for In_3SbTe_2 (R_p = 0.0583, R_{wp} = 0.0767, R_{Bragg} = 0.0141, *GooF* = 3.310) at 400 °C: experimental powder pattern (black), calculated pattern (light gray), difference plot (dark gray), peak positions of IST (black; straight lines), InSb (dark gray; straight lines) and InTe (light gray; straight lines); reflections caused by the furnace are marked with *.

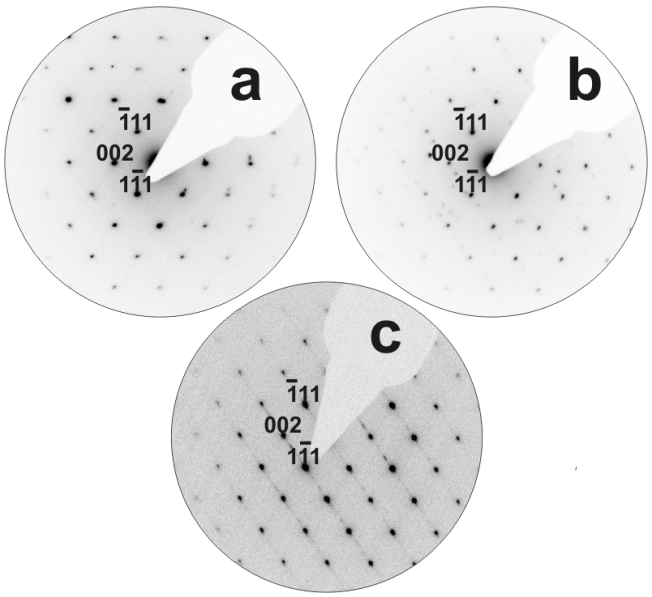

Fig. 5. SAED patterns of zone axis [110] of different crystallites of In_3SbTe_2.

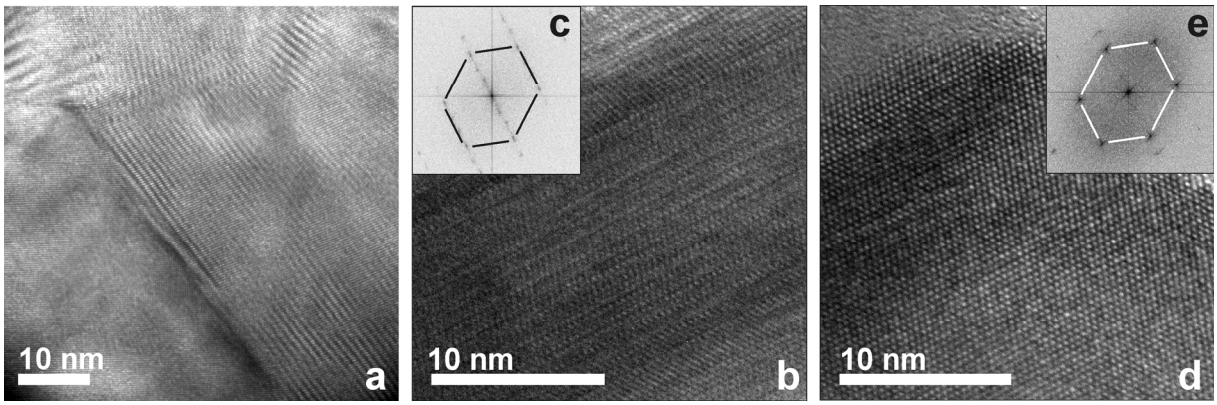

Fig. 6. HRTEM image of intergrown domains in In_3SbTe_2: overview (a, arbitrary orientation) and further images from the same particle (b and d, orientation corresponding to the zone axis [110] of the cubic domain) with Fourier transforms (c, e) whose superposition corresponds to the SAED shown in Figure 5c.

Fourier transforms of HRTEM images from different regions of a crystallite show that the additional reflections along <111>* result from the coexistence of domains with the cubic structure ($Fm\bar{3}m$, a = 6.125) and domains with 3 times larger d values (~ 11.0 Å) along one of the cubic <111>* directions. The measurement of d values in the overlapping SAED pattern, as a consequence, yields a slight rhombohedral distortion ($d_{\bar{1}11}$ = 3.66 Å and $d_{1\bar{1}1}$ = 3.70 Å, pseudocubic indexing). EDX measurements indicate that the composition of several domains with the metrics of In_3SbTe_2 is close to the expected nominal composition $In_{50}Sb_{16.6}Te_{33.3}$ (TEM-EDX: $In_{55(2)}Sb_{14.4(9)}Te_{30(3)}$; average from three point analyses). These are intergrown with InTe-rich domains (TEM-EDX: $In_{65(4)}Sb_{1.2(2)}Te_{34(5)}$; average from three point analysis) that exhibit a d-value of ~ 9.05 Å close to that of InTe (a = 8.44 Å). InSb-rich areas have also been detected (TEM-EDX: $In_{62(3)}Sb_{32(3)}Te_{6.0(3)}$; average from three point analysis). The compositions given for the InTe- and InSb-rich areas are rough approximations as the electron beam cannot be focused exclusively on one domain. In conclusion, the metastable phase obviously decomposes upon electron irradiation and forms InTe, probably doped with Sb (which would explain the larger d-values). Therefore, the apparent "superstructure reflections" (Figure 5 b and c) result from intergrowth phenomena rather than from Sb/Te ordering.

3.2.2.4 Thermoelectric properties

Metastable quenched IST exhibits a rather high thermal conductivity (κ) of ~ 23 W/Km between RT and 250 °C (Figure 7, bottom), i. e. below the decomposition temperature. This

high κ is primarily caused by the high electrical conductivity (σ) (Fig.7, top); the phononic contribution can be neglected. IST is a metal with σ = ~ 32500 S/cm at roomtemp., one order of magnitude higher than the reported value (1389 S/cm) for IST with InSb impurities.[2] σ decreases almost linearly with respect to the temperature up to the decomposition at 320 °C. After the decomposition the slope is flatter. Upon cooling, σ slightly increases towards lower temperature; however, the absolute value for the decomposed sample is about 3 times smaller than the one for metastable IST. The absolute values of the Seebeck coefficient (S) (Fig. 7, second from top) are very low (~ -3 µV/K at 450 °C) as expected for good metals over the entire temperature range. The low S in combination with the high κ leads to very low ZT values. After the decomposition, the κ measurements were repeated (Fig.7, bottom); the absolute values of κ of the decomposed sample are about 6 W/Km smaller than the one of the metastable phase and remain almost constant at ~ 15 W/Km. The high values for σ and κ are probably caused by InTe which is formed upon decomposition and is a good electrical conductor.[20]

3.2.3 Conclusion

The average structure of IST corresponds to a rocksalt-type structure with Sb and Te randomly disordered on the anion position. Neutron data gave no indication of anti-site disorder and electron microscopy gave no indication of superstructure formation; additional reflections can be explained by the formation of (probably Sb-doped) InTe upon electron irradiation. Diffuse intensities in both reciprocal lattice sections from single crystal diffraction and SAED patterns indicate displacements of the atoms from the average positions, predominantly along <100>, as a consequence of the different sizes of Sb and Te. IST is a metal; therefore, ionic concepts do not apply and it can formally be understood as $(In^{3+})_3Sb^{3-}(Te^{2-})_2 \cdot 2e^-$. According the Wiedemann-Franz law, high electrical conductivity leads to a high thermal conductivity. In combination with the low Seebeck coefficient this material is not suited for thermoelectric applications. Below 420 °C, the stable state corresponds to a mixture of InSb and InTe. Even the decomposed compound still exhibits rather high thermal and electrical conductivities, because one of the phases formed is InTe, a good metal. However, forming heterostructures with other rocksalt-type tellurides with low electrical conductivities might be a possibility to use IST for improving thermoelectric materials.

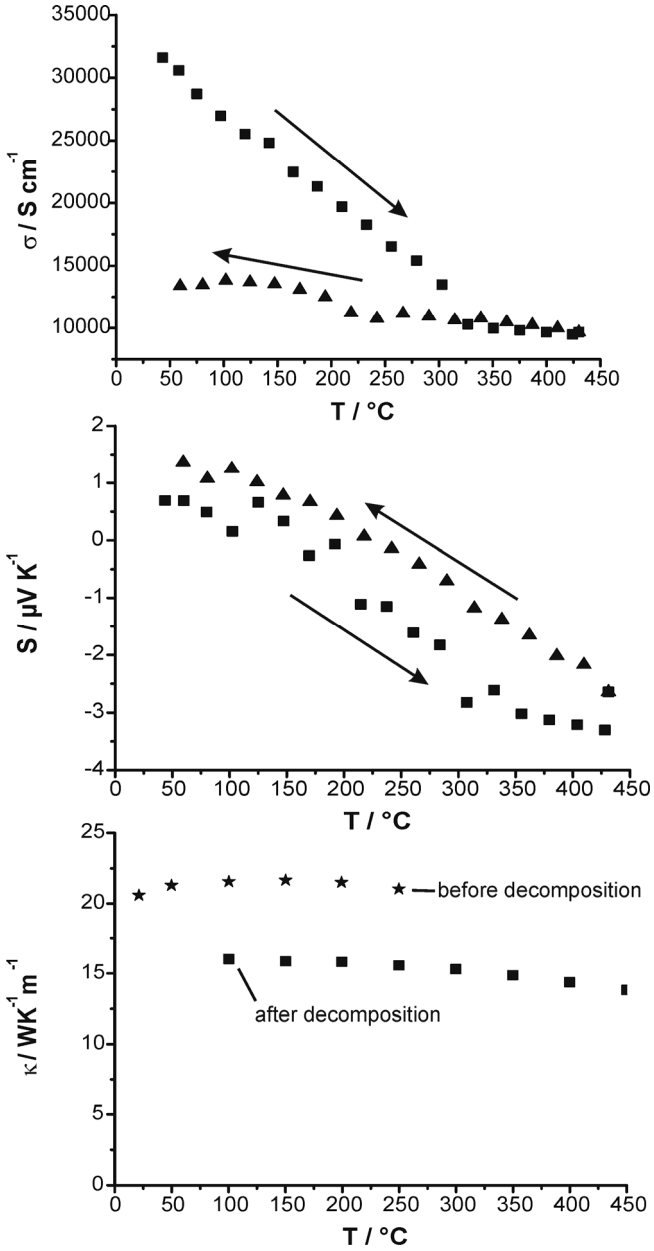

Fig. 7. Electrical conductivity (top) measured from RT to 450 °C up (■) and down (▲), Seebeck coefficient (middle) measured from RT to 450 °C up (■) and down (▲) and thermal conductivity (bottom) measured from RT to 250 °C before (★) and from RT to 450 °C after (■) decomposition, respectively.

3.2.4 Experimental Section

Synthesis

Bulk samples of In_3SbTe_2 (IST) were prepared by melting stoichiometric mixtures (e. g. 2 g) of the pure elements (indium 99.999%, Smart Elements; antimony 99.9999%, Smart Elements; tellurium 99.999 %, Alfa Aesar) in sealed silica glass ampoules at 950 °C under argon atmosphere. The resulting melts were quenched to room temperature (RT) and

subsequently annealed at 450 °C (i. e., in the stability range of the IST high-temperature phase) for 4 weeks to ensure homogeneity. After annealing, the ingots were quenched to RT in order to avoid eutectoid decomposition. Shorter annealing times led to impurities of InSb and InTe. Single crystals were selected out of crushed bulk samples.

Diffraction methods

X-ray powder patterns of representative pieces of crushed bulk samples, which were fixed on Mylar foils using vacuum grease, were recorded on a Huber G670 Guinier camera equipped with a fixed imaging plate and integrated read-out system using Cu-$K_{\alpha 1}$ radiation (Ge monochromator, λ = 1.54051 Å).

For measurements of temperature-dependent powder diffraction patterns, a STOE Stadi P powder diffractometer with Mo-$K_{\alpha 1}$ radiation (Ge monochromator, λ = 0.71093 Å) in a modified Debye–Scherrer geometry was used. It was equipped with an imaging-plate detector system. The powdered samples were filled into silica glass capillaries with 0.3 mm diameter (sealed with vacuum grease under argon atmosphere) and heated up to 600 °C in a graphite furnace with a heating rate of 10 K/min.

Neutron powder diffraction patterns were acquired on the SPODI diffractometer at the neutron source FRM II in Munich (λ = 1.5484 Å, detector array of 80 position-sensitive ^{3}He tubes with 300 mm active height, fixed Soller collimators of 10’ horizontal divergence). The angular range of $0° < 2\theta < 155°$ was covered by stepwise positioning of the detector array to obtain a diffraction pattern of 0.05° step width (2°/40 steps). The crushed sample (~ 3.0 g) was filled into niobium crucibles which caused two parasitic reflections at 39° and 139° 2θ; the respective parts of the pattern were discarded.

The phase homogeneity, lattice parameters and occupancy factors were determined by a joint Rietveld refinement of X-ray and neutron powder diffraction data using the program TOPAS (details are given in the Results and Discussion section).[21]

For single-crystal X-ray diffraction, the crystal quality was checked by Laue photographs using a Buerger precession camera. Intensity data was collected with a STOE IPDS-I diffractometer equipped with an imaging-plate detector using Ag-K_{α} radiation (graphite monochromator, λ = 0.56085 Å). Reciprocal lattice sections were calculated and numerical absorption correction was performed using the diffractometer software. The full-matrix least-squares refinement of the final model was performed with SHELXL-97.[22]

Electron microscopy and X-ray spectroscopy

EDX (energy dispersive X-Ray) spectra of IST were recorded using a JSM-6500F (Jeol, USA) scanning electron microscope with EDX detector (model 7418, Oxford Instruments, Great Britain). The results of 5 point analyses on fragments of the ingot and of a 3 point analyses for the single crystal, respectively, were averaged and the errors were estimated from their variance. The analyses agree well with the composition of the starting mixture – atom-% calculated for In_3SbTe_2 / sample fragments / single crystal: In 50 / 49.4(1) / 50.5(3); Sb 16.7 / 17.4(3) / 16.5(10); Te: 33.3 / 33.1(3) / 32.9(8).
For transmission electron microscopy, finely ground samples were dispersed in ethanol and distributed on copper grids coated with a holey carbon film (S166-2, Plano GmbH, Germany). The grids were fixed on a double-tilt holder (tilt range ±30°). Selected area electron diffraction (SAED), high resolution transmission electron micrographs (HRTEM) and additional EDX measurements were obtained on a Titan 80-300 (FEI, USA) with a field emission gun operated at 300 kV. It was equipped with a TEM TOPS 30 EDX spectrometer (EDAX, Germany); images were recorded using an UltraScan 1000 camera (Gatan, USA, resolution: 2k x 2k). HRTEM and SAED data were evaluated using the programs Digital Micrograph[23] and EMS,[24] EDX data were processed with ES Vision.[25]

Electrical and thermal transport measurements

With respect to the kinetical stability regions of the metastable phase, the thermal diffusivity D_{th} was initially measured between room temperature and 250 °C using a laser-flash apparatus (LFA 427, Netzsch GmbH & Co., Germany). The thermal conductivity κ was calculated according to $\kappa = D_{th} \cdot \rho \cdot C_p$. For the evaluation of this first measurement, the heat capacity C_p was measured using a differential scanning calorimeter (DSC 404, Netzsch GmbH & Co., Germany). The density ρ was determined by means of a Mohr's balance. Subsequently, the Seebeck coefficient S and the electrical conductivity σ were measured up to 450 °C under He using a custom built setup of the DLR (Cologne, Germany). This system measures the electrical conductivity in four-point inline geometry concurrently with the Seebeck coefficient. Details about measurement procedure, reference measurements and employed hardware can be found in ref.[26] while details about the Seebeck coefficient data analysis can be found in ref.[27]. As a further step, the measurements of D_{th} and C_p were repeated up to 450 °C in order to calculate κ after decomposition of IST.

Acknowledgement

We thank C. Minke for SEM operation and EDX analyses and T. Miller for the temperature-dependent powder diffraction experiments and single crystal measurements. M. Hölzel and S. Schwarzmüller are acknowledged for help with the neutron diffraction experiments. We are grateful to Prof. Dr. W. Schnick for his generous support of this study. This investigation was funded by the Deutsche Forschungsgemeinschaft (grant OE530/1-2) and the Studienstiftung des deutschen Volkes.

References

[1] D. T. Morelli, V. Jovovic, J. P. Heremans, *Phys. Rev. Lett.* **2008**, *101*, 035901.

[2] K. Deneke, A. Rabenau, *Z. Anorg. Allg. Chem.* **1964**, *333*, 201.

[3] C. S. Kim, J. Y. Lee, Y. T. Kim, *Appl. Phys. Lett.* **2012**, *100*, 151903.

[4] A. Rabenau, K. Deneke, M. M. van der Meij, *Angew. Chem. Int. Ed.* **1964**, *3*, 588.

[5] E. T. Kim, J. Y. Lee, Y. T. Kim, *Phys. Status Solidi (RRL)* **2009**, *3*, 103.

[6] Y. I. Kim, E. T. Kim, J. Y. Lee, Y. T. Kim, *Appl. Phys. Lett.* **2011**, *98*, 091915.

[7] S. Raoux, R. M. Shelby, J. Jordan-Sweet, B. Munoz, M. Salinga, Y.-C. Chen, Y.-H. Shih, E.-K. Lai, M.-H. Lee, *Microelectron. Eng.* **2008**, *85*, 2330.

[8] T. Matsunaga, Y. Umetani, N. Yamada, *Phys. Rev. B* **2001**, *64*, 184116.

[9] T. Matsunaga, J. Akola, S. Kohara, T. Honma, K. Kobayashi, E. Ikenaga, R. O. Jones, N. Yamada, M. Takata, R. Kojima, *Nature Mater.* **2011**, *10*, 129.

[10] W. Bensch, M. Wuttig, *Chem. Unserer Zeit* **2010**, *44*, 92.

[11] S. Raoux, *Annu. Rev. Mater. Res.* **2009**, *39*, 9.

[12] T. Matsunaga, H. Morita, R. Kojima, N. Yamada, K. Kifune, Y. Kubota, Y. Tabata, J.-J. Kim, M. Kobata, E. Ikenaga, K. Kobayashi, *J. Appl. Phys*. **2008**, *103*, 093511.

[13 K. Wang, C. Steimer, D. Wamwangi, S. Ziegler, M. Wuttig, *Appl. Phys. A: Mater. Sci. Process.* **2005**, *80*, 1611.

[14] A. Benayad, Y. S. Kang, H.-J. Shin, K. Kim, D.-S. Suh, K. J. Kim, C. K. Kim, T.-Y. Lee, J.-S.Noh, J. C. Lee, Y. H. Khang, *J. Appl. Phys.* **2009**, *106*, 043701.

[15] M. N. Schneider, T. Rosenthal, C. Stiewe, O. Oeckler, *Z. Kristallogr.* **2010**, *225*, 463.

[16] T. Rosenthal, M. N. Schneider, C. Stiewe, M. Döblinger, O. Oeckler, *Chem. Mater.* **2011**, *23*, 4349.

[17] M. Pasciak, T. R. Welberry, *Z. Kristallogr.* **2011**, *226***,** 113.

[18] T. R. Welberry, D. J. Goossens, *Acta Crystallogr. Sect. A* **2008**, *64*, 23.

[19] I. B. Ramsteiner, A. Schöps, H. Reichert, H. Dosch, V. Honkimäki, Z. Zhong, J. B. Hastings, *Acta Crystallogr. Sect. A* **2009**, *42*, 392.

[20] M. D. Banus, R. E. Hanneman, M. Strongin, K. Tooen, *Science* **1963**, *142,* 662.

[21] *TOPAS-Academic*, *V. 4.1*, Coelho Software, Brisbane, Australia, **2007**.

[22] G. M. Sheldrick, *Acta Crystallogr. Sect. A* **2008**, *64*, 112.

[23] *DigitalMicrograph 3.6.1*, Gatan Software, Pleasanton, USA, **1999**.

[24] P. A. Stadelmann, *Ultramicroscopy* **1987**, *21*, 131.

[25] *ESVision*, *4.0.164*, Emispec Systems Inc., Tempe, USA, **1994-2002**.

[26] J. de Boor, C. Stiewe, P. Ziolkowski, T. Dasgupta, G. Karpinski, E. Lenz, F. Edler, E. Müller, *J. Electron. Mater.* **2013**, *42*, 1711.

[27] J. de Boor, E. Müller, *Rev. Sci. Instrum.* **2013**, *84*, 065102.

3.3 Nanostructures in Te/Sb/Ge/Ag (TAGS) thermoelectric materials induced by phase transitions associated with vacancy ordering

Thorsten Schröder, Tobias Rosenthal, Nadja Giesbrecht, Markus Nentwig, Stefan Maier, Heng Wang, G. Jeffrey Snyder, Oliver Oeckler

Inorg. Chem. **2014**, *53*, 7722 – 7729.

Abstract

Te/Sb/Ge/Ag (TAGS) materials with rather high concentrations of cation vacancies exhibit improved thermoelectric properties as compared to corresponding conventional TAGS (with constant Ag/Sb ratio of 1) due to a significant reduction of the lattice thermal conductivity. There are different vacancy ordering possibilities depending on the vacancy concentration and the history of heat treatment of the samples. In contrast to the average α-GeTe-type structure of TAGS materials with cation vacancy concentrations < ~3%, quenched compounds like $Ge_{0.53}Ag_{0.13}Sb_{0.27}\square_{0.07}Te_1$ and $Ge_{0.61}Ag_{0.11}Sb_{0.22}\square_{0.06}Te_1$ exhibit "parquet-like" multi-domain nanostructures with finite intersecting vacancy layers. These are perpendicular to the pseudo-cubic <111> directions but not equidistantly spaced, comparable to the nanostructures of compounds $(GeTe)_nSb_2Te_3$. Upon heating, the nanostructures transform into long-periodically ordered trigonal phases with parallel van der Waals gaps. These phases are slightly affected by stacking disorder but distinctly different from the α-GeTe-type structure reported for conventional TAGS materials. Deviations from this structure type are evident only from HRTEM images along certain directions or very weak intensities in diffraction patterns. At temperatures above ~ 400 °C, a rocksalt-type high-temperature phase with statistically disordered cation vacancies is formed. Upon cooling, the long-periodically trigonal phases are reformed at the same temperature. Quenched nanostructured $Ge_{0.53}Ag_{0.13}Sb_{0.27}\square_{0.07}Te_1$ and $Ge_{0.61}Ag_{0.11}Sb_{0.22}\square_{0.06}Te_1$ exhibit ZT values as high as 1.3 and 0.8, respectively, at 160 °C, which is far below the phase transition temperatures. After heat treatment, i. e. without pronounced nanostructure and when only reversible phase transitions occur, the ZT values of $Ge_{0.53}Ag_{0.13}Sb_{0.27}\square_{0.07}Te_1$ and $Ge_{0.61}Ag_{0.11}Sb_{0.22}\square_{0.06}Te_1$ with extended van der Waals gaps amount to 1.6 at 360 °C and 1.4 at 410 °C, respectively, which is at the top end of the range of high-performance TAGS materials.

3.3.1 Introduction

Facing the current energy problems, many ways of increasing the efficiency of energy transformation processes have been evaluated, among them the interconversion of heat and electrical energy by thermoelectric materials. Their efficiency is characterized by the dimensionless figure of merit $ZT = S^2\sigma T/\kappa$ (with the Seebeck coefficient S, the electrical conductivity σ, the temperature T and the thermal conductivity κ). At moderately high temperatures between 150 and 600 °C, chalcogenides with high ZT values are the materials of choice.[1] Many different materials, e. g. tellurides with rocksalt-type structure like $AgSbTe_2$[2,3] or $AgIn_xSb_{1-x}Te_2$[4,5] as well as heterogeneous $(PbTe)_mAgSbTe_2$ (LAST)[6] materials were recently investigated, along with chalcogenides derived from the sphalerite structure type, such as $Cu_2Zn_{1-x}Fe_xGeSe_4$,[7] $CuGaTe_2$,[8,9] or $CuInTe_2$.[10] The so-called TAGS-x materials $(GeTe)_x(AgSbTe_2)_{100-x}$, which crystallize in the α-GeTe structure type at ambient conditions and exhibit rocksalt-type high-temperature (HT) phases represent some of the classical and best characterized thermoelectric materials with ZT values above 1.[11-14] They can be understood as quasi-binary solid solutions between $AgSbTe_2$ and GeTe[15,16] and reach ZT values of up to 1.7 at 500 °C.[17] In order to optimize the thermoelectric properties of TAGS, many different substitution variants were investigated, e. g. Ge^{2+} was replaced by Sn^{2+} in $(SnTe)_xAgSbTe_2$,[18] Ag^+ by Li^+ in $(GeTe)_x(LiSbTe_2)_2$[19] and Sb^{3+} by In^{3+} in $(GeTe)_xAgInTe_2$ and $(GeTe)_xAgIn_{0.5}Sb_{0.5}Te_2$.[20] Even doping with rare earth metals was considered.[21,22] Extending the compositional range of TAGS materials beyond pseudobinary solid solutions $(GeTe)_x(AgSbTe_2)_{100-x}$ leads to compounds $(GeTe)_x[(Ag_2Te)_y(Sb_2Te_3)_{1-y}]_{100-x}$,[23] where the Ag/Sb ratio is variable. This approach leads to improved thermoelectric properties in high-performance TAGS materials like $(GeTe)_{85}(Ag_ySbTe_{y/2+1.5})_{15}$, where the thermal conductivity is reduced without significantly affecting the electrical conductivity[24] and the power factor is increased due to an optimized charge carrier concentration without decreasing the carrier mobility.[25,26] This extension involves cation vacancies for all values of $y < 1$, because y atoms of Ag but only y/2 atoms of Te are removed as compared to TAGS-x, which results in a larger number of anions than cations. The impact and the ordering possibilities of cation vacancies have not been taken into consideration so far in the literature. In compounds $(GeTe)_nSb_2Te_3$ (n = 12, 19), which correspond to TAGS $(GeTe)_x(Ag_ySbTe_{y/2+1.5})_{100-x}$ with $y = 0$ and consequently exhibit maximal cation vacancy concentrations, different cation vacancy ordering motifs were described, depending on the composition (n) and the thermal treatment.[27] Upon quenching,

these compounds $(GeTe)_nSb_2Te_3$ form metastable pseudo-cubic phases in contrast to the α-GeTe-type structure of vacancy-free TAGS, whose cubic HT phase cannot be retained at ambient temperature by quenching as the phase transition is displacive. The reason for the formation of such pseudo-cubic structures lies in their "parquet-like" nanoscale domain structures produced by short-range vacancy ordering in layers perpendicular to the cubic <111> directions.[28] These layers are not equidistantly spaced, which results in diffuse streaks along <111>* in diffraction patterns. Upon heating, the atoms next to the vacancy layers rearrange to form extended parallel van der Waals gaps. Stacking disorder is typical and results in an α-Hg-type average structure. At higher temperatures (typically above ~500 °C), a rocksalt-type HT phase with randomly disordered cation vacancies is formed. If this is slowly cooled, the above mentioned trigonal phase is formed.

The formation of comparable "parquet-like" nanostructures can be expected to be beneficial for the thermoelectric properties of high-performance TAGS materials, too, although the existence of multiple phase transitions might be a drawback for the thermal cycling behavior of these materials. In the present work, the effects of the cation vacancy concentration on the structure, stability and properties of TAGS materials with cation vacancies are studied.

3.3.2 Experimental

Synthesis

Samples with the nominal compositions $Ge_{0.53}Ag_{0.13}Sb_{0.27}Te_1$, $Ge_{0.61}Ag_{0.11}Sb_{0.22}Te_1$ and $Ge_{0.77}Ag_{0.07}Sb_{0.13}Te_1$ were synthesized by melting stoichiometric mixtures (typically 2.0 g) of the pure elements (silver 99.9999%, Alfa Aesar; germanium 99.999%, Sigma-Aldrich; antimony 99.9999%, Smart Elements; tellurium 99.999 %, Alfa Aesar) at 900 °C under Ar atmosphere in silica glass ampoules for 1 day and subsequently quenching the ampoules to room temperature (RT) by removing from the furnace. The samples were then annealed at 500 °C for 3 days and again quenched to RT in the same fashion. Samples for thermoelectric characterization were synthesized in the same manner; however, larger ampoules (diameter 1.2 cm) with a flat bottom were used to quench the melts in order to obtain ingots with dimensions as required for the measurements. The disc-shaped ingots were subsequently ground down until the round faces were parallel and finally polished. For these discs, homogeneity and absence of side phases were verified in the same manner as for all samples; the synthesis is well reproducible.

Diffraction methods

A Huber G670 Guinier camera equipped with a fixed imaging plate and integrated read-out system using Cu-$K_{\alpha 1}$ radiation (Ge(111) monochromator, λ = 1.54051 Å) was used for the collection of powder X-ray diffraction (PXRD) patterns of representative parts of the crushed samples, which were fixed between two Mylar foils using vacuum grease. A STOE Stadi P powder diffractometer equipped with an imaging-plate detector system using Mo-$K_{\alpha 1}$ radiation (Ge(111) monochromator, λ = 0.71093 Å) in a modified Debye–Scherrer geometry equipped with a graphite furnace was used for the collection of temperature-dependent powder diffraction patterns from RT to 600 °C with a heating rate of 10 K/min and from 600 °C back to RT with cooling rate of 5 K/min (faster cooling is impossible with the setup used). For these temperature-dependent measurements, powdered samples were filled into silica glass capillaries (0.3 mm diameter), which were then sealed with vacuum grease under argon atmosphere. Rietveld refinements were carried out using the program TOPAS,[29] phase homogeneity and the temperature-dependent powder diffraction patterns were evaluated using WINXPOW.[30]

Electron microscopy, diffraction and X-ray spectroscopy

X-ray spectra of representative parts of the samples were recorded with an energy dispersive X-ray (EDX) detector (model 7418, Oxford Instruments, Great Britain) mounted on a JSM-6500F (Jeol, USA) scanning electron microscope (SEM). The results of 6 point analyses were averaged. Detailed results are given in Table S1 in the Supplementary Information.
Finely ground samples were dispersed in ethanol and distributed on copper grids coated with holey carbon film (S166-2, Plano GmbH, Germany) for high-resolution transmission electron microscopy (HRTEM). The copper grids were subsequently fixed on a double-tilt holder and investigated in a Titan 80-300 (FEI, USA) equipped with a TEM TOPS 30 EDX spectrometer (EDAX, Germany) and a field-emission gun operated at 300 kV. Selected-area electron diffraction (SAED) patterns and HRTEM images were recorded using an UltraScan 1000 camera (Gatan, USA, resolution 2k x 2k). The Digital Micrograph[31] and EMS software packages[32] were used for HRTEM and SAED data evaluation; EDX data were evaluated with ES Vision.[33]

Thermoelectric characterization

For the characterization of the thermoelectric properties of $Ge_{0.53}Ag_{0.13}Sb_{0.27}\square_{0.07}Te_1$ and $Ge_{0.61}Ag_{0.11}Sb_{0.22}\square_{0.06}Te_1$ between 50 °C and 450 °C, three samples of each composition were synthesized as irreversible phase transitions (see thermal behavior section) were expected, which affect the transport properties. In order to obtain reliable ZT values for quenched samples at low temperatures, i. e. where the nanostructure is inert, each property was measured using a sample that had not undergone previous heating cycles. All analytical methods applied did not indicate any differences between samples with the same composition and thermal treatment. The electrical conductivity σ was measured in-plane using pressure-assisted Nb contacts in an in-house built facility at Caltech[34] using the van der Pauw method[35] (heating rate 150 K/h, measurement in 50 K steps). A LFA457 MicroFlash (Netzsch, Germany) laser flash system was used for the out-of-plane measurement the thermal diffusivity D_{th}. The thermal conductivity was calculated as $\kappa = D_{th} \cdot C_p \cdot \rho$ where C_p is the heat capacity calculated cording to the Dulong-Petit approximation, which has turned out to be valid for telluride thermoelectric materials in the temperature range investigated; in such cases experimental values affected by baseline shifts may lead to a larger uncertainty than the theoretical values,[36] i. e., 0.226 J/gK for $Ge_{0.53}Ag_{0.13}Sb_{0.27}\square_{0.07}Te_1$ and 0.230 J/gK for $Ge_{0.61}Ag_{0.11}Sb_{0.22}\square_{0.06}Te_1$ (ρ = density determined by weighing the sample and measuring its dimensions). The Seebeck coefficient S was determined out-of-plane using Chromel-Nb thermocouples in steps of 61 K at a heating rate of 150 K/h and a temperature oscillation rate of ± 7.5 K.[37] The combined uncertainty of the measurements is ca. 20% for the ZT value.

3.3.3 Results and discussion

3.3.3.1 Overview and sample characterization

In principle, there are three ways (and combinations of them) of introducing cation vacancies (□) in TAGS materials without affecting the overall charge neutrality: (1) the exchange of 1 Ag^+ by 0.5 Ge^{2+} and 0.5 □, (2) the exchange of 1 Ag^+ by 1/3 Sb^{3+} and 2/3 □ and (3) the exchange of 1 Ge^{2+} by 2/3 Sb^{3+} and 1/3 □. These different possibilities make it difficult to maintain the widespread TAGS-x nomenclature (with x given by $(GeTe)_x(AgSbTe_2)_{100-x}$). For example, $Ge_{0.53}Ag_{0.13}Sb_{0.27}\square_{0.07}Te_1$ may be written as $Ge_4AgSb_2Te_{7.5}$, which on the one hand could be understood as a variant of TAGS-80 = $(GeTe)_{80}(AgSbTe_2)_{20}$ = $(GeTe)_4AgSbTe_2$ =

$Ge_4AgSbTe_6$ with additional 0.5 Sb_2Te_3 per formula unit, on the other hand it can also be viewed as TAGS-85 = $(GeTe)_{85}(AgSbTe_2)_{15} \approx (GeTe)_{5.5}AgSbTe_2 = Ge_{5.5}AgSbTe_{7.5}$ with 1.5 Ge^{2+} being replaced by 1 Sb^{3+}. Therefore, the comparison of vacancy-containing compounds with conventional TAGS-x is not unequivocal. Similarly, a given vacancy concentration is not sufficient to characterize modified TAGS materials, because there are different element combinations that correspond to the same amount of cation vacancies. For the sake of clarity, we use normalized formulas that immediately show the vacancy concentration as a consequence of the site occupancies in possibly distorted rocksalt-type structures that are characteristic for all compounds discussed here: they exhibit just one cation and one anion position. For example $Ge_4AgSb_2Te_{7.5}$ is written as $Ge_{0.53}Ag_{0.13}Sb_{0.27}\square_{0.07}Te_1$.
Many experiments have shown that all of these variations lead to single-phase samples as long as charge neutrality is not violated. If the anion and cation charges are not balanced, binary side phases or remaining elemental Ge or Te are observed. All samples discussed in this manuscript are single-phase as shown by Rietveld refinements (cf. next section), typically the weight of the ingot differs from that of the mixture of starting materials by less than 1%. The composition and homogeneity are further confirmed by SEM-EDX results (cf. Table S1 in the Supplementary Information).

3.3.3.2 Crystal structures of the quenched compounds

All reflections in the PXRD patterns of $Ge_{0.53}Ag_{0.13}Sb_{0.27}\square_{0.07}Te_1$ and $Ge_{0.61}Ag_{0.11}Sb_{0.22}\square_{0.06}Te_1$ can be indexed assuming the rocksalt type's cubic metrics. In contrast, reflection splitting indicates that $Ge_{0.77}Ag_{0.07}Sb_{0.13}\square_{0.03}Te_1$ is rhombohedral; the unit cell corresponds to the α-GeTe type. The latter compound is discussed in order to demonstrate the influence of the vacancy concentration on the average structure in the case of high Ge contents; however, it was not further characterized as its expected low Seebeck coefficient (already lowered for $Ge_{0.53}Ag_{0.13}Sb_{0.27}\square_{0.07}Te_1$ compared to $Ge_{0.61}Ag_{0.11}Sb_{0.22}\square_{0.06}Te_1$; see thermoelectric properties section) precludes promising thermoelectric properties. Rietveld refinements for $Ge_{0.53}Ag_{0.13}Sb_{0.27}\square_{0.07}Te_1$ and $Ge_{0.61}Ag_{0.11}Sb_{0.22}\square_{0.06}Te_1$ confirm the presence of rocksalt-type average structures. In order to exclude rhombohedral structures with pseudocubic metrics, which have been reported in the Ag/Ge/In/Sb/Te system,[20] various test refinements were performed. Layer formation like in α-GeTe reduces the symmetry from $Fm\bar{3}m$ to $R3m$. A measure of this layer formation is the z parameter of the cations which is

0.5 in the trigonal setting of the cubic unit cell. No significant deviations from this value were detected. In the final refinements, common atom coordinates and displacement parameters were refined for all cations. Cation site occupancies were taken from the nominal composition and not refined; tentative refinements did not indicate significant changes. The Te anion position was assumed as completely occupied with an independent displacement parameter. For the refinements in the space group *R*3*m*, preferred orientation was considered as a flat sample holder was used (4^{th} order spherical harmonics with 3 parameters). The profile fits are depicted in Fig. 1, the results of the refinement and the atomic parameters are given in Tables 1 and 2, respectively. Further details of the crystal structure investigations may be obtained from Fachinformationszentrum Karlsruhe, 76344 Eggenstein-Leopoldshafen, Germany (fax: (+49)7247-808-666; e-mail: crysdata@fiz-karlsruhe.de, http://www.fiz-karlsruhe.de/request_for_deposited_data.html) on quoting the depository numbers CSD 427403, 427405 and 427404 for $Ge_{0.53}Ag_{0.13}Sb_{0.27}\square_{0.07}Te_1$, $Ge_{0.61}Ag_{0.11}Sb_{0.22}\square_{0.06}Te_1$ and $Ge_{0.77}Ag_{0.07}Sb_{0.13}\square_{0.03}Te_1$, respectively.

The rocksalt-type average structure of $Ge_{0.53}Ag_{0.13}Sb_{0.27}\square_{0.07}Te_1$ and $Ge_{0.61}Ag_{0.11}Sb_{0.22}\square_{0.06}Te_1$ is an uncommon observation for TAGS materials, because usually it is not possible to quench their cubic HT phase due to the displacive character of the phase transition. This hints at the crucial role of cation vacancy ordering in the compounds investigated (see below). With increasing GeTe content, the lattice parameter decreases. In addition to the metrics indicated by reflection splitting, the α-GeTe type structure of $Ge_{0.77}Ag_{0.07}Sb_{0.13}\square_{0.03}Te_1$ is corroborated by the cation z parameter of 0.4834(2) which indicates pronounced layer formation.

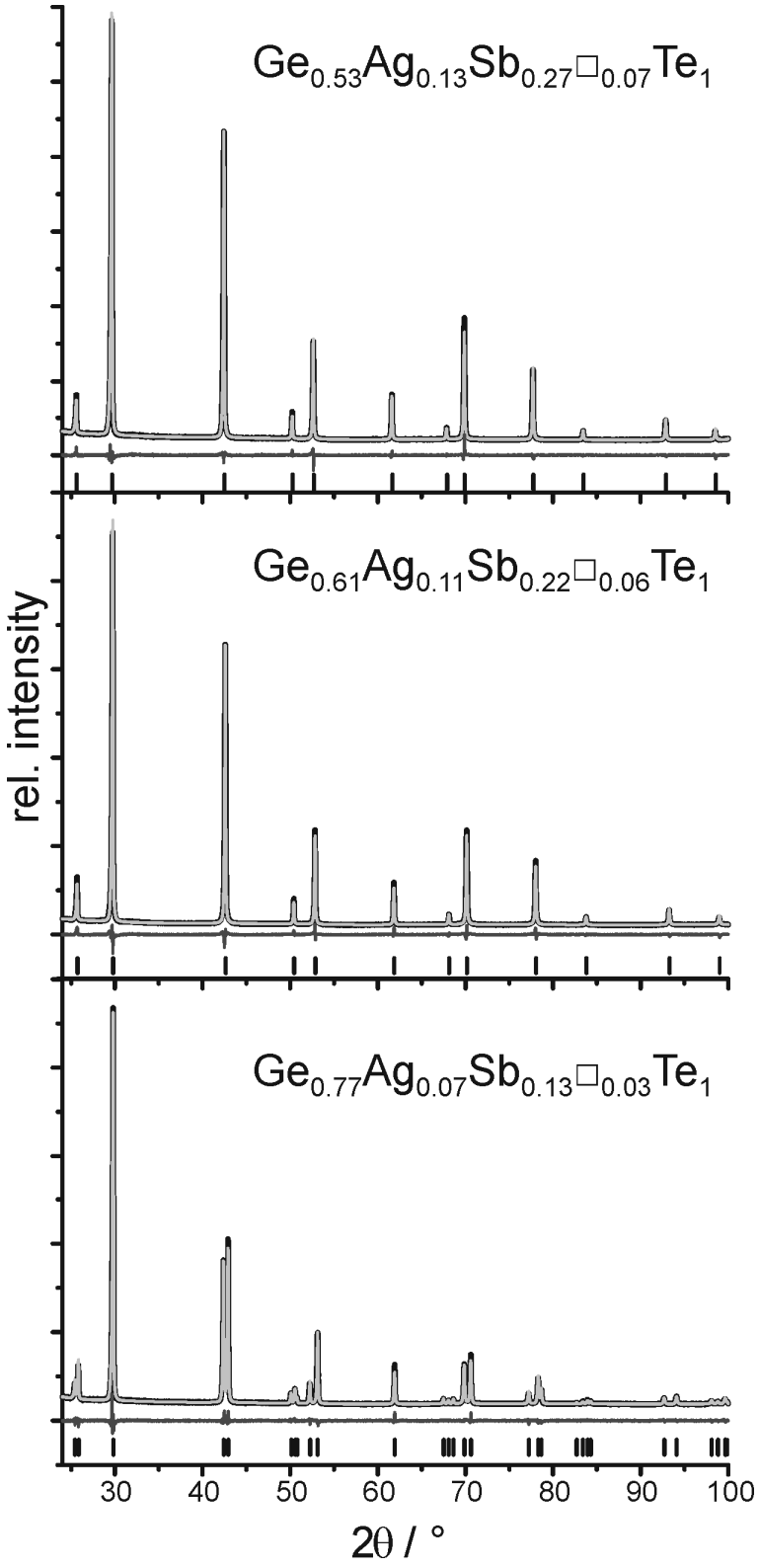

Fig. 1. Experimental (black) and calculated (light gray) powder diffraction patterns according to the Rietveld refinement of $Ge_{0.53}Ag_{0.13}Sb_{0.27}\square_{0.07}Te_1$, $Ge_{0.61}Ag_{0.11}Sb_{0.22}\square_{0.06}Te_1$ and $Ge_{0.77}Ag_{0.07}Sb_{0.13}\square_{0.03}Te_1$ (top to bottom), with difference plots (black, below the profiles) and peak positions (black lines).

Table 1. Crystal data and results of the Rietveld refinement of $Ge_{0.53}Ag_{0.13}Sb_{0.27}\square_{0.07}Te_1$, $Ge_{0.61}Ag_{0.11}Sb_{0.22}\square_{0.06}Te_1$ and $Ge_{0.77}Ag_{0.07}Sb_{0.13}\square_{0.03}Te_1$.

Sample	$Ge_{0.53}Ag_{0.13}Sb_{0.27}\square_{0.07}Te_1$	$Ge_{0.61}Ag_{0.11}Sb_{0.22}\square_{0.06}Te_1$	$Ge_{0.77}Ag_{0.07}Sb_{0.13}\square_{0.03}Te_1$
molar mass (of asymmetric unit) / g mol^{-1}	213.16	210.97	206.71
crystal system / spacegroup (no.)	cubic / $Fm\bar{3}m$ (no. 225)		trigonal / $R3m$
Z	4		3
F(000)	355.7	352.4	259.4
lattice parameters / Å	6.01175(2)	5.99253(2)	a = 4.20935(2) c = 10.4922(1)
cell volume / Å^3	217.272(2)	215.194(2)	161.001(3)
density (X-ray) / g cm^{-3}	6.52	6.51	6.40
absorption coefficient / mm^{-1}	147.2	143.9	134.8
radiation	Cu-$K_{\alpha1}$ (λ = 1.540596 Å)		
2θ range / °	24 – 100		
no. of data points	15201		
no. of reflections	13		31
constraints	2		4
refined parameters / thereof background	22 / 12		27 / 12
R_p / R_{wp}	0.0173 / 0.0275	0.0254 / 0.0371	0.0181 / 0.0280
R_{Bragg}	0.0139	0.0182	0.0147
Goof	0.997	1.430	0.947

Table 2. Atom positions, occupancy factors (s.o.f.), and displacement parameters (B_{iso} in Å^2) of $Ge_{0.53}Ag_{0.13}Sb_{0.27}\square_{0.07}Te_1$, $Ge_{0.61}Ag_{0.11}Sb_{0.22}\square_{0.06}Te_1$ and $Ge_{0.77}Ag_{0.07}Sb_{0.13}\square_{0.03}Te_1$.

sample	atom	x y z	s.o.f.	B_{iso}
$Ge_{0.53}Ag_{0.13}Sb_{0.27}\square_{0.07}Te_1$	Ge/Ag/Sb	0 0 0	0.533/0.133/0.267	2.66(1)
	Te	0.5 0.5 0.5	1	0.96(1)
$Ge_{0.61}Ag_{0.11}Sb_{0.22}\square_{0.06}Te_1$	Ge/Ag/Sb	0 0 0	0.611/0.111/0.222	2.76(2)
	Te	0.5 0.5 0.5	1	1.05(1)
$Ge_{0.77}Ag_{0.07}Sb_{0.13}\square_{0.03}Te_1$	Ge/Ag/Sb	0 0 0.4834(2)	0.767/0.067/0.133	2.12(3)
	Te	0 0 0	1	1.35(2)

3.3.3.3 Transmission electron microscopy

HRTEM investigations (cf. Figure 2) reveal the ordering of cation defects in a sample of $Ge_{0.61}Ag_{0.11}Sb_{0.22}\square_{0.06}Te_1$, which was quenched after being annealed in the stability range of the cubic HT phase (see section below). The nanostructure is comparable to the one observed for Ag-free $(GeTe)_nSb_2Te_3$ thermoelectric materials.[28] The average lateral extension of the defect layers (measured in HRTEM images) is 9(2) nm in good agreement with the lateral extension of 11(3) nm observed for $(GeTe)_7Sb_2Te_3$, which exhibits a similar cation vacancy concentration.[38] The defect layers in both compounds are perpendicular to the cubic <111> directions; they intersect and thereby form a "parquet-like" multi-domain nanostructure (cf. Figure 2, top). The observation that the defect layers form van der Waals gaps at higher temperatures (see next section) and the fact that the average structure of the investigated compound is cubic ($Fm\bar{3}m$) corroborates that the planar defects correspond to cation vacancy layers as opposed to twin boundaries in conventional trigonal TAGS materials (corresponding to the symmetry reduction from $Fm\bar{3}m$ to $R3m$ upon cooling the HT phase). The average distance between the vacancy layers is 4(1) nm; however, they are not equidistant as corroborated by diffuse streaks that interconnect Bragg reflections along <111>* in the SAED patterns taken along the [110] zone axis and the corresponding Fourier transforms of HRTEM images. This nanostructure is not limited to thin fringes of the particles, but extends over the whole crystallites (cf. Fig. S2 bottom in the Supplementary Information). Due to their special orientation, defect layers and corresponding diffuse intensities cannot be observed in HRTEM images or SAED patterns along most zone axes (e.g. [100], cf. Fig. S2 top). The same type of nanostructure is also observed in quenched $Ge_{0.53}Ag_{0.13}Sb_{0.27}\square_{0.07}Te_1$ (cf. Fig. S1).

Larger areas with parallel defect layers (lateral extension > 25 nm), which are more regularly spaced (average spacing: 3.5(5) nm) and correspond to extended van der Waals gaps, were observed after prolonged exposure to the electron beam (cf. Figure 2, bottom). This indicates a tendency towards long-range order comparable to that in annealed samples of $(GeTe)_nSb_2Te_3$.[28]

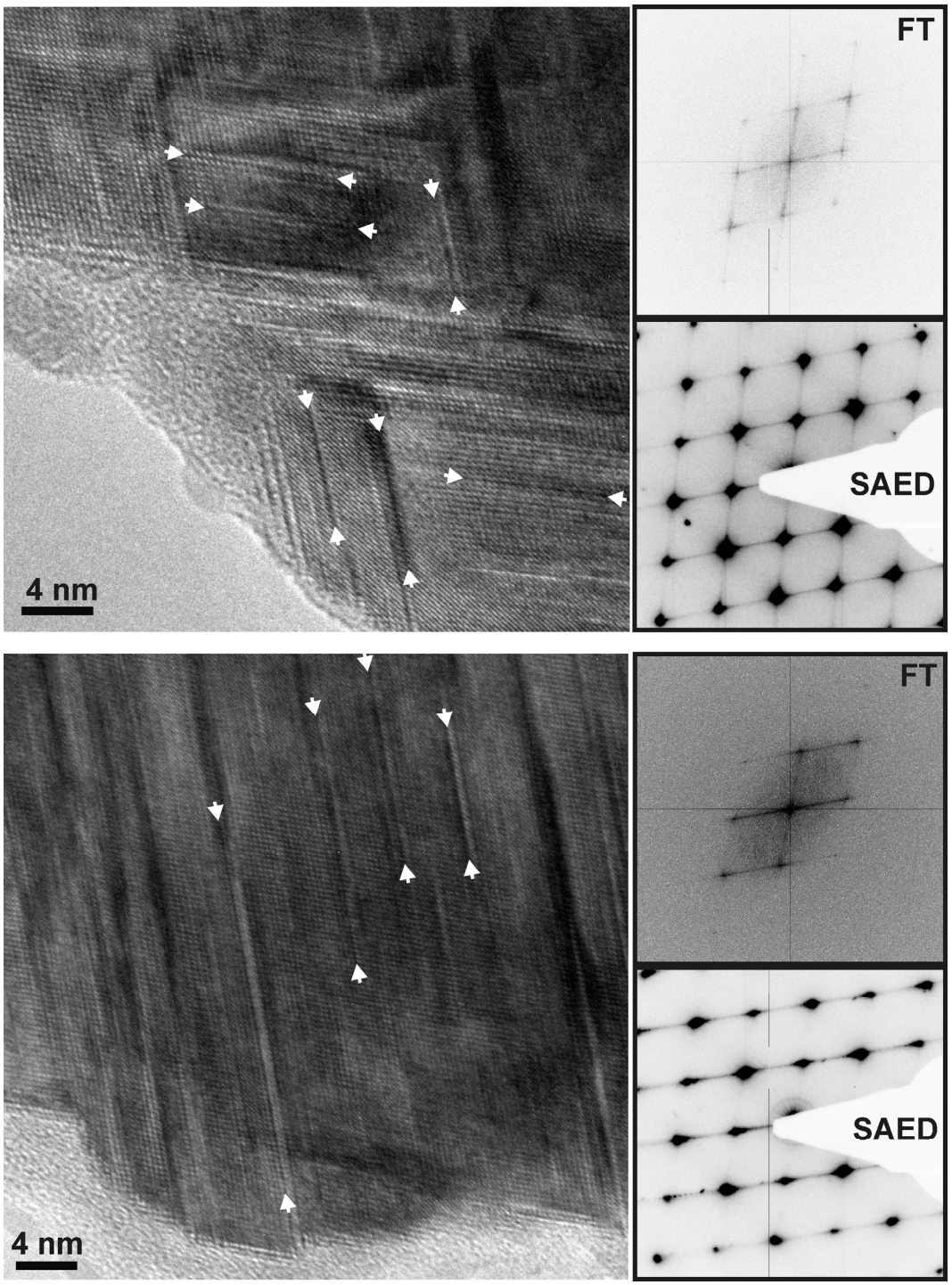

Fig. 2. HRTEM images of quenched $Ge_{0.61}Ag_{0.11}Sb_{0.22}\square_{0.06}Te_1$ (top) and a different area of the same crystallite after prolonged exposure to the electron beam (bottom) with the corresponding Fourier transforms (FT) and SAED patterns of the crystallite (all along the zone axis [110] with respect to cubic indexing). Some selected vacancy layers are highlighted by white arrows, and their arrangement is indicated.

3.3.3.4 Stability ranges and phase transitions

Temperature-dependent PXRD patterns of quenched $Ge_{0.53}Ag_{0.13}Sb_{0.27}\square_{0.07}Te_1$ and $Ge_{0.61}Ag_{0.11}Sb_{0.22}\square_{0.06}Te_1$ (see Fig. 3) show that upon heating in both compounds the pseudocubic phase (with "parquet-like" multi-domain nanostructure) transforms to a trigonal, long-periodically ordered phase at ca. 200 °C. This is indicated by reflection splitting and additional weak reflections, e. g. at $2\theta = 14°$ and 20°. During heating, these reflections are rather broad, which indicates severe stacking disorder and impedes the assignment of a distinct structure type. At ca. 400 °C, both compounds form their rocksalt-type HT phases with statistically disordered cation vacancies. Upon cooling, they retransform to the trigonal long-periodically ordered structures. A schematic illustration of the rearrangements of the vacancy layers is depicted in Fig. 4. Owing to the slow cooling process, the weak reflections of the trigonal phase are sharper that during the heating process. Therefore, the $Ge_5As_2Te_8$ structure type with a 15*P* stacking sequence (space group $P\bar{3}m1$ (no. 164), $a = 4.2136(3)$ Å; $c = 27.711(4)$ Å) can be assigned for $Ge_{0.53}Ag_{0.13}Sb_{0.27}\square_{0.07}Te_1$ (cf. Fig. S3 and Table S2 in the Supplementary Information). This structure can be understood as a sequence of slightly distorted 15-layer slabs cut out of the rocksalt-type structure, which are terminated by Te atom layers and separated by van der Waals gaps (cf. Fig. S4). Around the latter, the Te-Te stacking sequence corresponds to a hexagonal ABAB one. This rearrangement of cation vacancies corresponds to a reconstructive phase transition. For such layered phases, the number of layers between the van der Waals gaps can be estimated from the vacancy concentration as detailed in the literature.[39] In the case of $Ge_{0.53}Ag_{0.13}Sb_{0.27}\square_{0.07}Te_1$ the expected number of layers (1/0.067 = 15) corresponds exactly the observed one.

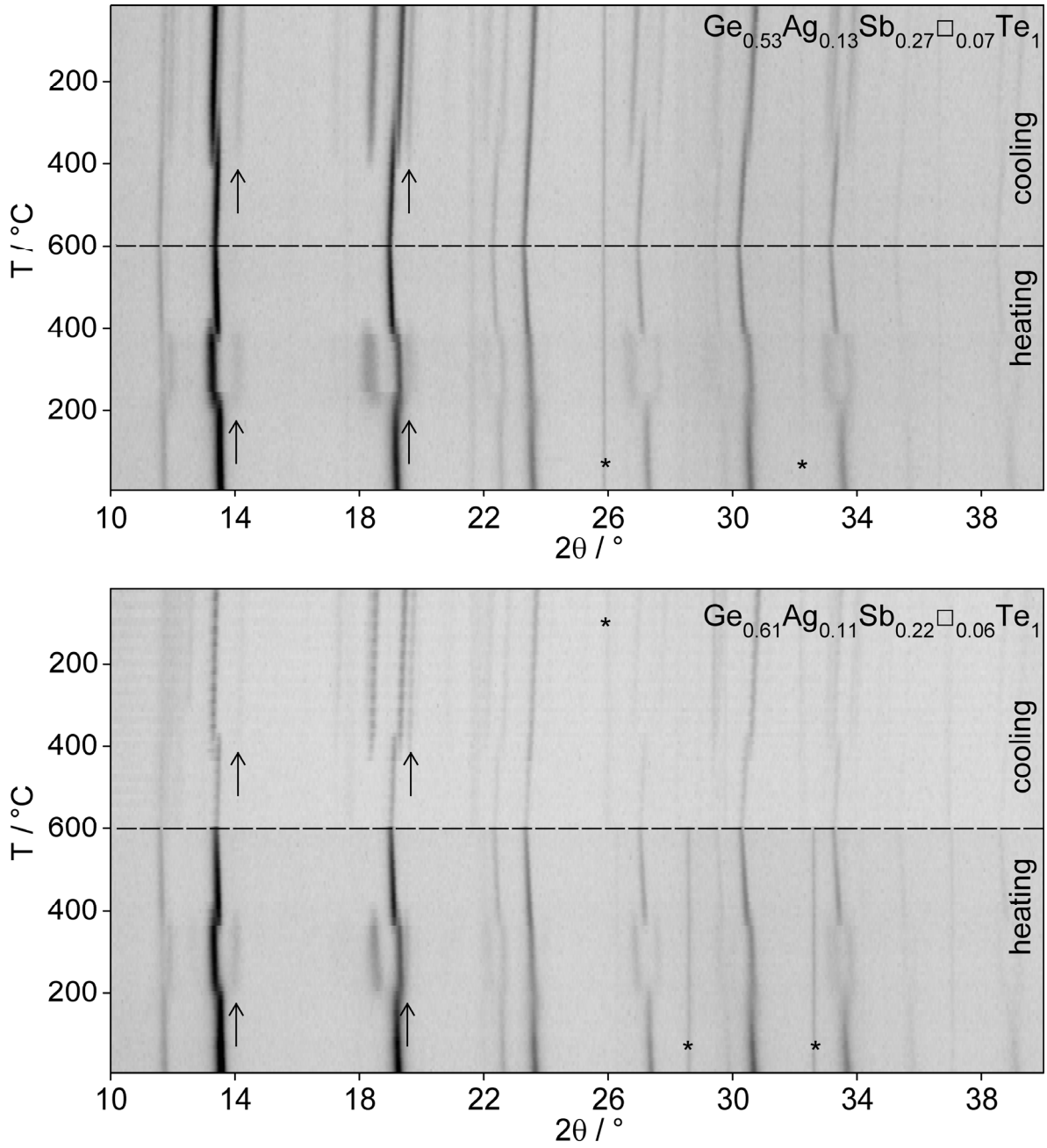

Fig. 3. Temperature-dependent PXRD patterns of $Ge_{0.53}Ag_{0.13}Sb_{0.27}\square_{0.07}Te_1$ (top) and $Ge_{0.61}Ag_{0.11}Sb_{0.22}\square_{0.06}Te_1$ (bottom, note that different contrast of the cooling section is due to the use of another measurement, asterisks mark the positions of reflections caused by the furnace); two of the strongest additional reflections that indicate the formation of a long-periodically ordered trigonal phase are marked with arrows; the dashed horizontal line marks the highest temperature.

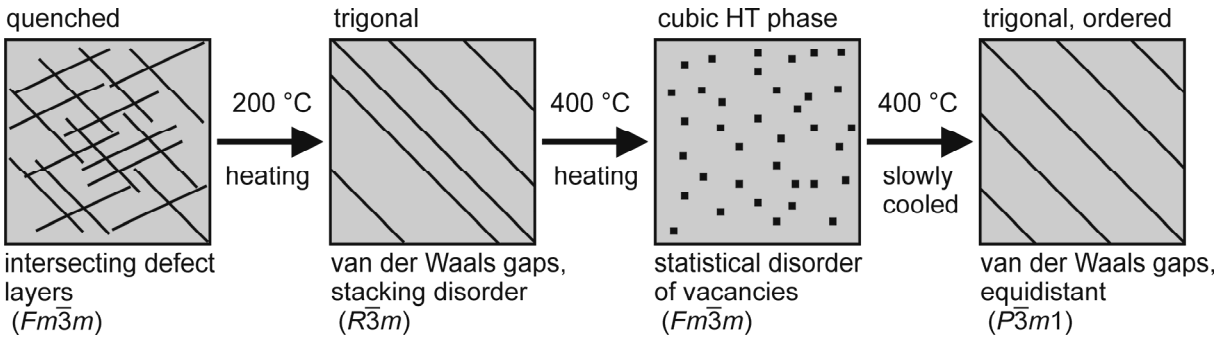

Fig. 4. Schematic illustration of the rearrangement of the vacancies during heating and cooling.

3.3.3.5 Thermoelectric properties of $Ge_{0.53}Ag_{0.13}Sb_{0.27}\square_{0.07}Te_1$ and $Ge_{0.61}Ag_{0.11}Sb_{0.22}\square_{0.06}Te_1$

The thermoelectric properties of nanostructured $Ge_{0.53}Ag_{0.13}Sb_{0.27}\square_{0.07}Te_1$ and $Ge_{0.61}Ag_{0.11}Sb_{0.22}\square_{0.06}Te_1$ (cf. Fig. 5) as measured at the beginning of the first heating cycle change after heating over 200 °C as expected by the phase transitions as described above, when the finite intersecting defect layers become extended and parallel. As the structural changes during the first heating measurement between 200 °C and 450 °C can be viewed as a slow ongoing ordering process, the measured properties in this range shall not be discussed as they may be extremely time-dependent and during a phase transition, assuming a constant C_p is not justified. Subsequent heating and cooling cycles show no further significant irreversibility within the accuracy of the measurements, which is expected because without further quenching steps the samples that were heated once retain only one reversible phase transition at 400 °C from a long periodically trigonal phase to the cubic HT phase. The density of the samples does not change significantly among the differently ordered variants of the compounds after the phase transitions. Both quenched and HT phases are cubic so that anisotropy effects should not affect the measurements; they may, however, occur in the trigonal phase in the same way as they do in “classical” TAGS materials.

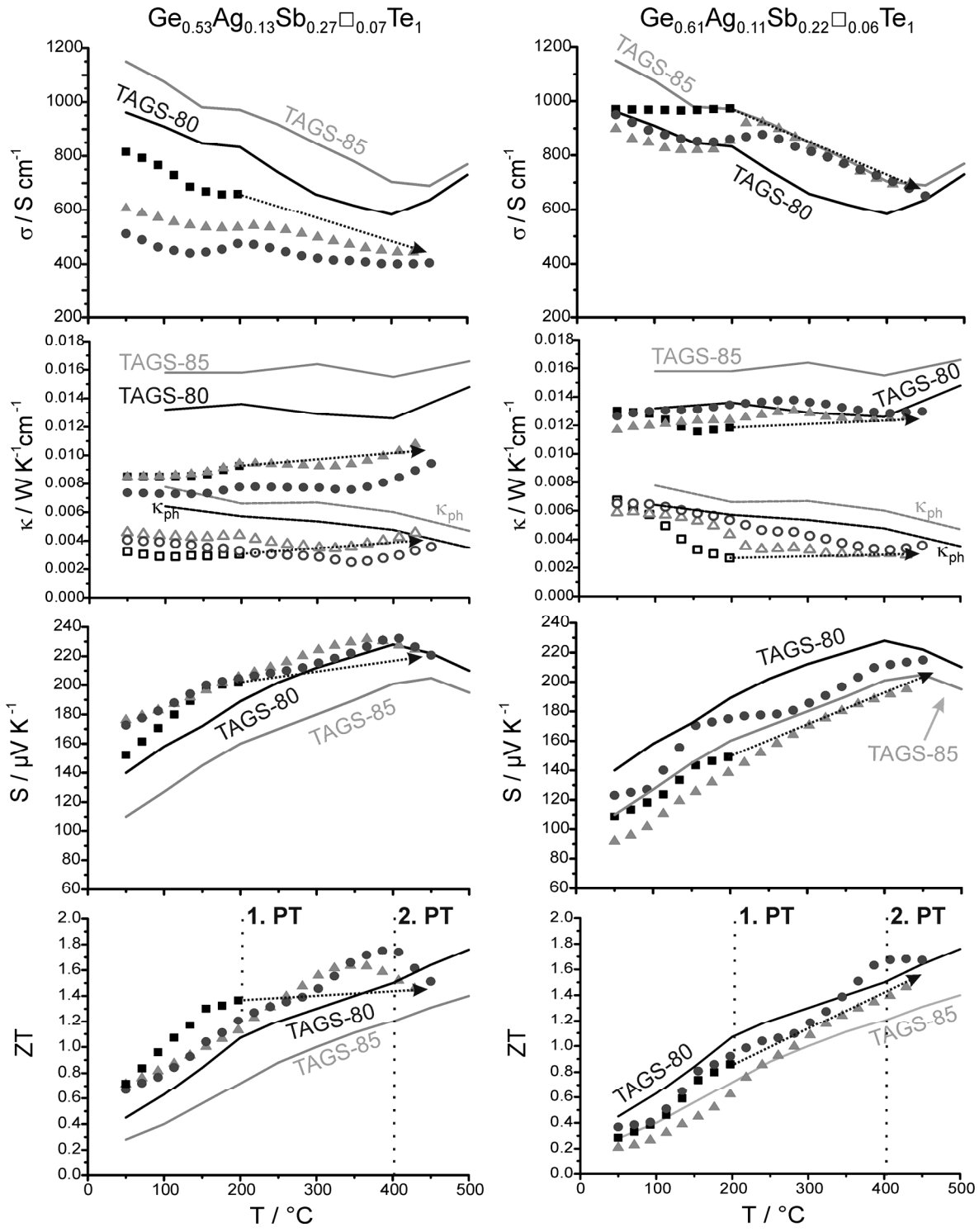

Fig. 5. Electrical conductivity σ, thermal conductivity κ (phononic contribution κ_{ph} with empty symbols), Seebeck coefficient S and ZT values (top to bottom; first heating cycle: black squares, first cooling cycle: gray triangles, second heating cycle: dark gray circles – some slight offsets are within the error limits of the methods and result from remounting the samples) of $Ge_{0.53}Ag_{0.13}Sb_{0.27}\square_{0.07}Te_1$ (left) and $Ge_{0.61}Ag_{0.11}Sb_{0.22}\square_{0.06}Te_1$ (right) in comparison to TAGS-80 (black line) and TAGS-85 (gray line) as taken from ref. [17] with recalculated κ_{ph} (marked by black/gray κ_{ph} for TAGS-80 and TAGS-85, respectively). In the ZT plot the phase transition temperatures (1. and 2. PT as discussed in the text) are marked by dotted lines; the values between 200 °C and 450 °C during the first heating cycle are not shown (the arrows just indicate further heating) because they are strongly affected by slow irreversible phase transitions (see discussion).

Below 200 °C, $Ge_{0.53}Ag_{0.13}Sb_{0.27}\square_{0.07}Te_1$ outperforms both TAGS-80, TAGS-85 and other recently reported high-performance TAGS materials.[17,24] The properties of the isotropic nanostructured modification at the beginning of the first heating cycle are remarkable although they could only be exploited if the samples are never heated over 200 °C. The ZT value of 1.3 at 160 °C, i. e. below any phase transition temperature, is higher than that of TAGS-80 (or any other TAGS sample) at the same temperature. While σ and S of $Ge_{0.53}Ag_{0.13}Sb_{0.27}\square_{0.07}Te_1$ are comparable to those of TAGS-80, the high ZT value is due to the low thermal conductivity; especially its phononic contribution (calculated with a Lorenz number as reported for TAGS materials with vacancies of $2 \cdot 10^{-8}$ V^2K^{-2})[24] is significantly reduced in comparison to TAGS materials without vacancies. However, these favorable values may additionally be associated with a change in the carrier concentration and mobility, which is another consequence of the adjusted Ag/Sb ratio.[26] For the consecutive cooling and heating cycle, the ZT values are in good accordance with the values recently published for TAGS materials with Ag/Sb ratios deviating from 1.[24,26]

For $Ge_{0.61}Ag_{0.11}Sb_{0.22}\square_{0.06}Te_1$, consecutive heating and cooling cycles vary less than for the sample with the slightly higher cation vacancy concentration. The lattice contribution to the thermal conductivity is again lower than the one observed for conventional TAGS materials, but not as low as for $Ge_{0.53}Ag_{0.13}Sb_{0.27}\square_{0.07}Te_1$, and increases when the nanostructure vanishes. σ and S are comparable to TAGS-85, while κ corresponds to TAGS-80. This leads to slightly higher ZT values than those of TAGS-85, but it does not outperform TAGS-80 and other high-performance TAGS materials. These observations clearly show the huge influence of minor changes of the vacancy concentration.

3.3.4 Conclusion

The best conventional vacancy-free TAGS materials, i. e. TAGS-80 and TAGS-85 differ only little concerning their chemical composition: by 6 atom% for Ge and 3 atom% for Ag and Sb. Thus, there is a rather limited compositional range for further optimization. We focus on two homogeneous compounds with optimized Ag/Sb ratio, involving the presence of cation vacancies. According to the present investigation, the enhanced thermoelectric properties result from these more or less short-range ordered cation vacancies. They might act as phonon scattering centers as indicated by the significant reduction of the phononic contribution to the thermal conductivity while the good electrical properties remain almost unchanged in comparison to conventional vacancy-free TAGS materials. The cation vacancy concentration

also plays a crucial role concerning the structural chemistry of TAGS materials. For high cation vacancy concentrations, the structures are in remarkable contrast to those reported for conventional TAGS materials.[11-14,17] Both $Ge_{0.53}Ag_{0.13}Sb_{0.27}\square_{0.07}Te_1$ and $Ge_{0.61}Ag_{0.11}Sb_{0.22}\square_{0.06}Te_1$ can be quenched to form metastable compounds with a rocksalt-type average structure and layer-like short-range ordered vacancies. In contrast, lower vacancy concentrations as in $Ge_{0.77}Ag_{0.07}Sb_{0.13}\square_{0.03}Te_1$ lead to a TAGS-like α-GeTe-type structure which implies that cation ordering effects do not play an important role.

Quenched, nanostructured compounds with high cation vacancy concentrations exhibit two phase transitions. An irreversible transition leads from a (pseudo-)cubic "parquet-like" multi-domain nanostructure to a long-periodically ordered trigonal one and a second, reversible transition to a cubic rocksalt-type HT phase. Although the partial irreversibility and phase transitions in general may be viewed as drawbacks concerning thermal cycling, nanostructured $Ge_{0.53}Ag_{0.13}Sb_{0.27}\square_{0.07}Te_1$ may be applied far below any phase transition temperature, where it exhibits a ZT value of 1.3 at 160 °C. Annealed samples, or those heated over 200 °C just once, exhibit only one reversible phase transition. Their thermoelectric properties still differ from conventional vacancy-free TAGS, as do their structures. These findings are in good accordance with the values recently published for high-performance TAGS materials.[23,24,26] Our results clearly illustrate how the structural chemistry of this multinary system can be significantly changed even when the composition is varied only slightly as this involved a much more pronounced relative change of the vacancy concentration. In addition to altered charge carrier concentrations, different short- or long-range ordering variants of the cation vacancies significantly influence the thermoelectric properties and are one reason for the high performance of TAGS material with an Ag/Sb ratio differing from 1. It remains an open question if conventional TAGS materials, despite the fact that their chemical formulas formally suggest vacancy-free structures, may also exhibit a certain amount of vacancies that contribute to their performance.

Acknowledgement

We thank Thomas Miller and Christian Minke (LMU Munich) for the temperature-dependent powder diffraction experiments and for SEM-EDX analyses, respectively. We are grateful to Prof. Dr. W. Schnick (LMU Munich) for the generous support of this work. Furthermore, we thank Fivos Drymiotis (California Institute of Technology) for help with the thermoelectric

measurements. This investigation was funded by the Deutsche Forschungsgemeinschaft (grant OE530/1-2) and the Studienstiftung des deutschen Volkes (scholarship for T.S.).

Supplementary information

Table S1. Results from EDX analyses (SEM, 6 point analyses averaged per compound).

sample	atom-% (calculated)	atom-% (experimental)
$Ge_{0.53}Ag_{0.13}Sb_{0.27}\square_{0.07}Te_1$	Ge: 27.6; Ag: 6.9; Sb: 13.8; Te: 51.7	Ge: 29.0(12); Ag: 6.5(3); Sb: 14.6(4); Te: 49.9(7)
$Ge_{0.61}Ag_{0.11}Sb_{0.22}\square_{0.06}Te_1$	Ge: 31.4; Ag: 5.7; Sb: 11.4; Te: 51.4	Ge: 32.8(9); Ag: 5.2(2); Sb: 12.4(3); Te: 49.7(7)
$Ge_{0.77}Ag_{0.07}Sb_{0.13}\square_{0.03}Te_1$	Ge: 39.0; Ag: 3.4; Sb: 6.8; Te: 50.8	Ge: 39.9(4); Ag: 3.6(3); Sb: 6.9(3); Te: 49.8(6)

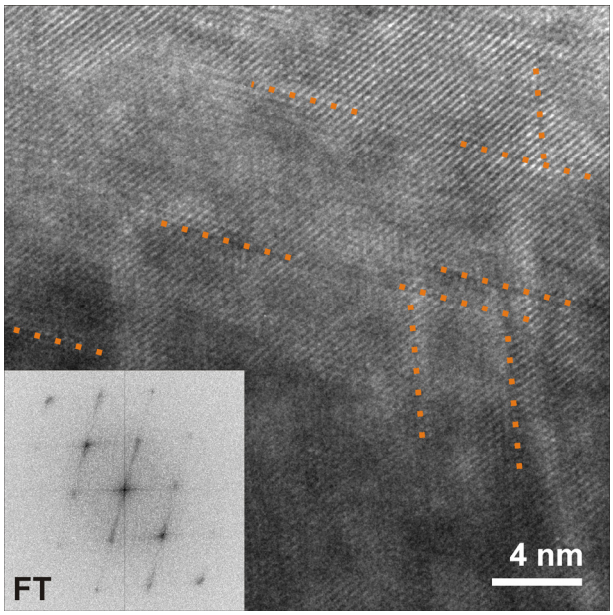

Fig. S1. HRTEM image of quenched $Ge_{0.53}Ag_{0.13}Sb_{0.27}\square_{0.07}Te_1$ (zone axis [110]) with the corresponding Fourier transform (inset). Some vacancy layers are highlighted (dotted orange lines).

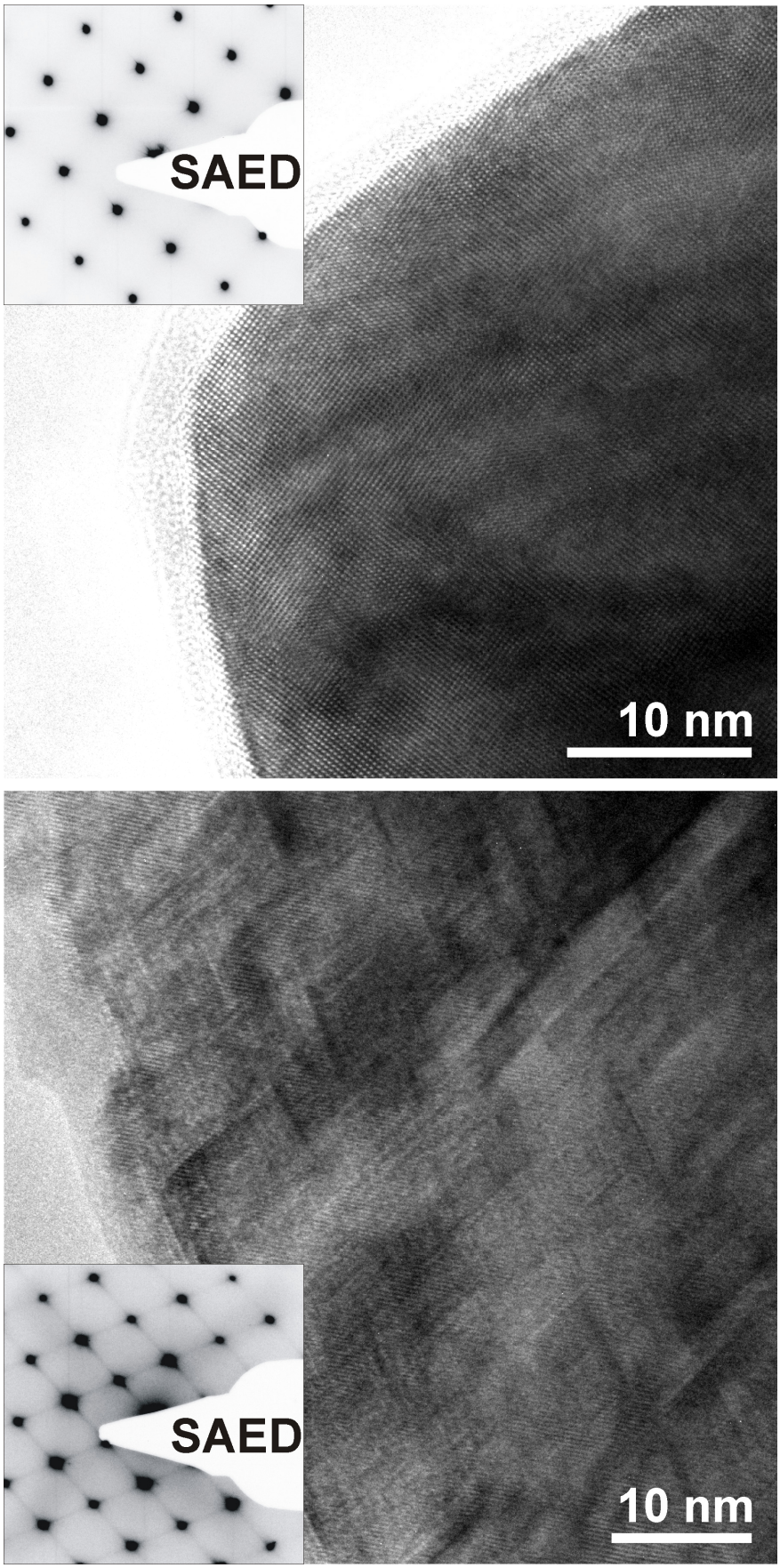

Fig. S2. HRTEM images of quenched $Ge_{0.61}Ag_{0.11}Sb_{0.22}\square_{0.06}Te_1$ (top: zone axis [100], bottom: zone axis [110]) with the corresponding selected-area electron diffraction patterns of the crystallites (insets).

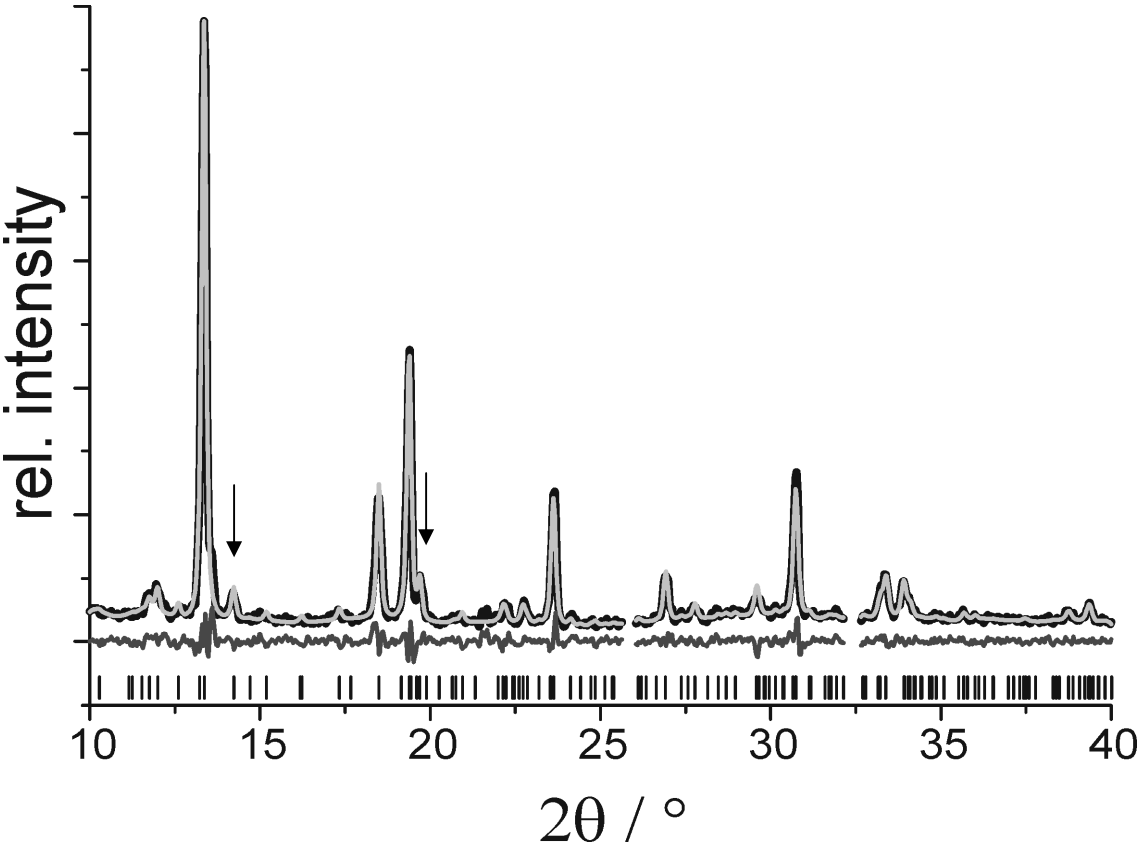

Fig. S3. Rietveld refinement of $Ge_{0.53}Ag_{0.13}Sb_{0.27}\square_{0.07}Te_1$ in its trigonal long-periodically ordered layered 15*P*-$Ge_5As_2Te_8$ type structure (slowly cooled from the HT phase after the heating experiment): experimental (black) and calculated (light gray) powder diffraction patterns, difference plots (dark gray) and peak positions (black lines); space group $P\bar{3}m1$ (no. 164), a = 4.2136(3) Å; c = 27.711(4) Å, R_p = 0.0812, R_{wp} = 0.1087, R_{Bragg} = 0.0275. Reflections caused by the furnace at ca. 26° and 32.4° 2θ were excluded; arrows highlight the most significant reflections indicating long-range order (also visible and highlighted in the temperature-dependent PXRD patterns in the text).

Table S2. Atom positions, occupancy factors (s.o.f., atom distribution not refined), and displacement factors (B_{iso} in Å^2, common for cations and anions respectively) of $Ge_5As_2Te_8$ type $Ge_{0.53}Ag_{0.13}Sb_{0.27}\square_{0.07}Te_1$

sample	atom	x y z	s.o.f.	B_{iso}
$Ge_{0.53}Ag_{0.13}Sb_{0.27}\square_{0.07}Te_1$	Ge Ag Sb	0 0 0	4/7 1/7 2/7	1.6(3)
	Te	2/3 1/3 0.064(1)	1	0.8(2)
	Ge Ag Sb	1/3 2/3 0.136(1)	4/7 1/7 2/7	1.6(3)
	Te	0 0 0.191(1)	1	0.8(2)
	Ge Ag Sb	2/3 1/3 0.254(2)	4/7 1/7 2/7	1.6(3)
	Te	1/3 2/3 0.320(1)	1	0.8(2)
	Ge Ag Sb	0 0 0.392(2)	4/7 1/7 2/7	1.6(3)
	Te	2/3 1/3 0.447(1)	1	0.8(2)

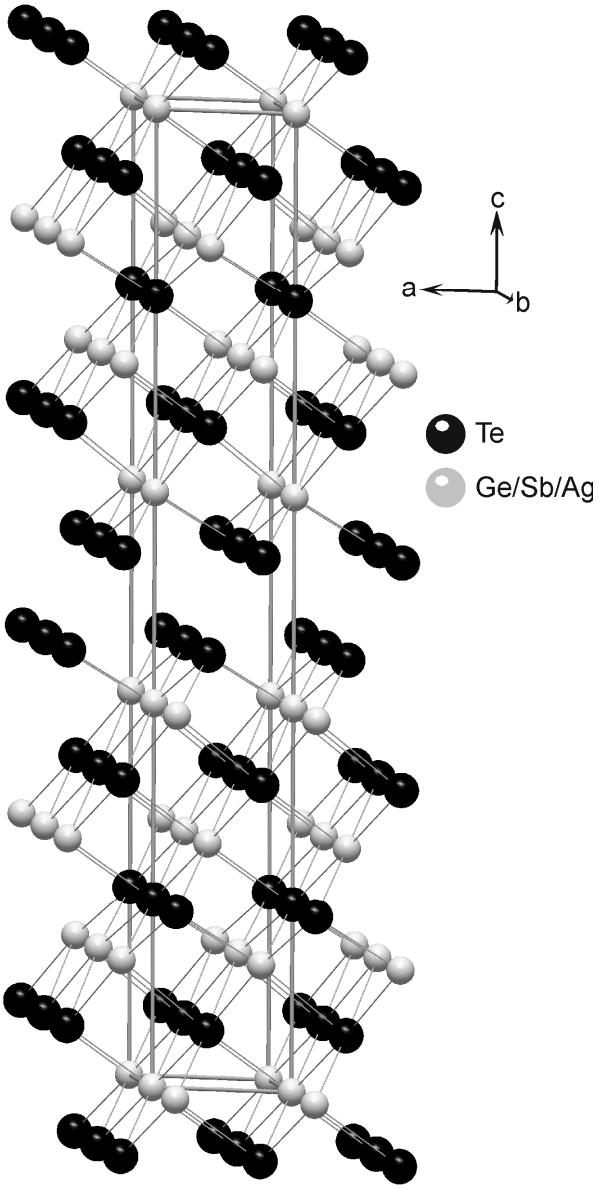

Fig. S4. Crystal structure of 15*P*-type $Ge_{0.53}Ag_{0.13}Sb_{0.27}\square_{0.07}Te_1$, formed after slowly cooling the cubic high-temperature phase to room temperature.

References

[1] J. R. Sootsman, D. Y. Chung, M. G. Kanatzidis, *Angew. Chem. Int. Ed.* **2009**, *48*, 8616.

[2] C. Wood, *Rep. Prog. Phys.* **1988**, *51*, 459.

[3] D. T. Morelli, V. Jovovic, J. P. Heremans, *Phys. Rev. Lett.* **2008**, *101*, 035901.

[4] T. Schröder, T. Rosenthal, D. Souchay, C. Petermayer, S. Grott, E.-W. Scheidt, C. Gold, W. Scherer, O. Oeckler, *J. Solid State Chem.* **2013**, *206*, 20.

[5] R. Mohanraman, R. Sankar, K. M. Boopathi, F.-C. Chou, C.-W. Chu, C.-H. Lee, Y.-Y. Chen, *J. Mater. Chem. A* **2014**, *2*, 2839.

[6] K. F. Hsu, S. Loo, F. Guo, W. Chen, J. S. Dyck, C. Uher, T. Hogan, E. K. Polychroniadis, M. G. Kanatzidis, *Science* **2004**, *303*, 818.

[7] W. G. Zeier, Y. Z. Pei, G. Pomrehn, T. Day, N. Heinz, C. P. Heinrich, G. J. Snyder, W. Tremel, *J. Am. Chem. Soc.* **2013**, *135*, 726.

[8] A. Yusufu, K. Kurosaki, Y. Ohishi, H. Muta, S. Yamanaka, *Jpn. J. Appl. Phys.* **2013**, *52*, 081801.

[9] T. Plirdpring, K. Kurosaki, A. Kosuaga, T. Day, S. Firdosy, V. Ravi, G. J. Snyder, A. Harnwunggmoung, T. Sugahara, Y. Ohishi, H. Muta, S. Yamanaka, *Adv. Mater.* **2012**, *24*, 3622.

[10] R. Liu, L. Xi, H. Liu, X. Shi, W. Zhang, L. Chen, *Chem. Commun.* **2012**, *48*, 3818.

[11] B.A. Cook, M. J. Kramer, X. Wei, J. L. Harringa, E. M. Levin, *J. Appl. Phys.* **2007**, *101*, 053715.

[12] S. K. Plachkova, *Phys. Status Solidi A* **1984**, *83*, 349.

[13] S. H. Yang, T. J. Zhu, T. Sun, S. N. Zhang, X. B. Zhao, J. He, *Nanotechnol.* **2008**, *19*, 245707.

[14] F. D. Rosi, J. P. Dismukes, E. F. Hockings, *Electron. Eng.* **1960**, *79*, 450.

[15] W. Klemm, G. Frischmuth, *Z. Anorg. Allg. Chem.* **1934**, *218*, 249.

[16] J. Goldak, C. S. Barrett, D. Innes, W. Youdelis, *J. Chem. Phys.* **1966**, *44*, 3323.

[17] J. Davidow, Y. Gelbstein, *J. Electron. Mater.* **2013**, *42*, 1542.

[18] X. Shi, J. R. Salvador, J. Yang, H. Wang, *Sci. Adv. Mater.* **2011**, *3*, 667.

[19] T. Schröder, S. Schwarzmüller, C. Stiewe, J. de Boor, M. Hölzel, O. Oeckler, *Inorg. Chem.* **2013**, *52*, 11288.

[20] T. Schröder, T. Rosenthal, N. Giesbrecht, S. Maier, E.-W. Scheidt, W. Scherer, G. J. Snyder, W. Schnick, O. Oeckler, *J. Mater. Chem. A* **2014**, *2*, 6384.

[21] E. M. Levin, B. A. Cook, J. L. Harringa, S. L. Bud'ko, R. Venkatasubramanian, K. Schmidt-Rohr, *Adv. Funct. Mater.* **2011**, *21*, 441.

[22] E. M. Levin, S. L. Bud'ko, K. Schmidt-Rohr, *Adv. Funct. Mater.* **2012**, *22*, 2766.

[23] G. C. Christakudis, S. K. Plachkova, L. E. Shelimova, E. S. Avilov, *Phys. Status Solidi A* **1991**, *128*, 465.

[24] T. Zhu, H. Gao, Y. Chen, X. B. Zhao, *J. Mater. Chem. A* **2014**, *2*, 3251.

[25] Y. Chen, B. He, T. J. Zhu, X. B. Zhao, *J. Phys. D: Appl. Phys.* **2012**, *45*, 115302.

[26] Y. Chen, C. M. Jaworski, Y. B. Gao, H. Wang, T. J. Zhu, G. J. Snyder, J. P. Heremans, X. B. Zhao, *New J. Phys.* **2014**, *16*, 013057.

[27] M. N. Schneider, T. Rosenthal, C. Stiewe, O. Oeckler, *Z. Kristallogr.* **2010**, *225*, 463.

[28] T. Rosenthal, M. N. Schneider, C. Stiewe, M. Döblinger, O. Oeckler, *Chem. Mater.* **2011**, *23*, 4349.

[29] *TOPAS-Academic*, *V. 4.1*, Coelho Software, Brisbane, Australia, **2007**.

[30] *WINXPOW*, *v2.12 ed.*, Stoe & Cie GmbH, Darmstadt, Germany, **2005**.

[31] *DigitalMicrograph*, *3.6.1*, Gatan Software, Pleasanton, USA, **1999**.

[32] P. A. Stadelmann, *Ultramicroscopy* **1987**, *21*, 131.

[33] *ESVision*, *4.0.164*, Emispec Systems Inc., Tempe, USA, **1994-2002**.

[34] K. A. Borup, E. S. Toberer, L. D. Zoltan, G. Nakatsukasa, M. Errico, J. P. Fleurial, B. B. Iversen, G. J. Snyder, *Rev. Sci. Instrum.* **2012**, *83*, 123902.

[35] L. J. van der Pauw, *Philips Res. Rep.* **1958**, *13*, 1.

[36] H. Wang, W. D. Porter, H. Böttner, J. König, L. Chen, S. Bai, T. M. Tritt, A. Mayolet, J. Senawiratne, C. Smith, F. Harris, P. Gilbert, J. W. Sharp, J. Lo, H. Kleinke, L. J. Kiss, *Electron. Mater.* **2013**, *42*, 1073.

[37] S. Iwanaga, E. S. Toberer, A. LaLonde, G. J. Snyder, *Rev. Sci. Instrum.* **2011**, *82*, 063905.

[38] T. Rosenthal, P. Urban, K. Nimmrich, L. Schenk, J. de Boor, C. Stiewe, O. Oeckler, *Chem. Mater.* **2014**, *26*, 2567.

[39] M. N. Schneider, O. Oeckler, *Z. Anorg. Allg. Chem.* **2008**, *634*, 2557.

3.4 The solid solution series $(GeTe)_x(LiSbTe_2)_2$ $(1 \leq x \leq 11)$ and the thermoelectric properties of $(GeTe)_{11}(LiSbTe_2)_2$

Thorsten Schröder, Stefan Schwarzmüller, Christian Stiewe, Johannes de Boor, Markus Hölzel, Oliver Oeckler

Inorg. Chem. **2013**, *52*, 11288 – 11294.

Abstract

Exchanging one Ge^{2+} with two Li^+ per formula unit in $(GeTe)_n(Sb_2Te_3)$ (n = 1, 2, 3, …) eliminates cation vacancies, because it leads to an equal number of cations and anions. This substitution results in the solid solution $(GeTe)_x(LiSbTe_2)_2$ (with x = n - 1, but n not necessarily an integer). For x < 6, these stable compounds crystallize in a rocksalt-type structure with random cation disorder. Neutron data show that a small fraction of Ge occupies tetrahedral voids for x = 2 and 3. For x > 6, $(GeTe)_x(LiSbTe_2)_2$ forms a GeTe-type structure that shows a phase transition to a cubic high-temperature phase at ca. 280 °C. The thermoelectric properties of $(GeTe)_{11}(LiSbTe_2)_2$ have been investigated and show that this compound is a promising thermoelectric material with a ZT value of 1.0 at 450 °C. The high ZT value of the thermodynamically stable compound is caused by a low phononic contribution to the thermal conductivity; probably Li acts as a "pseudo-vacancy".

3.4.1 Introduction

Compounds with the composition $(GeTe)_n(Sb_2Te_3)$ (so-called GST materials) represent the most important class of phase-change materials (PCMs) for both optical and nonvolatile electrical data storage. They are used in rewritable DVDs and Blu-ray discs as well as in random access memory devices.[1-4] At ambient conditions, the thermodynamically stable state of these compounds corresponds to trigonal long-periodically ordered layered structures, in which slightly distorted rock-salt type slabs are separated by van der Waals gaps with partially covalent Te-Te interactions.[5-7] For GeTe contents n ≥ 3, a rocksalt-type high-temperature (HT) phase exists.[8] In the trigonal modification, Ge and Sb are disordered on the cation positions, which in the cubic HT phase are shared by Ge, Sb and a fraction of $^1/_{(n+3)}$ cation vacancies. Thus, the HT phase corresponds to the metastable crystalline phase in thin

PCM films.[9,10] The disordered vacancies are a consequence of the fact that the charge balanced state contains fewer cations than anions. In PCMs, the origin of vacancies and their impact on properties has also attracted much attention recently.[11-14] In both trigonal and cubic phases, Te occupies the anion positions. Quenching the cubic HT phase leads to metastable (pseudo-)cubic compounds which are characterized by intersecting cation vacancy layers with limited lateral extension perpendicular to the cubic <111> directions. They are, however, not equidistantly spaced. The distorted NaCl-type building blocks between these planar defects form a "parquet-like" nanostructure. As the nanostructure depends on the defect concentration and diffusion, it is strongly influenced by the GeTe content n and the thermal treatment. For n = 12 and 19, these metastable compounds have remarkable thermoelectric properties and reach ZT values of ~ 1.3 at 450 °C.[8,15] The dimensionless figure of merit $ZT = S^2T / \kappa\rho$ (Seebeck coefficient S, electrical resistivity ρ, thermal conductivity κ) is a measure of the efficiency of thermoelectric materials, which are an intriguing research subject since they can be used to reversibly interconvert electrical and thermal energy.[16-19] However, the high ZT values of GST materials are observed at temperatures where dynamical diffusion processes already set in and the stable trigonal modification is slowly formed. Therefore, the application potential of metastable GST as a thermoelectric material is limited up to 350 °C, where the maximum ZT value amounts to ~ 0.7.

The instability of the (pseudo-)cubic phases is probably due their high concentration of vacancies which involves "incomplete" coordination spheres and a large energy gain when ordered structures are formed. Therefore, they may be stabilized as quaternary compounds when the vacancy concentration is reduced, e. g. by replacing Ge^{2+} by twice the amount of monovalent cations. This brings the cation/anion ratio closer to 1 and should increase the temperature range in which the materials can be applied. The use of Li^+ as a "pseudo-vacancy" may ensure a large mass difference between the atoms involved, which disturbs vibrational modes and hence lowers the phononic part of the thermal conductivity. Therefore, the thermoelectric properties of such quaternary phases are expected to be comparable to those of metastable quenched GST materials, including those that are used as PCMs.[20] In a comparable manner, a few percent of in $AgSbTe_2$ are beneficial for the thermoelectric properties by lowering κ without affecting ρ.[21]

3.4.2 Experimental

Synthesis

Samples with the composition $(GeTe)_x(LiSbTe_2)_2$ (x = 0, 1, 2, 3, 6 and 11) were synthesized by heating stoichiometric mixtures (e.g., 1.0 g) of the pure elements (lithium 99.999%, Alfa Aesar; germanium 99.999%, Sigma-Aldrich; antimony 99.9999%, Smart Elements; tellurium 99.999 %, Alfa Aesar) to 700 °C under Ar atmosphere for one hour. For high Li contents (x = 0, 1, 2, 3), graphite crucibles in sealed silica ampoules were used, for lower Li contents, graphitized silica glass ampoules proved to be sufficient. The ampoules containing the resulting melts were quenched to room temperature in water. In order to obtain the amounts required for neutron diffraction, several samples with the same composition were combined, finely ground and annealed for 12 h at 550 °C and cooled to RT in 2 hours to ensure homogeneity. For the thermoelectric characterization, three samples (1.5 g) of the composition $(GeTe)_{11}(LiSbTe_2)_2$ were prepared as described and subsequently fused together by combining the samples in a larger ampoule, melting them for 10 min at 700 °C and subsequently annealing them at 550°C for 48 h. All compounds are slightly sensitive to moisture and show a basic reaction when mixed with water.

Diffraction methods

X-ray powder patterns were recorded on a Huber G670 Guinier camera equipped with a fixed imaging plate and integrated read-out system using Cu-$K_{\alpha 1}$ radiation (Ge monochromator, λ = 1.54051 Å). Specimens were prepared by crushing the samples in a glove-box under Ar atmosphere and fixing the powder between two Mylar foils on a flat sample holder using vacuum grease. Temperature-dependent powder diffraction was performed with a STOE Stadi P powder diffractometer equipped with an imaging-plate detector system using Mo-$K_{\alpha 1}$ radiation (Ge monochromator, λ = 0.71093 Å) in a modified Debye–Scherrer geometry equipped with a graphite furnace. Powdered samples were filled into silica glass capillaries with 0.3 mm diameter and sealed with vacuum grease under argon atmosphere. The measurement was performed from room temperature (RT) to 600 °C with a heating rate of 10 K/min and from 600 °C back to RT with cooling rate of 5 K/min (faster cooling is impossible with the setup used).

Neutron powder diffraction patterns were acquired on the SPODI diffractometer at the neutron source FRM II (Munich, Germany, λ = 1.5484 Å, detector array of 80 position-

sensitive ^{3}He tubes with 300 mm active height, fixed Soller collimators of 10' horizontal divergence). The samples (~ 3.0 g) were filled in vanadium crucibles under Ar atmosphere. The angular range of $0° < 2\theta < 160°$ was covered by stepwise positioning of the detector array to obtain a diffraction pattern of 0.05° step width (2°/40 steps).
The phase homogeneity was determined by pattern fitting (Rietveld method) of X-ray data, structure data were obtained by joint refinements of X-ray and neutron data using the program TOPAS (details are given in the Results and Discussion section).[22]

ICP-OES

The chemical composition of the samples used for neutron diffraction was determined by inductively coupled plasma optical emission spectroscopy using a Varian Vista RL CCD Simultaneous ICP-OES. The samples (ca. 5 mg) were dissolved in a mixture of 1 ml conc. HNO_3, 0.5 ml conc. HCl and 0.1 ml HF (40% solution) and subsequently heated for 30 min at 105 °C. Two characteristic emission lines for each element were determined twice per sample and used to calculate an average. For Li only the characteristic emission line at 670.783 nm was used. Although the samples were weighed with an accuracy of 0.0001 mg, the sum of the weight fractions of Li, Ge, Sb and Te adds up to ~ 93 %. As no other heavy elements are present, this can be attributed to hydrolysis effects. As there are no volatile products, the element ratios remain reliable. The experimental values (cf. Table S1 in the Supplementary Information) are in excellent agreement with the ones corresponding to the starting mixture, which indicates that no significant amount of Li was lost by reaction with graphite crucibles.

Thermoelectric characterization

The Seebeck coefficient (S) and electrical resistivity (ρ) of $(GeTe)_{11}(LiSbTe_2)_2$ were measured up to 450 °C under He using an in-house-built (DLR, Cologne, Germany) setup and commercial facilities for the determination of the thermal conductivity. The electrical resistance R was measured with an in-line four-point-probe setup made of tungsten carbide to avoid cable and contact resistances affecting the measurement and by using an AC method with a frequency of 7 Hz in order to reduce Peltier influences. The electrical resistivity follows as $\rho = (1/G_F) \cdot R$ (with the correction factor G_F taking into account the cross-section and thickness of the sample and the distance between the probe tips). Seebeck coefficients were measured by establishing a small temperature gradient across the sample while the

sample's environment temperature was changed and stabilized for each temperature step. Type-N thermocouples attached directly to the sample's surface were used for both the Seebeck voltage pickup and the temperature measurement.[23,24] The relative errors of ρ(T) and S(T) are 5%, respectively. The thermal conductivity κ was calculated with $\kappa = D_{th} \cdot \rho_m \cdot C_p$ from measurements of the thermal diffusivity D_{th} (determined using a laser-flash apparatus, LFA 427, Netzsch GmbH & Co., Germany), the mass density ρ_m (determined using a Mohr's balance) and the heat capacity C_p (determined using a differential scanning calorimeter, DSC 404, Netzsch GmbH & Co., Germany). A Lorenz number of $1.44 \cdot 10^{-8}$ W Ω K^{-2} was used for calculating the electronic part of κ. The relative error of κ is ~8%, resulting from 3% for the D_{th} and 5% for the C_p.

3.4.3 Results and discussion

3.4.3.1 Crystal structure derived from X-ray and neutron powder diffraction data

The powder diffraction patterns of $(GeTe)_x(LiSbTe_2)_2$ for x = 0, 1, 2 and 3 could be indexed assuming cubic metrics (cf. Fig. 2). As Li does not significantly contribute to X-ray diffraction intensities, joint refinements on neutron and X-ray diffraction patterns were performed, lattice parameters, atom coordinates and displacement parameters were refined simultaneously on both data sets. In order to refine anisotropic broadening of the reflection profiles of the X-ray data, the LeBail-Jouanneaux algorithm was used.[25] The reflection broadening increases with the GeTe content x. A common displacement factor was refined for all cations and a separate one for Te.

Like $Li_2Sb_2Te_4$ (= $LiSbTe_2$, x = 0),[26] which was prepared for comparison, the average structure of $(GeTe)_x(LiSbTe_2)_2$ for x = 1, 2 and 3 corresponds to a cation-disordered rocksalt-type structure (space group $Fm\bar{3}m$, no. 225). Although profile fits assuming a trigonal setting do not reveal any deviations from cubic metrics, structure models (e. g., the GeTe type)[27,28] with other reasonable space groups that are typical for GST materials, i. e. $R\bar{3}m$ and $R3m$, were considered; however, the refined models showed no deviation from the rocksalt-type structure (e. g., no 3+3 instead of octahedral coordination polyhedra). In the rocksalt-type model, all three cations occupy the 4*a* position, while Te occupies the 4*b* anion position. For x = 2 and 3 small positive residual densities were present in the tetrahedral voids (8*c* position); however, only for neutron data (cf. Fig. 1, left). Li could be excluded because of its negative neutron scattering length. The strongest neutron scatterer involved is Ge. It was possible to

refine an occupancy factor of 0.005 for x = 2 and 0.01 for x = 3 of Ge on the 8*c* position. A sum formula constraint according to the nominal composition confirmed by ICP-OES (cf. Table S1 in the Supplementary Information) was used, which means introducing vacancies on the 4*a* position. In addition to its large neutron scattering length, the presence of Ge in part of the tetrahedral voids of fcc packing of Te is corroborated by the fact that for x = 0, i. e. the sample without Ge, no such residual density was observed. For x = 1, the residual density in the tetrahedral void was observed but the refined occupancy is not statistically significant, in contrast to higher Ge contents. Also note that in amorphous phases Ge may also be tetrahedrally coordinated by Te, which was shown for phase-change materials by EXAFS investigations (so-called "umbrella flip").[29] This tetrahedral coordination would imply a sp^3 hybridization of Ge in the amorphous phase in contrast to its p-type configuration in the crystalline GST phases. However, recent investigations show that while in amorphous phases most Ge atoms are coordinated octahedrally,[30] some Ge atoms in crystalline phases up may be coordinated tetrahedrally due to Ge-vacancy interactions, e. g. in rocksalt-type $Ge_2Sb_2Te_5$.[31] Yet, ^{125}Te solid state NMR studies have proven the tetrahedral coordination exclusively in nanocrystalline material.[32] In the cubic Li-doped GST phases discussed in this contribution, the Ge occupation of the tetrahedral void and the resulting cation vacancies probably lead to local distortions of the atomic structure.

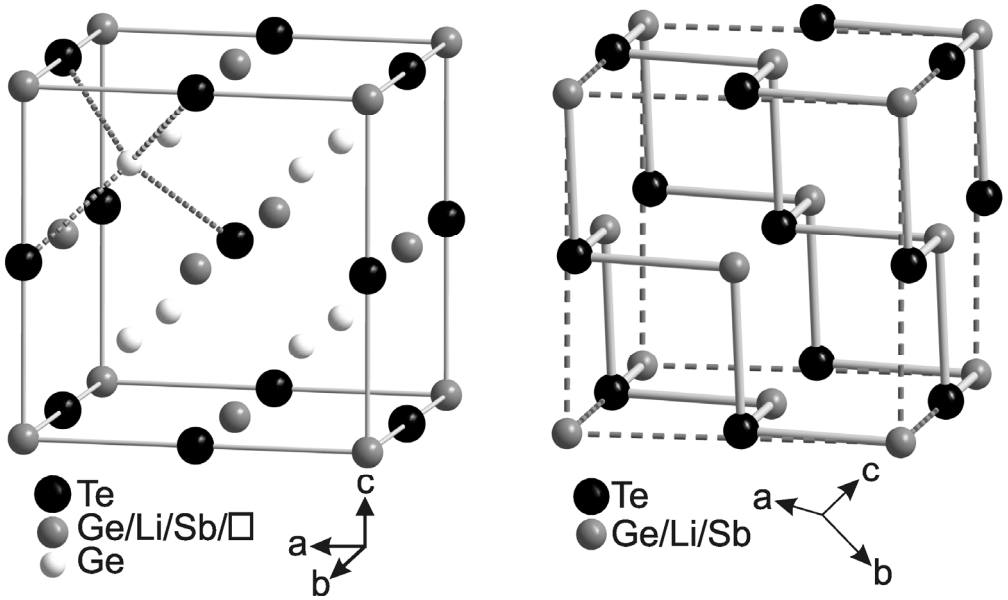

Fig. 1. Crystal structure of $(GeTe)_x(LiSbTe_2)_2$: NaCl type with partially filled tetrahedral voids of fcc packing of Te for x = 2, 3 (left, the occupancy factors of the Ge positions are small, cf. Table 2, the tetrahedral environment is indicated for one of the Ge atoms); GeTe type for x = 6, 11 (right, short interatomic distances are drawn as "bonds", the dotted line corresponds to the unit cell of the related NaCl-type structure, it is not the one of the GeTe type).

The powder patterns of $(GeTe)_6(LiSbTe_2)_2$ and $(GeTe)_{11}(LiSbTe_2)_2$ could be indexed assuming rhombohedral metrics, which is in accordance with the observed reflection splitting and broadening, respectively (cf. Fig. 2). Three structure models were taken into account: (a) the CuPt type (space group $R\bar{3}m$, no. 166),[33] which represents a rhombohedrally distorted (along <111>) variant of the rocksalt type structure without layer formation; (b) the GeTe type (space group $R3m$, no. 160),[27] a binary variant of the layered gray As type;[34] and the gray As type itself (space group $R\bar{3}m$, no. 166) which does not allow one to distinguish cations and anions as it has only one crystallographic position. It turned out that both compounds crystallize in a GeTe-type structure (cf. Fig. 1, right), because the different scattering densities on cation and anion positions, respectively, are obvious and 3+3 coordination of both cations and anions indicates the formation "As-type" layers as the *z* coordinate of the cations deviates significantly from 0.5. Such deviations from the NaCl type and the metric distortion become more pronounced for increasing GeTe contents x. All cations are disordered on the cation position; Te occupies the anion position. In these trigonal phases, no significant residual scattering densities were observed. Similar to the cubic phases, a common displacement parameter was refined for all cations and a separate one for Te; furthermore, slight preferred orientation was taken into account using spherical harmonics for the trigonal compounds.

The refined atomic parameters and the details of the structure refinements are given in Tables 1 and 2, respectively. Further details of the crystal structure investigations may be obtained from Fachinformationszentrum Karlsruhe, 76344 Eggenstein-Leopoldshafen, Germany (fax: (+49)7247-808-666; e-mail: crysdata@fiz-karlsruhe.de, http://www.fiz-karlsruhe.de/request_for_deposited_data.html) on quoting the depository numbers CSD 426293, 426294, 426295, 426296, 426297 and 426298 for x = 0, 1, 2, 3, 6 and 11, respectively.

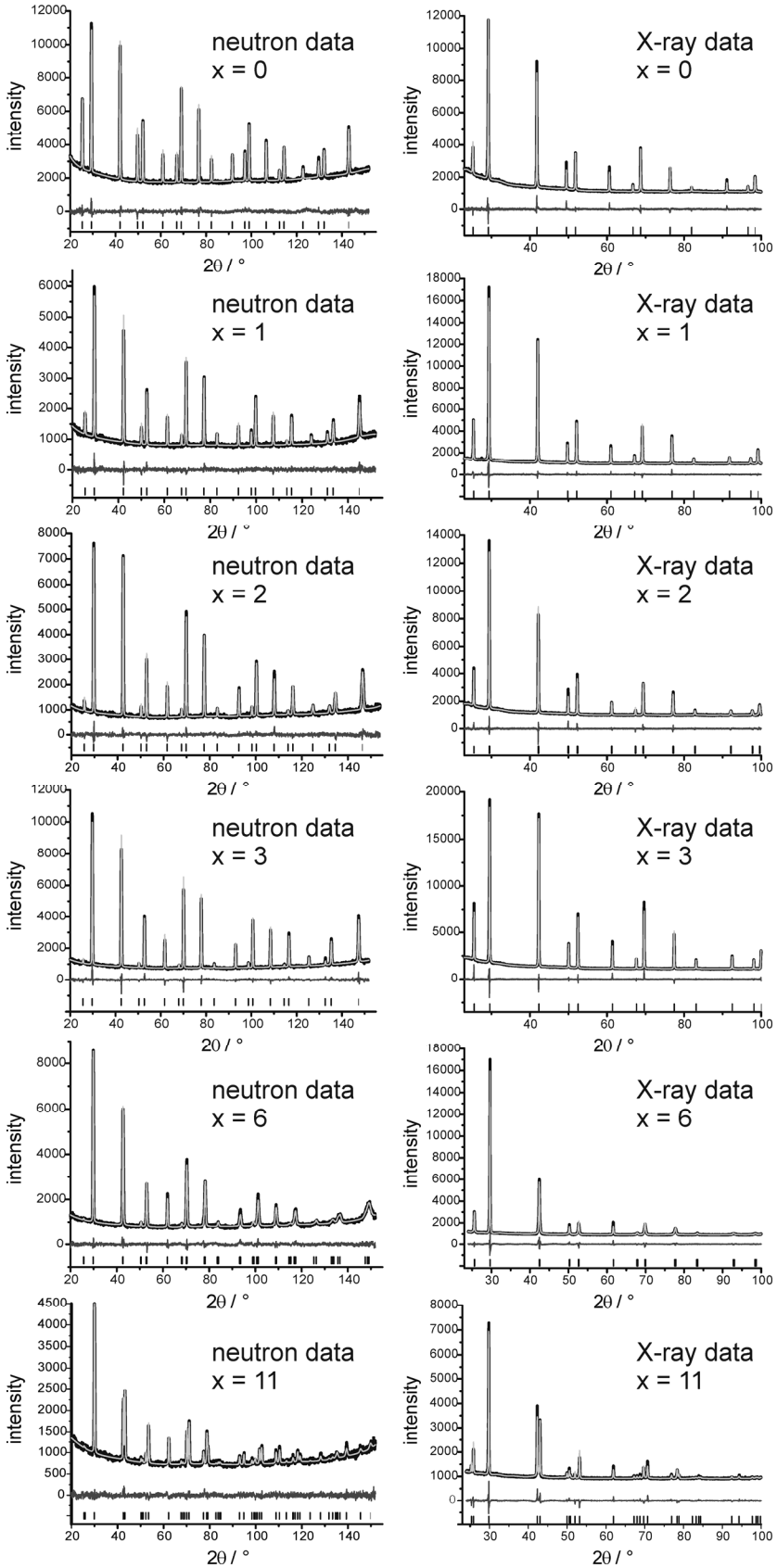

Fig. 2. Rietveld fits of the joint refinement of neutron data (left) and X-ray data (right) for $(GeTe)_x(LiSbTe_2)_2$ with x = 0, 1, 2, 3, 6 and 11 (top to bottom); experimental (black) and calculated data (light gray); difference plot (dark gray), peak positions (black, straight lines).

Table 1. Joint refinement results of neutron ($20° \leq 2\theta \leq 155°$; $\lambda = 1.5484$ Å) and X-ray ($23° \leq 2\theta \leq 100°$; $\lambda = 1.540596$ Å, i. e. Cu-$K_{\alpha 1}$) powder diffraction data for the $(GeTe)_x(LiSbTe_2)_2$ phases $Li_2Sb_2Te_4$, $Li_2GeSb_2Te_5$, $Li_2Ge_2Sb_2Te_6$, $Li_2Ge_3Sb_2Te_7$, $Li_2Ge_6Sb_2Te_{10}$ and $Li_2Ge_{11}Sb_2Te_{15}$ using the fundamental parameter approach.

compound	$Li_2Sb_2Te_4$	$Li_2GeSb_2Te_5$	$Li_2Ge_2Sb_2Te_6$	$Li_2Ge_3Sb_2Te_7$	$Li_2Ge_6Sb_2Te_{10}$	$Li_2Ge_{11}Sb_2Te_{15}$
asymmetric unit	$Li_{0.5}Sb_{0.5}Te$	$Li_{0.4}Ge_{0.2}Sb_{0.4}Te$	$Li_{0.33}Ge_{0.33}Sb_{0.33}Te$	$Li_{0.29}Ge_{0.43}Sb_{0.29}Te$	$Li_{0.2}Ge_{0.6}Sb_{0.2}Te$	$Li_{0.13}Ge_{0.73}Sb_{0.13}Te$
GeTe content x	0	1	2	3	6	11
molar mass / g mol^{-1}	191.95	193.6	194.7	195.5	196.9	198.0
Z	4				3	
$F(000)$	316	320	322.4	324.4	246	247.9
crystal system, space group	cubic, $Fm\bar{3}m$ (no. 225)				trigonal, $R3m$ (no. 160)	
lattice parameters / Å	6.10957(3)	6.06904(7)	6.05354(4)	6.03207(6)	a = 4.24590(7) c = 10.4382(2)	a = 4.20290(6) c = 10.5360(2)
volume / Å^3	228.051(3)	223.542(8)	221.834(4)	219.482(7)	162.966(7)	161.178(6)
constraints	1	2	4	4	2	2
number of reflections (neutron)	23	23	23	23	56	54
number of reflections (X-ray)	15	15	15	15	34	31
refined parameters / background	28 / 48	28 / 48	29 / 48	29 / 48	25 / 48	25 / 48
R_p / R_{wp} (neutron)	0.0246 / 0.0312	0.0325 / 0.0408	0.0359 / 0.0454	0.0367/ 0.0475	0.0341 / 0.0438	0.0314 / 0.0396
R_p / R_{wp} (X-ray)	0.0161 / 0.0246	0.0168 / 0.0280	0.0165 / 0.0251	0.0207 / 0.0359	0.0209 / 0.0357	0.0170 / 0.0275
Gof (neutron)	1.327	1.280	1.401	1.516	1.415	1.184
Gof (X-ray)	0.920	0.973	0.886	1.375	1.163	0.876

Table 2. Atom positions, site occupancy factors (s.o.f.) and displacement factors (B_{iso}) for the $(GeTe)_x(LiSbTe_2)_2$ phases $Li_2Sb_2Te_4$, $Li_2GeSb_2Te_5$, $Li_2Ge_2Sb_2Te_6$, $Li_2Ge_3Sb_2Te_7$, $Li_2Ge_6Sb_2Te_{10}$ and $Li_2Ge_{11}Sb_2Te_{15}$.

Sum formula	GeTe content x	Atom	Wyckoff position	x y z	s.o.f.	B_{iso}
$Li_2Sb_2Te_4$	0	Li, Sb	4*a*	0 0 0	½, ½	1.86(2)
		Te	4*b*	$^1/_2$ $^1/_2$ $^1/_2$	1	0.67(2)
$Li_2GeSb_2Te_5$	1	Li, Ge, Sb	4*a*	0 0 0	$^2/_5$, $^1/_5$, $^2/_5$	2.56(1)
		Te	4*b*	$^1/_2$ $^1/_2$ $^1/_2$	1	1.02(1)
$Li_2Ge_2Sb_2Te_6$	2	Li, Ge, Sb	4*a*	0 0 0	$^1/_3$, 0.322(1), $^1/_3$	2.56(2)
		Ge	8*c*	$^1/_4$ $^1/_4$ $^1/_4$	0.0054(6)	= B_{iso}(4*a*)
		Te	4*b*	$^1/_2$ $^1/_2$ $^1/_2$	1	1.36(1)
$Li_2Ge_3Sb_2Te_7$	3	Li, Ge, Sb	4*a*	0 0 0	$^2/_7$, 0.407(1), $^2/_7$	2.28(2)
		Ge	8*c*	$^1/_4$ $^1/_4$ $^1/_4$	0.0104(7)	= B_{iso}(4*a*)
		Te	4*b*	$^1/_2$ $^1/_2$ $^1/_2$	1	1.42(2)
$Li_2Ge_6Sb_2Te_{10}$	6	Li, Ge, Sb	3*a*	0 0 0.4860(4)	$^1/_5$, $^3/_5$, $^1/_5$	2.61(7)
		Te	3*a*	0 0 0	1	1.74(4)
$Li_2Ge_{11}Sb_2Te_{15}$	11	Li, Ge, Sb	3*a*	0 0 0.4817(3)	$^2/_{15}$, $^{11}/_{15}$, $^2/_{15}$	2.17(8)
		Te	3*a*	0 0 0	1	1.72(6)

3.4.3.2 Temperature dependent X-ray powder diffraction

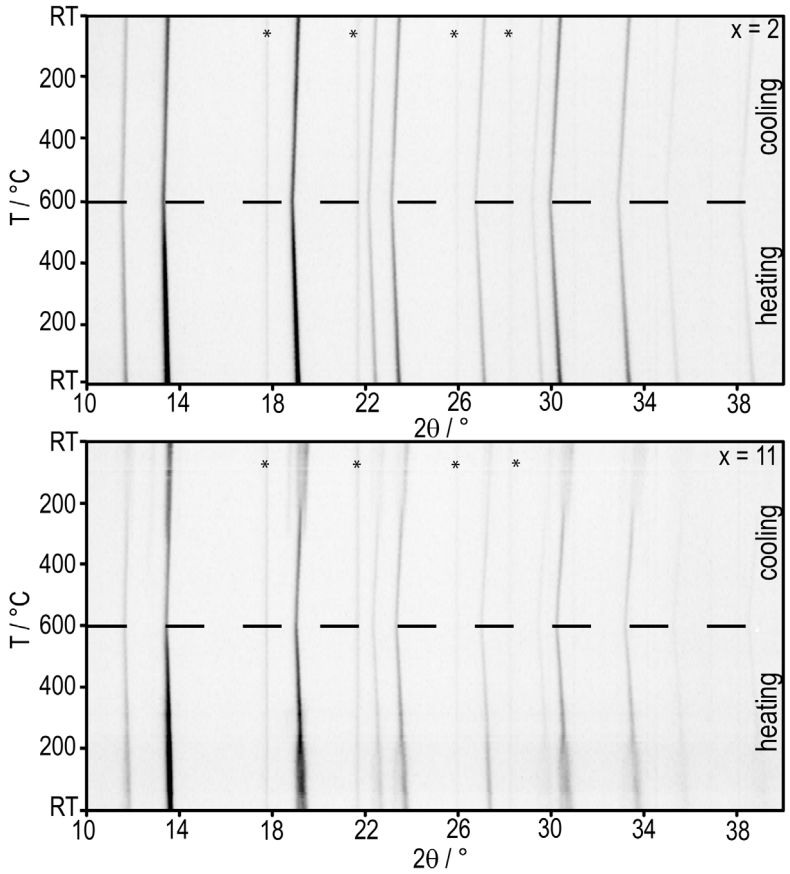

Fig. 3. Temperature dependent powder X-ray diffraction patterns of $(GeTe)_x(LiSbTe_2)_2$ for x = 2 (top) and x = 11 (bottom); the dashed line marks the highest temperature; asteriscs (*) mark the reflections caused by the furnace.

As explained in the Introduction, quenched $(GeTe)_nSb_2Te_3$ (GST) compounds with n > 3 show a phase transitions from the metastable (pseudo-)cubic to the trigonal layered phases at ~ 350°C and another one to the stable rocksalt-type HT phase at ~450 °C, which is characterized by random disorder of Ge, Sb and vacancies.[15,35] In contrast to GST, cubic $(GeTe)_x(LiSbTe_2)_2$ compounds (cf. Fig. 3 top for x = 2) show no such phase transitions, they are stable between room temperature and the melting point. Due to the exchange of Ge^{2+} with twice the amount of Li^+, no or just very few (for x = 2, 3) cation vacancies remain so that vacancy ordering is not a characteristic structural feature. The full width at half maximum of the reflections does not change with respect to the temperature; however, the intensities at high angles decrease at higher temperature due to the increasing displacement parameters.

Trigonal $(GeTe)_x(LiSbTe_2)_2$ compounds with $x \geq 6$ (cf. Fig. 3 bottom for x = 11) show a phase transition from an average GeTe-type structure to a rocksalt-type cubic high-temperature phase. At temperatures above 280 °C (for x = 11), the coordination number

changes from 3 + 3 to 6. This phase transition is similar to that of GeTe itself and has also been observed for TAGS materials $(GeTe)_xAgSbTe_2$.[27,28,36-40] It implies twinning upon cooling the cubic high-temperature phase due to the *translationengleiche* symmetry reduction from $Fm\bar{3}m$ to $R3m$. The temperature of the phase transition is lower than for $(GeTe)_nSb_2Te_3$, which might be explained by the lack of cation vacancies. The octahedral coordination of Te in $(GeTe)_x(LiSbTe_2)_2$ is impossible for rocksalt-type GST as cation defects, of course, mean incomplete polyhedra around anions. The higher the temperature, the more dominant are entropy effects which are not required for forming a defect-free rocksalt type.

3.4.3.3 Thermoelectric properties of $(GeTe)_{11}(LiSbTe_2)_2$

$(GeTe)_{11}(LiSbTe_2)_2$ can be viewed as the Li-substituted variant of metastable $(GeTe)_{12}Sb_2Te_3$; the stoichiometry is also quite similar to that of the well-known thermoelectric material TAGS-85 $(GeTe)_{85}(AgSbTe_2)_{15} = (GeTe)_{11.33}(AgSbTe_2)_2$.[38-40] In contrast to $LiSbTe_2$, which has a bandgap of 4.46 eV,[41] the compounds discussed in this section show metallic behavior. The electrical resistivity (ρ) increases with increasing temperature, the absolute values for $(GeTe)_{11}(LiSbTe_2)_2$ are between those of $(GeTe)_{12}Sb_2Te_3$ and TAGS-85 (Fig. 4 top). This is probably due to the higher ionicity of the Li-containing compound in comparison to $(GeTe)_{12}Sb_2Te_3$ and a lower charge carrier concentration in comparison to TAGS-85 as indicated by the latter's higher Seebeck coefficient (S). All compounds are p-type conductors as S is positive. In comparison to $(GeTe)_{12}Sb_2Te_3$, S of $(GeTe)_{11}(LiSbTe_2)_2$ is higher at room temperature, but does not increase as much as that of $(GeTe)_{12}Sb_2Te_3$ with respect to the temperature, so that it becomes lower at 300 °C (Fig. 4, third from top). Both compounds do not reach the extremely high S of TAGS-85; however, they approach it at higher temperatures.

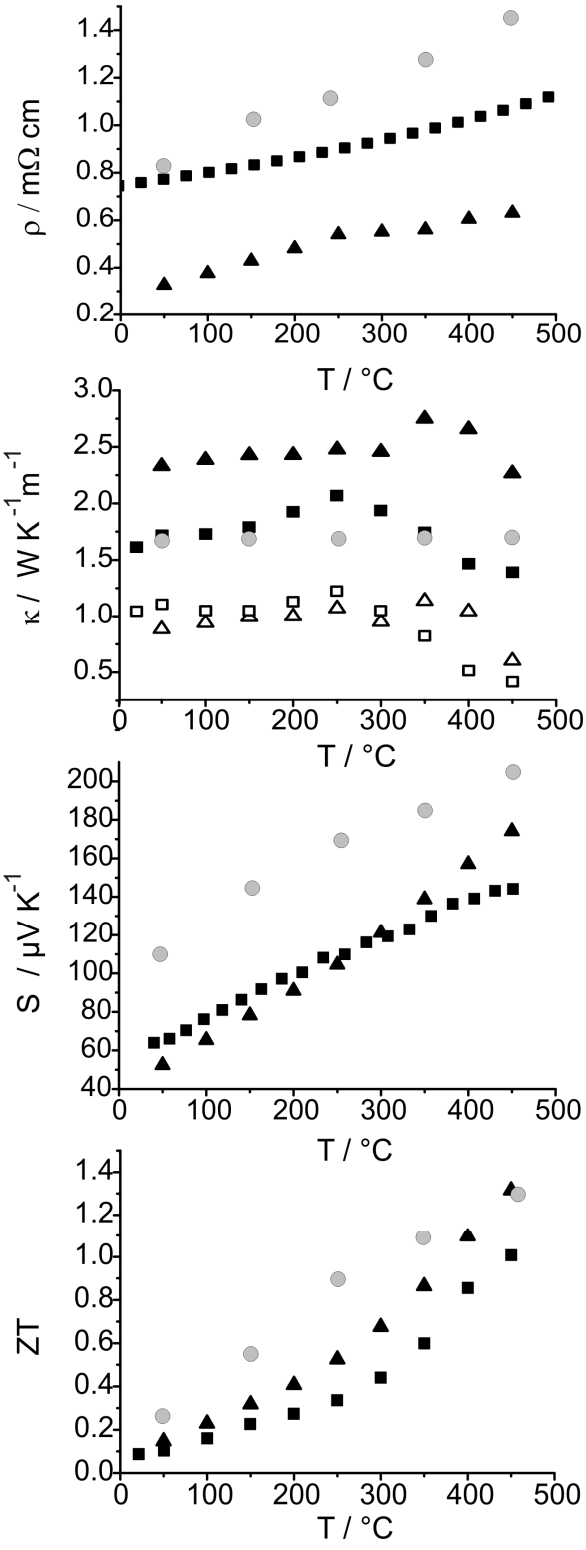

Fig. 4. Thermoelectric properties of $(GeTe)_{11}(LiSbTe_2)_2$ (■) in comparison with $(GeTe)_{12}Sb_2Te_3$ [from ref. [15]] (▲) and $(GeTe)_{11.3}(AgSbTe_2)_2$ [TAGS-85, from ref. [42]] (●), electrical conductivity (top); total thermal conductivity (second from top) with the phononic part given as empty symbols; Seebeck coefficient (third from top) and the ZT value (bottom).

Due to its higher ρ, $(GeTe)_{11}(LiSbTe_2)_2$ exhibits a lower thermal conductivity (κ) than the unsubstituted GST compound (Fig. 4, second from top). The phononic contribution to κ is in the same range for both compounds; however, in the low-temperature regime it is slightly lower for GST, whose crystal structure is characterized by intersecting defect layers. The temperature characteristics of κ reflect the phase transitions. At ~ 280 °C, $(GeTe)_{11}(LiSbTe_2)_2$ shows one phase transition before melting; κ increases with respect to the temperature until the rocksalt type is formed and then decreases at higher temperatures. Thus, in the 3D rocksalt-type phase, phonon scattering is more effective than in the layered GeTe type, probably because the cation disorder is dynamic up to a certain degree. For $(GeTe)_{12}Sb_2Te_3$, in contrast, κ reflects the two phase transitions described above at 350 °C and 450 °C, respectively. In this compound, ρ is also affected by the structural changes because the rearrangement of vacancy layers is reconstructive, while for the Li containing phase the phase transition just involves slight distortions. In contrast, κ of TAGS-85 is almost constant up to 450 °C. $(GeTe)_{11}(LiSbTe_2)_2$ possesses both a lower κ and a lower ρ and thus a lower phononic contribution of κ than TAGS-85 above 350 °C. This corroborates that Li atoms can be viewed as "pseudo"-vacancies. In comparison to $(GeTe)_{12}Sb_2Te_3$, the lower κ of $(GeTe)_{11}(LiSbTe_2)_2$ nearly compensates the higher ρ. This results in a *ZT* value of 1.0 at 450 °C (Fig. 4, bottom). This is lower than the one of metastable $(GeTe)_{12}Sb_2Te_3$; however, for $(GeTe)_{11}(LiSbTe_2)_2$ it corresponds to a thermodynamically stable phase that does not change its structure upon long-term annealing. The higher *ZT* value of TAGS-85 is a consequence of its very high *S*.

3.4.4 Conclusion

Exchanging Ge^{2+} by twice the amount of Li^+ reduces the concentration of vacancies in $(GeTe)_nSb_2Te_3$ and yields stable compounds of the solid solution series $(GeTe)_x(LiSbTe_2)_2$. These can be viewed as the Li variant of TAGS materials $(GeTe)_xAgSbTe_2$. Li-doped GST elegantly combines the high thermal stability of TAGS with the low phononic contribution to the thermal conductivity of GST compounds, because Li fills the cation vacancies and is very light, i.e. it can be viewed as a "pseudo-vacancy". The various defect ordering processes and diffusion phenomena of $(GeTe)_nSb_2Te_3$ [15,35] are not observed in $(GeTe)_x(LiSbTe_2)_2$, simply because there are no cation vacancies. Both the average crystal structures and the thermal behavior, i. e. the phase transition from the GeTe-type to the rocksalt-type, are comparable to the corresponding features of TAGS materials. However, neutron data for $(GeTe)_x(LiSbTe_2)_2$ (x = 2, 3) indicate that few percent of the Ge atoms occupy the tetrahedral voids which

probably cause distortions of the Te substructure. On the other hand, Li disorder might be dynamic at high temperature. Solid-state NMR might be an intriguing method to further investigate such phenomena.

The thermoelectric properties of $(GeTe)_{11}(LiSbTe_2)_2$ are promising, especially as the compound is long-term stable at all temperatures. The ZT value can probably be further improved by adjusting the GeTe content x and varying the cation vacancy concentration by not completely "filling" all vacancies. Due to the higher ionicity of the Li-doped compounds, the GeTe content of samples with the optimal *ZT* value is expected to be different from that of GST (n = 12, 19) and TAGS (x = 4, 5.67), respectively.

Acknowledgement

We thank T. Miller for the temperature-dependent powder diffraction experiments and H. Hartl for ICP-OES analyses. We are grateful to Prof. Dr. W. Schnick for the generous support of this work. This investigation was funded by the Deutsche Forschungsgemeinschaft (grant OE530/1-2) and the Studienstiftung des deutschen Volkes.

Supplementary information

Table S1. ICP-OES results for $Li_2Sb_2Te_4$, $Li_2GeSb_2Te_5$, $Li_2Ge_2Sb_2Te_6$, $Li_2Ge_3Sb_2Te_7$, $Li_2Ge_6Sb_2Te_{10}$ and $Li_2Ge_{11}Sb_2Te_{15}$ (experimental values normalized to add up to 100%).

sum formula	weight-% (calc.)	weight-% (found)
$Li_2Sb_2Te_4$	Li: 1.81, Sb: 31.72, Te: 66.48	Li: 2.05, Sb: 31.25, Te: 66.13
$Li_2GeSb_2Te_5$	Li: 1.43, Ge: 7.50, Sb: 25.16, Te: 65.91	Li: 1.55, Ge: 7.09, Sb: 25.09, Te: 65.66
$Li_2Ge_2Sb_2Te_6$	Li: 1.19, Ge: 12.43, Sb: 20.85, Te: 65.54	Li: 1.25, Ge: 12.18, Sb: 20.77, Te: 65.21
$Li_2Ge_3Sb_2Te_7$	Li: 1.01, Ge: 15.92, Sb: 17.80, Te: 65.27	Li: 1.09, Ge: 15.82, Sb: 17.65, Te: 64.70
$Li_2Ge_6Sb_2Te_{10}$	Li: 0.71, Ge: 22.13, Sb: 12.37, Te: 64.80	Li: 0.79, Ge: 21.59, Sb: 12.19, Te: 65.00
$Li_2Ge_{11}Sb_2Te_{15}$	Li: 0.47, Ge: 26.89, Sb: 8.20, Te: 64.44	Li: 0.51, Ge: 26.11, Sb: 7.97, Te: 64.67

References

[1] M. Wuttig, S. Raoux, *Z. Anorg. Allg. Chem.* **2012**, *638*, 2455.

[2] T. Siegrist, P. Merkelbach, M. Wuttig, *Annu. Rev. Condens. Matter Phys*. **2012**, *3*, 215.

[3] S. Raoux, *Annu. Rev. Mater. Res.* **2009**, *39*, 9.

[4] T. Matsunaga, H. Morita, R. Kojima, N. Yamada, K. Kifune, Y. Kubota, Y. Tabata, J.-J. Kim, M. Kobata, E. Ikenaga, K. Kobayashi, *J. Appl. Phys.* **2008**, *103*, 093511.

[5] P. P. Konstantinov, L. E. Shelimova, E.S. Avilov, M. A. Kretova, V. S. Zemskov, *Inorg. Mater.* **2001**, *37*, 788.

[6] L. E. Shelimova, O. G. Karpinskii, M. A. Kretova, V. I. Kosyakov, V. A. Shestakov, V. S. Zemskov, F. A. Kuznetsov, *Inorg. Mater.* **2000**, *36*, 928.

[7] L. E. Shelimova, O. G. Karpinskii, P. P. Konstantinov, M. A. Kretova, E.S. Avilov, V. S. Zemskov, *Inorg. Mater.* **2001**, *37*, 421.

[8] M. N. Schneider, T. Rosenthal, C. Stiewe, O. Oeckler, *Z. Kristallogr.* **2010**, *225*, 463.

[9] T. Matsunaga, N. Yamada, Y. Kubota, *Acta Crystallogr. Sect. B* **2004**, *60*, 685.

[10] M. Wuttig, N. Yamada, *Nature Mater.* **2007**, *6*, 824.

[11] M. Wuttig, D. Luesebrink, D. Wamwangi, W. Welnic, M. Gillessen, R. Dronskowski, *Nature Mater.* **2007**, *6*, 122.

[12] M. Wuttig, *Phys. Status Solidi B* **2012**, *249*, 1843.

[13] W. Zhang, A. Thiess, P. Zalden, R. Zeller, P. H. Dederichs, J.-Y. Raty, M. Wuttig, S. Blügel, R. Mazzarello, *Nature Mater.* **2012**, *11*, 952.

[14] R. Waser, R. Dittmann, M. Salinga, M. Wuttig, *Int. J. Mater. Res.* **2010**, *101*, 182.

[15] T. Rosenthal, M. N. Schneider, C. Stiewe, M. Döblinger, O. Oeckler, *Chem. Mater.* **2011**, *23*, 4349.

[16] D. L. Medlin, G. J. Snyder, *Curr. Opin. Colloid Interface Sci.* **2009**, *14*, 226.

[17] M. G. Kanatzidis, *Chem. Mater.* **2010**, *22*, 648.

[18] Y. C. Lan, A. J. Minnich, G. Chen, Z. F. Ren, *Adv. Funct. Mater.* 2010, *20*, 357.

[19] J. R. Sootsman, D. Y. Chung, M. G. Kanatzidis, *Angew. Chem. Int. Ed.* **2009**, *48*, 8616.

[20] E.-R. Sittner, K. S. Siegert, P. Jost, C. Schlockermann, F. R. L. Lange, M. Wuttig, *Phys Status Solidi A* **2013**, *1*, 147.

[21] S. N. Zhang, T. J. Zhu, S. H. Yang, C. Yu, X. B. Zhao, *Acta Mater.* **2010**, *58*, 4160.

[22] *TOPAS-Academic*, *V. 4.1*, Coelho Software, Brisbane, Australia, **2007**.

[23] J. de Boor, C. Stiewe, P. Ziolkowski, T. Dasgupta, G. Karpinski, E. Lenz, F. Edler, E. Müller, *J. Electron. Mater.* **2013**, *42*, 1711.

[24] J. de Boor, E. Müller, *Rev. Sci. Instrum.* **2013**, *84*, 065102.

[25] A. LeBail, A. Jouanneaux, *J. Appl. Crystallogr.* **1997**, *30*, 265.

[26] M. Evain, F. Boucher, R. Brec, J. Rouxel, J. S. Jung, C. J. O'Connor, *Eur. J. Sol. State Inorg. Chem.* **1992**, *29*, 1055.

[27] W. Klemm, G. Frischmuth, *Z. Anorg. Allg. Chem.* **1934**, *218*, 249.

[28] T. Chattopadhyay, J. Boucherle, H. von Schnering, *J. Phys. C* **1987**, *20*, 1431.

[29] A. V. Kolobov, P. Fons, A. I. Frenkel, A. L. Ankudinov, J. Tominaga, T. Uruga, *Nature Mater.* **2004**, *3*, 703.

[30] M. Xu, Y. Q. Cheng, H. W. Sheng, E. Ma, *Phys Rev. Lett.* **2009**, *103*, 195502.

[31] X. Q. Liu, X. B. Li, L. Zhang, Y. Q. Cheng, Z. G. Yan, M. Xu, X. D. Han, S. B. Zhang, Z. Zhang, E. Ma. *Phys Rev. Lett.* **2011**, *106*, 025501.

[32] S. Sen, T. G. Edwards, J.-Y. Cho, Y.-C. Joo, *Phys Rev. Lett.* **2012**, *108*, 195506.

[33] C. H. Johannson, J. O. Linde, *Ann. Phys. (Leipzig)* **1927**, *82*, 449.

[34] A. J. Bradley, *Phil. Mag.* **1924**, *47*, 657.

[35] M. N. Schneider, X. Biquard, C. Stiewe, T. Schröder, P. Urban, O. Oeckler, *Chem. Commun.* **2012**, *48*, 2192.

[36] J. Goldak, C. S. Barrett, D. Innes, W. Youdelis, *J. Chem. Phys.* **1966**, *44*, 3323.

[37] P. Fons, A. V. Kolobov, M. Krbal, J. Tominaga, K. S. Andrikopoulos, S. N. Yannopoulos, G. A. Voyiatzis, T. Uruga, *Phys. Rev. B* **2010**, *82*, 155209.

[38] B. A. Cook, M. J. Kramer, X. Wei, J. L. Harringa, E. M. Levin, *J. Appl. Phys.* **2007**, *101*, 053715.

[39] C.Wood, *Rep. Prog. Phys.* **1988**, *51*, 459.

[40] F. D. Rosi, J. P. Dismukes, E. F. Hockings, *Electron. Eng.* **1960**, *79*, 450.

[41] S.-G. Kang, W.-S. Chae, Y.-R. Kim, J.-S. Jung, S.-H. Lee, *Chem. Phys.* **2000**, *256*, 295.

[42] J. Davidow, Y. Gelbstein, *J. Electron. Mater.* **2013**, *42*, 1542.

4 Conclusion and Outlook

The results of this thesis about rocksalt-type and related disordered tellurides demonstrate how thermoelectric materials can be optimized in order to exhibit high ZT values. In indium-containing compounds side phases often play a crucial role (cf. Chapters 2.3, 2.4, 2.5 and 3.2). As it is common for most stable In compounds at ambient conditions, In is coordinated tetrahedrally by Te in these side phases. This tendency towards fourfold coordination makes the synthesis of homogeneous disordered compounds with octahedral or trigonal antiprismatic 3+3 In-atom coordination difficult. It is remarkable that on the one hand high-pressure conditions favor higher coordination numbers of In and thus make the synthesis of homogeneous compounds possible, whereas on the other hand in some cases high temperature (HT) is sufficient. Usually, these parameters have opposite effects, because high pressure favors a higher density and HT favors a lower density. Obviously, in addition to enthalpic reasons, entropy plays a decisive role for the synthesis of In-containing disordered tellurides that exhibit the rocksalt-type or related structures with sixfold coordination. The need of high-pressure conditions as well as limited insight into the structural chemistry, both of which are required for the successful synthesis of rocksalt-type tellurides with high In contents, may be the main reasons why so far the substitution of Sb^{3+} with In^{3+} had not been pursued in order to optimize the thermoelectric properties. It is difficult to confirm that the incorporation of 6-fold coordinated In is beneficial for the thermoelectric properties of disordered tellurides by comparing $AgIn_{0.5}Sb_{0.5}Te_2$ (cf. Chapter 2.4) with $AgSbTe_2$ and $AgInTe_2$, because the latter compound crystallizes in the chalcopyrite-type structure, and its rocksalt-type HP phase quickly retransforms to the chalcopyrite type at ambient pressure. However, solid solutions with GeTe such as $(GeTe)_{5.5}AgInTe_2$ exhibit higher ZT values below 125 °C than its corresponding antimony variant, namely the intensively investigated compound TAGS-85 = $(GeTe)_{5.5}AgSbTe_2$ (cf. Chapter 2.5). When preparing such solid solutions, it is essential to keep two things in mind: The thermoelectric properties are not only influenced by the crystal and real structure of the polycrystalline samples, but also by their texture, i. e. grain size and grain boundary concentration (c.f. Chapter 2.2). In addition, the compounds' anion and cation charges should be balanced. Otherwise, delocalized electrons, e. g. as observed for In_3SbTe_2, can lead to metal-like absolute values of the electrical conductivity and accordingly high thermal conductivity which precludes thermoelectric application (cf. Chapter 3.2).

In general, the idea of investigating and understanding the structural chemistry, phase transitions and decomposition reactions of bulk phase-change materials (PCMs) in order to

obtain thermoelectric materials led to many novel solid solutions. For example, the formation of chalcopyrite-type $AgInTe_2$ and the existence of its rocksalt-type high-pressure polymorph plays a crucial role for the synthesis of $Ag_{3.4}In_{3.7}Sb_{76.4}Te_{16.5}$ (cf. Chapter 2.3), $AgIn_xSb_{1-x}Te_2$ (cf. Chapter 2.4) and $(GeTe)_xAgIn_ySb_{1-y}Te_2$ (cf. Chapter 2.5). The similarity of the compositions, crystal structures as well as key properties like a low thermal conductivity of PCMs to thermoelectric materials was further complemented by the similarity between the most prominent thermoelectric material $(GeTe)_x(AgSbTe_2)_{100-x}$ (TAGS-x) and the metastable as well as the HT phases of the PCMs $(GeTe)_nSb_2Te_3$ (GST). Due to this relationship, it was possible to optimize the properties of TAGS and closely related materials by different synthetic approaches and concepts. The ideas pursued and results of the investigations on $(GeTe)_xAgIn_ySb_{1-y}Te_2$ (cf. Chapter 2.5), $Ge_{0.53}Ag_{0.13}Sb_{0.27}\square_{0.07}Te_1$, $Ge_{0.61}Ag_{0.11}Sb_{0.22}\square_{0.06}Te_1$ (cf. Chapter 3.3) and $(GeTe)_x(LiSbTe_2)_2$ (cf. Chapter 3.4) have to be understood as an optimization of both TAGS and GST materials. The optimizations presented in this thesis by suitable substitutions of the elements in TAGS materials have advantages as well as disadvantages. The substitution of Sb^{3+} by In^{3+} in TAGS increases the ZT value but leads to decomposition above 200 °C (cf. Chapter 2.5). However, this decomposition can be taken as a chance, because the highest ZT values were observed after the decomposition for $(GeTe)_xAgIn_{0.5}Sb_{0.5}Te_2$ samples. This observation might lead to a novel interesting heterogeneous system $AgInTe_2$/TAGS, which could be comparable to the well-known LAST materials $AgSbTe_2$/PbTe. Another approach to obtaining nanostructured In-containing compounds can be pursued by varying the Ag/In ratio of $(GeTe)_xAgInTe_2$ materials.

The introduction of cation vacancies in TAGS materials leads to a significant improvement of the thermoelectric properties. The nanostructured phase of $Ge_{0.53}Ag_{0.13}Sb_{0.27}\square_{0.07}Te_1$ exhibits a ZT value of 1.3 at 160 °C, which is higher than for any reported TAGS or GST materials at this temperature. However, this compound can only be applied below 200 °C, i. e. before the nanostructure is lost due to an irreversible phase transition to a long-periodically ordered trigonal phase (cf. Chapter 3.3). The ZT values of the trigonal phases of $Ge_{0.53}Ag_{0.13}Sb_{0.27}\square_{0.07}Te_1$ and $Ge_{0.61}Ag_{0.11}Sb_{0.22}\square_{0.06}Te_1$ are still in the top range of TAGS materials with vacancies; yet, these might be affected by stacking disorder of the van der Waals gaps. However, these modifications with stacking disordered van der Waals gaps might be regenerated by oscillating around the phase-transition temperatures to their cubic HT phases. Furthermore, the two phase transitions from the nanostructured phase to the trigonal phase and from the trigonal phase to the cubic HT phase upon heating both involve cation-

vacancy ordering phenomena that may cause severe stress due to volume differences of the involved phases and thus might influence the thermal cycling capacity.

One of the most promising approaches to increasing the ZT value of TAGS and GST materials is the use of Li^+ instead of Ag^+. This synthetic approach elegantly combines the thermal stability of vacancy-free compounds, e. g. only displacive phase transitions between an α-GeTe type and rocksalt-type HT phase, with a low phononic contribution to the thermal conductivity like the one observed for $Ge_{0.53}Ag_{0.13}Sb_{0.27}\square_{0.07}Te_1$ and $Ge_{0.61}Ag_{0.11}Sb_{0.22}\square_{0.06}Te_1$ (cf. Chapter 3.3) due to the large mass difference of Li and Te. $(GeTe)_x(LiSbTe_2)_2$ compounds exhibit promising thermal stabilities and ZT values of 1 at 450 °C (cf. Chapter 3.4) due to their low thermal conductivities. In order to obtain compounds that outperform TAGS and GST materials, the electrical properties of $(GeTe)_x(LiSbTe_2)_2$ could further be optimized, e. g. by adjusting the GeTe content, by using a different light monovalent cation like Na^+ or by only partially substituting Ag^+ in compounds like $(GeTe)_x(Ag_yLi_{1-y}SbTe_2)_{100-x}$ and $(GeTe)_x(Ag_yNa_{1-y}SbTe_2)_{100-x}$, respectively. The introduction of cation vacancies might lead to similar ordering motifs as observed for GST and TAGS materials with cation vacancies. This may be influenced by the Li/Sb or Na/Sb ratio, resulting in $Ge_{0.61}Li_{0.11}Sb_{0.22}\square_{0.06}Te_1$ and $Ge_{0.61}Na_{0.11}Sb_{0.22}\square_{0.06}Te_1$, respectively. This approach has been pursued but leaves intriguing open questions for further work.

It is remarkable that the ZT values of even the best investigated and understood thermoelectric materials, e. g. TAGS, can be significantly increased by using novel synthetic approaches, e. g. substitution of Sb with In under high-pressure conditions, and by exploiting the structure-property relationships of related materials, as was shown by the introduction of cation vacancies due to an adjusted Ag/Sb ratio.

5 Summary

Nanostructures in metastable $GeBi_2Te_4$ obtained by high-pressure synthesis and rapid quenching and their influence on physical properties

In the course of the present thesis, a variety of new metastable solid solutions and modifications of disordered tellurides were obtained using high-pressure (HP) high-temperature (HT) syntheses. For $GeBi_2Te_4$, which has been proposed as a phase-change material (PCM), this synthesis route yields metastable modifications whose real structure strongly depends on the thermal treatment under high pressure. The average structure of the metastable compounds corresponds to the trigonal CuPt type (space group $R\bar{3}m$), which can be understood as a NaCl-type structure "stretched" along [111]. While quenching melts of $GeBi_2Te_4$ under a pressure of 12 GPa yields randomly oriented grains with sizes < 10 nm, which are semiconducting, slowly cooling the samples to room temperature (RT) at the same pressure before decompression leads to particle sizes ≥ 100 nm with twinned as well as single-domain areas and metal-like characteristics of the electrical resistivity. Upon heating, the long-periodically ordered stable In_3Te_4-type modification of $GeBi_2Te_4$ with a 21*R* stacking sequence is formed. In contrast to the HP experiments, rapid quenching by melt spinning at ambient pressure also yields the 21*R* type phase, however, with much smaller crystallite sizes. The differences in the characteristics of the resistivity and the different absolute values of all investigated samples can be attributed to the variation of the grain boundary concentration and the grain size distribution. Consistently, the comparison of the thermoelectric properties of an annealed ingot of 21*R*-type $GeBi_2Te_4$, a cold pressed powder pellet of 21*R*-type $GeBi_2Te_4$ and a cold pressed powder pellet of melt-spun 21*R*-type $GeBi_2Te_4$ shows that with decreasing grain size the resistivity dramatically increases and the ZT value drops by more than one order of magnitude.

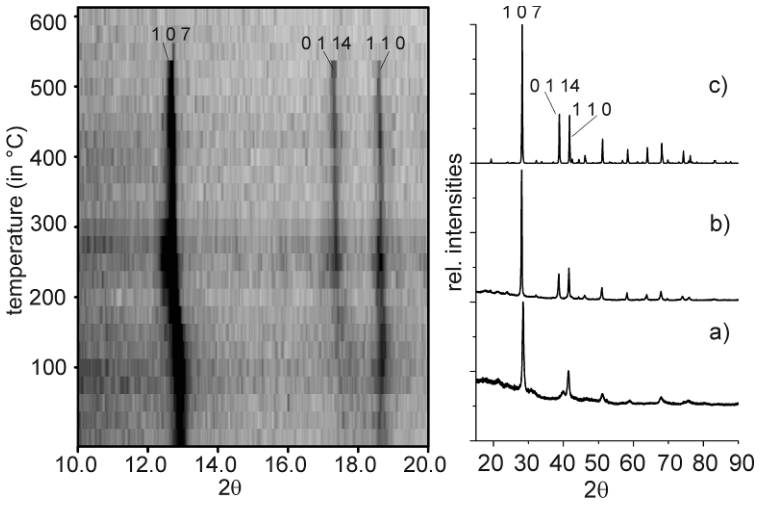

Two synthetic approaches to $Ag_{3.4}In_{3.7}Sb_{76.4}Te_{16.5}$ bulk samples and their transport properties

In contrast to $GeBi_2Te_4$, the PCM $Ag_{3.4}In_{3.7}Sb_{76.4}Te_{16.5}$ (AIST), which is used in rewritable CDs, has no thermodynamically stable modification; its stable state corresponds to a mixture of chalcopyrite-type $AgInTe_2$ and a trigonal In-doped Sb-rich antimony telluride $Sb_{7.9}Te$:In with a gray As type (*A*7) average structure. Whereas conventional solid-state syntheses do not yield bulk samples of homogeneous AIST material, both HP syntheses (12 GPa, quenching from 850 °C) and melt-spinning afforded quaternary samples. Their average structures correspond to the *A*7 structure type, i. e. all atoms share the same Wyckoff position. However, the metrics and the atom-layer distances differ significantly for the two synthesis routes. Probably there is a quaternary cubic HP phase, which upon decompression transforms into multiply twinned *A*7-type AIST. This involves stress and therefore the metrics remains strained and closer to that of the HP phase than the one of the melt-spun sample. Upon heating, both samples decompose to form $AgInTe_2$ and $Sb_{7.9}Te$:In. The metrics of HP-AIST relaxes before this decomposition and thus become comparable to that of the melt-spun sample. It is remarkable but well understood why both routes lead to comparable samples. One the one hand, the solidification of AIST during melt-spinning is faster than the nucleation of $AgInTe_2$. One the other hand, indium prefers tetrahedral coordination of Te at ambient conditions whereas under HP conditions $AgInTe_2$ forms a rocksalt-type structure in which In is octahedrally coordinated and thus forms solid solutions with other compounds in which the coordination number is 6 or 3+3, respectively. Thermoelectric measurements of annealed, partially decomposed, melt-spun AIST show a very low thermal conductivity, but the low Seebeck coefficient limits the thermoelectric figure of merit ZT to only 0.003 at RT.

A high pressure route to thermoelectrics with low thermal conductivity: the solid solution series $AgIn_xSb_{1-x}Te_2$

The rocksalt-type HP phase of $AgInTe_2$ is not stable at ambient pressure and thus retransforms to the chalcopyrite-type structure upon decompression. However, rocksalt-type solid solutions $AgIn_xSb_{1-x}Te_2$ (x = 0.1, 0.2, 0.4, 0.5 and 0.6) obtained under high pressure conditions (2.5 GPa, 400 °C), which again promote the octahedral coordination of In by Te, are metastable at ambient conditions. The lattice parameter decreases with increasing In content and all cations share the same Wyckoff position. There is no pronounced short-range order. The random cation disorder further reduces the low thermal conductivities of both

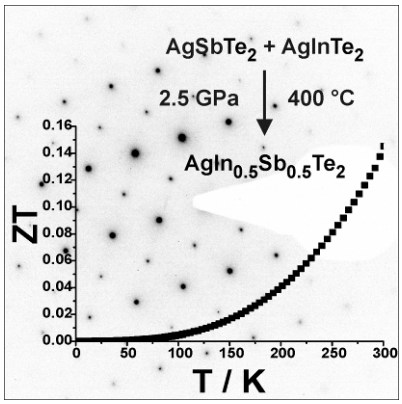

$AgSbTe_2$ and chalcopyrite-type $AgInTe_2$ to < 0.5 W/Km, which represent the lowest values observed for rocksalt-type tellurides. Among the investigated compounds, $AgIn_{0.5}Sb_{0.5}Te_2$ exhibits the best ZT value of 0.15 at RT. Although the low thermal conductivities of rocksalt-type tellurides are a promising outlook concerning thermoelectric properties, the decomposition into chalcopyrite-type $AgInTe_2$ and rocksalt-type $AgSbTe_2$, which takes place at 140 °C, as well as the rather low Seebeck coefficients and thus lower ZT values in comparison to the benchmark system $AgSbTe_2$ remain as drawbacks.

TAGS-related indium compounds and their thermoelectric properties – the solid solution series $(GeTe)_xAgIn_ySb_{1-y}Te_2$ (x = 1 – 12; y = 0.5 and 1)

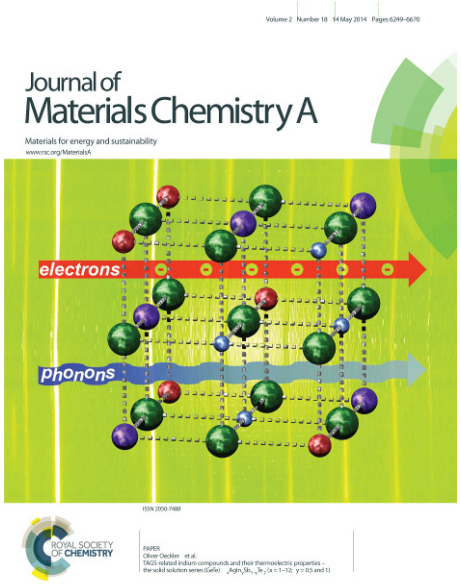

In order to improve the electronic properties of $AgIn_xSb_{1-x}Te_2$, solid solutions of GeTe and $AgIn_{0.5}Sb_{0.5}Te_2$, which showed optimal properties among the members of the solid-solution series $AgIn_xSb_{1-x}Te_2$, were synthesized along with solid solutions between GeTe and $AgInTe_2$. In all compounds In is sixfold coordinated by Te. In contrast to $AgIn_xSb_{1-x}Te_2$ and $Ag_{3.4}In_{3.7}Sb_{76.4}Te_{16.5}$, HP conditions are not generally required for solid solutions $(GeTe)_xAgIn_{0.5}Sb_{0.5}Te_2$ and $(GeTe)_xAgInTe_2$ (TIGS). For In contents of 7-8 atom%, e. g. $(GeTe)_5AgInTe_2$, stable cubic HT phases are favored by entropy. For In contents ≤ 3.6 atom% (such as $(GeTe)_{12}AgInTe_2$ and $(GeTe)_xAgIn_{0.5}Sb_{0.5}Te_2$ with $x \geq 5$), quenching almost completely suppresses the nucleation of chalcopyrite-type $AgInTe_2$ and thus these materials could be obtained without applying HP. Yet, HRTEM reveals a small amount of nanoscopic precipitates, which do not contribute to PXRD patterns. The synthesis of samples with higher In contents (such as $(GeTe)_xAgInTe_2$ with $x \leq 12$ and $(GeTe)AgIn_{0.5}Sb_{0.5}Te_2$) again requires HP conditions (2.5 GPa, 350 °C). While the existence of HT phases, and decomposition reactions into $AgInTe_2$ and GeTe or $(GeTe)_{2x}AgSbTe_2$, respectively, are dominated by the In content, the crystal structures mainly depend on the GeTe content. Both $(GeTe)_xAgInTe_2$ and $(GeTe)_xAgIn_{0.5}Sb_{0.5}Te_2$ crystallize in the rocksalt

type for $x \leq 5$ and in the α-GeTe type for $x > 5$ with 3 or 4 cations, respectively, sharing the same Wyckoff position. The cubic lattice parameter is smaller for TIGS compounds and the tendency to form layers in the α-GeTe-type phases is less pronounced than in the corresponding quinary compounds. While the thermoelectric properties of $(GeTe)_{5.5}AgIn_{0.5}Sb_{0.5}Te_2$ are comparable to those of the corresponding TAGS-85 material $(GeTe)_{5.5}AgSbTe_2$ up to the decomposition temperature, $(GeTe)_{5.5}AgInTe_2$ exhibits better thermoelectric properties due to a higher Seebeck coefficient than both the corresponding quinary compound and TAGS-85 itself. The higher ZT value of TIGS in combination with the possibility to synthesize some of these samples without HP renders these compounds with octahedrally coordinated In as promising thermoelectric materials which may further be optimized.

Disorder and transport properties of In_3SbTe_2 – an X-ray, neutron and electron diffraction study

In_3SbTe_2, which was also proposed for PCM applications, is another interesting In compound with a rocksalt-type HT phase. Like $Ag_{3.4}In_{3.7}Sb_{76.4}Te_{16.5}$, it does not have a thermodynamically stable modification at ambient conditions, where the stable state corresponds to a mixture of sphalerite-type InSb and TlSe-type InTe, both containing tetrahedrally coordinated In. Quenching the HT phase yields metastable rocksalt-type In_3SbTe_2. A combined approach applying electron, neutron and X-ray diffraction showed that In occupies the cation position and, in contrast to the other compounds investigated in this thesis, the anion position is shared by Sb and Te. Atoms are locally displaced from the average positions along <100>, which is indicated by diffuse scattering in X-ray and electron diffraction patterns. No superstructure formation could be observed. Both upon heating and upon electron irradiation, the compound decomposes into the two-phase stable state. As there is Sb/Te disorder and In^{2+} is very unlikely, the compound may be understood as $(In^{3+})_3Sb^{3-}(Te^{2-})_2 \cdot 2e^-$. This is supported by the metallic characteristics and high absolute values of the electrical conductivity both before and after decomposition which together with the associated high thermal conductivity precludes the thermoelectric application of this material.

Nanostructures in Te/Sb/Ge/Ag (TAGS) thermoelectric materials induced by phase transitions associated with vacancy ordering

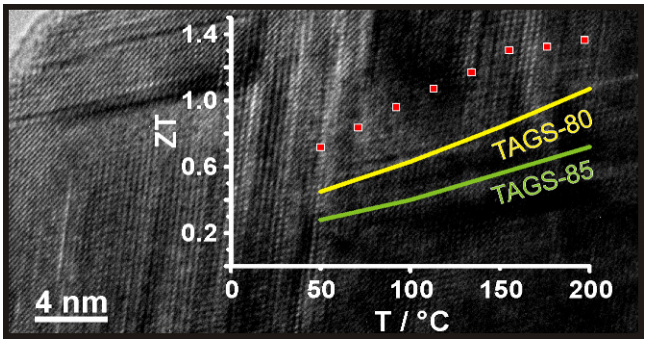

The introduction of cation vacancies in well-known thermoelectric TAGS materials $(GeTe)_xAgSbTe_2$ (TAGS) involves a similar structural chemistry as observed for $(GeTe)_nSb_2Te_3$ materials, and the cation vacancies strongly influence the thermoelectric properties, nanostructures and phase transitions of e.g. $Ge_{0.53}Ag_{0.13}Sb_{0.27}\square_{0.07}Te_1$, $Ge_{0.61}Ag_{0.11}Sb_{0.22}\square_{0.06}Te_1$ and $Ge_{0.77}Ag_{0.07}Sb_{0.13}\square_{0.03}Te_1$. Such vacancy-containing TAGS materials are rather different from conventional ones with a constant Ag/Sb ratio of 1. While quenched $Ge_{0.77}Ag_{0.07}Sb_{0.13}\square_{0.03}Te_1$ exhibits the α-GeTe-type structure of conventional TAGS materials, quenched $Ge_{0.53}Ag_{0.13}Sb_{0.27}\square_{0.07}Te_1$ and $Ge_{0.61}Ag_{0.11}Sb_{0.22}\square_{0.06}Te_1$ adopt rocksalt-type average structures. These are associated with short-range ordering of the cation vacancies which form layers with limited lateral extension perpendicular to the cubic <111> directions. These layers intersect and thereby form parquet-like nanostructures comparable to those in Ag-free $(GeTe)_{12}Sb_2Te_3$ and related phases. At 200 °C, long-periodically ordered trigonal phases with parallel van der Waals gaps are formed, which transform into a rocksalt-type HT phase with statistically disordered cation vacancies at 400 °C. The nanostructure cannot be retrieved without repeating the quenching process. Slow cooling affords the long-periodically trigonal modification with equidistant van der Waals gaps. In case of $Ge_{0.53}Ag_{0.13}Sb_{0.27}\square_{0.07}Te_1$, the trigonal $Ge_5As_2Te_8$-type structure with a 15*P* stacking sequence could be assigned. The thermal conductivity of the cation vacancy containing compounds, especially the phononic contribution, is lowered up to 450 °C, while the electronic properties remain almost unchanged compared to conventional TAGS materials. The ZT value of nanostructured $Ge_{0.53}Ag_{0.13}Sb_{0.27}\square_{0.07}Te_1$ of 1.3 at 160 °C is significantly higher than those of the best TAGS materials at this temperature. Furthermore, the thermoelectric properties of the trigonal phases are in good accordance to other TAGS materials with Ag/Sb ratio < 1. While the investigated compounds exhibit improved thermoelectric properties, the reconstructive phase transitions that involve cation ordering processes are a drawback for the thermal cycling capacities, i. e. the materials could only be applied in limited temperature ranges.

The solid solution series $(GeTe)_x(LiSbTe_2)_2$ ($1 \leq x \leq 11$) and the thermoelectric properties of $(GeTe)_{11}(LiSbTe_2)_2$

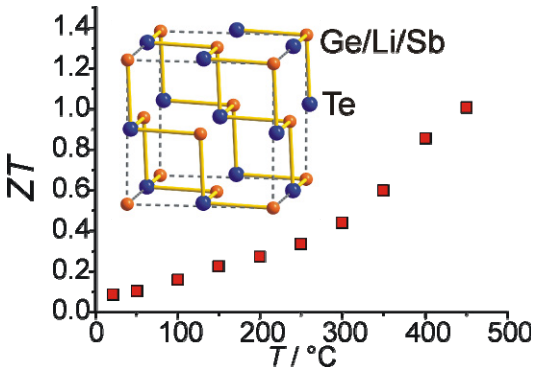

In order to preserve the low phononic contribution to the thermal conductivity and at the same time restrict phase transitions to displacive ones, light Li^+ cations instead of Ag^+ may mimic vacancies from the point of view of phonon proliferation but avoid structural instabilities. The solid-solution series $(GeTe)_x(LiSbTe_2)_2$ ($1 \leq x \leq 11$) reflects the approach of exchanging one Ge^{2+} by two Li^+ in $(GeTe)_nSb_2Te_3$. Comparable to $(GeTe)_xAgIn_{0.5}Sb_{0.5}Te_2$ and $(GeTe)_xAgInTe_2$, the crystal structure of the Li-containing compounds depends mainly on their GeTe content. For $(GeTe)_x(LiSbTe_2)_2$ with $x < 6$, they crystallize in a rocksalt-type structure, which is stable up to ~600 °C. Neutron diffraction shows that for $x = 2$ and 3 small fractions of Ge occupy tetrahedral voids. For $x \geq 6$, the α-GeTe-type structure is observed, with a reversible displacive phase transition to a rocksalt-type HT phase at ~ 280 °C. $(GeTe)_{11}(LiSbTe_2)_2$ exhibits a promising ZT value of 1 at 450 °C, mainly due to the low phononic contribution to the thermal conductivity. This ZT value is slightly lower than those of the corresponding TAGS-85 and $(GeTe)_{12}Sb_2Te_3$ compounds; however, no metastable phases are involved. Introducing Li in disordered tellurides is thus an elegant way to combine the thermal stability of vacancy-free compounds with the low phononic contribution to the thermal conductivity of vacancy-containing compounds.

6 Publications

6.1 Part of this thesis

This section lists the contributions of the individual authors to the publications that are part of this thesis. Oliver Oeckler, who is the supervisor of this PhD thesis, initiated the projects, contributed to their development and the discussion of the results and revised all manuscripts.

[1] **Nanostructures in metastable $GeBi_2Te_4$ obtained by high-pressure synthesis and rapid quenching and their influence on physical properties**
T. Schröder, M. N. Schneider, T. Rosenthal, A. Eisele, C. Gold, E.-W. Scheidt, W. Scherer, R. Berthold, O. Oeckler
Phys. Rev. B **2011**, *84,* 184104.

Thorsten Schröder wrote the publication, prepared the samples and evaluated all data, except TEM data, which were collected and evaluated by Tobias Rosenthal, who also revised the manuscript and supplied the TEM-related figures. Andreas Eisele performed preliminary experiments under the supervision of Matthias Schneider. Rico Berthold helped with the operation of the melt-spinning apparatus at the Max Planck Institute for Chemical Physics of Solids. The transport property measurements were carried out by Christian Gold, Ernst-Wilhelm Scheidt and Wolfgang Scherer at the University of Augsburg; all of them also contributed to the interpretation of the data and revised the manuscript.

[2] **Two synthetic approaches to $Ag_{3.4}In_{3.7}Sb_{76.4}Te_{16.5}$ bulk samples and their transport properties**
T. Schröder, T. Rosenthal, C. Gold, E.-W. Scheidt, W. Schnick, O. Oeckler
Z. Anorg. Allg. Chem. **2013**, *639*, 2868 – 2874.

Thorsten Schröder wrote the publication, prepared the samples and evaluated all data, except TEM data, which were collected by Tobias Rosenthal, who also helped with their evaluation. Thermoelectric measurements were carried out by Christian Gold and Ernst-Wilhelm Scheidt at the University of Augsburg; who also contributed to the interpretation of the data. Wolfgang Schnick contributed to the discussion. All coauthors revised the manuscript.

[3] **A high-pressure route to thermoelectrics with low thermal conductivity: the solid solution series $AgIn_xSb_{1-x}Te_2$**
T. Schröder, T. Rosenthal, D. Souchay, C. Petermayer, S. Grott, E.-W. Scheidt, C. Gold, W. Scherer, O. Oeckler
J. Solid State Chem. **2013**, *206*, 20 – 26.

Thorsten Schröder wrote the publication, prepared most samples and evaluated all data. Under his supervision, some samples were prepared and preliminary experiments were carried out by Daniel Souchay as part of his research internship, and by Christian Petermayer and Sebastian Grott as part of their bachelor theses. TEM experiments were carried out and the text was revised by Tobias Rosenthal. The thermoelectric measurements were carried out by Christian Gold, Ernst-Wilhelm Scheidt and Wolfgang Scherer at the University of Augsburg; all of them also contributed to the interpretation of the data and revised the manuscript.

[4] **TAGS-related indium compounds and their thermoelectric properties – the solid solution series $(GeTe)_xAgIn_ySb_{1-y}Te_2$ (x = 1 – 12; y = 0.5 and 1)**
T. Schröder, T. Rosenthal, N. Giesbrecht, S. Maier, E.-W. Scheidt, W. Scherer, G. J. Snyder, W. Schnick, O. Oeckler
J. Mater. Chem. A **2014**, *2*, 6384 – 6395.

Thorsten Schröder wrote the publication, synthesized some samples to complete the solid solution series and evaluated all data. Under his supervision, the other samples were prepared and thermoelectric measurements were carried out by Nadja Giesbrecht and Stefan Maier as part of their research internships. Tobias Rosenthal carried out the TEM experiments and, in close collaboration with Thorsten Schröder, evaluated the corresponding data and developed the figures and text concerning the TEM section. The high-temperature thermoelectric measurements were carried out at the California Institute of Technology under the supervision of G. Jeffrey Snyder, who added to the discussion of the data and revised the text. The low-temperature thermoelectric measurements were carried out by Ernst-Wilhelm Scheidt and Wolfgang Scherer at the University of Augsburg; all of them contributed to the interpretation of the data and revised the manuscript. Wolfgang Schnick contributed to the discussion and revised the text.

[5] **Disorder and transport properties of In_3SbTe_2 – an X-ray, neutron and electron diffraction study**
T. Schröder, T. Rosenthal, S. Grott, C. Stiewe, J. de Boor, O. Oeckler
Z. Anorg. Allg. Chem. **2013**, *639*, 2536 – 2541.

Thorsten Schröder wrote the publication, prepared the samples and evaluated all data, except TEM data. Under his supervision, Sebastian Grott helped with the synthesis of other samples as part of his bachelor thesis. Tobias Rosenthal contributed to this publication by TEM data collection, their evaluation and providing the resulting figures as well as the revision of the

manuscript. Thermoelectric characterization was carried out by Johannes de Boor and Christan Stiewe at the German Aerospace Center.

[6] **Nanostructures in Te/Sb/Ge/Ag (TAGS) thermoelectric materials induced by phase transitions associated with vacancy ordering**
T. Schröder, T. Rosenthal, N. Giesbrecht, M. Nentwig, S. Maier, H. Wang, G. J. Snyder, O. Oeckler
Inorg. Chem. **2014**, *53*, 7722 – 7729.

Thorsten Schröder wrote the manuscript, prepared samples for TEM and PXRD investigations and evaluated all data. Markus Nentwig performed preliminary experiments and provided one sample for the Rietveld refinement as part of his bachelor thesis. Nadja Giesbrecht and Stefan Maier prepared the samples for thermoelectric characterization under Thorsten Schröder's supervision as part of their research internships and they also carried out the thermoelectric measurements at the California Institute of Technology under the supervision of G. Jeffrey Snyder and Heng Wang, who also discussed the results and revised the text. Tobias Rosenthal conducted the TEM experiments and revised the manuscript.

[7] **The solid solution series $(GeTe)_x(LiSbTe_2)_2$ $(1 \leq x \leq 11)$ and the thermoelectric properties of $(GeTe)_{11}(LiSbTe_2)_2$**
T. Schröder, S. Schwarzmüller, C. Stiewe, J. de Boor, M. Hölzel, O. Oeckler
Inorg. Chem. **2013**, *52*, 11288 – 11294.

Thorsten Schröder wrote the publication and evaluated all data. Stefan Schwarzmüller assisted him with the preparation of the samples as part of his bachelor thesis and helped with the collection of the neutron-diffraction data. Markus Hölzel helped with the operation of the SPODI neutron diffractometer at the FRMII and revised the manuscript. Thermoelectric characterization was carried out by Johannes de Boor and Christan Stiewe at the German Aerospace Center.

6.2 Other Publications

[1] **Mercury azides and the azide of Millon's Base**
H. Lund, O. Oeckler, T. Schröder, A. Schulz, A. Villinger
Angew. Chem. Int. Ed. **2013**, *52*, 10900 – 10904.

[2] **From metastable to stable modifications - *in situ* Laue diffraction investigation of diffusion processes during the phase transitions of $(GeTe)_nSb_2Te_3$ ($6 < n < 15$) crystals**
M. N. Schneider, X. Biquard, C. Stiewe, T. Schröder, P. Urban, O. Oeckler
Chem. Commun. **2012**, *48*, 2192 – 2194.

[3] **$(GeTe)_nSbInTe_3$ ($n \leq 3$) – element distribution and thermal behavior**
F. Fahrnbauer, P. Urban, S. Welzmiller, T. Schröder, T. Rosenthal, O. Oeckler
J. Solid State Chem. **2013***, 208*, 20 – 26.

[4] **Thermoelectric properties of metastable Ge/Sb/Te and Ge/Bi/Te compounds**
T. Schröder, M. N. Schneider, T. Rosenthal, P. Urban, F. Fahrnbauer, C. Stiewe, C. Gold, E.-W. Scheidt, W. Scherer, O. Oeckler
AIP Conf. Proc. **2012**, *1449,* 159 – 162.

[5] **$Ba_6Si_6N_{10}O_2(CN_2)$ – a nitridosilicate with a NPO-zeolite structure type containing carbodiimide ions**
S. Pagano, O. Oeckler, T. Schröder, W. Schnick
Eur. J. Inorg. Chem. **2009**, 2678 – 2683.

6.3 Conference contributions

[1] **Solid solutions of $CdIn_2Te_4$ and silver indium tellurides: structure and element distribution by resonant X-ray scattering**
S. Welzmiller, F. Hennersdorf, T. Schröder, G. Wagner, O. Oeckler
22nd Annual Meeting of the German Crystallographic Society, Berlin **2014**

[2]* **Tuning the thermoelectric properties of quaternary tellurides by varying the vacancy concentration**
T. Schröder, T. Rosenthal, S. Maier, M. Nentwig, O. Oeckler
32th International Conference on Thermoelectrics, Kobe (Japan) **2013**

[3] **Influencing the thermoelectric properties of germanium antimony tellurides (GST) by substitution with In, Sn and Se**
T. Rosenthal, T. Schröder, P. Urban, S. Welzmiller, C. Stiewe, O. Oeckler
32th International Conference on Thermoelectrics, Kobe (Japan) **2013**

[4] **Real-structure effects of quaternary and quinary germanium antimony telluride thermoelectrics caused by doping with silver and indium**
L. Neudert, T. Rosenthal, T. Schröder, M. Döblinger, O. Oeckler
Microscopy Conference 2013, Regensburg **2013**

[5] **Optimizing thermoelectric properties of germanium antimony tellurides in different temperature ranges by substitution**
S. Welzmiller, T. Rosenthal, T. Schröder, F. Schleife, S. Schwarzmüller, L. Neudert, K. Nimmrich, P. Ganter, P. Huth, B. Kersting, O. Oeckler
11th European Conference on Thermoelectrics, Noordwijk (Niederlande) **2013**

[6] **Skutterudit in Ge/Sb/Te und Ge/As/Te**
F. Fahrnbauer, T. Rosenthal, S. Maier, M. Kasprick, T. Schröder, O. Oeckler
Hirschegg-Seminar für Festkörperchemie, Hirschegg (Österreich) **2013**

[7] **Tuning real-structure effects and physical properties of germanium antimony tellurides by substitution**
S. Welzmiller, T. Rosenthal, T. Schröder, F. Schleife, S. Schwarzmüller, L. Neudert, P. Ganter, P. Huth, B. Kersting, O. Oeckler
XIV^th European Conference on Solid State Chemistry, Bordeaux (Frankreich) **2013**

[8] **Thermoelectric Germanium Antimony Tellurides: Tuning Nanostructures and Properties by Partial Vacancy Ordering and Doping**
O. Oeckler, T. Rosenthal, S. Welzmiller, T. Schröder, L. Neudert
2nd Inorg. EuCheMS Chemistry Congress, Jerusalem (Israel) **2013**

[9] **Thermal excitation of superionic Li-mobility: Interatomic potentials from (an)-harmonic temperature factors of Li_2Te**
J. Schneider, T. Schröder, M. Hölzel, O. Oeckler, W. W. Schmahl
21st Annual Meeting of the German Crystallographic Society, Freiberg **2013**

[10]* **Filling vacancies in Ge/Sb/Te materials with lithium**
T. Schröder, S. Schwarzmüller, M. N. Schneider, O. Oeckler
20th Annual Meeting of the German Crystallographic Society, München **2012**

**oral presentation*

[11]* **Influence of Sn, In and Li substitution on the structure and the thermoelectric properties of $(GeTe)_n(Sb_2Te_3)$ (1 < n < 20)**
T. Schröder, S. Schwarzmüller, T. Rosenthal, S. Welzmiller, C. Stiewe, O. Oeckler
31st International Conference on Thermoelectrics, Aalborg (Dänemark) **2012**

[12] **$CoSb_3$ precipitates in GST materials – a combination of two promising thermoelectric compounds**
F. Fahrnbauer, T. Rosenthal, S. Maier, T. Schröder, C. Stiewe, O. Oeckler
31st International Conference on Thermoelectrics, Aalborg (Dänemark) **2012**

[13] **$AgIn_xSb_{1-x}Te_2$ – Über Hochdrucksynthesen zu neuen Thermoelektrika**
T. Schröder, T. Rosenthal, D. Souchay, C. Petermayer, S. Grott, O. Oeckler
16. Vortragstagung der Wöhler-Vereinigung, Göttingen **2012**

[14] **Ternary metastable rocksalt-type tellurides**
O. Oeckler, T. Schröder, T. Rosenthal, S. Schwarzmüller, C. Petermayer, D. Souchay, S. Grott
27th European Crystallographic Meeting, Bergen (Norwegen) **2012**

[15] **Substituted Ge-Sb-Te materials: structure, element distribution and thermoelectric properties**
S. Welzmiller, T. Rosenthal, T. Schröder, P. Urban, F. Fahrnbauer, C. Stiewe, O. Oeckler
27th European Crystallographic Meeting, Bergen (Norwegen) **2012**

[16] **New thermoelectrics by combination of $CoSb_3$ with Ge/Sb/Te materials**
F. Fahrnbauer, T. Rosenthal, S. Maier, T. Schröder, C. Stiewe, O. Oeckler
4th EuCheMS Chemistry Congress, Prag (Tschechien) **2012**

[17] **Varying the nanostructure of ternary germanium tellurides and its influence on thermoelectric properties**
T. Rosenthal, T. Schröder, M. N. Schneider, C. Stiewe, O. Oeckler
4th EuCheMS Chemistry Congress, Prag (Tschechien) **2012**

[18] **High temperature neutron powder diffraction of the Li ion conductor Li_2Te**
J. Schneider, M. Hölzel, T. Schröder, O. Oeckler, W. W. Schmahl
13th European Powder Diffraction Conference, Grenoble (Frankreich) **2012**

[19] **Nanostrukturierung von Ge/Sb/Te-Materialien durch $CoSb_3$-Präzipitate – neue vielversprechende Thermoelektrika?**
F. Fahrnbauer, T. Rosenthal, S. Maier, R. Berthold, T. Schröder, O. Oeckler
10. Mitteldeutsches Anorganiker-Nachwuchssymposium, Jena **2012**

[20] **Element- und Leerstellenverteilung in multinären Telluriden und deren physikalische Eigenschaften**
O. Oeckler, S. Welzmiller, T. Rosenthal, T. Schröder, F. Fahrnbauer
16. Vortragstagung der Fachgruppe Festkörperchemie und Materialforschung der Gesellschaft Deutscher Chemiker, Darmstadt **2012**

[21] **Thermoelectric properties and element distribution in multinary antimony tellurides**
S. Welzmiller, T. Rosenthal, T. Schröder, P. Urban, F. Fahrnbauer, C. Stiewe, O. Oeckler
18th International Conference on Ternary and Multinary Compounds,
Salzburg (Österreich) **2012**

[22]* **Metastabile Telluride durch Kristallisation bei hohem Druck**
T. Schröder, O. Oeckler
Hirschegg-Seminar für Festkörperchemie, Hirschegg (Österreich) **2011**

**oral presentation*

[23]* **Thermoelectric properties of metastable Ge/Sb/Te and Ge/Bi/Te compounds**
T. Schröder, M. N. Schneider, T. Rosenthal, P. Urban, F. Fahrnbauer, C. Stiewe, C. Gold, E.-W. Scheidt, W. Scherer, O. Oeckler
9th European Conference on Thermoelectrics, Thessaloniki (Griechenland) **2011**

[24] **Wie Kristalle aufräumen - zeit- und ortsaufgelöste Laue-Beugungsexperimente an fehlgeordneten Ge/Sb/Te-Phasen**
M. N. Schneider, X. Biquard, T. Schröder, P. Urban, O. Oeckler
Festkörperchemie-Treffen "Hemdsärmelkolloqium", Dresden **2011**

[25] **Influence of real-structure effects on the properties of metastable tellurides**
O. Oeckler, T. Schröder, T. Rosenthal, M. N. Schneider
Trilateral Seminar "Advances in Inorganic Crystal Chemistry",
St. Petersburg (Russland) **2011**

[26] **Kubische Telluride von Antimon und Indium mit Silber oder Lithium**
O. Oeckler, S. Schwarzmüller, T. Schröder, S. Welzmiller, D. Souchay
Hirschegg-Seminar für Festkörperchemie, Hirschegg (Österreich) **2011**

[27] **Order-disorder transitions in GeTe-rich germanium antimony tellurides elucidated by *in situ* Laue microdiffraction**
P. Urban, M. N. Schneider, T. Schröder, X. Biquard, O. Oeckler
19th *Annual Meeting of the German Crystallographic Society*, Salzburg (Österreich) **2011**

[28] **Metastabile Phasen von $GeBi_2Te_4$ durch Kristallisation unter Hochdruck**
T. Schröder, M. N. Schneider, A. Eisele, O. Oeckler
15. Vortragstagung der Fachgruppe Festkörperchemie und Materialforschung der Gesellschaft Deutscher Chemiker, Berlin **2010**

[29] **Fehlordnungsvarianten und Nanostrukturen von $GeBi_2Te_4$ und deren Einfluss auf den elektrischen Widerstand**
T. Schröder, M. N. Schneider, T. Rosenthal, A. Eisele, C. Gold, E.-W. Scheidt, W. Scherer, O. Oeckler
15. Vortragstagung der Wöhler-Vereinigung, Freiburg **2010**

[30] **From Phase-Change Materials to Thermoelectrics?**
O. Oeckler, M. N. Schneider, T. Schröder, T. Rosenthal, F. Fahrnbauer, C. Stiewe
3rd International Symposium on Structure-Property Relationships in Solid State Materials, Stuttgart **2010**

[31] **Real-structure effects, diffusion processes and thermoelectric properties of tetradymite-type tellurides and related compounds**
O. Oeckler, M. N. Schneider, T. Rosenthal, T. Schröder, P. Urban, F. Fahrnbauer, C. Stiewe, M. Döblinger
Minerals as Advanced Materials II, Kirovsk (Russland) **2010**

[32] **Real structure of metastable Ge-Sb-Te and Ge-Bi-Te materials**
M. N. Schneider, T. Rosenthal, T. Schröder, O. Oeckler
European Phase Change and Ovonics Symposium, Mailand (Italien) **2010**

[33] **Metastabile (pseudo-)kubische Antimontelluride und verwandte Phasen**
O. Oeckler, P. Urban, T. Schröder, M. N. Schneider
Hirschegg-Seminar für Festkörperchemie, Hirschegg (Österreich) **2009**

[34] **Nitridosilicate im NPO-Zeolith-Typ**
S. Pagano, C. Hecht, O. Oeckler, T. Schröder, W. Schnick
17th Annual Meeting of the German Crystallographic Society, Hannover **2009**

**oral presentation*